Universidad de Alcalá
COMISIÓN DE ESTUDIOS OFICIALES
DE POSGRADO Y DOCTORADO

ACTA DE EVALUACIÓN DE LA TESIS DOCTORAL

(FOR EVALUATION OF THE ACT DOCTORAL THESIS)

Año académico (*academic year):* 2018/19

DOCTORANDO *(candidate PHD)*: **PASTOR GRAELLS, JUAN**
D.N.I./PASAPORTE (*Id.Passport*): ******4315Z**
PROGRAMA DE DOCTORADO *(Academic Committee of the Programme)*: **D441-ELECTRÓNICA: SISTEMAS ELECTRÓNICAS AVANZADOS. SISTEMAS INTELIGENTES**
DPTO. COORDINADOR DEL PROGRAMA *(Department)*: **ELECTRÓNICA**
TITULACIÓN DE DOCTOR EN *(Phd title)*: **DOCTOR/A POR LA UNIVERSIDAD DE ALCALÁ**

En el día de hoy 03/10/18, reunido el tribunal de evaluación, constituido por los miembros que suscriben el presente Acta, el aspirante defendió su Tesis Doctoral **con Mención Internacional** (*In today assessment met the court, consisting of the members who signed this Act, the candidate defended his doctoral thesis with mention as International Doctorate*), elaborada bajo la dirección de (*prepared under the direction of*) SONIA MARTÍN LÓPEZ // HUGO FIDALGO MARTINS.

Sobre el siguiente tema *(Title of the doctoral thesis)*: *CHIRPED-PULSE PHASE-SENSITIVE OPTICAL TIME DOMAIN REFLECTOMETRY*

Finalizada la defensa y discusión de la tesis, el tribunal acordó otorgar la CALIFICACIÓN GLOBAL[1] de (**no apto, aprobado, notable** y **sobresaliente**) *(After the defense and defense of the thesis, the court agreed to grant the GLOBAL RATING (fail, pass, good and excellent)*: SOBRESALIENTE

Alcalá de Henares, a 03 de octubre de 2018

Fdo. *(Signed)*: JUAN DIEGO ANIA

Fdo. *(Signed)*: FERNANDO NAVARRO

Fdo. *(Signed)*: Marcelo Soto

FIRMA DEL ALUMNO (candidate's signature),

Fdo. *(Signed)*: JUAN PASTOR GRAELLS

Con fecha 22 de octubre de 2018 la Comisión Delegada de la Comisión de Estudios Oficiales de Posgrado, a la vista de los votos emitidos de manera anónima por el tribunal que ha juzgado la tesis, resuelve:

☒ Conceder la Mención de "Cum Laude"
☐ No conceder la Mención de "Cum Laude"

La Secretaria de la Comisión Delegada

[1] La calificación podrá ser "**no apto**" "**aprobado**" "**notable**" y "**sobresaliente**". El tribunal podrá otorgar la mención de "cum laude" si la calificación global es de sobresaliente y se emite en tal sentido el voto secreto positivo por unanimidad. (*The grade may be "**fail**" "**pass**" "**good**" or "**excellent**". The panel may confer the distinction of "cum laude" if the overall grade is "Excellent" and has been awarded unanimously as such after secret voting.).*

INCIDENCIAS / OBSERVACIONES:
(Incidents / Comments)

Universidad de Alcalá

COMISIÓN DE ESTUDIOS OFICIALES DE POSGRADO Y DOCTORADO

En aplicación del art. 14.7 del RD. 99/2011 y el art. 14 del Reglamento de Elaboración, Autorización y Defensa de la Tesis Doctoral, la Comisión Delegada de la Comisión de Estudios Oficiales de Posgrado y Doctorado, en sesión pública de fecha 22 de octubre, procedió al escrutinio de los votos emitidos por los miembros del tribunal de la tesis defendida por *PASTOR GRAELLS, JUAN*, el día 3 de octubre de 2018, titulada *CHIRPED-PULSE PHASE-SENSITIVE OPTICAL TIME DOMAIN REFLECTOMETRY*, para determinar, si a la misma, se le concede la mención "cum laude", arrojando como resultado el voto favorable de todos los miembros del tribunal.

Por lo tanto, la Comisión de Estudios Oficiales de Posgrado **resuelve otorgar** a dicha tesis la

MENCIÓN "CUM LAUDE"

Alcalá de Henares, 22 de octubre de 2018
EL VICERRECTOR DE INVESTIGACIÓN Y TRANSFERENCIA

UNIVERSIDAD DE ALCALÁ · VICERRECTORADO DE INVESTIGACIÓN Y TRANSFERENCIA

F. Javier de la Mata de la Mata

Copia por e-mail a:
Doctorando: PASTOR GRAELLS, JUAN
Secretario del Tribunal: FERNANDO B. NARANJO VEGA.
Directores de Tesis: SONIA MARTÍN LÓPEZ//HUGO FIDALGO MARTINS

Universidad de Alcalá

ESCUELA DE DOCTORADO
Servicio de Estudios Oficiales de Posgrado

DILIGENCIA DE DEPÓSITO DE TESIS.

Comprobado que el expediente académico de D./Dª Juan Pastor Graells reúne los requisitos exigidos para la presentación de la Tesis, de acuerdo a la normativa vigente, y habiendo presentado la misma en formato: ☒ soporte electrónico ☐ impreso en papel, para el depósito de la misma, en el Servicio de Estudios Oficiales de Posgrado, con el nº de páginas: 182 se procede, con fecha de hoy a registrar el depósito de la tesis.

Alcalá de Henares a 10 de julio de 2018

Purificación Reviejo

Fdo. El Funcionario

Universidad de Alcalá

Escuela Politécnica Superior

Departamento de Electrónica

"Chirped-Pulse Phase-Sensitive Optical Time Domain Reflectometry"

Autor

Juan Pastor Graells

Directores

Dra. Sonia Martín López

Dr. Hugo Fidalgo Martins

2018

TESIS DOCTORAL

Universidad de Alcalá

DEPARTAMENTO DE ELECTRÓNICA

Edificio Politécnico

Campus Universitario s/n

28805 Alcalá de Henares (Madrid)

Teléfono: 91 885 65 40

Fax: 91 885 65 91

eldep@depeca.uah.es

rector@uah.es

Dra. Sonia Martín López
Dr. Hugo Fidalgo Martins
Dr. Miguel González Herráez

INFORMAN:

Que la Tesis Doctoral titulada "Chirped-Pulse Phase-Sensitive Optical Time Domain Reflectometry" presentada por D. Juan Pastor Graells, y realizada bajo la dirección de los doctores Dª. Sonia Martín López y D. Hugo Fidalgo Martins y Miguel González Herráez como tutor, dentro del campo de los Sensores de Fibra Óptica, reúne los méritos de calidad y originalidad para optar al Grado de Doctor.

Alcalá de Henares, 6 de julio de 2018

Fdo. Dr. Hugo Fidalgo Martins

Fdo. Dr. Miguel González Herráez

Fdo. Dra. Sonia Martín López

Universidad de Alcalá

DEPARTAMENTO DE ELECTRÓNICA

Edificio Politécnico

Campus Universitario s/n

28805 Alcalá de Henares (Madrid)

Teléfono: 91 885 65 40

Fax: 91 885 65 91

eldep@depeca.uah.es

rector@uah.es

Dr. D. Miguel González Herráez, coordinador del Programa de Doctorado "ELECTRÓNICA: Sistemas Electrónicos Avanzados. Sistemas Inteligentes"

INFORMA:

Que la Tesis Doctoral titulada "Chirped-Pulse Phase-Sensitive Optical Time Domain Reflectometry" presentada por D. Juan Pastor Graells, y realizada bajo la dirección de los doctores Dª. Sonia Martín López y D. Hugo Fidalgo Martins, reúne los requisitos científicos de originalidad y rigor metodológicos para ser defendida ante un tribunal. Esta Comisión ha tenido también en cuenta la evaluación positiva anual del doctorando, habiendo obtenido las correspondientes competencias establecidas en el Programa.

Para que así conste y surta los efectos oportunos, se firma el presente informe en Alcalá de Henares, 6 de julio de 2018.

Fdo. Dr. Miguel González Herráez

“Cant de Vicent”

Pense que ha arribat l’hora del teu cant a València.
Temies el moment. Confessa-t’ho: temies.
Temies el moment del teu cant a València.
La volies cantar sense solemnitat,
sense Mediterrani, sense grecs ni llatins,
sense picapedrers i sense obra de moro.
La volies cantar d’una manera humil,
amb castedat diríem. Veies el cant: creixia.
Lentament el miraves créixer com un crepuscle.
Arribava la nit, no escrivies el cant.
[...]
Aquell sol matiner, les Torres dels Serrans
amb aquell breu color inicial de geranis.
Veus, des del menjador, per la finestra oberta,
Benimaclet ací, enllà veus Alboraia,
escoltes des del llit les sirenes del port.

Vicent Andrés Estellés
Burjassot, 4 de setembre de 1924 – València, 27 de març de 1993

Agradecimientos

Las personas a las que primero me tengo que dirigir es a mis directores y mi tutor de tesis: Sonia Martín López, Hugo Fidalgo Martins y Miguel González Herráez. Tengo que darles las gracias por brindarme la oportunidad de trabajar junto a ellos en el grupo de Ingeniería Fótonica (GRIFO) de la Universidad de Alcalá (UAH). Bajo su supervisión, he podido crecer tanto personalmente como profesionalmente durante el tiempo que he pasado en su laboratorio. No sería la persona que soy ahora ni tendría las capacidades que tengo si no hubiera pasado los últimos casi 5 años de mi etapa profesional junto a estos grandes investigadores. Estos años de investigación en el seno de GRIFO han podido ser posibles gracias a la financiación conseguida por los investigadores responsables de mi periodo formativo. En particular el proyecto DESAFIO (donde Sonia Martin López es la investigadora principal) del Ministerio de Economía y Competitividad del Gobierno de España a través de la ayuda para la contratación de personal investigador (FPI) que ha financiado gran parte de mi etapa en la universidad. También debo nombrar al proyecto U-FINE (donde Miguel González Herráez es el investigador principal) financiado por la *European Research Council* (ERC) a través del programa *Starting Grant*, el cual ha pagado gran parte del instrumental de las instalaciones del grupo de investigación. Junto a estos proyectos, el proyecto SINFOTON de la Comunidad de Madrid también ha sido crucial en el correcto desarrollo de esta tesis doctoral.

En igual medida, quisiera agradecer a todas las personas que integran GRIFO. Hemos podido compartir muchos seminarios, congresos, comidas y experiencias. Mucho conocimiento que he plasmado en esta tesis doctoral y que me llevo conmigo lo he podido aprender de los distintos profesores y estudiantes del grupo. Me gustaría nombrar especialmente a los doctores Fernando Naranjo Vega y Óscar Esteban Martínez, los cuales he podido tener como profesores en el máster. Respecto a mis compañeros de laboratorio, comidas y viajes no puedo olvidarme de Xabier, Alexia, Alejandro, Andrés, Rosario, Regina, Luis, Marco, Arantxa, Laura, Javier Tejedor, Javier Nuño, Paco y Piedad. Feliz de seguir trabajando con alguno de la lista y que muchos (y sus respectivas parejas) sigan siendo compañeros de tapas. Me gustaría hacer hincapié en que los tres primeros de la lista, junto a Hugo (en aquel entonces aun estudiante de doctorado), han supuesto un referente para mí de los que he aprendido y sigo aprendiendo mucho, sobre todo en mi llegada inocente e inexperta al laboratorio.

Me gustaría agradecer al profesor José Luis Cruz, por iniciarme en la Universitat de València (UV) en el mundo de la fibra óptica. De él puedo decir que no solo he aprendido las materias que me ha impartido, sino también su correcta forma de ver y trabajar en la gestión universitaria. Pero sobre todo, por recomendarme para venir a trabajar a la UAH junto a mis directores y por haber seguido siendo un mentor para mí tras terminar mi etapa en la UV. Me gustaría también dedicarle unas palabras al profesor Benito Gimeno Martínez, por sus increíbles clases de electromagnetismo y electrodinámica clásica y por supervisar mi iniciación en el mundo de la investigación y también seguir siendo un referente al que acudir cuando lo he necesitado.

No querría olvidarme de mi paso por el Institut National de la Recherche Scientifique (INRS) de Montreal (Canadá) donde puede pasar 3 espectaculares meses bajo la supervisión del reconocido investigador José Azaña y trabajando codo con codo con Luis Romero Cortés, a quién le deseo grandes triunfos en el futuro. A parte de mejorar mi nivel de inglés, obtener considerables resultados que se muestran en esta tesis y aprender cosas que seguro me resultarán de utilidad en el futuro, puedo decir que mi estancia en el INRS también ha sido una experiencia a título personal que no podré olvidar.

Durante mi etapa predoctoral he podido trabajar, conocer y compartir conocimiento y experiencias con mucha gente de distintos grupos de investigación. Por parte del Consejo Superior de Investigaciones Científicas (CSIC) me gustaría nombrar a Pedro Corredera Guillén, Concepción Pulido, Aitor Villafranca y Juan Diego Ania Castañón. También me gustaría agradecer a Marcelo Soto Hernández, en aquel entonces investigador de la École Polytechnique Fédérale de Lausanne (EPFL), por sus aportaciones y el tiempo compartido como investigador visitante en la UAH.

Debo agradecer también a los miembros del tribunal y evaluadores externos por su tiempo leyendo y evaluando este manuscrito y el acto de defensa: José Azaña, Marcelo Soto, Juan Diego Ania y Fernando Naranjo.

Agradecer a las personas comprometidas con la gestión del Departamento de Electrónica y los planes de estudios en el que éste participa. En particular, a la directora del Departamento de Electrónica Sira Palazuelos y al personal de administración del departamento.

A mi familia, por dármelo todo. Porque sin ellos no sería quien soy ni habría llegado hasta donde he llegado. Pero sobre todo por su apoyo incondicional y ayuda estos años a pesar de la distancia.

A mis amigos valencianos por esos momentos en los que me he podido evadir cuando había demasiada presión. Porque es necesario disfrutar de la vida y con ellos se hace más fácil.

Y por último a la persona más importante, Paula. Porque estoy seguro de que sin ti no habría llegado ni a la mitad del camino (partiendo de que antes de conocerte no daba un palo al agua). Por los buenos momentos, por tu ayuda en todos los sentidos y por tu cariño, ¡GRACIAS!

Resumen

El mundo actual funciona gracias a las grandes infraestructuras que dotan de energía y transporte seguros a sus ciudadanos. Dichas infraestructuras (presas, diques, gaseoductos, oleoductos, puentes, líneas de ferrocarril, carreteras...) típicamente presentan grandes dimensiones y es especialmente difícil monitorizar su buen funcionamiento y su salud estructural además de protegerlas de posibles amenazas. Los sensores distribuidos de fibra óptica son una solución fiable y rentable para esta problemática, ya que permiten medir vibraciones, deformaciones y temperatura a lo largo de todos los puntos de una fibra óptica estándar de comunicaciones.

Los sensores de fibra óptica basados en *scattering* Rayleigh son particularmente útiles cuando las medidas deben ser realizadas en tiempo real, como por ejemplo en la detección y caracterización de vibraciones. En este trabajo de tesis, se ha realizado un estudio acerca de distintas soluciones y alternativas a las limitaciones de la tecnología ϕOTDR. Se ha propuesto una nueva técnica, derivada de ésta, que ofrece unas prestaciones que superan notablemente a las de los sistemas ϕOTDR tradicionales.

Para ello, en primer lugar, se ha procedido a realizar un estudio en profundidad de los fundamentos y el estado del arte de las técnicas de monitorización basadas en reflectometría óptica en el dominio del tiempo (OTDR, por sus siglas en inglés) y, en particular, sobre la implementación sensible a la fase, también conocida como ϕOTDR.

Se ha estudiado la limitación en rango y resolución de los sistemas ϕOTDR principalmente asociada a la aparición de efectos no lineales como la Inestabilidad de Modulación (MI, por sus siglas en inglés). Actualmente, un ϕOTDR tradicional presenta una resolución máxima del orden de los 10 metros para un rango de medida del orden de pocas decenas de km (si no se aplica ningún tipo de técnica de amplificación distribuida). Además de estudiar esta limitación y a qué es debida, se han propuesto dos técnicas para mitigar los efectos perjudiciales de la MI. En primer lugar, se ha realizado un estudio del efecto de la forma de los pulsos ópticos empleados en el sensor en la traza retrodispersada en un ϕOTDR. Se ha podido comprobar cómo los pulsos triangulares o gaussianos presentan mayor robustez que los pulsos rectangulares, tradicionalmente empleados, frente a la MI. En segundo lugar, se ha propuesto una técnica basada en el concepto de Amplificación de Pulsos Chirpeados (CPA, por sus siglas en inglés), que ha permitido desarrollar un ϕOTDR con resoluciones milimétricas. Hasta el momento ningún ϕOTDR había podido llegar a tales resoluciones, lo que abre un nuevo abanico de aplicaciones a la tecnología OTDR donde se requiera alta resolución espacial en la medida.

También se ha estudiado la otra gran limitación de este tipo de sensores: su comportamiento no lineal ante una perturbación. Actualmente, salvo que se implementen técnicas de recuperación de fase o barridos en longitud de onda que implican más complejidad, coste y tiempo de medida, no es posible realizar medidas cuantificables de temperatura o deformaciones. Del mismo modo, tampoco se pueden realizar medidas acústicas reales. En este trabajo, en primer lugar, se pro-

pone emplear la técnica de Reconstrucción de Fase empleando Diferenciación Óptica Ultrarápida (PROUD, por sus siglas en inglés) para recuperar el campo complejo de una señal ϕOTDR. Con esta medida, el sensor pasaría a comportarse de forma lineal sin la complejidad intrínseca de los métodos tradicionales de detección de fase. En segundo lugar, y de aquí viene el nombre de esta tesis doctoral, se propone el uso de pulsos chirpeados en los sensores ϕOTDR. La nueva técnica llamada Chirped-Pulse ϕOTDR, ha permitido la medida de forma lineal de cambios de temperatura y deformaciones, en un único disparo y sin la necesidad de realizar barridos en frecuencia o implementar detección coherente. A lo largo de este trabajo, se han alcanzado resoluciones de 0.5mK/4nε y se ha demostrado la posibilidad de hacer medidas acústicas reales. También se han estudiado las limitaciones de esta técnica y propuesto varias soluciones. Se ha demostrado que el ruido de fase del láser empleado en el sistema, puede ser mitigado con esta nueva técnica. Además, se ha propuesto el uso de amplificación distribuida basada en *scattering* Raman estimulado para alcanzar rangos de medida mayores, hasta 75 km con una resolución espacial de 10 m.

Abstract

The world today works thanks to big infrastructures, which provide safe energy and transport to its citizens. Such infrastructures (dams, pipelines, bridges, railways, roads...) typically present huge dimensions. Thus, the monitoring of its proper functioning and structural health and protecting them from possible threats is particularly difficult. Distributed optical fiber sensors are a reliable and efficient solution for this problem, since they allow the measurement of vibrations, strain and temperature along all the points of a conventional telecom fiber.

Distributed optical fiber sensors based on Rayleigh scattering are particularly useful when real time measurements are required (i. e. vibration detection). In this work, a study about different solutions and alternatives to ϕOTDR technology limitations has been realized. A new technique, derived from ϕOTDR, that offers performance features that are significantly superior to the ϕOTDR features, has been proposed.

To do this, first, a detailed study of the fundamentals and the state-of-the-art of the distributed monitoring techniques based on Optical Time Domain Reflectometry (OTDR), and particularly about the phase-sensitive implementation of OTDR (ϕOTDR), has been realized.

The limitation in range and resolution of ϕOTDR systems associated to the onset of non-linear effects such as Modulation Instability (MI) has been studied. A traditional ϕOTDR presents a maximum spatial resolution of tens of meters for a sensing range about a few tens of kilometers (if no distributed amplification technique is implemented). Two techniques for mitigating the non-desired MI effect were proposed. First, the impact of the probe pulse shape in the backscatter trace of ϕOTDR-based sensing systems is studied. The results show that Gaussian and triangular-shaped pulses present higher robustness against MI than the conventional square-shaped pulses. Secondly, a new technique based on the concept of Chirped Pulse Amplification (CPA) which achieves millimetric resolutions has been proposed. This new ϕOTDR performance opens to a wide range of applications where high spatial resolutions are required.

Another important limitation of these sensors has also been studied: its non-linear behavior when a perturbation is applied. Unless phase recovery techniques or frequency sweeps are implemented (increasing the complexity, cost and measurement time), quantifiable temperature and strain sensing is not possible using ϕOTDR technology. In the same way, real acoustic sensing is not possible either. To solve this, two techniques are proposed. First, the possibility of using Phase Reconstruction Using Optical Ultrafast Differentiation (PROUD) for recovering the complex field of the backscattered ϕOTDR signals is analyzed. Implementing PROUD, linear measurements would be possible without the intrinsic complexity of traditional coherence detection. Secondly, the use of chirped-pulses in ϕOTDR sensors is proposed. The new technique has been named Chirped-Pulse ϕOTDR. This new technique allows for the measurement of distributed strain and temperature changes, in a single shot and without the requirement of a frequency scan or coherent detection. Temperature/strain resolutions of 0.5mK/4nε and real

acoustic sensing have been demonstrated along this work. The limitations of this technique have also been studied and some solutions proposed. A method for mitigating the induced uncertainty introduced by the laser phase noise is proposed. Furthermore, the sensing range of this new sensor is increased using distributed amplification based on stimulated Raman scattering, achieving a sensing length of 75 km with 10 m spatial resolution.

Contents

List of Figures

List of Tables

Chapter 1

Introduction

1.1 Motivation

Large infrastructures have played a very important role in the development of civilizations from the beginning of humanity. The evolution of these facilities has been one of the key points in the periods of the history in which humans have got relevant improvements in their quality of life. Nowadays, they are very present around as. Dams and dikes are able to control water level in rivers and coasts. This in turn provides water supply, energy generation and land reclaiming from the sea. Furthermore, connection between cities and countries would not be possible without the use of bridges, highways, railways and airports. Unquestionably, all these infrastructures, and in general most of the services that society demands, require the production and transport of energy by means of power stations, pipelines and high power lines. What all these infrastructures have in common is that a failure or damage in their integrity (deliberate or not) can result in huge material, environmental and human losses. For this reason, it is fundamental the continuous monitoring of these structures for their integrity preservation, controlling their structural health or anticipating possible threats.

Until the end of the 20th century, the use of electrical sensors has been widely developed. However, these may not be suitable for some applications. Some structures can present strong electromagnetic fields that can disturb the reading of the sensors, such railways or energy transportation. Additionally, on corrosive environments or with risk of deflagration, the use of these sensors is not adequate either. Using the same examples, these structures are typically characterized by being considerably large and they can cover tens of kilometers. In that case, long cables are required which transfers noise to the signal and also a great amount of attenuation, thus limiting the maximum distance among the sensing elements. Furthermore, the complexity, price and weight of the sensing grid is increased when hundreds or thousands of sensing points are required for the full characterization of large structures.

Due to these impediments, in 1960s, fiber optic sensors attracted considerable attention thanks to their interesting capabilities and properties [1]. Optical fiber presents ultra-low loss (from 0.20 dB/km to 0.35 dB/km), large bandwidth, immunity to electromagnetic interference, low cost, small size and light weight. They can measure physical, chemical, biological or other quantities by detecting the variations of optical properties, such as intensity, frequency, polarization and phase. The most well-known fiber sensor is the Fiber Bragg Grating (FBG), which reflects a temperature/strain-dependent light wavelength [2]. It is considered a punctual sensor due to the physical parameter is measured in the fiber position where the FBG is placed. Using many FBG sensors, by means of wavelength multiplexing, it is possible to develop quasi-distributed sensing. However, it increases the system complexity and cost.

Distributed Optical Fiber Sensors (DOFSs) allow for the continuous measurement of different physical parameters (temperature, strain, birrefringence...) over long fiber distances and therefore provide a cost-effective solution for the monitoring of large civil infrastructures. DOFSs are based on Rayleigh, Brillouin or Raman scattering phenomena, which depend on strain, temperature or birrefringence changes within the optical fiber [3].

Using Raman-based sensing for static measurements, spatial/temperature resolutions of 1m/3K have been demonstrated over 26 km with measurement times of a few minutes [4, 5]. With traditional Brillouin Optical Time Domain Analysis (BOTDA), spatial/temperature/strain resolutions of 2m/1.2K/20$\mu\varepsilon$ over 100 km have been demonstrated [6], but, due to the requirement of a large of number averages and a frequency sweep, the measurement times are still typically of several minutes. Recently, schemes using Brillouin based sensing have been proposed for dynamic strain sensing [7–10]. In 2011, samplings of 20 Hz were demonstrated in a version of Brillouin Optical Correlation Domain Analysis (BOCDA) [7]. However, the range

is typically limited to 100 m in this type of sensors. With a fast implementation of BOTDA [8], samplings of 10 kHz with a standard deviation of strain/temperature of $5\mu\varepsilon/0.25$K were demonstrated, although the technique was best suited for short fibers (100 meters in [8]) and a low number of averages, as a frequency sweep was still required. The same group later demonstrated a practical utilization of the slope-assisted BOTDA to allow for strain measurements without requiring a frequency sweep [9]. In this case, the dynamic response is achieved by working tuned to the slope of the Brillouin gain response of the fiber. The proposed technique presented several limitations when compared to the conventional BOTDA, particularly concerning the strain dynamic range, which is limited by the width of the Brillouin gain spectrum of the tested fiber. Brillouin Optical Time Domain Reflectometry (BOTDR) implementations also allow to do dynamic strain measurements over 2 km with an accuracy of $50\mu\varepsilon/2.5$K and spatial resolution of 1.3 m [10]. However, sampling ratios higher than few Hz have not been achieved.

Rayleigh-based sensing is the technique in which this dissertation is focused on. It typically requires lower averaging than Raman or Brillouin, and is therefore better suited for dynamic measurements as vibration/acoustic sensing. In the frequency domain, Optical Frequency Domain Reflectometry (OFDR) can provide high spatial resolutions [11–18], but is typically limited to short fiber sections due to the sweeping laser requirements. As for measurements in the time domain, Phase-Sensitive Optical Time Domain Reflectometry (ϕOTDR) can perform measurements over 100 km with spatial resolutions of a few meters [19–27]. However, true strain/temperature readings can not be performed with this system unless complex coherent detection methods are deployed [28–33].

On the one hand, traditional ϕOTDR (without coherent detection) allows for distributed vibration measurements with a high bandwidth, only limited by the fiber length, ranging from tens of kHz for a few kilometers [34,35], to hundreds of Hz for more than 100 km [21–23]. These measurements however, are based on intensity variations of the ϕOTDR signal which does not show a linear variation with the applied perturbation. On the other hand, by precisely sweeping the frequency of the pulses step by step, ϕOTDR has been shown to allow for very sensitive measurements of refractive index variations, which can be used for very high resolution temperature [36], strain [37] and birefringence [38, 39] measurements. For instance, the demonstrated strain/temperature resolutions of $10\text{n}\varepsilon/1$mK [37] are three orders of magnitude below the typical resolutions of $20\mu\varepsilon/1$K provided by Brillouin sensors. However, due to the requirements of a frequency scan, in this case the measurement time and complexity of the system is increased. Thus, generally this technique is not well-suitable for dynamic sensing. By recovering the phase of the ϕOTDR signal, the dynamic measurement of strain has been demonstrated [31–33]. In this case however, the system is more complex and laser coherences of at least the fiber length are required in order to avoid noise when beating the signal with the local oscillator. The long term-stability of such systems (i.e. after several minutes or hours) and therefore feasibility for static temperature measurements over several hours has also not been clearly addressed either. Moreover, some applications require high resolution measurements, in some cases, millimetrical resolutions. This is the case of wall or pipeline crack development monitoring. To achieve these high resolutions it is required to employ extremely short pulses, reducing considerably the Signal to Noise Ratio (SNR) of the system which makes the measurement impossible in some cases.

Overall, this thesis is motivated by the mentioned two main limitations: the Signal to Noise Ratio and non-linear response of the ϕOTDR measurements. First, the beneficial effect of using Gaussian and triangular-shaped pulses against Modulation Instability is demonstrated. Second, or the first time to our knowledge, it is proposed a ϕOTDR capable to develop millimeter spatial resolution measuring. Thirdly, the possibility of using Phase Reconstruction using Optical Ultrafast Differentiation (PROUD) for linear sensing is discussed. Fourthly, a ϕOTDR based sensor that varies linearly with the applied perturbations is proposed. Thus, allowing for the

measurement of distributed strain and temperature changes, in a single shot and without the requirement of a frequency scan or coherent detection. Finally, the performance is improved by mitigating the effect of the laser phase-noise on this new sensor and increasing the sensing range using distributed amplification.

1.2 Objetives

From the previously cited motivations, the following objectives have been addressed over this thesis work:

- To study the main optical effects that light suffers when propagates through optical fibers relevant to distributed optical fiber sensors.
- To perform a broad study of the current limitations of the conventional ϕOTDR sensing scheme, especially the non-linear behavior with the applied perturbations and the SNR.
- To analyze the impact of the probe pulse shape in the backscattered trace of ϕOTDR-based sensing systems.
- To propose a ϕOTDR combined with Chirped Pulse Amplification (CPA) concepts to perform a millimeter spatial resolution ϕOTDR by increasing the SNR of the system.
- To analyzed the possibility of implementing Phase Reconstruction using Optical Ultrafast Differentiation (PROUD) in ϕOTDR to turn the sensor into lineal.
- To provide a method based on ϕOTDR using chirped pulses to allow for the measurement of distributed strain and temperature changes, in a single shot and without the requirement of a frequency scan or coherent detection. This new sensing method will be named Chirped-Pulse ϕOTDR.
- To analyze the impact of the laser phase-noise in Chirped-Pulse ϕOTDR systems and to propose a method to mitigate this detrimental effect.
- To increase the maximum measurable range of Chirped-Pulse ϕOTDR using first-order Raman amplification.

1.3 Structure of the Work

The work is divided in eight chapters. The six main ones content the eight objectives treated in this thesis dissertation and defined in the previous section:

- Chapter 2: "General Concepts in Fiber Optics" covers the basic theoretical fundamentals of the physical processes that take place within the fiber when implementing a ϕOTDR sensor. Losses and dispersion are discussed as linear effects. Then, some non-linear effects relevant to the content of the thesis are discussed: non-linear refraction, Self-Phase Modulation (SPM) and Modulation Instability (MI). The concept of Chirped Pulse Amplification (CPA) is introduced since it is the basis of Chapter 8. ϕOTDR is based on the use of highly coherent sources. To understand the concept of optical coherence, it is also explained in this chapter. All fiber sensors and distributed amplification processes are based on scattering processes. Thus, the three scattering processes (Rayleigh, Brillouin and Raman) are explained at the end of this chapter.

- Chapter 3: "ϕOTDR: Principles, Limitations and State of the Art" focuses on the principle of operation enabling the sensing technique, its main limitations and the current state of the art, providing an insight on some of the most-used approaches to enhance the performance.

- Chapter 4: "Addressing the Limits of ϕOTDR" presents two techniques to increase the SNR in ϕOTDR systems and one to turn ϕOTDR into linear. In the first part, the impact of the probe pulse shape in the backscattered trace of ϕOTDR-based sensing systems is analyzed. The tested shapes were: Gaussian-like, triangular, super-Gaussian (order 2), and rectangular. The results show Gaussian and triangular-shaped pulses show a better behavior in terms of evolution of the visibility along the distance, which should reflect into a better sensing performance. In the second part, the possibility of using CPA to increase the SNR in ϕOTDR systems is presented. An SNR increase of 20 dB over the traditional ϕOTDR architecture is demonstrated. This method allows for the detection of events with millimeter spatial resolution. Finally, the use of Phase Reconstruction using Optical Ultrafast Differentiation (PROUD) in ϕOTDR systems is analyzed. PROUD is a self-referenced technique which allows recovering the instantaneous frequency and phase of arbitrary optical signals in which no local oscillator is required. Thus, the method does not present polarization or phase-noise impediments. PROUD requires a linear optical filter with a bandwidth little wider than the optical signal to sample. Since the employed optical pulses in a traditional ϕOTDR present tens or at most a hundred of MHz, the required filter is not common. For this reason, no experimental phase-recovery of ϕOTDR signal has been developed since the laboratory did not have the adequate optical filter. The possibility of implementing PROUD to ϕOTDR signals is analyzed recovering the instantaneous frequency profile of optical pulses which have suffered non-linear propagation. Since the bandwidth of these pulses was around GHz, a simple and cheap Dense Wavelength Division Multiplexer (DWDM) allow us to develop the measurements. The technique shows a great potential if the optical filter fits correctly with the optical signal.

- Chapter 5: "Chirped-Pulse Phase Sensitive Optical Time Domain Reflectometry" presents a new method based on ϕOTDR using chirped pulses to allow for the measurement of distributed strain and temperature changes, in a single shot and without the requirement of a frequency scan or coherent detection. Temperature/strain resolutions of 0.5mK/4nε and real acoustic sensing are demonstrated in this chapter.

- Chapter 6: "Laser Phase-Noise Cancellation in Chirped-Pulse ϕOTDR" presents a theoretical and experimental analysis of the impact of the laser phase-noise in Chirped-Pulse ϕOTDR systems. Besides, a simple technique is presented to mitigate this effect. A SNR increase of 17 dB when this technique is implemented is demonstrated.

- Chapter 7: "Long Range Chirped-Pulse ϕOTDR" presents a Chirped-Pulse ϕOTDR assisted by first-order Raman amplification. Vibration measurements along 75 km with 10 meter spatial resolution are demonstrated.

Chapter 2

General Concepts in Fiber Optics

2.1 Introduction

In this chapter, we will describe some of the most relevant effects that can affect to the characteristics of any optical wave when it is traveling in a medium. Most of the times, the explanation and the theoretical models will be focused on fiber optics since it is the medium employed in this dissertation.

Firstly, the propagation of light in the linear regime will be described, presenting an overview of the losses and chromatic dispersion. Then, we will continue with the non-linear effects, which have a detrimental effect on the proper performance of our systems. The non-linear effects discussed are: the non-linear dependence of the refractive index on the optical power, the Self-Phase Modulation (SPM) and the Modulation Instability (MI). Next, it will be proposed the concept of Chirped Pulse Amplification (CPA) as a method to avoid the advent of non-linear effects in amplification processes. As it will be explained in future chapters, the sensor with which we have worked during this dissertation is based on Rayleigh scattering. Furthermore, Raman scattering was implemented in order to increase the maximum measurable range of the sensor. Thus, it is important to have a good understanding of the scattering effects. For this reason, an explanation of the physical principles behind Rayleigh and Raman scattering is developed in this chapter.

2.2 Interaction Light-Matter in Fiber Optics

The induced polarization $\mathbf{P}$ in a fiber when a electromagnetic wave $\mathbf{E}$ propagates through can be expressed as:

$$\nabla^2\mathbf{E} + \frac{1}{c^2}\frac{\partial^2\mathbf{E}}{\partial t^2} = -\mu_0\frac{\partial^2\mathbf{P}}{\partial t^2} \tag{2.1}$$

where t is the time parameter and c and μ_0 are the speed of light and the magnetic permeability in the vacuum, respectively. This relationship comes from the Faraday's Law considering some particularities of the optical fiber: it is a non-magnetic and dielectric medium (the induced magnetic polarization is zero and there are not free charges present) [40].

The relation between the induced polarization $\mathbf{P}$ and the electromagnetic wave $\mathbf{E}$ can also be expressed as a power of series as:

$$\mathbf{P}(\mathbf{r},t) = \varepsilon_0 \cdot \left(\chi^{(1)} \cdot \mathbf{E}(\mathbf{r},t) + \chi^{(2)} : \mathbf{E}\mathbf{E}(\mathbf{r},t) + \chi^{(3)} \vdots \mathbf{E}(\mathbf{r},t)\mathbf{E}(\mathbf{r},t)\mathbf{E}(\mathbf{r},t) + \ldots\right) \tag{2.2}$$

where ε_0 is the electric permittivity of free space and $\chi^{(1)}$ and $\chi^{(n)}$ $(n = 2, 3, \ldots)$ are the tensors that describe the linear and non-linear relationship between the polarization and the electric field, respectively. Thus, the induced polarization response in Equation 2.2 can be divided into two terms:

$$\mathbf{P} = \mathbf{P}_{\mathrm{L}} + \mathbf{P}_{\mathrm{NL}} \tag{2.3}$$

Typically, for condensed matter, $\chi^{(1)}$ is of the order of the unit, $\chi^{(2)} \approx 10^{-12}$ m/V and $\chi^{(3)} \approx 10^{-24}$ m^2/V^2 [41]. For this reason, non-linear propagation should be considered only when high

power is injected in a medium. If so, in our work regimes during this thesis, models can describe well the non-linear propagation neglecting $\chi^{(n)}$ of higher orders than three. Furthermore, as it was previously mentioned, the thesis is focused on distributed fiber sensors. Hence, the propagation medium will be always optical fibers and particularly silica (SiO_2) fibers. Since SiO_2 is a symmetric molecule and therefore its structure presents inversion symmetry, the even tensors $\chi^{(2n)}$ $(n = 1, 2, \ldots)$ are zero.

2.3 Linear Propagation

The propagation of an electromagnetic wave $\mathbf{E}$ through a medium is considered lineal when the optical power is below levels at which the non-linear coefficients become relevant. In that case, the induced polarization response $\mathbf{P}_{\mathrm{L}}$ of the medium to this electromagnetic wave is:

$$\mathbf{P}_{\mathrm{L}}(\mathbf{r}, t) = \varepsilon_0 \cdot \chi^{(1)} \cdot \mathbf{E}(\mathbf{r}, t) \tag{2.4}$$

where $\mathbf{r}$ is the position vector and $\chi^{(1)}$ is the linear optical susceptibility which can be described in the frequency domain as:

$$\chi^{(1)}(\omega) = \frac{1}{\varepsilon_0} \cdot \frac{\mathbf{P}_{\mathrm{L}}(\omega)}{\mathbf{E}(\omega)} \tag{2.5}$$

where ω is the optical frequency. The frequency dependent refractive index n, attenuation α and relative permittivity ε_{r} of the fiber are related to $\chi^{(1)}$ through [40]:

$$n(\omega) = 1 + \frac{1}{2}\,\mathrm{Re}[\chi^{(1)}(\omega)] \tag{2.6}$$

$$\alpha(\omega) = \frac{\omega}{nc}\,\mathrm{Im}[\chi^{(1)}(\omega)] \tag{2.7}$$

$$\varepsilon_{\mathrm{r}}(\omega) = 1 + \chi^{(1)}(\omega) \tag{2.8}$$

The relative permittivity is defined as the ratio of the absolute permittivity of the material ε and the permittivity of vacuum ε_0 ($\varepsilon_{\mathrm{r}}(\omega) = \varepsilon(\omega)/\varepsilon_0$). Considering only the linear induced polarization $\mathbf{P}_{\mathrm{L}}$, Equation 2.1 can be rewritten as:

$$\nabla^2\mathbf{E} + \frac{1}{c^2}\frac{\partial^2\mathbf{E}}{\partial t^2} = -\mu_0\frac{\partial^2\mathbf{P}_{\mathrm{L}}}{\partial t^2} \tag{2.9}$$

Substituting Equation 2.4 in 2.9, considering that the speed of light in the vacuum is defined as $c = 1/\sqrt{\mu_0\varepsilon_0}$ and assuming no losses within the fiber, the electric field $\mathbf{E}$ in the frequency domain will be obtained by solving the next equation:

$$\nabla^2\widetilde{\mathbf{E}} + n^2(\omega)\frac{\omega^2}{c}\widetilde{\mathbf{E}} = 0 \tag{2.10}$$

The generic Equation 2.10 can be solved considering the three components (x, y and z). In the case of optical fibers however, considering the cylindrical symmetry, usually only one axis is considered, typically $\widetilde{E}_z(\mathbf{r},\omega)$. Developing the variable separation method, the fundamental mode propagated in the fiber is:

$$\widetilde{E}_z(r,\omega) = \widetilde{A}(\omega)\cdot F(\rho_c)\cdot \exp\left(i\beta z\right) \tag{2.11}$$

where ρ_c is a radial coordinate (there is cylindric symmetry), $\widetilde{A}(\omega)$ is an amplitude term, z is the traveled distance and β is the fiber propagation constant. The distribution of the fundamental mode field $F(\rho_c)$ follows a Gaussian approachable law through:

$$F(\rho_c) \simeq \exp\left(-\frac{\rho_c^2}{\rho_{cw}^2}\right) \tag{2.12}$$

where ρ_{cw} measures the effective radius that occupies the mode. The $2\rho_{cw}$ quantity is denominated as the diameter of the modal field [42].

2.3.1 Optical Losses: Absorption and Scattering

Optical signals suffer power losses during their propagation along silica fibers. This attenuation can be described by the following decreasing exponential [40]:

$$P_T(L) = P_0\cdot e^{-\alpha L} \tag{2.13}$$

where P_0 is the power launched at the input of a fiber, $P_T(L)$ is the power after traveling along a distance L and α is the attenuation constant of the total fiber losses from all sources of that fiber. Generally the attenuation α is expressed in dB/km using the following relation:

$$\alpha_{dB} = \frac{10}{L}\cdot \log\left(\frac{P_T}{P_0}\right) = 4.343\alpha \tag{2.14}$$

The main sources of attenuation in an optical fiber can be broadly classified into two groups: absorptive and radiative [43].

Regarding absorption losses, silica glass has electronic resonances in the Ultraviolet (UV) region and vibrations resonances in the Far-Infrared (FIR) region. However, the most important impurity affecting fiber loss is the OH^- ion, which has a fundamental vibrational absorption peak at ~ 2.73 μm and three overtones near 1.37 μm, 1.23 μm and 0.95 μm [44].

Finally, Rayleigh scattering is predominantly responsible for radiative losses. It is a fundamental mechanism that is caused by small-scale (compared to the wavelength of the lightwave) inhomogeneities that are frozen into the fiber. These inhomogeneities are produced during the fabrication of the fiber and results in composition and density fluctuations. The loss due to Rayleigh scattering is proportional to λ^{-4} and follows the next relation:

$$\alpha_R(\lambda) = C_R/\lambda^4 \tag{2.15}$$

where the constant C_R is in the range of 0.7-0.9 dBμm^4/km depending on the constituents of the fiber core. Around $\lambda = 1.55$ μm, the attenuation due to Rayleigh scattering is $\alpha_R = 0.12$–0.15 dB/km, being the dominant loss in silica fibers.

Figure 2.1 shows the typical loss spectrum of an optical silica fiber. It is easy to observe the relative minimum of losses between the OH^- absorption peak and the infrared (near 1.55 μm). Here, the modern fibers exhibit a loss of ~ 0.2 dB/km.

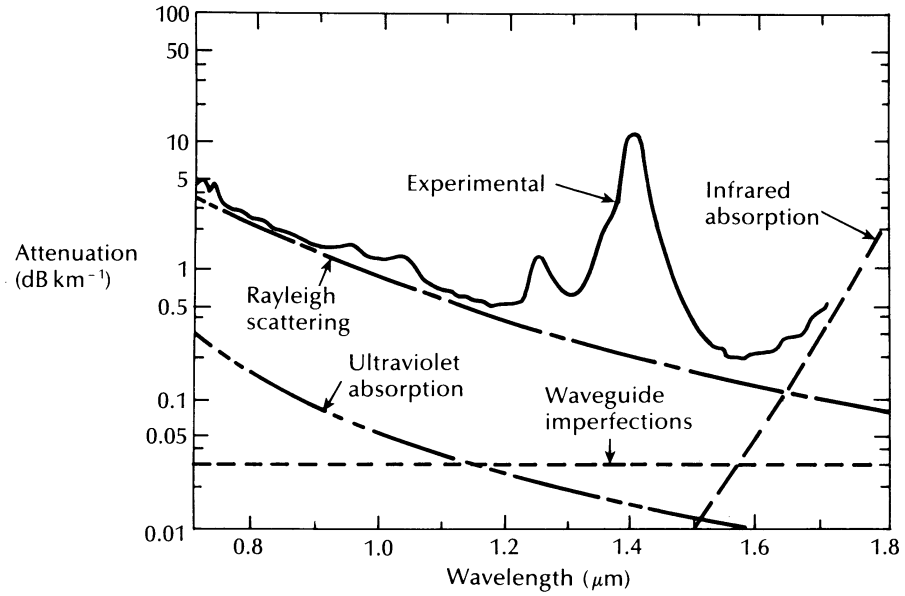

Figure 2.1: Loss spectrum of a silica fiber [43].

2.3.2 Phase Velocity, Group Velocity and Chromatic Dispersion

Fiber dispersion plays a critical role in the propagation of short optical pulses because different spectral components contained in the pulse travel at different speeds. This is given by the phase velocity:

$$v_p(\omega) = \frac{c}{n(\omega)} \tag{2.16}$$

Mathematically, the effects of fiber dispersion are accounted for by expanding the fiber propagation constant β in a Taylor series around the frequency ω_0 at which the pulse spectrum is centered [40]:

$$\beta = \frac{\omega \cdot n(\omega)}{c} = \beta_0 + \beta_1(\omega - \omega_0) + \frac{1}{2}\beta_2(\omega - \omega_0)^2 + \cdots \tag{2.17}$$

where

$$\beta_m = \left(\frac{d^m \beta}{d\omega^m}\right)_{\omega=\omega_0} \qquad (m = 0, 1, 2, \ldots) \tag{2.18}$$

Group velocity (v_g) is defined as the derivative of the frequency versus the propagation constant, and equals the inverse of β_1:

$$v_g = \frac{d\omega}{d\beta} = \frac{1}{\beta_1} \tag{2.19}$$

Group velocity is the velocity at which the envelope of an optical pulse moves through the fiber. Since β and ω are not necessarily linearly related (see Equation 2.17), v_p and v_g are not necessarily equal.

The variation of the group delay experienced by the different spectral components around the central frequency ω_0 is given by β_2:

$$\beta_2 = \frac{d^2\beta}{d\omega^2} = \frac{d\beta_1}{d\omega} = \frac{d}{d\omega}\left(\frac{1}{v_g}\right) = \frac{d\tau_g}{d\omega} \tag{2.20}$$

where τ_g is the group delay for unit of length. Therefore, β_2 is responsible for the temporal broadening of the pulses that propagate in linear regime along the fiber and it is known as Group-Velocity Dispersion (GVD) parameter [40,45]. Another parameter commonly used in the fiber-optics literature is the chromatic dispersion coefficient D, which is related to β_2 by the relation:

$$D = \frac{d\beta_1}{d\lambda} = -\frac{2\pi c}{\lambda^2}\beta_2 \tag{2.21}$$

where β_2 is measured in $\mathrm{ps}^2 \cdot \mathrm{km}^{-1}$ and D in $\mathrm{ps} \cdot \mathrm{nm}^{-1} \cdot \mathrm{km}^{-1}$. Figure 2.2 shows two different representations of the chromatic dispersion effect [46].

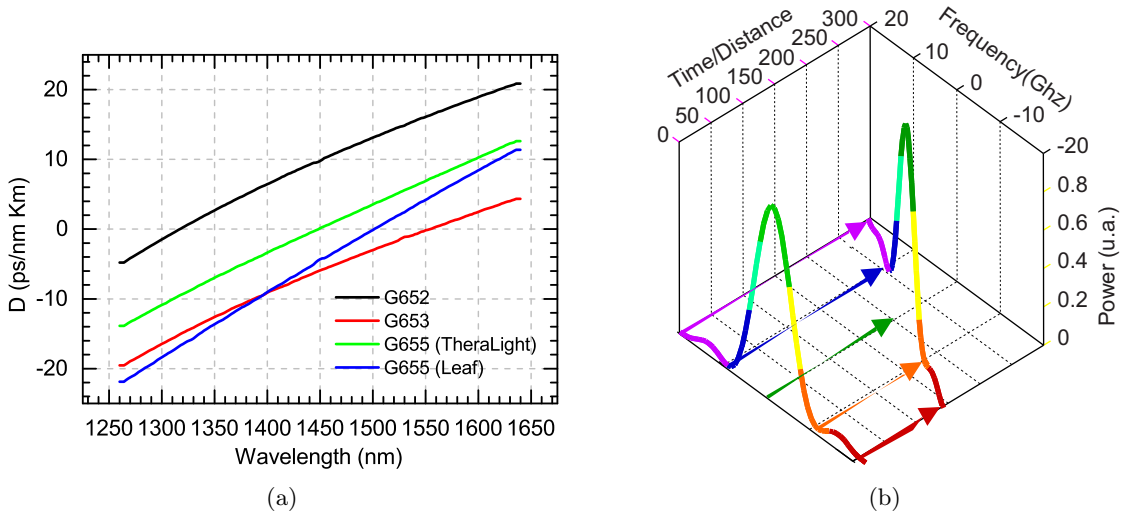

(a) (b)

Figure 2.2: Different representations of the chromatic dispersion effect. (a) Chromatic dispersion coefficient as a function of λ for different optical fibers; (b) Pulse behavior in an anomalous chromatic dispersion fiber [46].

As it can be observed in Figure 2.2(a), D can be zero at a certain wavelength, which is known as the zero dispersion wavelength λ_D and depends on the fiber-design parameters such as core radius and core-cladding index difference. Above this wavelength ($D > 0$, $\beta_2 < 0$) fibers show a dispersion regime known as anomalous (which effect on a gaussian pulse is represented in Figure 2.2(b)), and below ($D < 0$, $\beta_2 > 0$) the propagation is developed at normal dispersion regime.

During the fabrication process, it is possible to shift the zero-dispersion wavelength λ_D in the vicinity of 1.55 μm where the fiber loss is minimum. Such dispersion-shifted fibers [47] have found important applications in optical communication systems, since dispersion can be minimized, thus bounding the chromatic distortions. There is another type of fibers which allow to compensate the induced dispersion. They are known as Dispersion-Compensating Fibers (DCFs) and exhibit a large positive value of β_2. The chromatic dispersion can be also compensated using Linearly-Chirped Fiber Bragg Gratings (LC-FBGs). This element allows to compensate or induce (depending on the β_2 sign) high dispersion with low losses. It is particularly useful to develop Chirped Pulse Amplification [48, 49]. This technique will be described in Section 2.5, since it has been implemented in one of the developed sensors in this thesis (see Section 4.3 in Chapter 4).

2.4 Non-Linear Propagation

In this section, we discuss processes in which the medium/propagation properties are dependent on the optical power in the medium (i.e. Non-linear). The induced polarization in a medium when an electromagnetic wave $\mathbf{E}$ propagates through shows non-linear behavior when the optical power levels are high enough for the nonlinear coefficients $\chi^{(n)}$ ($n = 2, 3, \ldots$) to become relevant. As it was explained before, the even tensors $\chi^{(2n)}$ ($n = 1, 2, \ldots$) are zero in silica optical fibers and higher order than $\chi^{(3)}$ can be neglected in our work regimes. Thus, similarly to the linear polarization $\mathbf{P}_{\mathrm{L}}$ term, defined previously in Equation 2.4, the non-linear polarization term $\mathbf{P}_{\mathrm{NL}}$ is described as:

$$\mathbf{P}_{\mathrm{NL}}(\mathbf{r}, t) = \varepsilon_0 \cdot \chi^{(3)} \vdots \mathbf{E}(\mathbf{r}, t)\mathbf{E}(\mathbf{r}, t)\mathbf{E}(\mathbf{r}, t) \tag{2.22}$$

where $\chi^{(3)}$ is a tensor with rank 4 and only presents four components different to zero: $\chi^{(3)}_{xxxx}$, $\chi^{(3)}_{xxyy}$, $\chi^{(3)}_{xyxy}$ and $\chi^{(3)}_{xyyx}$. The molecular contributions to $\chi^{(3)}$ (Raman effect) can be neglected assuming instantaneous response, since the Raman response occurs over a time scale 60–70 ps. Considering a >1 ps monochromatic wave $\mathbf{E}$ then $\mathbf{P}_{\mathrm{NL}}$ will have a term oscillating at frequency ω and another at 3ω (Third-Harmonic Generation - THG). However, the THG term requires phase-matching and is usually negligible in optical fibers. In this case, $\mathbf{P}_{\mathrm{NL}}$ will be given by [40]:

$$\mathbf{P}_{\mathrm{NL}}(\mathbf{r}, t) \approx \varepsilon_0 \varepsilon_{\mathrm{r,NL}} \cdot \mathbf{E}(\mathbf{r}, t) \tag{2.23}$$

where the non-linear contribution to the relative permittivity $\varepsilon_{\mathrm{r,NL}}$ is defined as:

$$\varepsilon_{\mathrm{r,NL}} = \frac{3}{4}\chi^{(3)}_{xxxx}|\mathbf{E}|^2 \tag{2.24}$$

Thus, the dielectric constant will be defined as:

$$\varepsilon_{\mathrm{r}}(\omega) = 1 + \chi^{(1)}(\omega) + \varepsilon_{\mathrm{r,NL}} \tag{2.25}$$

Considering both linear $\mathbf{P}_{\mathrm{L}}$ and non-linear $\mathbf{P}_{\mathrm{NL}}$ induced polarization, Equation 2.1 can be rewritten as:

$$\nabla^2\mathbf{E} + \frac{1}{c^2}\frac{\partial^2\mathbf{E}}{\partial t^2} = -\mu_0\frac{\partial^2\mathbf{P}_{\mathrm{L}}}{\partial t^2} - \mu_0\frac{\partial^2\mathbf{P}_{\mathrm{NL}}}{\partial t^2} \tag{2.26}$$

To obtain the slowly varying amplitude of $\mathbf{E}(\mathbf{r}, t)$, it is more convenient to work in the Fourier domain:

$$\widetilde{E}(\mathbf{r}, \omega - \omega_0) = \int_{-\infty}^{\infty} E(\mathbf{r}, t)\exp[-i(\omega - \omega_0)t]dt \tag{2.27}$$

where ω_0 is the central angular frequency of the electromagnetic wave. Substituting Equations 2.4 and 2.23 in Equation 2.26, and working in the frequency domain, we found that it is satisfied the next Helmholtz equation [40]:

$$\nabla^2\widetilde{E} + \varepsilon(\omega)k_0^2\widetilde{E} = 0 \tag{2.28}$$

where $k_0 = \omega/c$. Therefore, Equation 2.28 can be solved by using the method of separation of variables, in which is assumed a solution of the form:

$$\widetilde{E}(\mathbf{r}, \omega - \omega_0) = F(x, y)\widetilde{A}(z, \omega - \omega_0)\exp(i\beta_0 z) \tag{2.29}$$

where $\widetilde{A}(z, \omega)$ is the slowly varying function of z and β_0 is the wave number. Considering from Equations 2.12 and 2.17 that the higher-order terms are small if the pulse is monochromatic ($2\pi\Delta f \ll \omega_0$, being Δf the light linewidth) and that $\beta \approx \beta_0$, it is possible to obtain [40]:

$$\frac{\partial A}{\partial z} + \beta_1\frac{\partial A}{\partial t} + \frac{i\beta_2}{2}\frac{\partial^2 A}{\partial t^2} + \frac{\alpha}{2}A = i\gamma|A|^2 A \tag{2.30}$$

where A is the scalar envelope of the electric field normalized to the optical power of the pulse ($|A|^2 = P_0$) and γ is defined as the non-linear parameter:

$$\gamma = \frac{n_2\omega_0}{cA_{eff}} \tag{2.31}$$

where n_2 is the non-linear refractive index and will be presented better in the next subsection and A_{eff} is the effective area of the guided mode and presents a typical value of 50 μm^2 for conventional Single Mode Fibers (SMF) at 1550 nm. Equation 2.30 is commonly known as Non-Linear Schrödinger's Equation (NLSE) [40] due to its similarities to Schrödinger's equation with a non-linear potential.

2.4.1 Non-Linear Refraction

Several of the non-linear effects in optical fibers are originated from non-linear refraction (Kerr effect), a phenomenon referring to the refractive index dependency on the optical intensity propagating. This dependence can be expressed as [40, 41]:

$$n = n_0 + n_2|E|^2 \tag{2.32}$$

where n_0 and n_2 are the linear and non-linear refractive indexes, respectively. These parameters can be expressed in terms of $\chi^{(1)}$ and $\chi^{(3)}_{xxxx}$ as:

$$n_0 = \mathrm{Re}\left(\sqrt{1+\chi^{(1)}}\right) \tag{2.33}$$

$$n_2 = \frac{3}{8n_0}\mathrm{Re}\left(\chi^{(3)}_{xxxx}\right) \tag{2.34}$$

The value of n_2 is very small in optical fibers ($\approx 2 \cdot 10^{-20}$ $\mathrm{m^2W^{-1}}$). However, the obtained modulation in the refractive index for high powers and long distances is enough to notice phase differences. This intensity dependence of the refractive index leads to the Self-Phase Modulation (SPM) and Modulation Instability (MI) effects, among others. However, SPM and MI are the most relevant effects to this thesis that will be described in the following subsections.

2.4.2 Self-Phase Modulation – SPM

Self-Phase Modulation (SPM) can be described using the NLSE (see Equation 2.30). However, the analytical solution is obtained more easily redefining the time reference and simplifying some terms in Equation 2.30. First, the time reference is changed to follow the pulse propagation as:

$$\tau = \frac{t - z/v_g}{T_0} \tag{2.35}$$

where T_0 is the temporal pulse length. As it was explained before, A is the scalar envelope of the electric field normalized to the optical power of the pulse ($|A|^2 = P_0$). Thus, it can be written in terms of the normalized amplitude U as:

$$A(z,\tau) = \sqrt{P_0}U(z,\tau) \tag{2.36}$$

Finally, if the losses within the fiber and the dispersion of the group velocity are considered inexistent, Equation 2.30 can be rewritten as:

$$\frac{\partial U(z,\tau)}{\partial z} = i\gamma P_0|U(z,\tau)|^2 U(z,\tau) \tag{2.37}$$

Solving the differential Equation 2.37, the transmitted pulse after a distance L through an optical fiber is:

$$U(L,\tau) = U(0,\tau) \cdot e^{i\phi_{\mathrm{NL}}} \tag{2.38}$$

where the non-linear phase ϕ_{NL} induced by SPM is:

$$\phi_{NL} = \gamma P_0 |U(z,\tau)|^2 L \tag{2.39}$$

From Equation 2.39 it can be observed that the induced non-linear phase depends on the pulse peak power P_0 and the pulse shape $|U(z,\tau)|^2$. Thus, the instantenous frequency profile is:

$$\Delta\omega(\tau) = -\frac{\partial\phi_{NL}}{\partial\tau} = -\gamma P_0 L \frac{\partial}{\partial\tau}\left(|U(z,\tau)|^2\right) \tag{2.40}$$

Here it is shown that the instantaneous frequency will displace to the red-color region in the rising edge of the pulse ($\Delta\omega < 0$) and to the blue-color region in the falling edge ($\Delta\omega > 0$). This is effectively evidenced as a broadening of the pulse spectrum although, not in the temporal shape. This phenomenon will be an important limitation in Chapter 4 (Section 4.3).

2.4.3 Modulation Instability – MI

Modulation Instability (MI) results from the interplay of Kerr effect and anomalous GVD ($\beta_2 < 0$, $D > 0$). In the spectral domain, MI results in the appearance of two gain sidebands on each side of the central wavelength [50,51]. It can be described using the NLSE 2.30 considering that losses within the fiber are inexistent:

$$\frac{\partial A}{\partial z} + \frac{i\beta_2}{2}\frac{\partial^2 A}{\partial T^2} = i\gamma|A|^2 A \tag{2.41}$$

where $T = t - z/v_g = t - \beta_1 z$. The stationary solution to this equation is [46]:

$$A(z,T) = \sqrt{P_0}e^{i\gamma P_0 z} \tag{2.42}$$

This solution, however, is not stable against perturbations. It can be demonstrated that small perturbations $a(z,T)$ in A will evolve as [40,41,46]:

$$a(z,T) = a_1 e^{i(Kz-\Omega T)} + a_2 e^{-i(Kz-\Omega T)} \tag{2.43}$$

where K and Ω are the wave number and the angular frequency of the perturbation $a(z,T)$, respectively, and satisfy the dispersion relation [40,46]:

$$K = \pm\frac{1}{2}|\beta_2\Omega|\sqrt{\Omega^2 + \frac{4\gamma P_0}{\beta_2}} \tag{2.44}$$

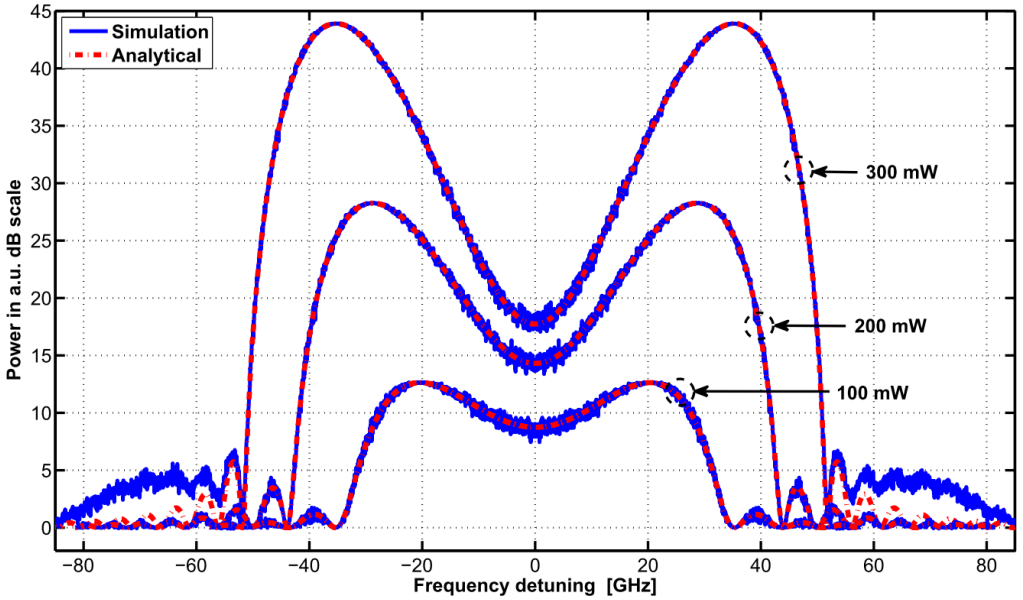

Figure 2.3: MI gain spectrum for a 10-km lossless SMF with different input powers and typical parameters $\beta_2 = -22$ ps^2 and $\gamma = 1.8$ W^{-1}km^{-1} [51].

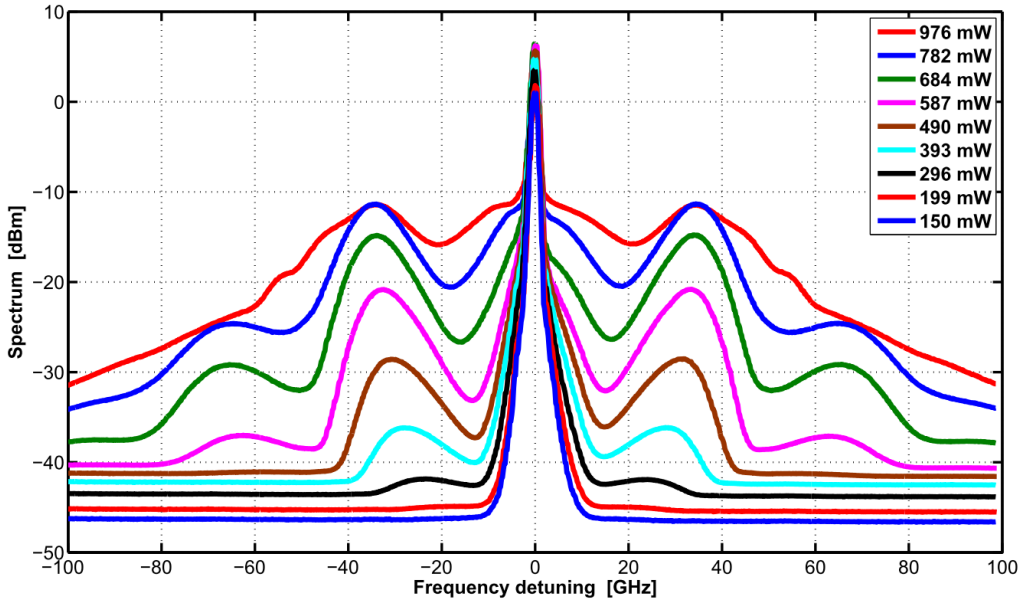

Figure 2.4: MI spectra measured for different levels of input power in a standard SMF with L = 11.1 km and $\gamma = 1.6$ W^{-1}km^{-1} [51].

Some important conclusions can be obtained from Equation 2.44. If the sign of β_2 is positive, then the wave number K is real at any frequency around the central frequency. Thus, all the solutions will have constant amplitude and the stationary solution of the Equation 2.41 will be stable in the presence of small perturbations. However, for negative values of β_2 (anomalous GVD), K becomes imaginary for frequencies $|\Omega| < \sqrt{4\gamma P_0 \beta_2^{-1}}$, and the amplitude of these perturbation frequencies will grow exponentially with z. The gain spectrum g_{MI} due to MI is then given by [40, 46]:

$$g_{\mathrm{MI}}(\Omega) = |\beta_2 \Omega| \sqrt{\frac{4\gamma P_0}{|\beta_2|} - \Omega^2} \tag{2.45}$$

where $g_{\mathrm{MI}}(\Omega) = 2\mathrm{Re}(K)$. The two maximums of g_{MI} are situated at $\Omega_{\max} = \pm\sqrt{2\gamma P_0/|\beta_2|}$ and its value is $g_{\mathrm{MI}}(\Omega_{\max}) = 2\gamma P_0$ [46]. The spectrum of $g_{\mathrm{MI}}(\Omega)$ is shown in Figure 2.3 obtained with different input powers, showing clearly the appearance of spectral sidebands symmetrically placed around ω_0.

Figure 2.4 plots the output spectrum of a 11.1 km long standard SMF for different levels of input peak power. We can see the onset of modulation instability at powers around 300 mW and by increasing the optical power the amplitude and spectral width of MI gain sidebands increase [51].

2.5 Chirped Pulse Amplification − CPA

The onset of non-linear effects in optical amplifiers limits the amplification of optical pulses. These non-linear effects appear when the pulse presents enough peak power before amplification. In 1985 the concept of Chirped Pulse Amplification (CPA) in optics regime was proposed to solve this problem [48].

The technique involves the physical time stretching and amplification of an ultra-short optical pulse in a dispersive medium, followed by the compression of the amplified pulse using the conjugated dispersive medium. To describe this process, we define first the complex envelope $P_{\mathrm{in}}(t)$ of the optical pulse. Thus, the induced dispersion process can be described in the spectral domain as:

$$P_{\mathrm{disp}}(\omega) = P_{\mathrm{in}}(\omega) e^{i\left(\ddot{\Phi}/2\right)\omega^2} \tag{2.46}$$

where $\ddot{\Phi}$ is the second-order dispersion coefficient of the dispersive device. It can be calculated from an equivalent fiber with length z and GVD coefficient β_2 as $\ddot{\Phi} = \beta_2 z$. After this process, the pulse has been temporally stretched and hence, the peak power is reduced to maintain the total amount of energy. For this reason, now the pulse can be amplified without the advent of non-linear effects. Considering G the total gain in this amplification process, the resulting amplified pulse is:

$$P_{\mathrm{ampl}}(\omega) = G \cdot P_{\mathrm{disp}}(\omega) = G \cdot P_{\mathrm{in}}(\omega) e^{-i\left(\ddot{\Phi}/2\right)\omega^2} \tag{2.47}$$

Finally, the dispersed and amplified pulse $P_{\text{ampl}}(\omega)$ is recompressed compensating the induced dispersion by a second dispersive device with the same value but opposite sign than the first one:

$$P_{\text{final}}(\omega) = P_{\text{ampl}}(\omega) \cdot e^{-i\left(\ddot{\Phi}/2\right)\omega^2} = G \cdot P_{\text{in}}(\omega) \tag{2.48}$$

which represented in the temporal domain is:

$$P_{\text{final}}(t) = G \cdot P_{\text{in}}(t) \tag{2.49}$$

The resulting optical pulse from the CPA process has the same characteristics as the initial pulse (temporal length and spectral content) but higher energy (Equation 2.49). Thus, CPA is an interesting technique when high energy optical powers are employed and it is necessary to avoid the advent of non-linear effects.

2.6 Optical coherence

The concept of coherence is essential for the understanding of the bases of the proposed sensor, particularly the concept of temporal coherence.

2.6.1 Temporal coherence

Temporal coherence is a measure of the degree of correlation between the phase of the electric field at two different instants t_1 y t_2 [52, 53]. For a stationary wave, the degree of temporal coherence is usually quantified by the coherence time τ_c defined as:

$$\tau_c = \int_{-\infty}^{\infty} |g(\mathbf{r}, \tau)|^2 d\tau \tag{2.50}$$

where $\tau = t_2 - t_1$ is the delay time. $g(\mathbf{r}, \tau)$ is the complex degree of temporal coherence, which is defined as:

$$g(\mathbf{r}, \tau) = \frac{\langle U^*(\mathbf{r}, t) U(\mathbf{r}, t + \tau) \rangle}{\langle U^*(\mathbf{r}, t) U(\mathbf{r}, t) \rangle} \tag{2.51}$$

where $U(\mathbf{r}, t)$ is the complex wavefunction. The numerator in Equation 2.51 is known as the autocorrelation function $G(\mathbf{r}, r)$. The absolute value of $g(\mathbf{r}, \tau)$ takes values between 0 and 1 $0 \leq |g(\mathbf{r}, \tau)| \leq 1$. Zero corresponding to a totally incoherent source and one corresponding to a perfectly monochromatic light. Furthermore, a perfectly monochromatic light has an infinite coherence time τ_c and a Dirac delta Power Spectral Density (PSD).

This idea is represented in Figure 2.5(a). However, a real light source presents a finite coherence time. Thus, $g(\mathbf{r}, \tau) = 1$ in $\tau = 0$ and drops for increasing values of τ, approaching zero for sufficiently large values of τ (see Figure 2.5(b) - middle) [54]. The coherence length l_c of a light source is defined as:

$$l_c = c/n\tau_c \tag{2.52}$$

where n is the refractive index of the propagation medium. When the coherence time τ_c is much greater than the length of the interferometers encountered in the optical system (or, equivalently, the coherence length is much longer than the optical path-length difference), the light source can be considered completely coherent [53].

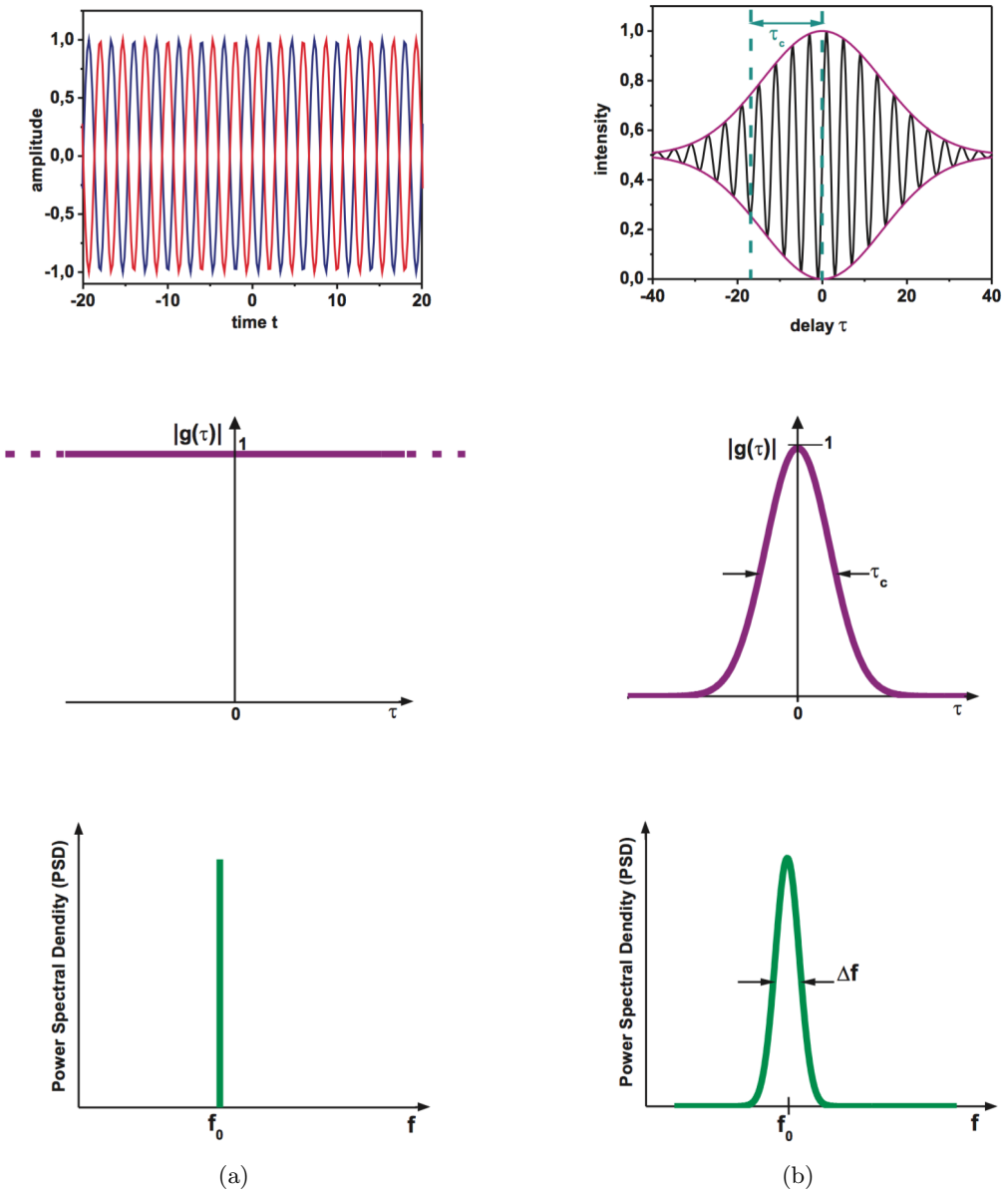

Figure 2.5: Representation of the temporal coherence concept. (a) An ideal perfect monochromatic wave presents a Dirac delta PSD and an infinite coherence time. Its superposition with a copy of itself delayed by any time τ gives constructive interference (top) and a constant and unity value of $|g(\tau)|$ (middle). (b) Representation of a real partially coherent wave: autocorrelation (top); magnitude of its complex degree of temporal coherence and coherence time τ_c (middle); power spectral density and spectral width Δf (bottom) [54].

The coherence time τ_c is related with the spectral width Δf of the light source by [52, 53]:

$$\tau_c \Delta f \sim 1/\pi \tag{2.53}$$

where Δf is the Full Width at Half Maximum (FWHM) of the optical spectrum. Equation 2.53 is valid for Lorentzian shape spectrum, the most common one.

According to Equation 2.53, a highly coherent laser (quasi-monochromatic) presents a great coherence time. For example, a laser with a linewidth of $\Delta f = 1$ MHz presents a coherence time of $\tau_c = 0.32$ μs and a coherence length of $l_c = 64$ m (considering a SMF and $n = 1.5$).

In Table 2.1 we compare the coherence length (for SMF) and spectral bandwidth Δf of different light sources:

Source	Δf (Hz)	$\tau_c = 1/\pi\Delta f$	l_c
Filtered sunlight ($\lambda = 0.4 - 0.8$ μm)	3.74×10^{14}	0.9 fs	170 nm
Supercontinuum ($\lambda = 1550$ nm, $\Delta\lambda = 200$ nm)	2.5×10^{13}	13 fs	2.5 μm
Light-emitting diode ($\lambda = 1$ μm, $\Delta\lambda = 500$ nm)	1.5×10^{13}	20 fs	4 μm
Low-pressure sodium lamp	5×10^{11}	640 fs	130 μm
Multimode He-Ne laser ($\lambda = 633$ nm)	1.5×10^{9}	210 ps	4 cm
Single-mode He-Ne laser ($\lambda = 633$ nm)	1×10^{6}	320 ns	64 m
Semiconductor laser RIO PLANEX$^{\text{TM}}$ ($\lambda = 1550$ nm)	$< 1 \times 10^{3}$	> 320 μs	> 64 km

Table 2.1: Coherence length in SMF ($n \approx 1.5$) and spectral bandwidth of different light sources [53].

As it will be introduced in the next section and studied deeply in the next chapter, Phase-Sensitive Optical Time Domain Reflectometry (ϕOTDR) resembles to the use of an interferometer with the size of the optical pulse. In this case, the coherence length of the used optical source will be directly related to the noise of this interferometer, and therefore this technique requires the use of a light source with a coherence time much greater than the optical pulses duration. Thus, the use of a highly coherent laser will be imperative in this technique.

2.7 Scattering Effects in Fiber Optics

When the light is propagated, the photons can be absorbed by the atoms or molecules of the medium. Then, other photons with different direction, frequency or phase are emitted. This process is known as scattering and it is represented in Figure 2.6.

If the medium is dense and perfectly homogeneous, light can be scattered only in the forward direction [55]. To demonstrate this, we suppose that a volume element δV_1 scatters light into the θ direction. However, for any direction, for except the exact forward direction ($\theta = 0$), there must be a nearby volume element (labeled δV_2) whose scattered field interferes destructively with that from δV_1. Since the same argument can be applied to any volume element in the medium, we conclude that there cannot be scattering in any direction except $\theta = 0$ [41]. This is the basis of the origin of the refractive index [56]. In contrast, scattering in all directions can occur as the result of fluctuations in any of the optical properties of the medium. For example, if the density of the medium is nonuniform, then the total number of molecules in a volume element δV_1 may not be equal to the number of molecules in a volume element δV_2, and

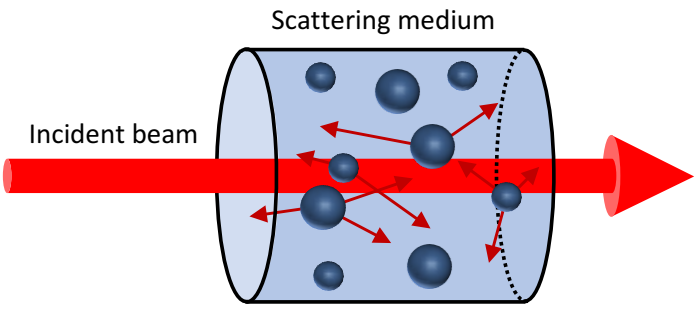

Figure 2.6: Scattering phenomena representation.

consequently, the destructive interference between the fields scattered by these two elements will not be exact [41].

The scattering can be considered linear (spontaneous) if the light power is lower than a certain threshold or non-linear (stimulated) if it is higher [45]. In the spontaneous case, the response of the medium remains unchanged in the interaction with light. On the contrary, the optical properties of the medium are changed in the stimulated case [57].

Depending on whether the scattered photons present the same or different frequency, the scattering is considered elastic or inelastic, respectively. Following this criterion, the three scattering processes that appear in optical fibers [45, 58] are:

- Elastic Scattering: The incident and scattered photons have the same energy (and therefore the same frequency) and there is no exchange of energy with the medium. However, since the scattered photon can have a different direction of propagation from that of the incident photon, the medium can absorb momentum.
  - Rayleigh Scattering: It is the unique elastic scattering phenomenon since it does not produce a frequency shift. It arises from non-propagating density fluctuations of the medium which could result from degree variations of molecular organization states. In optical fibers Rayleigh scattering is one of the main mechanisms leading to losses, as it was discussed in Section 2.3.1.
- Inelastic Scattering: The incident and the scattered photons have different energies (and therefore different frequencies), due to the medium absorption or release of energy. If the energy of the incident photon is higher than the energy of the scattered photon (i.e. the medium absorbs energy), the process is called Stokes scattering, and if it is lower (i.e. the medium releases energy), the process is called Anti-Stokes scattering.
  - Brillouin Scattering: It is an inelastic scattering process originated from propagating pressure waves, generated by acoustic phonons, whose frequency shift is determined by the acoustic velocity in the medium.
  - Raman Scattering: It is a highly inelastic scattering process since the interaction is developed between photons and optical phonons. This arises since the nature of the process is based in the interaction between light and molecular vibrational modes.

The three scattering process explained before are represented in Figure 2.7. As it is shown, the induced frequency shift by Brillouin and Raman scattering is ∼11 GHz and ∼13 THz from

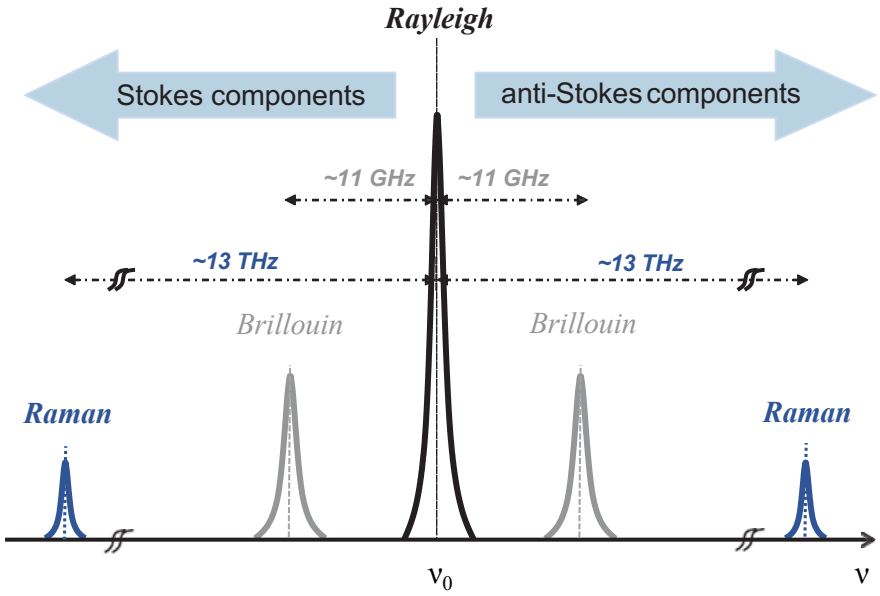

Figure 2.7: Different spectral components arisen from scattered light in an inhomogeneous medium [59].

the incident wave, respectively. These approximated values are reliable if the incident wave is centered around 1550 nm.

The induced frequency shift by Brillouin scattering, known as Brillouin Frequency Shift (BFS) depends linearly on strain/temperature ($C_{\nu_B\varepsilon} \approx 50$ MHz/$\mu\varepsilon$ and $C_{\nu_B T} \approx 0.95$ MHz/K at 1550 nm for typical SMFs). For this reason, Brillouin scattering is widely used in the field of distributed optical fiber sensors for strain and temperature sensing [6]. Furthermore, this effect could be used for distributed amplification. However, the sensor developed in this thesis is based on scattering Rayleigh and its range was increased by means of first-order Raman amplification. For this reason, these two scattering effects (Rayleigh and Raman) will be explained further in the next sections.

2.7.1 Elastic Scattering: Rayleigh Scattering

Rayleigh scattering was discovered by John William Strutt (Lord Rayleigh) in the 19^{th} century [60]. It is the elastic scattering of light by density fluctuations of the medium with a size much smaller than its wavelength (typically <10%) and presents strong spectral dependence ($\sim \lambda^{-4}$).

It can be seen as the radiation of the dipole induced by the applied electromagnetic field in the small molecules [61]. As shown in Figure 2.8, the incident electric field causes the electrons inside small particles to oscillate, resulting in dipoles that radiate electromagnetic field with the same frequency as incident wave into all directions [57]. It can be considered that the particle sees the incident wave as an uniform and oscillating field, since the size of the particle is much smaller than the wavelength.

The expression that describes the induced dipole moment is [62]:

$$\mathbf{p} = 4\pi\varepsilon_1 \left(\frac{\varepsilon_2 - \varepsilon_1}{3\varepsilon_1}\right) a^3 \mathbf{E} \tag{2.54}$$

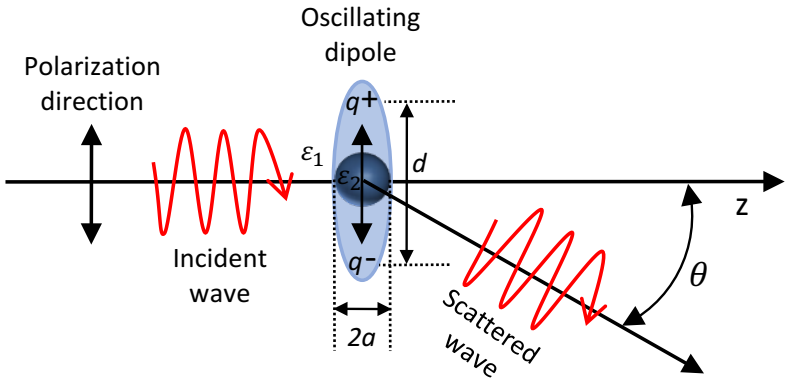

Figure 2.8: Radiation of the oscillating dipole caused by incident electric field.

where $2a$ is the particle diameter and $\varepsilon_1 - \varepsilon_2$ is the difference in the absolute permittivity between the medium and the particle. In this expression is was assumed that $\varepsilon_2 \simeq \varepsilon_1$. The oscillating charges q^+ and q^- cause a radiation described by a very simple description coming from the antenna theory (Hertizan dipole). In this description, two charges q^+ and q^- are separated a distance d as it is shown in Figure 2.8. Thus, the induced dipole is [62]:

$$\mathbf{p} = qd\frac{\mathbf{E}}{|\mathbf{E}|} \tag{2.55}$$

The originated electric-far-field by this oscillating dipole is [62]:

$$\mathbf{E}_{\text{far-field}} = \frac{jkid}{4\pi\varepsilon_1 cr}\sin\theta e^{-jkr}\boldsymbol{\theta} \tag{2.56}$$

where r is the distance of the observer, k is the wave vector ($k = 2\pi/\lambda$), θ is the direction with respect to z (see Figure 2.8) and i is the electrical current generated by the oscillating charges. The current i can be calculated as:

$$i = j\omega q \tag{2.57}$$

Thus, this current depends on the frequency ω (wavelength λ) of the incident wave. Multiplying by d Equation 2.57, it is simple to find that:

$$id = j\omega|\mathbf{p}| \tag{2.58}$$

Substituting Equations 2.54 and 2.58 in Equation 2.56, we obtain the following expression:

$$\mathbf{E}_{\text{far-field}} = -\frac{k^2a^3}{r}\frac{\varepsilon_2 - \varepsilon_1}{3\varepsilon_1}|\mathbf{E}|\sin\theta e^{-jkr}\boldsymbol{\theta} \tag{2.59}$$

Defining the intensities of the incident wave (E) and the electric-far-field ($E_{\text{far-field}}$) as:

$$I = \frac{\varepsilon_1 c}{2}|\mathbf{E}|^2 \tag{2.60}$$

$$I_{\text{far-field}} = \frac{\varepsilon_1 c}{2}|\mathbf{E}_{\text{far-field}}|^2 \tag{2.61}$$

The scattered power P_{s} by only one particle is simply the integration of the intensity $I_{\text{far-field}}$ over all the surface at a distance r:

$$P_{\text{s}} = \int_0^{2\pi}\int_0^{\pi} I \sin\theta d\theta d\phi = \frac{8\pi}{3}k^4 a^6 \left(\frac{\varepsilon_2 - \varepsilon_1}{3\varepsilon_1}\right)^2 I \tag{2.62}$$

It can be concluded from Equation 2.62 that the scattered power from one particle presents, as it was previously mentioned, a strong wavelength ($k^4 \propto \lambda^{-4}$) and particle size (a^6) dependence. Furthermore, it depends linearly on the incident optical intensity (I) and the difference of absolute permittivity ($\varepsilon_2 - \varepsilon_1$).

From this result, it is possible to obtain an expression of the scattering loss coefficient α_{R} (introduced in Subsection 2.3.1). First it is assumed a small cylinder of volume $\Delta V = S \cdot \Delta l$ where S and Δl are the cross section and length, respectively. This small volume is irradiated with an optical power $P = IS$, being I the intensity of the incoming light. The scattering media is composed by scattering particles of volume $\delta V = \frac{4}{3}\pi a^3$. Assuming that the scattering particles are densely packed (like in optical fibers), the particle density will be $N = 1/\delta V$. Thus, the power loss that an optical signal suffer during its propagation through ΔV can be defined as:

$$\Delta P = -\alpha_{\text{R}} P \Delta l \tag{2.63}$$

where P is the input power, Δl is the traveled length and α_{R} is scattering loss coefficient. ΔP can be calculated from the power scattered by only one particle as:

$$\Delta P = -N P_{\text{s}} \Delta V = -N P_{\text{s}} S \Delta l \tag{2.64}$$

From Equations 2.63 and 2.64, the scattering loss coefficient α_{R} can be expressed as:

$$\alpha_{\text{R}} = NS\frac{P_{\text{s}}}{P} = \frac{1}{\delta V}\frac{P_{\text{s}}}{I} \tag{2.65}$$

Substituting Equation 2.65 in Equation 2.62, α_{R} can be rewritten as:

$$\alpha_{\text{R}} = \frac{8\pi^3}{3\lambda_0^4}\left\langle(\Delta\varepsilon)^2\right\rangle \delta V \tag{2.66}$$

where λ_0 is the wavelength in the vacuum and $\left\langle(\Delta\varepsilon)^2\right\rangle$ is the average of $\Delta\varepsilon^2 = (\varepsilon_2 - \varepsilon_1)^2$, since all the particles do not present the same absolute permittivity.

Some thermodynamic formalism is necessary to obtain an expression for $\left\langle (\Delta\varepsilon)^2 \right\rangle$ and δV. It is known that $\Delta\varepsilon$ depends on the material density ρ and temperature T as:

$$\Delta\varepsilon = \left(\frac{\partial\varepsilon}{\partial\rho}\right)_T \Delta\rho + \left(\frac{\partial\varepsilon}{\partial T}\right)_\rho \Delta T \tag{2.67}$$

However, for solid state materials the dependence with the density is much higher than with temperature $\left(\frac{\partial\varepsilon}{\partial\rho}\right)_T \gg \left(\frac{\partial\varepsilon}{\partial T}\right)_\rho$ [41]. Thus, the effect of compression in the refractive index is higher than the temperature. Neglecting the temperature contribution, it can be found that:

$$\left\langle (\Delta\varepsilon)^2 \right\rangle \cong \left(\frac{\partial\varepsilon}{\partial\rho}\right)_T^2 \left\langle (\Delta\rho)^2 \right\rangle \tag{2.68}$$

From the theory of thermodynamic fluctuations, the average square density fluctuations can be expressed as:

$$\left\langle (\Delta\rho)^2 \right\rangle = \frac{\rho^2}{\delta V} k_\mathrm{B} T_\mathrm{f} \beta_\mathrm{c} \tag{2.69}$$

where k_B is the Boltzmann constant, T_f is a fictitious temperature which represents the temperature when all density fluctuations get frozen (material solidification) and β_c is the isothermal compressibility $\beta_\mathrm{c} = -\frac{1}{\delta V}\left(\frac{\partial\delta V}{\partial P}\right)_T = 6.9 \cdot 10^{-11}\ \mathrm{m^2 J^{-1}}$ in silica. In the case of optical fibers, the presence of this inhomegeneities $\Delta\rho$ (Δn) results from the fabrication process. Using these thermodynamic expressions, Equation 2.66 can be rewritten as:

$$\alpha_\mathrm{R} = \frac{8\pi^3}{3\lambda_0^4}\left(\rho\frac{\partial\varepsilon}{\partial\rho}\right)_T^2 k_\mathrm{B} T_\mathrm{f} \beta_\mathrm{c} \tag{2.70}$$

Since silica is a isotropic solid state material, the following term can be made explicit using the theory of photoelasticity:

$$\left(\rho\frac{\partial\varepsilon}{\partial\rho}\right)_T^2 = n^4 p_{12} \tag{2.71}$$

where $p_{12} = 0.286$ is the photoelastic coefficient. Considering this, the final expression for α_R is:

$$\alpha_\mathrm{R} = \frac{8\pi^3}{3\lambda_0^4} n^8 p_{12}^2 k_\mathrm{B} T_\mathrm{f} \beta_\mathrm{c} \tag{2.72}$$

The spectral dependence (λ^{-4}) of α_R, which was introduced in Subsection 2.3.1, is finally demonstrated here. Thus, shorter wavelengths will be scattered much more than longer wavelengths. It is interesting to note that this phenomenon is the responsible for seeing the sky blue (reddish during the sunrise and sunset) [60, 63]. From Equation 2.72 it is possible to conclude that choosing a material with low refractive index and comprenssibility will reduce the optical losses due to Rayleigh scattering.

2.7.1.1 Rayleigh Backscattering

As it was explained in the previous section, when an electromagnetic wave is transmitted through a condensed and inhomogeneous medium, the light is scattered into all directions ($\theta \in [0, 2\pi]$). The co-propagating scattered light ($\theta = 0$) travels in the same direction and with the same frequency than the propagating signal. Since it does not affect the transmitted signal, it does not present great interest. However, note that this phenomenon is the physical origin of the refractive index, as the phase of the total light in the forward direction propagates with a velocity that is smaller than c. The rest of the directions contribute directly to the optical losses of the propagating wave, as it was explained in Subsection 2.3.1. This is because many of these directions escape from the fiber core without being guided by the fiber. However, for $\theta \approx \pi$, light can be recaptured by the fiber, resulting in a wave propagating in the opposite direction - Rayleigh backscattering. This phenomenon, represented in Figure 2.9, creates a counter-propagating wave with the same frequency of the initial wave. It appears in optical fibers and the Rayleigh backscattering coefficient in a SMF is $\alpha_{\mathrm{Rb}} \approx -72$ dB/m [64]. Note that it is possible to calculate this value from the Rayleigh scattering coefficient using geometrical arguments.

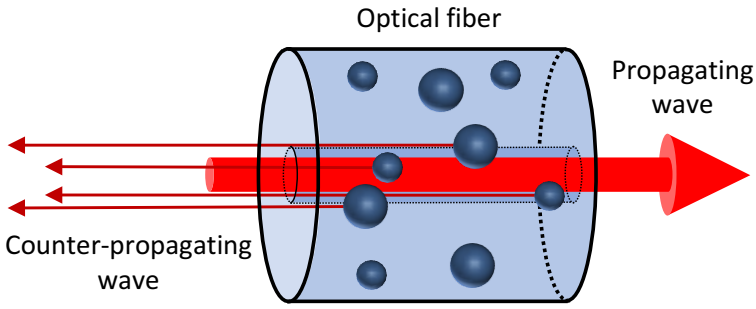

Figure 2.9: Counter-propagating wave generated by Rayleigh backscattering in fibers.

This concept is fundamental for the understanding of the Optical Time Domain Reflectometry (OTDR)-based sensors which employ optical pulses in their operation. In this case, the backscattered signal comes from the multiple reflections of one of these optical pulses in the different scattering centers during its propagation through the optical fiber. The backscattered signals in the different scattering centers will sum incoherently or coherently depending on the coherence of the light source. If the coherence length is much lower than the pulse length, the sum will be incoherent. In contrast, when the coherence length is much higher than the pulse length, the sum will be coherent and an interference phenomenon will be produced. As it will be deeply explained in the next chapter, this is the main difference between a standard OTDR (non-coherent light source) and a Phase-Sensitive OTDR (highly coherent light source).

As the reader can imagine, the counter-propagating wave generates Rayleigh scattering in the direction of the initial propagating wave. This phenomenon is known as double Rayleigh backscattering. However, this phenomenon will be neglected in this thesis due to the low value of α_{Rb}.

2.7.2 Inelastic Scattering: Raman Scattering

Raman scattering is the effect resulting from the interaction of an incident light with the resonant modes of the molecules in a medium. Since the molecule's modes can be vibrational or rotational,

the Raman scattering can be manifested in such ways; vibrational Raman scattering or rotational Raman scattering. Nonetheless, the vibrational mode is dominant over the rotational mode when generating the Raman scattering [65]. As it was explained before, this scattering process is inelastic, therefore the photon energy is not conserved. Thus, the scattered light contains frequencies different from those of the excitation source (ω_p). Those new components shifted to lower frequencies are called Stokes components ($\omega_{\mathrm{S}} = \omega_{\mathrm{p}} - \Omega_{\mathrm{R}}$), and those shifted to higher frequencies are called anti-Stokes components ($\omega_{\mathrm{AS}} = \omega_{\mathrm{p}} + \Omega_{\mathrm{R}}$).

The spontaneous Raman effect was discovered by C.V. Raman in 1928 [66]. It was observed by illuminating a material sample (which can be a solid, liquid, or gas) with a beam of light. In condensed matter, only $\sim 10^{-6}$ of the incident light is inelastically scattered when interacting with the medium, which means that a small fraction of the incident light suffers a frequency shift to higher and/or lower frequencies [41].

In optical fibers this phenomenon can be used to develop distributed temperature sensors, since the ratio between powers scattered by the stocks and anti-stoks depends on the temperature of the medium [4, 5]. It is worth to note that the spontaneous Raman effect is immune to the strain. For this reason, implementing a distributed strain sensor based on this effect is not possible. As it will be studied in the next section, Raman scattering can be used as a signal amplifier, compensating the intrinsic fiber losses and allowing to increase the performance of distributed optical fiber sensors [45].

2.7.2.1 Stimulated Raman Scattering – SRS

If another field is introduced in the medium at a frequency $\omega_{\mathrm{S}} = \omega_{\mathrm{p}} - \Omega_{\mathrm{R}}$, i.e. matching the Raman Stokes frequency, a highly efficient scattering can occur as a result of the Stimulated version of the Raman Scattering process. Thus, the process becomes intensity dependent and the scattered radiation tend to have the same frequencies of the pre-existent radiation [41]. The phenomenon of Stimulated Raman Scattering (SRS) was discovered by Woodbury and Ng [67] in 1962, and then described in detail by Eckhardt et al. [68].

While spontaneous Raman scattering process leads to emission in the form of a dipole radiation pattern, the stimulated process leads to emission in a narrow cone in the forward and backward directions. Thus, compared to the Stimulated Brillouin Scattering (SBS) process [41], SRS can amplify the Stokes signals in a co- and counter-propagating way, whereas SBS can only excite in opposite direction [45].

For this reason, SRS is commonly exploited as a distributed signal amplifier. Since, SRS can amplify the Stokes signals in a co- and counter-propagating way, it is very well suited for distributed fiber sensors, where both signals (probe and backscattered signal) will be amplified. This will be explained better in Chapter 7, where SRS will be employed to increase the maximum measurable range of the proposed sensor.

2.7.2.2 Raman Gain Spectrum

The evolution of the Stokes wave when SRS is generated is described by [41]:

$$\frac{dI_{\mathrm{S}}}{dz} = g_{\mathrm{R}}(\Omega) I_{\mathrm{p}} I_{\mathrm{S}} \tag{2.73}$$

where I_{S} is the Stokes intensity, I_{p} is the pump intensity and g_{R} is the Raman gain coefficient,

which is dependent on Ω (the frequency difference between the pump and Stokes waves). In silica fibers, the Raman gain spectrum ($g_R(\Omega)$) extends up to $\sim$ 40 THz [40], with a maximum peak at $\sim$ 13 THz and a FWHM of $\sim$ 7 THz, as it can be seen in Figure 2.10.

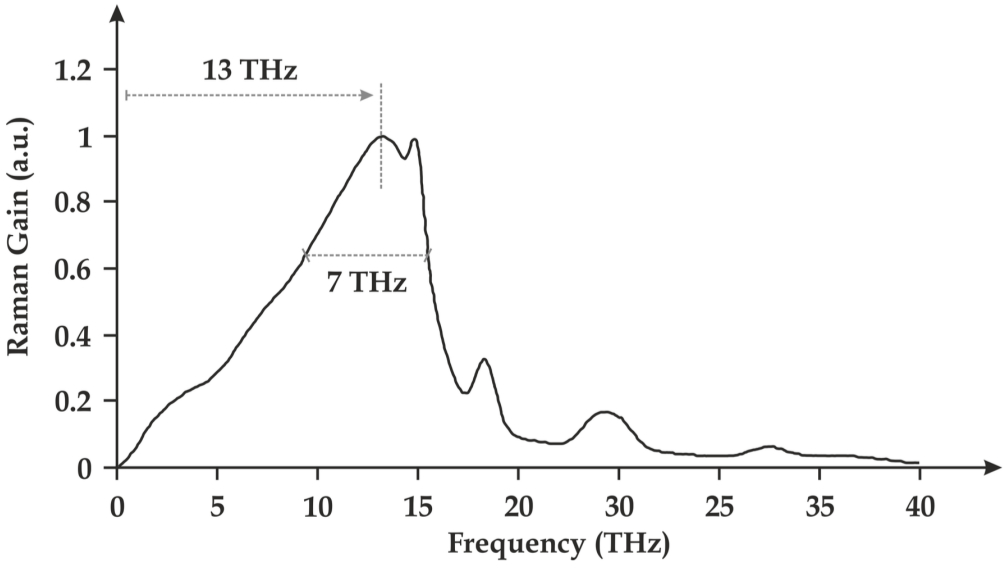

Figure 2.10: Representation of the Raman gain typical in silica fibers [40, 45].

The Raman gain generated by a primary Raman pump has also been used as a secondary Raman pump to generate a second-order Raman gain spectrum [69]. The 2nd order spectra will be shifted by the amount that the seed 1st order frequency laser is shifted. If it is generated from the peak of the 1st order, it is shifted by some 13 THz.

2.7.2.3 Intensity evolution and threshold for noise amplification

The evolution of the intensities of the Raman pump and the Stokes wave in a SRS process is described by the following two coupled equations [40]:

$$\frac{dI_p}{dz} = -\frac{\omega_p}{\omega_S} g_R(\Omega) I_p I_S - \alpha_p I_p \tag{2.74}$$

$$\frac{dI_S}{dz} = g_R(\Omega) I_p I_S - \alpha_S I_S \tag{2.75}$$

where α_S and α_p are the fiber losses at the Stokes and pump frequencies respectively. If it is assumed that $I_p \gg I_S$, the Raman pump depletion (variation of I_p due to the gain provided to I_S) can be neglected [70], and Equation 2.74 can be rewritten as:

$$\frac{dI_p}{dz} = -\alpha_p I_p \tag{2.76}$$

Solving this differential equation, the evolution of I_p along z is:

$$I_p(z) = I_p(0) \cdot e^{-\alpha_p z} \tag{2.77}$$

Finally, substituting Equation 2.77 in Equation 2.75 and solving the resulting differential equation, the evolution of I_S along z will be given by:

$$I_S(z) = I_S(0) \cdot \exp\Big(g_R(\Omega) I_p(0) L_{eff} - \alpha_s z\Big) \tag{2.78}$$

where the effective length L_{eff} is defined as:

$$L_{eff} = \frac{1 - e^{-\alpha_p z}}{\alpha_p} \tag{2.79}$$

L_{eff} will be lower than z, and for long fiber lengths ($\alpha_p z \gg 1$) L_{eff} is reduced to $1/\alpha_p$. L_{eff} is of the order of ~ 20 km for a typical fiber loss, at 1550 nm, of $\alpha_p \approx 0.047$ km$^{-1} \approx 0.2$ dB/km.

As Equation 2.78 requires an input intensity $I_S(0)$ at $z = 0$, this is translated in practice as to injecting one fictitious photon per mode at the input end of the fiber. Therefore, the critical pump power to reach the Raman threshold (P_{th}^{SRS}) is given by [71]:

$$P_{th}^{SRS} = 16 \frac{A_{eff}}{g_R L_{eff}} \tag{2.80}$$

Using the typical values of a SMF at a wavelength of 1550 nm (effective mode area $A_{eff} = 50$ μm^2, $g_R = 6.6 \cdot 10^{-14}$ m/W and $L_{eff} \approx 20$ km), the Raman threshold will be $P_{th}^{SRS} \approx 600$ mW for forward SRS. In the case of backward SRS, the numerical factor 16 is replaced by 20 [40], therefore, will equal approximately ~ 750 mW.

Chapter 3

ϕOTDR: Principles, Limitations and State of the Art

3.1 Introduction

Distributed fiber sensors based on Rayleigh scattering can be divided into two groups depending on whether they operate in the time or frequency domain: Optical Time Domain Reflectometry (OTDR) [21–39,72–84] and Optical Frequency Domain Reflectometry (OFDR) [11–18]. OTDRs can then be subdivided into incoherent OTDR [73–75], Polarization OTDR (POTDR) [76–84] and Phase-Sensitive OTDR (ϕOTDR) [34, 35, 72]. When coherent detection is implemented in a ϕOTDR, generally this technique is known as Coherent OTDR (COTDR) [28–33].

The main focus of this thesis dissertation is to propose improvements on ϕOTDR systems. That is why, in this chapter, a description of the technique will be presented, including a theoretical model and its limitations: range, resolution and non-linear behavior. The techniques employed until this moment to solve these limitations will be explained, such as distributed amplification [19–27], coding techniques [4, 5, 85–93], Optical Pulse Compression Reflectometry (OPCR) [94–96], signal post-processing [24, 30, 35, 97–100], coherent detection [28–33] and frequency sweep [36–39]. In the last section of the chapter the main Distributed Optical Fiber Sensors (DOFSs) based on the three different scattering phenomena (Rayleigh [17,31,33,34,37], Brillouin [6–10] and Raman [4, 5]) will be compared in terms of their linearity, speed, accuracy, range and spatial resolution measurement.

3.2 Basis of OTDR Technology

Optical Time Domain Reflectometry (OTDR) has been used for decades to characterize anomalies in optical fiber links [73] and its extension to single-mode fibers followed few years later [75]. It works by injecting incoherent optical pulses into a Fiber Under Test (FUT). The backscattered light from the fiber produced by Rayleigh backscattering is guided into a photodetector through an optical circulator. The general setup for a typical incoherent OTDR system is shown in Figure 3.1.

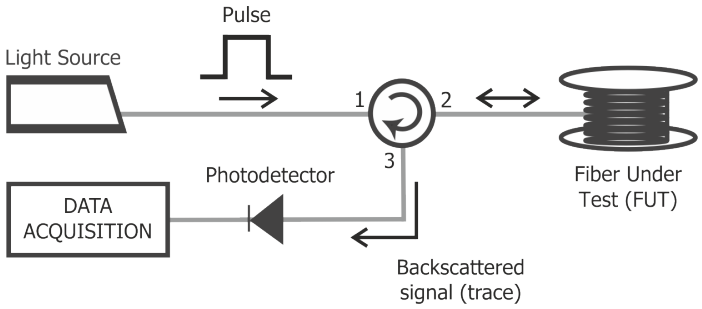

Figure 3.1: Typical OTDR system.

The backscattered signal, commonly known as OTDR trace, is then digitized and processed in the time domain. Figure 3.2 shows a representation of a typical OTDR and its utility, where it is possible to observe the different loss contributions of a fiber link (specially important to manage the power budget of an optical network). For a state of the art Single Mode Fibers (SMF), the fiber round trip attenuation is ∼0.4 dB/km (around 1550 nm) [101]. Note that the net attenuation suffered by the optical trace is twice that of a single pass, as the pulse is attenuated in the forward direction and the backscattered light is attenuated in the backward direction. The losses produced by connectors or splices can severely contribute to the total attenuation that telecom signals suffer during its propagation through fiber links.

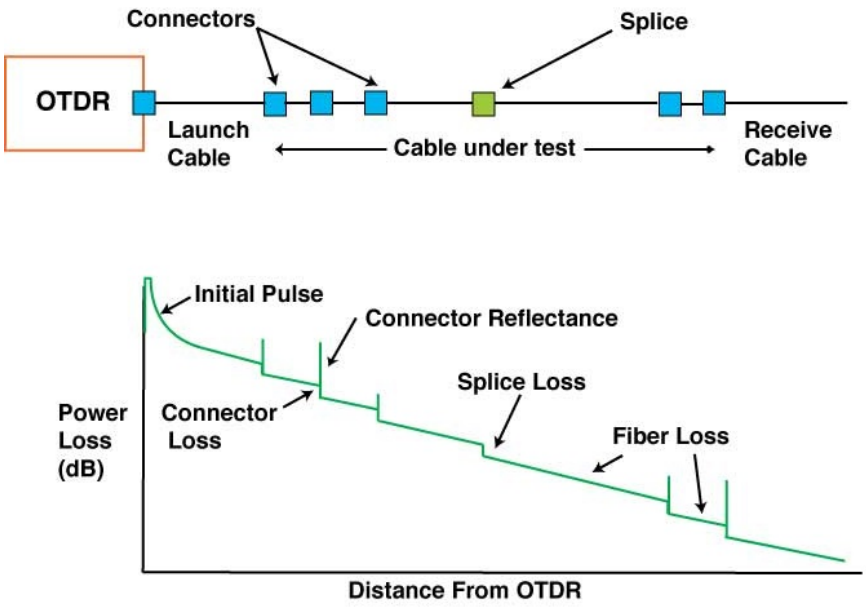

Figure 3.2: Representation of an OTDR signal which shows the state of a fiber link.

The spatial resolution, defined as the minimum distance between two events that allows them to be labeled separately, is a really important parameter of a distributed sensor. The resolution of a OTDR can be understood analyzing the evolution of the pulse propagation along the fiber and the respective backscattered signal, as it is represented in Figure 3.3.

Considering an optical pulse with temporal width τ_p that is propagating through an optical fiber at a group velocity $v_g = c/n_g$, where n_g is the group refractive index of the fiber, the reflected (backscattered) pulse is generated at every scattering point and propagates backward. Figure 3.3(a) shows that the optical pulse is reflected when its leading edge reaches a location at time $t = t_0$. Then the pulse continues traveling and another scattering center is illuminated at time $t = t_0 + t'$. However, the optical pulse reflected at time t_0 and $t_0 + t'$ would partially overlap if $0 < t' < \tau_p/2$ as presented in Figure 3.3(b). In order to avoid overlap of the signals reflected from different points, which would allow the independent monitoring of events occurring in those points, the time difference must be larger than $\tau_p/2$, shown in Figure 3.3(c) [57]. Thus, the spatial resolution is expressed as:

$$W = \frac{\tau_p}{2} \cdot v_g = \frac{\tau_p c}{2n_g} \tag{3.1}$$

Using a typical value for silica fibers of $n_g = 1.47$ [101], the spatial resolution will be ~10 m for a 100 ns pulse width.

These optical pulses are injected one by one in the optical fiber with a repetition rate denoted as f_{trigger}. This frequency is limited by the following condition: superposition of signals backscattered from different pulses cannot occur. If this happens, both backscattered signals would interfere between them affecting the contained phase information thus making the perturbation measurement impossible in the superposition region. Hence, the repetition rate is limited by the inverse of the round trip of the light in the fiber, which can be expressed mathematically as:

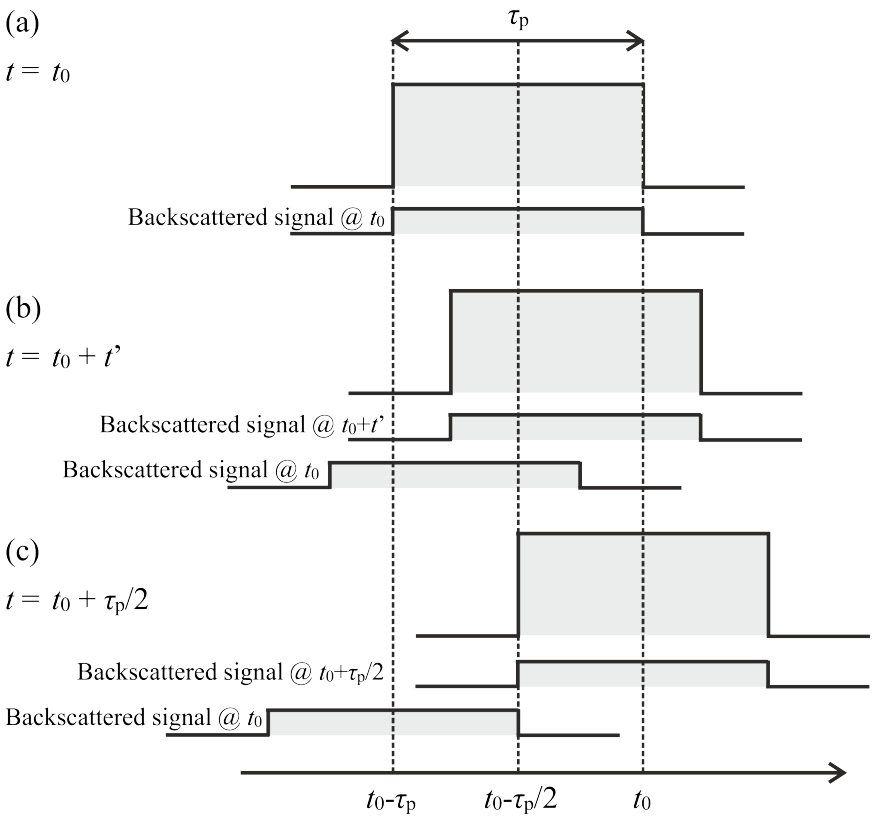

Figure 3.3: Propagation of an optical pulse in the fiber and its Rayleigh backscattered light at: (a) $t = t_0$, (b) $t = t_0 + t'$ and (c) $t = t_0 + \tau_p/2$ [57].

$$f_{\text{trigger}} < \frac{c}{2Ln_g} \tag{3.2}$$

where L is the fiber length. In the case of vibration sensing, the maximum measurable vibration frequency will be, by Nyquist theorem, the half of f_{trigger} [102, 103].

3.3 Fundamentals of ϕOTDR Technology

The use of incoherent light only allows to study the optical power losses in a fiber link. However, when highly coherent light is employed, the backscattered light pattern is sensitive to the relative phases of the backscattered waves, considerably changing the behavior of a reflectometer based on Rayleigh scattering. This idea is the basis of a Phase-Sensitive OTDR (ϕOTDR). Along the following section, the fundamentals and applications of ϕOTDR technology will be described.

3.3.1 Operational Principle

The operational principle of a ϕOTDR, which is based on the use of highly coherent light, is introduced by using an extremely simplified fiber model where only two scattering centers are considered (z_A and z_B), instead of the millions of scattering centers present in one meter of SMF.

We consider both scattering centers present the same reflectivity r and are illuminated by an electromagnetic wave of amplitude E_0 and angular frequency ω.

A scheme of this simple introductory model is shown in Figure 3.4(a), where E_A and E_B are the backscattered signals detected in z_0 which come from the scattering centers z_A and z_B, respectively, and are defined as:

$$E_\mathrm{A}(z = z_0) = E_0 r \cdot \exp[i\omega t + i\phi_0] \tag{3.3}$$
$$E_\mathrm{B}(z = z_0) = E_0 r \cdot \exp[i\omega\,(t - t_\mathrm{AB}) + i\phi_0] \tag{3.4}$$

where the optical path difference $t_\mathrm{AB} = 2n_1(z_\mathrm{B} - z_\mathrm{A})/c$ induces an extra phase $\phi_\mathrm{AB} = \omega t_\mathrm{AB}$ which allows to rewrite Equation 3.4 as:

$$E_\mathrm{B}(z = z_0) = E_0 r \cdot \exp[i\omega t + i(\phi_0 + \phi_\mathrm{AB})] \tag{3.5}$$

Thus, the induced phases ϕ_0 and $\phi_0 + \phi_\mathrm{AB}$ can be understood as the traveled optical paths along $[z_0, z_\mathrm{A}]$ and $[z_0, z_\mathrm{B}]$.

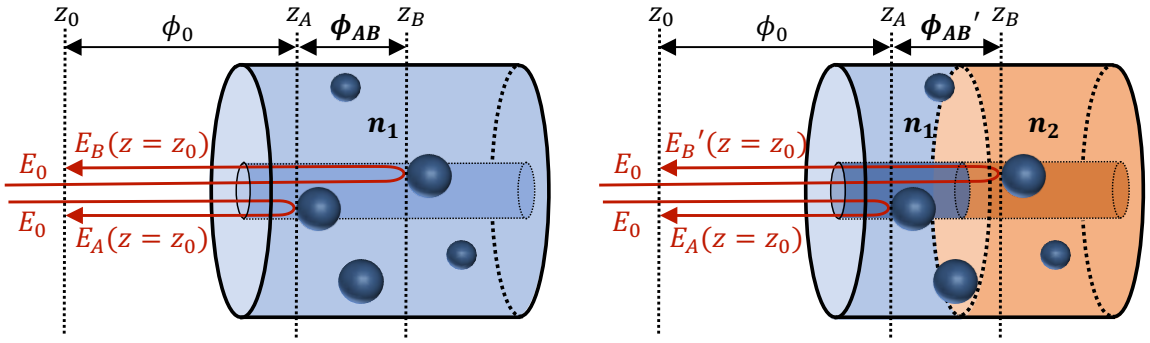

(a) Non-disturbed section

(b) Disturbed section

Figure 3.4: A simplified representation of a ϕOTDR: two scattering centers behaving as two reflectors.

The optical intensity which would be detected in z_0 is:

$$I(z = z_0) = |E_\mathrm{A} + E_\mathrm{B}|^2 = 2|E_0 r|^2\Big(1 + \cos(\phi_\mathrm{AB})\Big) \tag{3.6}$$

Equation 3.6 describes the behavior of a ϕOTDR and shows a relative phase dependence ϕ_AB, which is the main difference with a conventional OTDR. Since OTDR employs an incoherent light source, the average value of the interference term disappears $\langle\cos(\phi_\mathrm{AB})\rangle = 0$ since the phase of the light source is random. Thus, the optical intensities which would be detected in z_0 for the cases of an incoherent and a coherent light source are:

$$I_\mathrm{Incoherent}(z = z_0) = 2|E_0 r|^2 \tag{3.7}$$
$$I_\mathrm{Coherent}(z = z_0) = 2|E_0 r|^2\Big(1 + \cos(\phi_\mathrm{AB})\Big) \tag{3.8}$$

Thus, if the term ϕ_{AB} changes by any disturbance in the fiber, a ϕOTDR sensor is sensitive to it whereas a conventional OTDR is not. Figure 3.4(b) shows the same optical fiber, as the represented in Figure 3.4(a), where a section which contains the second scattering center presents a different refractive index n_2. This refractive index change generates a difference in the optical path $[z_{\mathrm{A}}, z_{\mathrm{B}}]$ and consequently, a variation of the relative phase difference $\Delta\phi$. In this case, the backscattered signal from z_{B} is described as:

$$E'_{\mathrm{B}}(z = z_0) = E_0 r \cdot \exp[i\omega t + i(\phi_0 + \phi'_{\mathrm{AB}})] \tag{3.9}$$

where $\phi'_{\mathrm{AB}} = \phi_{\mathrm{AB}} + \Delta\phi$. The intensity detected if a coherent light source is employed (ϕOTDR) is:

$$I'_{\mathrm{Coherent}}(z = z_0) = |E_{\mathrm{A}} + E'_{\mathrm{B}}|^2 = 2|E_0 r|^2\Big(1 + \cos(\phi_{\mathrm{AB}} + \Delta\phi)\Big) \tag{3.10}$$

This result shows the clear sensitivity of a ϕOTDR to changes in the relative phases among the reflected fields coming from different scattering centers. These changes arise from n_2 variations which can be originated by perturbations such as temperature or strain.

Following the simple model based only on two scattering centers, now we propose the model extended to a high number of scattering centers. As it has been mentioned before, the scattering centers are random density fluctuations produced during the fabrication process of the fiber. Despite the fact that the Rayleigh scattering process is random, the amplitude and relative phases of the scattered waves are deterministic and remain unalterable if the fiber is perfectly stable. This means that the values of ϕ_{AB} (which have a random value but are fixed) contribute to the final backscattered trace.

As the light propagates inside the fiber, using the model defined above, a section with the size of the optical pulse is illuminated at each instant. The section of reflectors that is illuminated will change as the pulse propagates in time. This is shown in Figure 3.5. In Figure 3.5(a) the pulse is at time t_1 illuminating one set of reflectors. Then it travels along the fiber, and at time t_2, another set of reflectors is illuminated. We can see that the signal from more than one reflector will be generated during an overlapping period of time. During this period, the reflected signals from both scattering centers will arrive at the same time at the origin, and will interfere with each other [104].

The time that the pulse requires to reach a position z in the fiber is $T = z/v_g$. Hence, the backscattered light from that point will require a time $t = 2T$ to reach the position $z = 0$, where it is detected. The detected optical field from every fiber point will be the sum of the fields reflected from the M scattering points contained in half of the section illuminated by the optical pulse $z \in [Tv_g - \tau_p/2, Tv_g]$ (as deducted from Figure 3.3):

$$E(t = 2T, z = 0) = E_0 e^{-2\alpha\overline{z}} e^{i\omega t} \sum_{m=1}^{M} r_m e^{i\phi_m} \tag{3.11}$$

where $\overline{z} = Tv_g - \tau_p/4$ is the position corresponding to the center of the fiber section from which the signal is being collected. The reflectivity of each scattering center is $r_m \in [0, 1]$ but usually is $\ll 1$. The corresponding phase of the waves reflected in the scatering centre m is given by

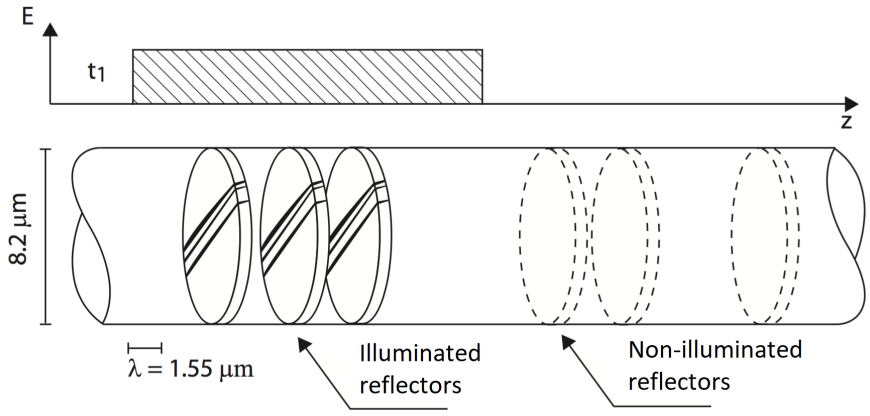

(a) The pulse in the fiber at time t_1 illuminates one set of reflectors

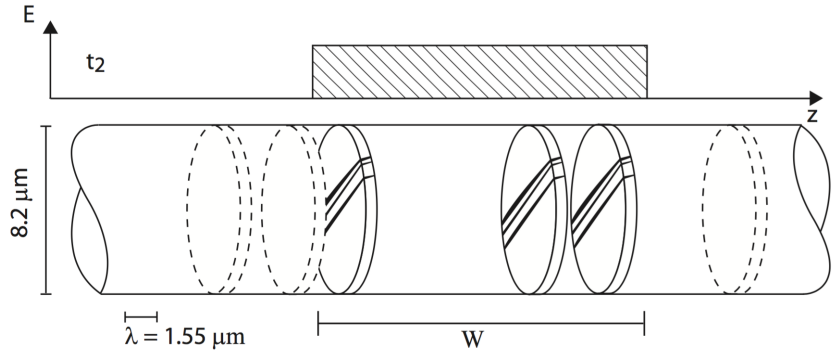

(b) The same pulse at time t_2

Figure 3.5: Pulse traveling inside the fiber [104].

the optical path $\phi_m = 2\pi n/\lambda \cdot z_m$. The normalized intensity (I) received at the beginning of the fiber ($z = 0$), neglecting losses, will be [104]:

$$I = |E|^2 = \left| \sum_{m=1}^{M} r_m e^{i\phi_m} \right|^2 = \sum_{m=1}^{M} r_m^2 + 2 \sum_{i=1}^{M-1} \sum_{j=i+1}^{M} r_i r_j \cos\left(\phi_i - \phi_j\right) \tag{3.12}$$

Equation 3.12 clearly shows how the light reflected from different scattering centers (Rayleigh backscattered light) interferes coherently to produce the detected optical power trace. Since the position of these scattering centers is random, the ϕOTDR trace typically has random oscillations along the fiber. An example of ϕOTDR trace is represented in Figure 3.6.

It is interesting to note that the probability distribution of I (Equation 3.12) follows an exponential distribution [104]:

$$P\left(I_M\right) = \frac{1}{M} e^{\left(\frac{-I_M}{M}\right)} \tag{3.13}$$

From Equation 3.13 we can find that the average intensity detected from a given position is proportional to the total number of scattering centers (M) in the section illuminated by the optical pulse in that position:

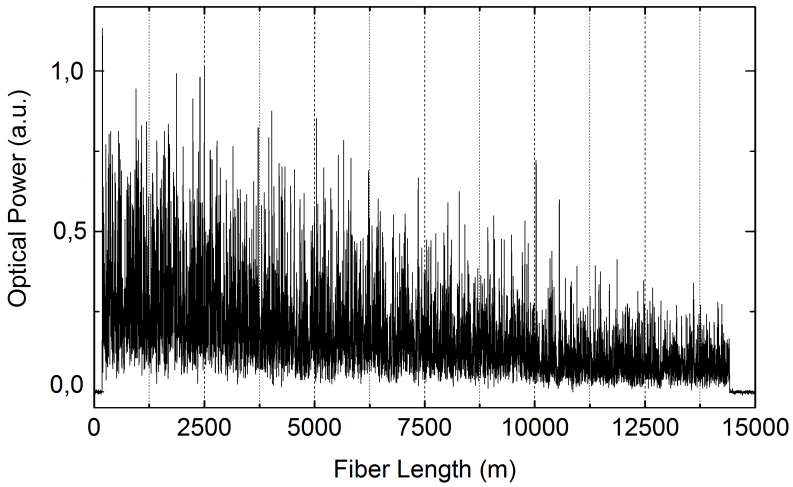

Figure 3.6: Example of a 14 km ϕOTDR trace obtained with a 100 ns optical pulse. Experimental measurement realized in our laboratory with a standard telecommunications optical fiber and a traditional ϕOTDR setup.

$$\langle I_M \rangle = \int_0^{+\infty} I_M P(I_M) dI_M = M \tag{3.14}$$

In OTDR operation, this random pattern along the fiber is a detrimental feature called fading or coherent noise [105]. In the case of ϕOTDR however, the technique is focused on measuring the temporal variations of this pattern, since the detected trace is sensitive to the changes in the relative phases among the reflected fields from the different scattering centers. The random pattern trace remains constant over the time if the fiber (scattering centers) do not suffer any change. However, if the relative phases among the reflected fields coming from the different scattering centers are changed at a given location due to a disturbance (e.g. due to local strain or temperature changes), the ϕOTDR trace at that position will vary [58]. This allows the detection of disturbances along the whole fiber, such as vibrations [34, 35], strain changes [36] or temperature changes [37].

From Equation 3.13 is possible to find a certain probability of having a signal intensity close-to-zero (i.e. a signal below the noise level of the detector) from a given position. In these positions, it is not possible to track signal variations, generating blind spots where the sensor will not give any information - fading points.

Following the static fiber description, now the behavior of the intensity trace when a punctual phase perturbation θ_p is applied in the q^{th} point ($q \in [1, M]$) is presented. The corresponding intensity variation I_Δ between the non-perturbed (I) and perturbed (I') signals is [34]:

$$I_\Delta = I - I' = 2 \sum_{i=1}^{q-1} \sum_{j=q}^{M} r_i r_j [\cos(\phi_i - \phi_j) - \cos(\phi_i - \phi_j - \theta_p)] \tag{3.15}$$

The probability distribution of the intensity variation will be Laplace-distributed [104], since the perturbed and unperturbed signals have correlated exponential probability distributions. From Equation 3.15 it is possible to conclude that only the relative phases $\phi_i - \phi_j$ contained at

the pulse resolution ($\tau_p/2$) around the q^{th} point participate in the intensity variation I_Δ. Thus, the perturbation only affects the region where it is applied while the rest of the optical trace I remains constant. This behavior allows ϕOTDR (and distributed sensors in general) to locate along the fiber different perturbations at different points. Furthermore, the intensity change induced by the disturbance in the fiber is not linear, except for very small values of θ_p. For this reason, other techniques such as frequency scan [36, 37] or phase detection [31–33] should be implemented if a linear response is required.

The model that describes a punctual perturbation can be extended to a distributed perturbation considering a section which contains an amount of points affected by a refractive index change Δn. In that case, all the scattering centers contained in the perturbed section will suffer a small phase change. The total accumulated phase change from the beginning to the end of the perturbed section is:

$$\Delta\phi = 2\frac{2\pi}{\lambda}\Delta n\Delta z \tag{3.16}$$

where Δn is the induced refractive index change by temperature (ΔT) or strain ($\Delta\varepsilon$) changes along the fiber section Δz. The accumulated phase difference $\Delta\phi$ is twice the optical path since the pulse travels in one direction and the backscattered signal in the opposite one. It is worth to note that a strain perturbation does not induce a real refractive index change but an optical path difference. However, this optical path difference can be described from an equivalent refractive index change. As usually occurs in the literature, during this dissertation we will refer to the equivalent refractive index change induced by a strain perturbation directly as the refractive index change.

To visualize this idea, Figure 3.7 shows a ϕOTDR trace before (black line) and after (red dotted line) a disturbance occurs at a point in an optical fiber. In green the trace difference is plotted is plotted. We can observe that only the region affected by the disturbance presents intensity variations (from meter 290 to 310), while the rest of the trace remains stable.

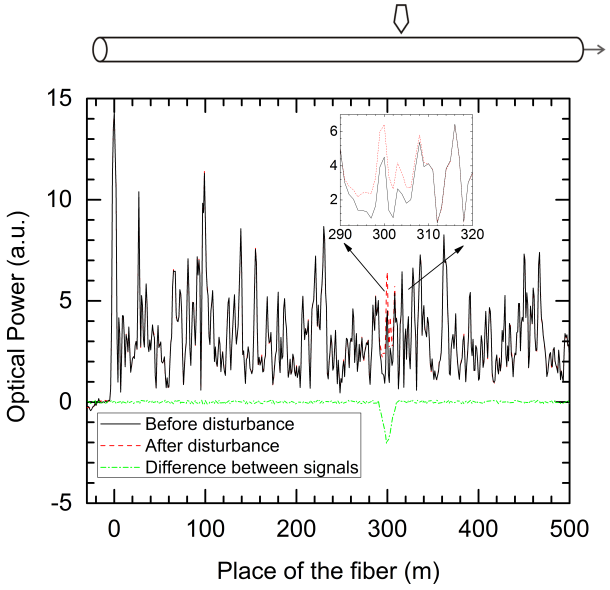

Figure 3.7: ϕOTDR trace before and after a disturbance occurs at a point in the fiber [58].

The relationships between Δn and the quantities ΔT and $\Delta\varepsilon$ were obtained experimentally by [36]:

$$\frac{\Delta n}{n} \approx -0.78 \cdot \Delta\varepsilon \tag{3.17}$$

$$\frac{\Delta n}{n} \approx -\left(6.92 \cdot 10^{-6}\right) \cdot \Delta T \tag{3.18}$$

In the paper published by Koyamada in 2009 [36], Equations 3.17 and 3.18 are expressed in term of $\Delta\nu/\nu$ instead of $\Delta n/n$, since a frequency (wavelength) shift can compensate a small refractive index change (see Equation 3.16). This idea will be explained in more detail in Subsection 3.4.3.

3.3.1.1 Typical Setup in a Conventional ϕOTDR

In this subsection an example of experimental setup of a ϕOTDR is presented. The main components that form the sensor and their functions in it are explained. Furthermore, some vibrations measurements will be presented in order to clarify the sensing method.

The experimental setup used to explain the performance of a ϕOTDR is shown in Figure 3.8. This setup and some of the following experimental examples are obtained from the thesis dissertation of Martins in 2014 [58].

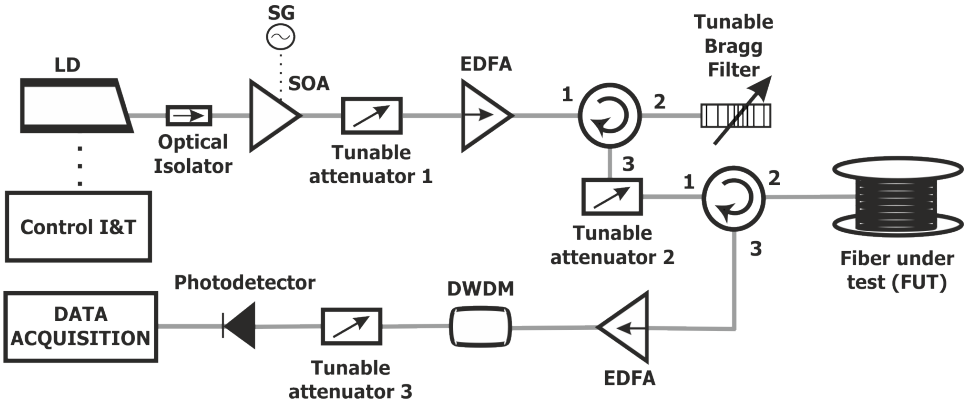

Figure 3.8: Experimental setup of a conventional ϕOTDR [58]. LD, Laser Diode; SOA, Semiconductor Optical Amplifier; EDFA, Erbium Doped Fiber Amplifier; DWDM, Dense Wavelength Division Multiplexer; I&T, Intensity & Temperature.

The coherence time of the light source employed in a ϕOTDR is critical as it has been mentioned before. A ϕOTDR sensor employs high coherence sources since the light backscattered from the scattering centers illuminated by an optical pulse must interfere between them. To do so, it is indispensable that the coherence length of the light source be greater than the optical pulse duration. Otherwise, phase variations appears along the optical pulse which generates intensity noise in the Rayleigh backscattered signal (see Equations 3.8 and 3.12.) The chosen light source in the setup shown in Figure 3.8 is a Laser Diode (LD) with a linewidth of 1.6 MHz [58], whose coherence length would be $\sim$40 m (see Equations 2.52 and 2.53). Thus, the laser would fit satisfactorily with spatial resolutions in the order of tens of meters (5 meters in this particular setup). The LD is driven by a standard current and temperature controller to select the central wavelength. An isolator has been used to avoid possible reflections being directed to the laser, which could affect the laser stability.

The optical pulses are created outside the LD avoiding instabilities. The Signal to Noise Ratio (SNR) of the detected trace will directly depend on the Extinction Ratio (ER) of the

device employed to create the optical pulses [34]. This idea will be explained in more detail in Section 3.5. The electro-optic device used for creating pulses is a Semiconductor Optical Amplifier (SOA) since it presents an ER of >50 dB. The device presents rise/fall times in the order 2.5 ns and driven by a waveform Signal Generator (SG) it is used to create 50 ns almost square pulses. The spatial resolution of the system is determined basically by the duration of the pulse [72], as described in Section 3.2. Therefore, the spatial resolution is 5 m in this case. Between the signal pulses, the SOA is negatively biased so as to enhance the Extinction Ratio (ER) of the delivered pulses.

In order for the backscatered signal to have an optical power suitable for detection, since the Rayleigh backscattering coefficient in a SFM is low ($\alpha_{\mathrm{Rb}} \approx -72$ dB/m) [64], high energy pulses (typically in the order of a few hundred mW) are required. To do so, an Erbium-Doped Fiber Amplifier (EDFA) is used to boost the power of the ϕOTDR pulses before sending them into the fiber.

In order to minimize the effect of the Amplified Spontaneous Emission (ASE) added by the EDFA it is convenient to use an optical filter to mitigate it. In this case, a tunable Fiber Bragg Grating (FBG) working in reflection performs this function. The spectral profile is the typical spectrum of a 100% reflection FBG, and its spectral width is 0.8 nm.

However, as it will be explained later, the peak power cannot be indefinitely increased due to the advent of non-linear effects such as Modulation Instability (MI) [40, 106, 107]. For this reason, before being coupled the optical pulse into the FUT, light passes through an attenuator, which allows to adapt the input power in the fiber below the non-linear effects threshold.

The backreflected signal from the fiber is also amplified using an EDFA and filtered by another optical filter. In this particular case, ASE is filtered through a Dense Wavelength Division Multiplexer (DWDM) with a spectral width of 0.8 nm.

Finally, the backscattered signal is photodetected and digitized. Since the ϕOTDR traces exhibit high-contrast rapid oscillations, the detector bandwidth should ideally be much larger than the trace spectral bandwidth. In this particular case, the pulse spectral bandwidth is around 20 MHz (generating a trace of similar bandwidth) and the detector has a bandwidth of 125 MHz, which is enough to adequately represent the process.

Figure 3.9 shows an example of vibration monitoring using the experimental setup explained before. In this particular case, the FUT was a 10 km SMF and a 20.3 Hz vibration was applied close to the end of the fiber [58]. The detected trace is represented in Figure 3.9(a), where it is shown a good SNR along the entire fiber. This ensures the full distributed measurement of vibrations using this technique. Comparing trace to trace it is possible to obtain the power variation along the time of the perturbed point. Figure 3.9(b) shows a clear pattern, with peaks synchronized with the applied frequency.

Phase-Sensitive OTDR (with direct detection) was introduced by Henry F. Taylor and Chung E. Lee in 1993 as a powerful tool for fiber optic intrusion sensing [72]. The same group continued researching in this topic verifying its applicability [108, 109]. As it was explained, the linewidth of the laser (directly associated to its coherence) is vital for this application. For this reason, this group developed an specific laser, based on Er^{3+} doped fiber [110] to be applied as pump in this system. This laser presented a very narrow linewidth (< 3 kHz) and a frequency-drift rate < 1 MHz/min. With a ϕOTDR pumped with this laser, they arranged to detect perturbations along 12 km with an spatial resolution of 1 km [111]. Two years later, the authors improved the detection system achieving to detect intruders on foot and vehicles over 19 km with 200 m spatial resolution [112]. Around 2014, a typical ϕOTDR was capable to achieve sensing ranges of tens of kilometers and meter spatial resolution [98, 113]. However, when ϕOTDR is assisted

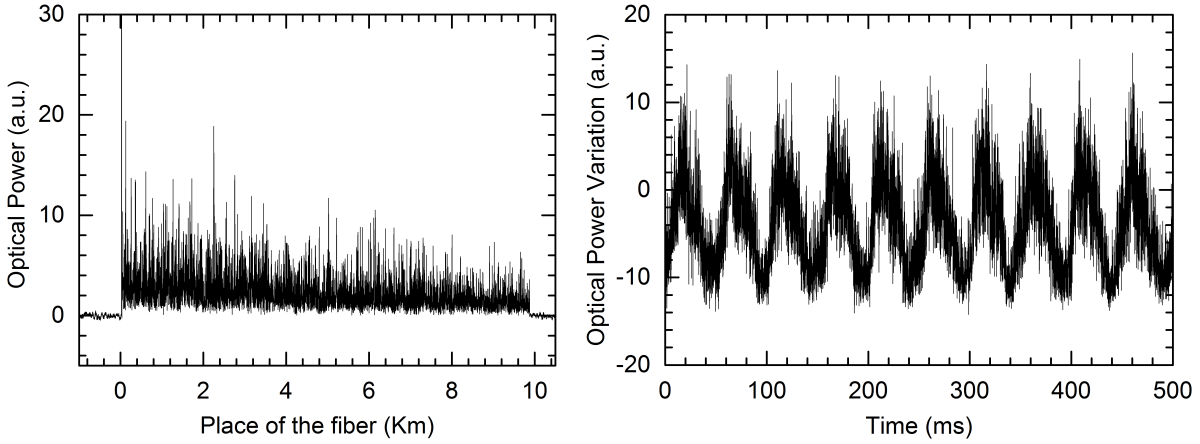

(a) Detected ϕOTDR trace from a 10 km SMF.

(b) Optical power variation along the time of the perturbed point.

Figure 3.9: Detection with a ϕOTDR of a 20 Hz vibration in the last meters of a 10 km SMF [58].

by distributed Raman amplification, sensing ranges over >100 km and 10 m spatial resolution have been demonstrated [21].

3.4 Non-linear Behavior and Solutions for Linear Sensing

In this section, the non-linear behavior of a ϕOTDR system when a perturbation is applied to the optical FUT will be discussed. Equation 3.15 describes the intensity variation that a point of the trace suffers when the fiber is perturbed by any disturbance (such as temperature, strain or vibration) in that point. Since the dependency of the intensity with the perturbation follows a cosine, it can be considered linear only if the perturbation is very small. However, this is not always the case.

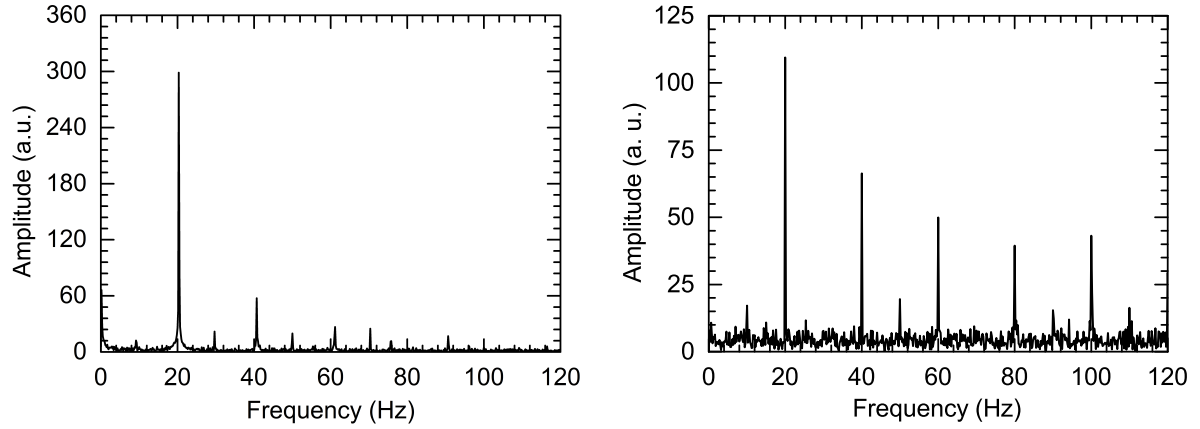

(a) Weak vibration.

(b) Strong vibration.

Figure 3.10: Spectral analysis of a 20 Hz vibration applied in the last meters of a 10 km SMF [58].

The pattern presented in Figure 3.9(b) is analyzed in the frequency domain by means of a Fast Fourier Transform (FFT), and the obtained results are represented in Figure 3.10(a). Here, a clear peak at 20.3 Hz appears, as well as smaller peaks in the second harmonic (40.6 Hz), and

multiples of half of the fundamental frequency (10 Hz, 30 Hz).

The experiment developed in 2014 [58] was replicated but inducing a vibration of higher amplitude in the excited point. The resulting spectrum of the detected vibration is represented in Figure 3.10(b), in which the harmonics and sub-harmonics have a higher amplitude than in the previous example. This shows good agreement with the theoretical model. If we reanalyze the Equation 3.15, it is simple to observe that perturbations of higher amplitude θ_p will give a system with a higher non-linear behavior. This was explored by Shatalin et al. in 1998 [114].

3.4.1 Vibration Simulation

Following the examples that experimentally illustrates the non-linear behavior of a ϕOTDR, now we continue analyzing this limitation by means of computational simulations. This is done for the conventional intensity ϕOTDR, but also for typically employed variations of the technique (coherent detection [31–33] and frequency sweep [36, 37]).

The simulated perturbation is applied along a fiber section of 20 meters and is sensed using a 50 ns optical pulse. This pulse duration gives a spatial resolution of 5 meters, allowing for the correct detection of the perturbation. The perturbation is a vibration of 20 Hz with a maximum strain of $\varepsilon_{\max} = 130 \cdot 10^{-9}$ which corresponds to an equivalent refractive index change of $\Delta n_{\max} = 1.47 \cdot 10^{-7}$. Thus, the applied perturbation along the time can be described as:

$$\Delta n(t) = 1.47 \cdot 10^{-7} \cdot \sin(20 \cdot 2\pi t) \tag{3.19}$$

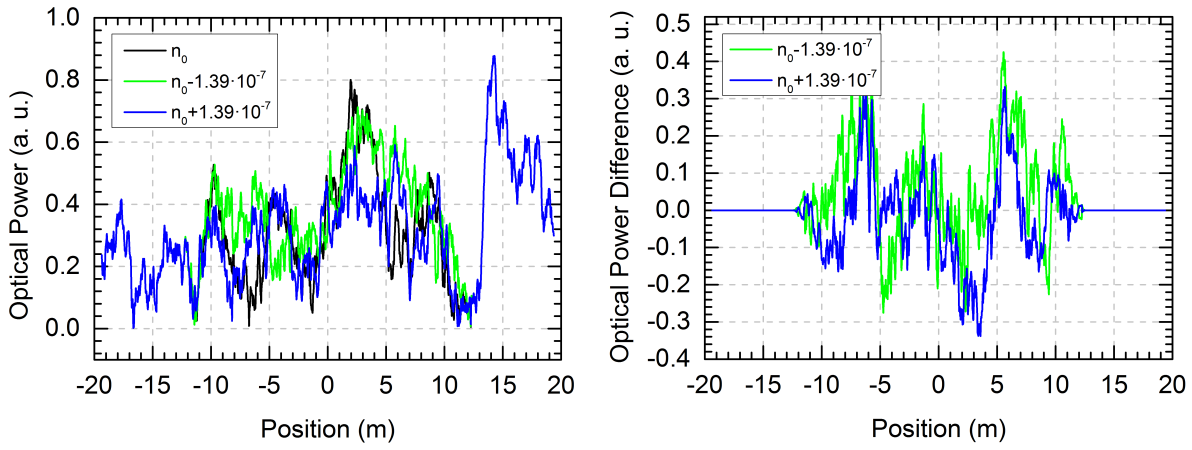

(a) Optical power traces

(b) Optical power traces differences

Figure 3.11: ϕOTDR traces simulation with optical pulses of 50 ns (5 m spatial resolution). Refractive index changes are applied along 20 meters of fiber. The zero of the position axis is located at the point where the simulated perturbation is applied.

The optical pulses are injected into the optical fiber with a repetition rate of $f_{\text{trigger}} = 500$ Hz during 2 seconds. Hence, the 20 Hz vibration can be monitored correctly. The resulting number of simulated optical power traces is 1000 (500 Hz $\times$ 2 s). The resulting traces, for three different refractive index changes (n_0, $n_0 - 1.39 \cdot 10^{-7}$ and $n_0 + 1.39 \cdot 10^{-7}$), are represented in Figure 3.11(a). The optical power differences with the first trace (n_0) are shown in Figure 3.11(b). Here it is simpler to observe the affected region, which is 25 meters (20 m for the perturbed region and another 5 m for optical pulse length), and the non-affected region by the perturbation.

When the optical power evolution of the most excited point is analyzed, the highly non-linear response of the system for high amplitude perturbations is clearly observed. This is shown in Figure 3.12. While the applied perturbation follows a 20 Hz sinusoidal function, the optical power variation response does not follow it (see Figure 3.12(a)). Developing a spectral analysis, by means of FFT of the temporal evolution, the appearance of harmonics is observed in the optical power variation. In fact, the 40 Hz peak (first harmonic) is higher than the fundamental frequency.

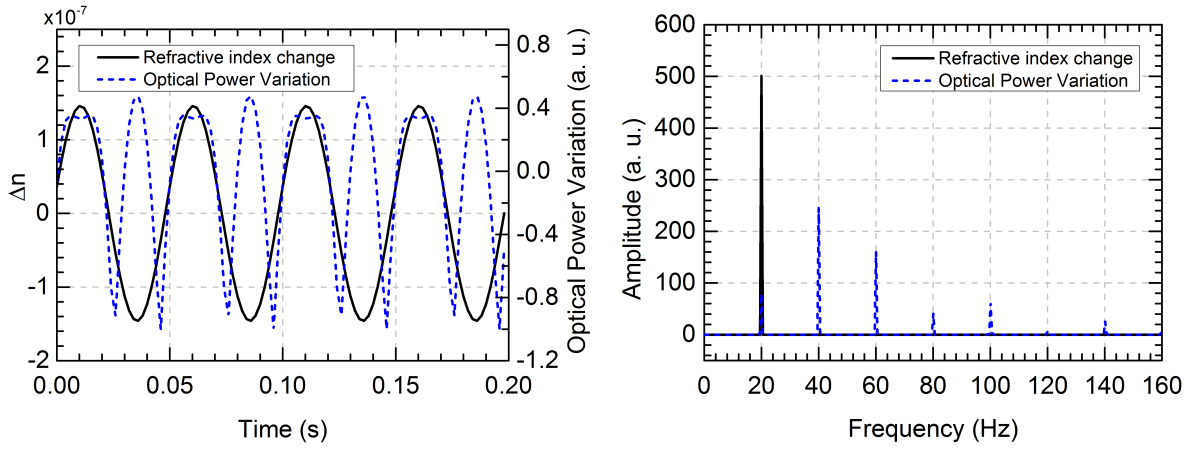

(a) Temporal evolution

(b) Frequency analysis

Figure 3.12: Comparison between the optical power variation and the induced refractive index change in the most excited point.

As the reader can imagine, this non-linear behavior represents a huge limitation in ϕOTDR based systems, since it makes the real and linear measurement of temperature or strain almost impossible to achieve. In the next subsections, the basis of two of the most important techniques (coherent detection [31–33] and frequency scan [36,37]), which allow for a linear measurement of refractive index variations using ϕOTDR, will be explained. The limitations of these techniques will also be explained here and they motivate part of the work developed during this doctoral thesis. In Chapter 5, a new method based on ϕOTDR using chirped pulses will be demonstrated. It solves the non-linear limitation of traditional ϕOTDR without the requirement of a frequency scan or coherent detection. It allows for the measurement of distributed strain and temperature changes, in a single shot with temperature/strain resolutions of 0.5mK/4nε while maintaining a low complexity. Furthermore, real acoustic sensing is demonstrated using this new ϕOTDR-based sensor.

3.4.2 Coherent Detection

An extensively used technique to achieve linear measurements of strain or temperature with ϕOTDR is coherent detection. Equation 3.16 shows the induced phase change $\Delta\phi$ by a refractive index change Δn in a fiber section Δz. It shows a linear dependence between $\Delta\phi$ and Δn. Thus, the phase information in the backscattered electric field will give quantitative information of an induced refractive index change, allowing for the linear measurement of strain, temperature and vibrations.

This idea was also simulated for the better understanding of the reader. As it was explained before, Figure 3.11 shows the obtained optical power traces when a perturbation is applied in a 20 m fiber section. It is simple to observe the unperturbed and perturbed (from -12.5 m

to 12.5 m) sections. With this methodology, instead of using the intensity changes between traces, we work with the phase of the electric field backscattered from the fiber. It is studied the phase difference between two fiber points: before and after the perturbation. The obtained results are represented in Figure 3.13. The temporal evolution of the induced refractive change and the obtained phase change are represented in Figure 3.13(a). Here, it is shown a perfect synchronization between both signals, giving a pure linear response. This is also well shown in the spectral analysis of these signals (see Figure 3.13(b)).

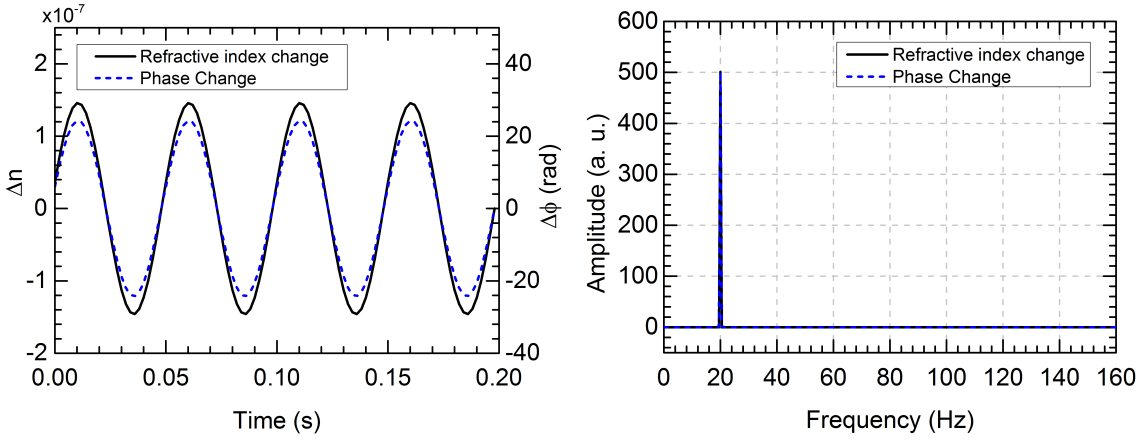

(a) Temporal evolution

(b) Frequency analysis

Figure 3.13: Comparison between the resulting ϕOTDR phase change and the induced refractive index change (before and after the perturbation).

The implementation of this technique relies on the phase recovery of the backscattered electric field. Generally, this is implemented by means of coherent detection, also known as heterodyne or homodyne detection depending on whether the Local Oscilator (LO) is frequency shifted or not, respectively [115]. Generally, the ϕOTDR which employs coherent detection is known as Coherent OTDR (COTDR) [28–31]. A ϕOTDR based sensor which employs heterodyne detection was developed in 1976 by Healey et al. [28]. However, the use of coherent detection was only employed for SNR increase purposes in this case [28]. The first ϕOTDR system based on the phase of backscattered signal was proposed by Posey et al. in 2000 [29]. This system provided a mean to quantify the strain. However, this system was only able to monitor the dynamic strain at a single section of the fiber at each time. In 2010, Lu et al. developed a COTDR able to measure vibrations up to 1 kHz along 1.2 km with 5 m spatial resolution [30]. Three years later, Masoudi et al. developed a similar system that detected vibrations up to 5 kHz along 1 km with a spatial resolution of 2 m [31]. These last two techniques were capable of quantifying multiple dynamic strain perturbations along the whole sensing fiber simultaneously.

In a coherent detection system, the optical signal and the LO signal are mixed before photodetection [116]. This was initially proposed in the context of the usage of ϕOTDR for distributed vibrations in 2010 [30]. Although, the use of coherent detection in ϕOTDR for static measurements had previously been reported as well [36].

Figure 3.14 shows a simplified typical setup of ϕOTDR using coherent detection ϕOTDR. A Continuous Wave (CW) laser light with an optical frequency ω is divided by an optical coupler into two parts, one to be used as LO (E_{LO}) and the other to be used as the ϕOTDR pulse, which will generate the backscattered signal E_{b}. The pulse is generated using an intensity modulator. The same modulator (or a second one) can shift the pulse frequency in $\Delta\omega$ (typically in a few hundreds of MHz [24, 30]) when heterodyne detection wants to be implemented. If the pulse

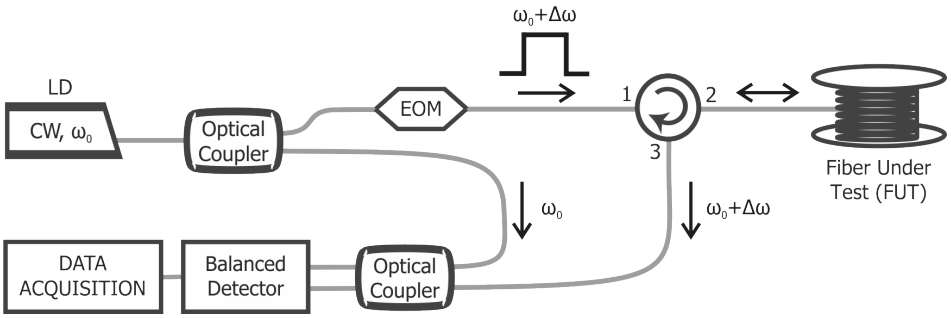

Figure 3.14: Practical setup of a ϕOTDR using coherent detection.

frequency is not shifted the detection is known as homodyne. Homodyne detection requires lower detection bandwidth compared to heterodyne. However, it presents some drawbacks such as the use of two balanced detectors (instead of one) and a more complex optical hybrid [115]. Overall, the main differences (benefits and limitations) of both implementations employing phase demodulation (homodyne and heterodyne) compared to direct detection are similar. For this reason, we focus the description on heterodyne detection, since it is the easiest to understand and simplest to implement coherent detection.

In the case of heterodyne detection, the Rayleigh backscattered signal $E_b(t)\exp(i\omega t + i\Delta\omega t + \phi(t))$ is mixed with the LO light $E_{\mathrm{LO}}(t)\exp(i\omega t)$ by another 3 dB coupler. The mixed signal is then launched to a balanced detector. The optical power $I(t)$ resulting from the interference of the LO signal (E_{LO}) with the backscattered signal (E_{b}) will be given by:

$$I(t) \propto E_{\mathrm{LO}}(t)^2 + E_{\mathrm{b}}(t)^2 + 2E_{\mathrm{LO}}(t)E_{\mathrm{b}}(t)\cos(\theta_P(t))\cos\left(\Delta\omega t + \phi(t)\right) \tag{3.20}$$

where $\theta_P(t)$ and $\phi(t)$ are the relative polarization angle and phase between the LO signal (E_{LO}) and the backscattered signal (E_{b}), respectively. It is worth to note that, provided that the 180 degree phase shift between the two outputs of the 3 dB coupler is preserved, the use of balanced detection will eliminate the Direct Current (DC) and common mode components and will improve the SNR by 3 dB [30]. Furthermore, since the optical amplitude of the LO is typically much higher than the backscattered signal $E_{\mathrm{LO}} \gg E_{\mathrm{b}}$, the signal of interest $\propto E_{\mathrm{LO}}E_{\mathrm{b}}$ (obtained using coherent detection) will be also much higher than E_{b}^2 (the detected using direct detection). Thus, the coherent detection can provide a considerable higher sensitivity for detection of weak Rayleigh backscattered signals than the direct detection [30].

However, the amplitude of the interference between E_{LO} and E_{b} strongly depends on their relative state of polarization and can even reach zero for the case of orthogonal polarizations. Coherent detection is therefore generally dependent on changes of the State Of Polarization (SOP) along the optical paths of E_{LO} and E_{b} before these are mixed, and the setup is therefore very sensitive to SOP changes [58]. Some possible solutions are using Polarization-Maintaining Fibers (PMFs) or using dual-polarization coherent receivers [115]. However, this increases the complexity/cost and can decrease the system performance. PMFs are expensive and present high losses, which severely limits the sensing range when compared to the use of SMF.

Another important limitation of this technique is related to the required coherence length of the laser. In direct detection, coherence length of the laser required is of the order of the pulse width (l_c ~64 m, Δf ~1 MHz) [34]) since interference occurs between waves separated by as much as that length. However, the required laser coherence length for coherent detection schemes will be of the order of twice the fiber size ($\Delta f \approx 32$ kHz for 1 km of fiber and $\Delta f \approx 320$

Hz for 100 km of fiber). This requirement can considerably increase the complexity and cost of the system and/or limits the system performance.

In Chapter 4 (Section 4.4), the possibility of using Phase Reconstruction using Optical Ultrafast Differentiation (PROUD) in a ϕOTDR sensor will be studied. PROUD is a self-referenced technique which allows recovering the instantaneous frequency and phase of arbitrary optical signals [117–119]. Since beating with a LO is not required, the technique does not present polarization or phase-noise impediments. Therefore, the implementation of PROUD in a ϕOTDR sensor could be really interesting for recovering the complex field of the backscattered trace (amplitude and phase).

3.4.3 Frequency Scan

Another technique used to obtain a linear response using ϕOTDR is by employing a frequency scan. From Equation 3.16 it can be concluded that a refractive index change Δn can be compensated by an optical pulse central wavelength shift $\Delta\lambda$. This can be expressed mathematically in term of the optical pulse central frequency as [36]:

$$\frac{\Delta n}{n} = \frac{\Delta \nu}{\nu} \tag{3.21}$$

The methodology to implement a distributed sensor based on this phenomenon is by means of frequency scans. The data collection consists in measuring with a conventional ϕOTDR repeatedly while changing the laser frequency step by step (from an initial to a final frequency) and recording the measured backscattered power as a function of laser frequency and distance $I_1(\nu, z)$. This process is repeated and another data collection $I_2(\nu, z)$ is obtained. If there are no changes in the strain or the temperature in the fiber during the two intervals, $I_2(\nu, z)$ becomes similar to $I_1(\nu, z)$. On the other hand, if the strain or the temperature changes, $I_2(\nu, z)$ is different from $I_1(\nu, z)$. Instead, $I_2(\nu + \Delta\nu, z)$ becomes similar to $I_1(\nu, z)$, where $\Delta\nu$ is the change in the laser frequency that compensates for the change in the strain or the temperature so that the phase difference becomes the same as that for the initial measurement [36]. Using Equation 3.21 and the measured $\Delta\nu$ is possible to obtain the refractive index change.

This technique has been used for the measurement of strain and temperature changes [36] and birefringence [38, 39]. However, this technique is not well suitable for dynamic measurements, since the measurement time is increased by the number of pulses used in the frequency scan. There are some examples of dynamic sensing with this method although the complexity of its implementation is considerably increased [37].

Simulations under similar conditions to the presented in Figure 3.11(a) have been realized. In Figure 3.15 are represented the resulting traces when a refractive index variation is applied, and the optical pulse is correspondingly shifted to compensate for that variation. The induced refractive index changes are $\Delta n = \pm 1.39 \cdot 10^{-7}$ and the corresponding frequency shifts are $\Delta\nu = \pm 18.4$ MHz (obtained from Equation 3.21). Thus, the centered region remains unchanged (the refractive index is compensated) and the rest of the fiber presents variations (see Figure 3.15(a)). The optical power differences with the first trace (n_0 and ν_0) are shown in Figure 3.15(b). Here it is simpler to observe the mentioned above. Hence, realizing frequency scans, it is possible to search the refractive index change that is affecting any fiber section.

The index variation $\Delta n(t) = 1.47 \cdot 10^{-7} \cdot \sin(20 \cdot 2\pi t)$ can be correctly measured as it is represented in Figure 3.16. The temporal evolution of the induced refractive change and the

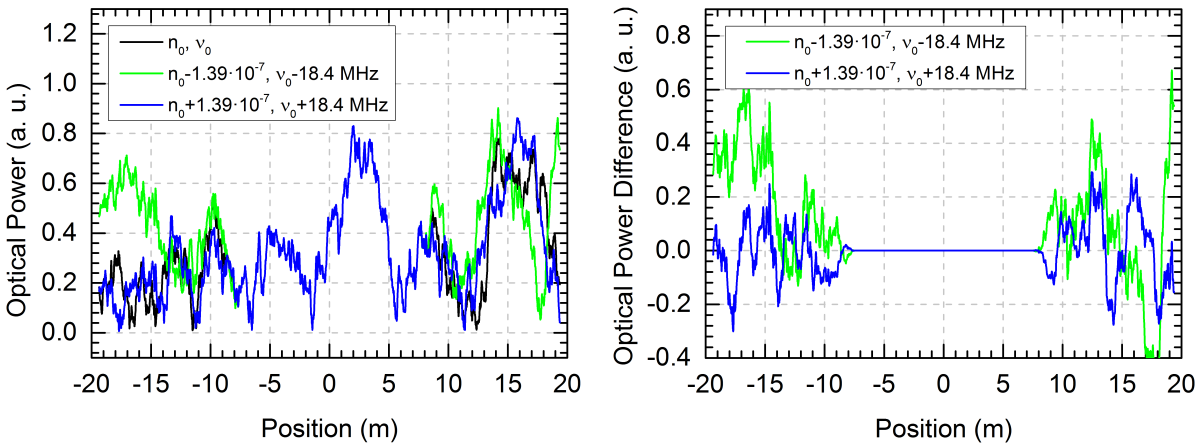

(a) Optical power traces

(b) Optical power traces differences

Figure 3.15: ϕOTDR traces simulation where refractive index changes are applied. The laser frequency is tuned to compensate the refractive index change. The zero of the position axis is located at the point where the simulated perturbation is applied.

obtained frequency shift is represented in Figure 3.16(a). Here, as in the coherent detection method, it is shown a perfect synchronization between both signals, giving a pure linear response. This is also well shown in the spectral analysis of these signals (see Figure 3.16(b)).

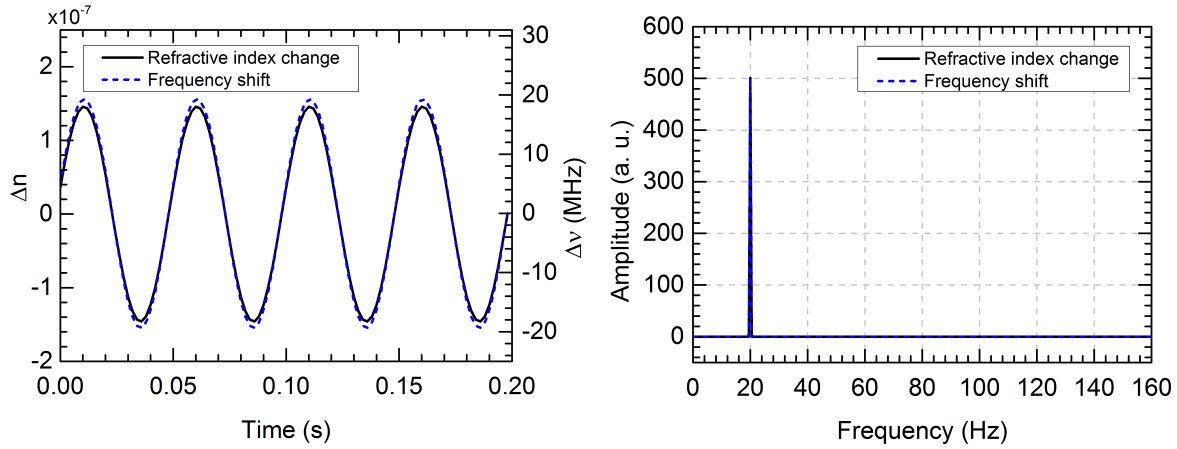

(a) Temporal evolution

(b) Frequency analysis

Figure 3.16: Comparison between the induced frequency shift and the induced refractive index change in the most excited point.

3.5 Signal to Noise Ratio (SNR): Range and Resolution

The Signal to Noise Ratio (SNR) of a ϕOTDR depends on the amount of energy of the employed optical pulses. Both signals, pulse and backscattered signal, suffer attenuation during their propagation along the fiber ($\alpha \sim 0.2$ dB/km). This means that the SNR of the trace decreases exponentially as the pulse moves away from the fiber beginning (see Equation 2.13 and Figure 3.6), which limits the maximum measurable range of the system. The Rayleigh backscattering coefficient in a SFM is $\alpha_{\mathrm{Rb}} \approx -72$ dB/m [64]. Thus, the intensity of the backscattered from a

position L and observed in the fiber input ($P_b(z = 0, L)$) depends linearly on the input peak power (P_{peak}) and the pulse duration (τ_p) as:

$$P_b(z = 0, L) = \alpha_{\text{Rb}} \frac{\tau_p}{2} P_{\text{peak}} e^{-2\alpha L} = \alpha_{\text{Rb}} W P_{\text{peak}} e^{-2\alpha L} \tag{3.22}$$

An increase in τ_p implies more power backscattered from the scattering centers. However, the resolution of the system decreases (see Equation 3.1). For this reason, if the resolution of the system (W) must be preserved and the SNR (range) augmented, the peak power should be enhanced. However, the peak power cannot be increased indefinitely due to the onset of non-linear effects [40, 106, 107], as it will be explained further in the next subsection. Thus, as the reader can imagine, there is always a critical trade-off between the spatial resolution and range (SNR) in ϕOTDR based sensors. To overcome this trade-off, implementing other techniques such as distributed amplification [21–27], coding techniques [4, 5, 85–92], Optical Pulse Compression Reflectometry (OPCR) [94, 95] or signal post-processing [24, 30, 35, 97–100] would be necessary.

The noise level in a ϕOTDR system comes from two main noise sources: electrical noise caused by the photodetection process and optical noise which causes fluctuations in the input power to the detector. The photodetector noise is composed mainly by shot noise and thermal noise. Considering a commercial photodetector and typical values for these type of systems of peak power on the order of hundreds of milliwatts and pulse lengths of a few meters, the SNR given by pure detection processes in a 100 MHz detector is of the order of 20 dB, using the traditional formula for a p-i-n receiver [120]. However, the electrical noise induced is higher when greater bandwidths are employed. This noise can be mitigated reducing the operation temperature of the detector, considering that the noise contributions introduced by the photodetection process are close to the fundamental minimum.

Regarding the optical noise, it is introduced backscattered ASE from the optical amplifiers and the non-infinite ER of the pulse generator. Signal-ASE and ASE-ASE noise can be reduced using an optical filter centered around the ϕOTDR pulse frequency, since the ASE presents a broadband spectrum. The other source of noise comes from technological limitations when generating the optical pulse. Optical pulses are typically generated with an Electro-Optic Modulator (EOM) or a Semiconductor Optical Amplifier (SOA). Since the ER of these devices is not infinite, there is optical power (at the ϕOTDR pulse frequency) outside the ϕOTDR pulse. Due to this, intra-band noise is generated. This phenomenon is represented in Figure 3.17.

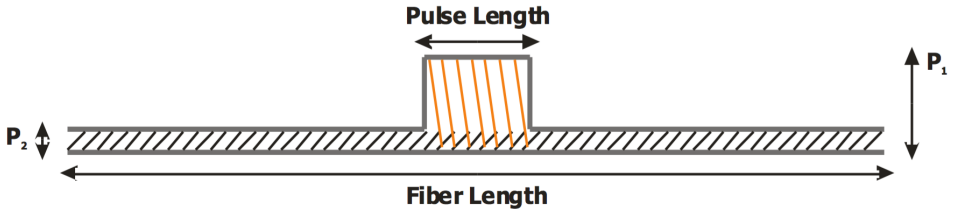

Figure 3.17: Power distribution along the fiber for a ϕOTDR pulse with finite ER [58].

The optical pulse generator ER is defined as the ratio between the pulse peak power (P_1) and the CW (P_2) at the central laser frequency (ER= P_1/P_2). An ideal optical pulse generator would present an infinite ER. When the light source is incoherent the intra-band noise is also incoherent. The SNR in this case is:

$$\mathrm{SNR} \propto \mathrm{ER} \cdot \frac{L_{\mathrm{pulse}}}{L_{\mathrm{fiber}}} \tag{3.23}$$

where L_{fiber} and L_{pulse} are the lengths of the fiber and the pulse in the fiber, respectively. However, in a common ϕOTDR the light sources are highly coherent. In that case, the coherent length can be as long as the fiber length, making possible the interference between the backscattered CW and the backscattered pulse. Thus, the detected power will have three terms. One proportional to the pulse power ($\alpha_{\mathrm{Rb}} P_1 L_{\mathrm{pulse}}$), another proportional to the CW ($\alpha_{\mathrm{Rb}} P_2 L_{\mathrm{fiber}}$) and the interference of the two ($\alpha_{\mathrm{Rb}} \sqrt{P_1 L_{\mathrm{pulse}} P_2 L_{\mathrm{fiber}}}$). If it is considered good ER ($P_1 L_{\mathrm{pulse}} \gg P_2 L_{\mathrm{fiber}}$), the SNR associated to the coherent intra-band noise is:

$$\mathrm{SNR} \propto \sqrt{\mathrm{ER} \cdot \frac{L_{\mathrm{pulse}}}{L_{\mathrm{fiber}}}} \tag{3.24}$$

Here it is shown the importance of using a pulse generator with high ER. Generally, the conventional EOM only presents an ER of 20–30 dB. However, a SOA can achieve an ER of 50 dB. That is the reason why in the results presented in this thesis a SOA instead of an EOM is employed. A SNR of >20 dB can be obtained with a SOA operating in a typical ϕOTDR of 10 km range and 10 m pulse length.

3.5.1 Peak power limitations due to onset of non-linear effects – MI

Modulation Instability (MI), explained in Chapter 2, is the first non-linear effect to arise under normal operation conditions (almost square pulses from tens to hundreds of ns duration). It results in the appearance of two gain sidebands on each side of the central wavelength [50, 51] and only occurs in anomalous regime ($\beta_2 < 0$). MI mainly depends on four parameters: input peak power (P_{peak}), Group Velocity Dispersion (GVD) coefficient (β_2), non-linear parameter (γ) and the noise level (see Equation 2.45). Thus, for low pulse peak powers, the effect of MI is negligible and the spectrum remains unaltered along the pulse propagation.

However, when high peak powers are employed, the MI effect cannot be neglected. Figure 3.18 shows the simulation of the ϕOTDR pulse spectrum evolution for a peak power of 1.25 W. The simulation was realized by solving the Non-Linear Schrödinger Equation (NLSE) 2.30 and using a split-step Fourier algorithm [121] with adaptive step size. The considered parameters were: attenuation coefficient $\alpha = 0.2$ dB/km, non-linear parameter $\gamma = 1.3$ W^{-1}km^{-1}, GVD coefficient $\beta_2 = -22.8$ ps^{2}km^{-1} and fiber length of 10 km [106].

The use of traditional rectangular probe pulses generally induces a power exchange between the pump and the sidebands known as Fermi-Pasta-Ulam (FPU) recurrence [122, 123]. During the pulse propagation depletion of the main laser line in favor of the sidebands occurs. However, after a certain distance the sidebands transfer back some power to the central wavelength. By increasing the input peak power, the observed minima in the central wavelength are more numerous and the first one appears closer to the fiber beginning. This also happens for other pulse shapes such as Gaussian-like, triangular and super-Gaussian, although to a minor extent [124], as it will be demonstrated in Chapter 4 (Suction 4.2).

These induced power minima around the central wavelength are revealed in the trace as a visibility fading at certain specific positions. Figure 3.19 shows the evolution of a ϕOTDR trace obtained with an optical pulse of ∼1.25 W and 50 ns duration along 10 km. The visibility is

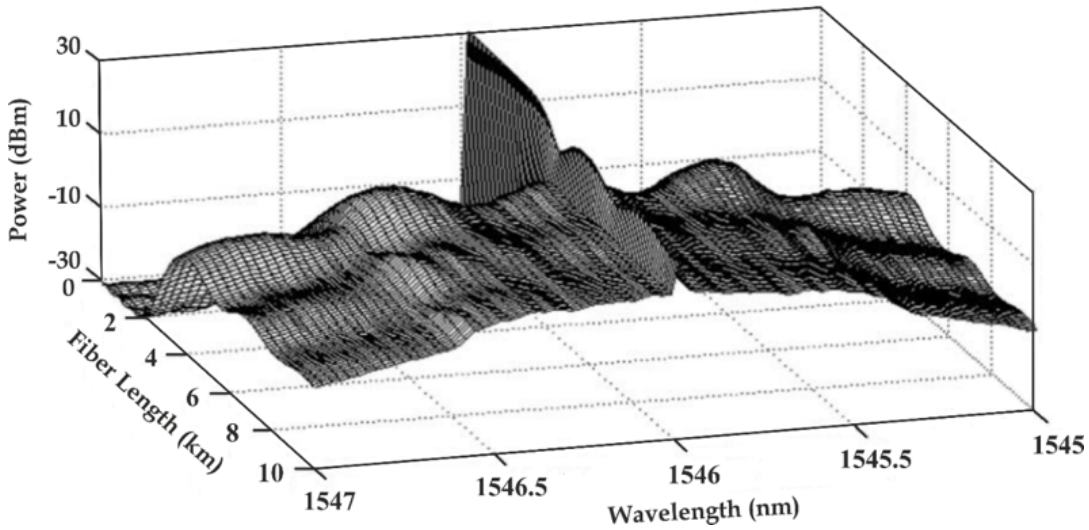

Figure 3.18: Simulation of the ϕOTDR pulse spectrum evolution along a SMF for a ϕOTDR pulse peak power of 1.25 W [106].

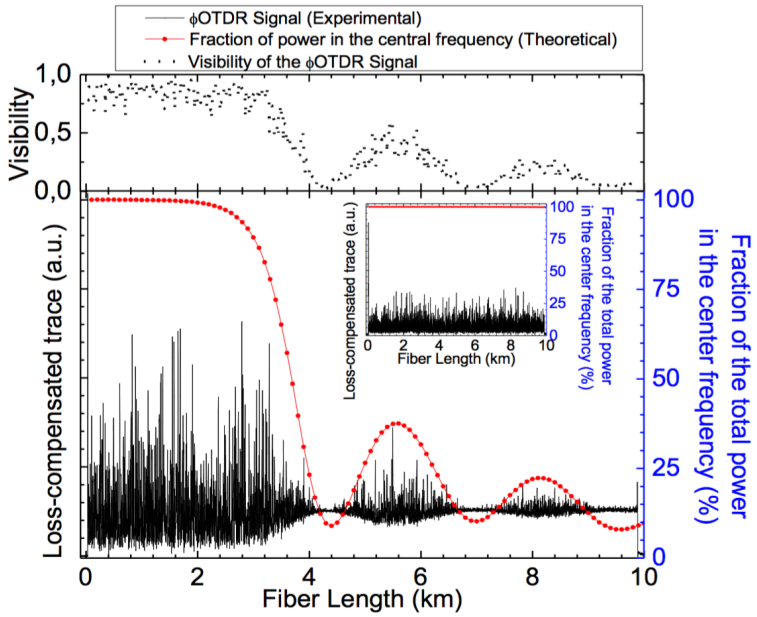

Figure 3.19: ϕOTDR trace and theoretical fraction of power contained in the central wavelength along the FUT for a ϕOTDR pulse peak power of ∼1.25 W (main figure) and ∼0.35 W (figure inset). The top figure shows the visibility of the ϕOTDR interference signal for the main figure signal. Losses were compensated numerically [106].

represented in the top of Figure 3.19 and it is calculated as $V = (T_{max} - T_{min})/(T_{max} + T_{min})$, where T_{max} and T_{min} are the maximum and minimum values of the trace over a window of 40 m [106].

It is simple to observe the points (4.4 km, 6.8 km and 9.5 km) where visibility of the interference is lost or greatly decreased and therefore the sensing sensitivity of the system is almost null at those positions. It is also worth to note that the overall visibility would also be decreasing rapidly, thus severely reducing the performance of the sensor. The inset represented in Figure 3.19 shows the trace when the pulse peak power is ∼0.35 W, where no FPU recurrence is observed. From this study, developed by Martins in 2013 [106], it is concluded that the appearance of MI is an important limitation in ϕOTDR based systems. The peak power always must be below the MI threshold. For sensing fibers around 10 km, this threshold was situated for standard SMF close to 400 mW.

3.5.2 Proposed methods to increase range and resolution

In the previous subsection the MI effect in ϕOTDR sensors was presented, which depends directly on the pulse peak power. For this reason, if the sensing range has to be increased without a resolution detriment (and the pulse peak power cannot be increased due to the onset of nonlinear effects) other techniques must be implemented. Some of this techniques will be presented in this subsection.

3.5.2.1 Distributed Amplification

The stimulated versions of Raman and Brillouin scattering are interesting techniques to increase the range of optical fiber sensors [19–27, 70, 125–127]. For more than three decades, distributed Raman amplification has been used to increase the performance of optical communication systems [128–130]. Regarding optical fiber sensing, Raman amplification has been used to assist punctual [127] and distributed sensors [19–24, 70, 125, 126]. Typically, first-order [19–21, 24, 70, 125] and second-order [22, 23, 69, 126] pumping configurations are the most employed.

Regarding ϕOTDR-based sensors, Raman amplification can be used to maintain both ϕOTDR pulse and backscattered signal powers at suitable power levels the whole fiber length, while avoiding excessively high peak powers, thus extending the sensing range. First-order Raman amplification was implemented to achieve sensing distances over 62 km [19] and 74 km [20] with spatial resolutions of 100 m and 20 m respectively. However, since no vibration measurement was performed in these cases, the performance as a vibration sensor was not clearly established.

One of the main concerns of Raman amplification is the RIN transfer from the Raman pumps to the amplified signal [21,131–133]. In 2014, the use of balanced detection to mitigate the effect of the RIN transfer from the Raman pumps was reported [21], allowing to measure vibrations up to 390/250 Hz over 100/125 km with a spatial resolution of 10 m. A performance improvement using second-order over first order Raman amplification (under similar measurement conditions) was reported by the same authors [22, 23]. Figures 3.20(a) and 3.20(b) show a comparison between the detected ϕOTDR traces when first and second-order Raman amplification are performed. The duration of the employed optical pulses was 100 ns and the both Raman pump powers (propagating and counter-propagating with the pulse) were around 28.5 dBm. As it is observed in Figures 3.20(a) and 3.20(b), the advantage of using second-order Raman amplification over first-order Raman amplification is clear as the trace presents higher flatness along the fiber under similar measurement conditions. This ensures the best performance as

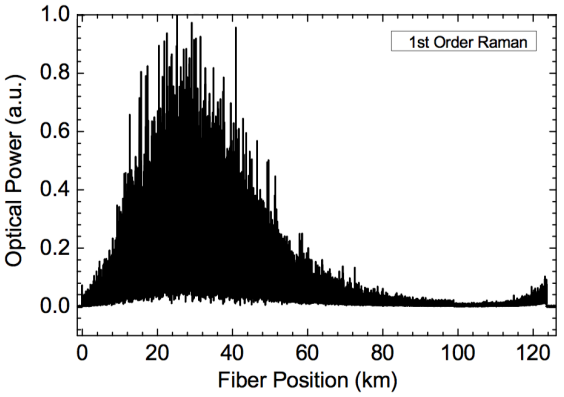

(a) First-order Raman amplification [22].

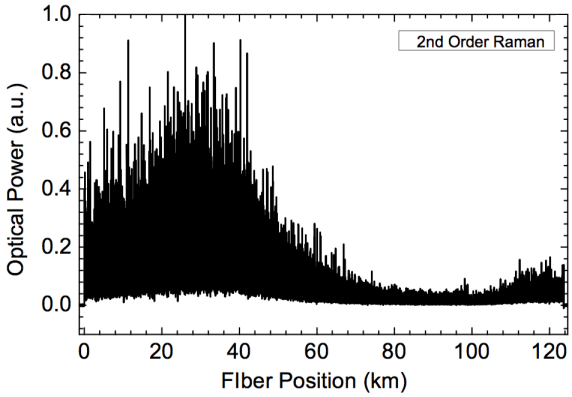

(b) Second-order Raman amplification [22].

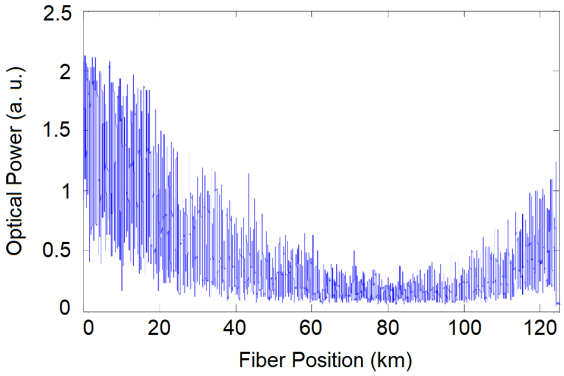

(c) Brillouin amplification [25].

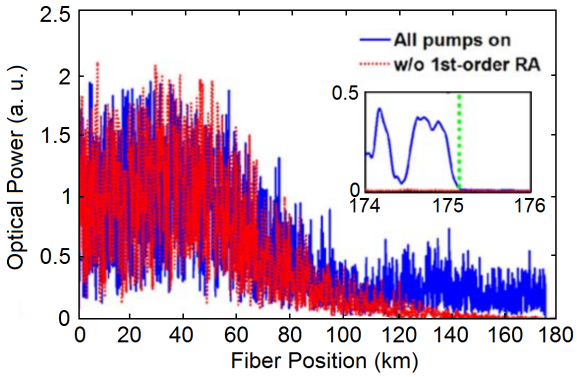

(d) Combination of first and second-order Raman amplification with Brillouin amplification [27].

Figure 3.20: Obtained ϕOTDR traces with different distributed amplification techniques.

higher amplitude of oscillations and therefore higher SNR is achieved in the lowest sensitivity point [22].

Regarding ϕOTDR with coherent detection, first-order Raman amplification has been also implemented [24], achieving an SNR improvement compared to [22, 23]. In this case, similar frequencies (up to 375 Hz) over 125 km, with a spatial resolution of 8 m were achieved. However, as it was presented in Subsection 3.4.2, the complexity of the scheme is considerably increased since coherent detection is implemented (requiring a laser with a linewidth three orders of magnitude lower than the one needed in direct detection scheme).

The use of high pump powers required in Raman amplification is another concern of this technique. Since Stimulated Brillouin Scattering (SBS) presents higher gain coefficient (three orders of magnitude) than Stimulated Raman Scattering (SRS), Brillouin amplification can be a quite interesting alternative to Raman amplification. A ϕOTDR assited by Brillouing amplification for intrusion sensing over 124 km was demonstrated [25, 26]. The duration of the pulses was 400 ns and the Brillouin pump presented a power of only 9.5 dBm, considerably lower than the Raman case [22]. An example of the ϕOTDR traces obtained with these parameters is shown in Figure 3.20(c) [25]. Furthermore, in this case, coherent detection (with an ultra-narrow linewidth laser of 100 Hz) and wavelet denoising, were used. Brillouin gain is dependent on the frequency difference between the signal and the pump, known as Brillouin Frequency Shift (BFS). Since BFS depends on strain/temperature, the system can become unstable. This is one of the main limitations of this technique.

The maximum sensing range achieved at the present time is 175 km without the use of repeaters. This record was achieved combining first and second-order Raman amplification with Brillouin amplification [27]. Additionally, a customized fiber link with varying BFS gain was required in order to achieve non-uniform Brillouin gain along the fiber. In this example, Raman pump power in both directions was around 30 dBm and the Brillouin pump power around 0.75 dBm. The employed optical pulses presented a duration of 250 ns which implies 25 m of spatial resolution. The resulting ϕOTDR trace is represented in Figure 3.20(d) (blue), in which it is proved the SNR is maintained along the entire fiber. The obtained trace when the Raman pump is turned off is represented in red [27].

In this work, first-order Raman amplification has been used combined with linearly-chirped pulses. The results will be explained in Chapter 7, where a Long Range Chirped-Pulse ϕOTDR will be presented. In this case, the maximum measurable range achieved was 75 km (10 m spatial resolution), in front of the 11 km without Raman amplification, previously reported [134].

3.5.2.2 Coding Techniques

As it is well known, the maximum repetition ratio with which optical pulses are sent to the fiber is limited (see Equation 3.2), since the superposition of traces generated from different pulses must be avoided. However, pulse coding offers an interesting solution to this limitation, allowing to send multiple pulses within one T_{trigger} ($T_{\text{trigger}} = 1/f_{\text{trigger}}$) [4, 5, 85–93]. Thus, the energy imputed to the fiber is increased and the SNR of the trace is higher if the signal can be correctly demodulated. This allows to increase the sensing distance without loss of resolution, maintaining the same pulse peak power. The SNR improvement when return-to-zero (RZ) simplex codes of length L are employed is $(L+1)/(2\sqrt{L})$ [5, 87–89].

The use of pulse coding in Raman OTDR [4, 5], Brillouin optical time-domain analysis (BOTDA) [85–87] and incoherent OTDR [88, 89] is well demonstrated since the addition of the intensity of the traces generated from each bit is linear. In that case, the implementation of pulse coding and corresponding signal trace demodulation can be carried out only using simple direct detection.

However, in the case of ϕOTDR, the traces backscattered from the different bits are coherent and will interfere making the addition of intensity of traces a non-linear process. Thus, the decoding process will present major distortions when direct detection is used. In 2016, the idea of pulse coding in ϕOTDR using only direct detection was proposed [90, 91]. It was achieved tuning the relation between the laser linewidth and the size/separation of the bits, so that the laser coherence length was lower than the bit separation (avoiding interference between traces) but was higher than the bit size (indispensable condition in ϕOTDR systems). In the experiment, a ∼9 dB SNR improvement (255 bit) was achieved. The authors compared a measured vibration spectra obtained with cyclic coding and a Distributed Feedback (DFB) laser with $\Delta f \approx 4$ MHz and that with single pulse and a highly stabilized External Cavity Laser (ECL) with $\Delta f \approx 50$ kHz. To do this, a 500 Hz sinusoidal vibration was applied to the fiber using a Piezoelectric Transducer (PZT) with the two lasers using the same parameters including the pulse width, sensing distance and optical power at the input of the FUT. The measured vibration was represented in Figure 3.21 [91]. These results show that the technique proposed in [90,91] allows decreasing the linewidth requirements of the master laser while maintaining the SNR of the measurement, but not increasing the SNR of a configuration using a high-coherence laser.

In the same year, random and non-periodical Non-Return-to-Zero (NRZ) Phase-Shift Keying (PSK) pulse coding was implemented in a ϕOTDR [92]. For this, it was required an I/Q

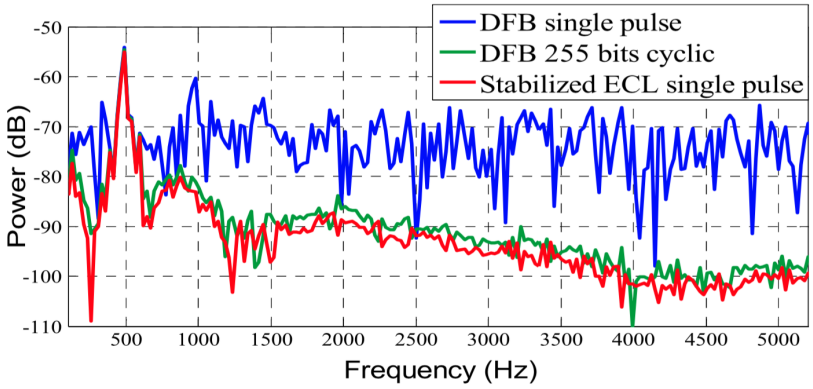

Figure 3.21: Vibration spectra using DFB laser (single pulse and 255 bits cyclic code) and a frequency stabilized ECL [91].

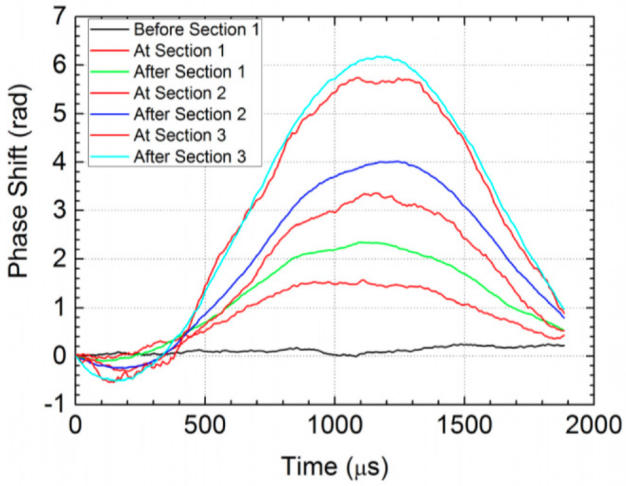

Figure 3.22: Phase variation of the ϕOTDR signal over time for different fiber points when a 500 Hz strain variation is applied to three fiber sections using a dual polarization QPSK data format [92].

(homodyne) detection unit for a full (amplitude, phase and polarization) characterization of the backscattered optical signal. Thus, a fully linear system in terms of ϕ OTDR trace coding/decoding was achieved [92]. In the proposed technique, using a code exceeding $N = 32767$ $(2^{15}-1)$ bits over a duration of 8.2 μs (4 Gbaud), distributed sensing of dynamic strain with a sampling of 125 kHz and a spatial resolution of 2.5 cm (set by the bit size) over 500 m was demonstrated. The theoretical gain G in SNR (using PSK) due to the use of coding was $G = (N+1)/\sqrt{2N} = 21$ dB [92]. Some of the obtained results are represented in Figure 3.22 which shows the phase variation of several points, before, at, and after three strained fiber sections when a sinusoidal strain variation of 500 Hz was applied by a translation stage (using dual polarization QPSK).

The presented results demonstrated that the proposed approach is valid for arbitrary data modulation formats, using random data comparable to that obtained in real communication links. One year later, the same authors upgraded the results using a 2000 m fiber and a cyclic Pseudorandom Binary Sequence (PRBS) pulse modulation, modulated using binary PSK (BPSK) at 4 Gbaud and with 1 million $(2^{20}-1)$ bits of period i.e., 0.26 ms [93]. The estimated gain using this high number of bits is $G = 28.6$ dB.

The main limitations of this technique are directly related to the limitations of the actual

phase recovering methods, which are greatly dependent on the laser phase-noise and temperature fluctuations in the FUT.

3.5.2.3 Optical Pulse Compression Reflectometry – OPCR

In this subsection, a technique called Optical Pulse Compression Reflectometry (OPCR) is presented [94–96]. It is inspired by the concept of pulse-compression radar [135]. This technique involves the use of optical pulses with Linear Frequency Modulation (LFM) and relatively wide pulse widths. Thus, the power of the returned wave is high enough to achieve long sensing distances with high SNR. Followed by numerical compression of the received backscattered trace using a simulated matched filter, the technique gives an spatial resolution determined by the sweeping range of the LFM (B) rather than the pulse width. This overcomes the trade-off between spatial resolution and measurement range in the conventional pulse-based optical time domain reflectometry.

Figure 3.23 shows a qualitative description of pulse-compression process. The original LFM pulse (see Figure 3.23(a)) is compressed by the matched filtering process as a narrow sinc-like pulse (see Figure 3.23(b)), since the shape of the original pulse is square. If the sweeping range of the LFM is B, the Full Width at Half Maximum (FWHM) or 3 dB width of the main lobe would be determined by 1/B. In this process, the total energy of the original pulse is conserved. Thus, the resulting compressed pulse will present a higher peak power (not represented by the authors in 3.23(b) [94]). In OPCR the match filter is applied to the backscattered signal and the resulting trace presents higher SNR and resolution.

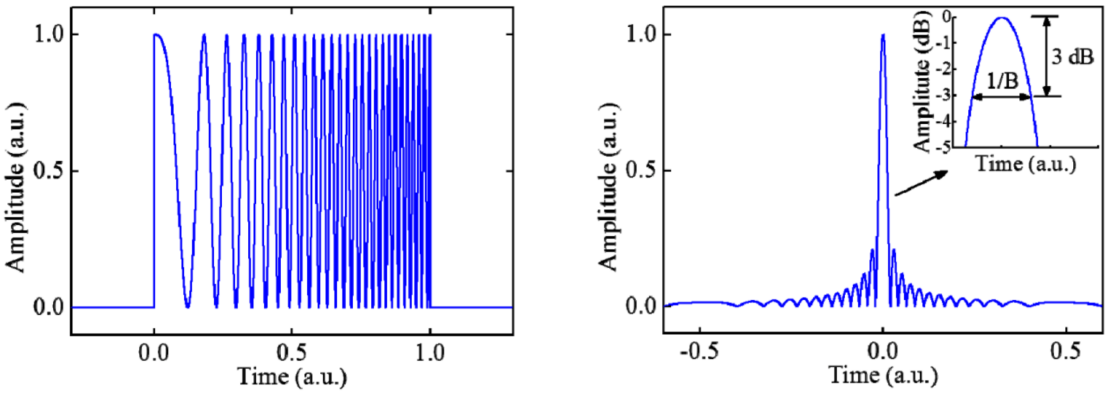

(a) Time-domain profile of LFM pulse.

(b) Compressed pulse (3-dB width equal to 1/B).

Figure 3.23: Qualitative description of pulse-compression process [94].

In 2017, a verification experiment was implemented by using a source with a linear frequency sweeping range of 420 MHz achieving a spatial resolution of 30 cm. Vibrations of 200 Hz were detected with an SNR of 10 dB at a sensing distance of 19.8 km [95]. Recently, vibrations of 700 Hz along 50 km with a spatial resolution of 34 cm has been demonstrated [96].

Similarly to coding techniques, the limitations of OPCR are directly related to the limitations of the actual phase recovering methods, since the phase information of the backscattered signal is required to implement the matched filter. The effect of laser phase-noise and the effect of random polarization evolution along the trace limit the technique performance.

In Chapter 4 (Section 4.3), a new ϕOTDR configuration inspired by the concept of Chirped Pulse Amplification (CPA) [48, 49] will be presented. This method is conceptually similar to

that of OPCR, with the critical advantage that the process of pulse compression is directly realized in the optical domain, avoiding the need for phase detection of the backscattered trace and subsequent digital processing. This process not only greatly simplifies the scheme, but also largely reduces the polarization sensitivity. The method proposed achieves spatial resolutions in the millimeter range, while increasing the SNR by several orders of magnitude with respect to conventional ϕOTDR techniques.

3.5.2.4 Post-Processing

The noise sources previously discussed can mask or deteriorate the ϕOTDR signals. Until this moment, the proposed solutions have been based on the use of optical improvements (distributed amplification [19–27], coding techniques [4,5,85–93] and OPCR [94,95]. However, there are some post-processing methods for increasing the SNR of ϕOTDR signals that are worth noting.

The most conventional post-processing method is averaging the ϕOTDR traces. If traces are averaged N times, the signal fluctuations will be reduced by $\sqrt{N}$ resulting in an SNR increase. However, this method decreases the measuring repetition rate (f_{trigger}) by N, which is a huge limitation when dynamic measurements must be implemented. Furthermore, moving averaging [30] can be an interesting method for noise reduction, which essentially removes high frequencies and retains low frequencies, and therefore a reduction of the detection bandwidth occurs.

In signal processing of image, edges which are used for labeling the abrupt points or the points with a significant variation in gray level can provide the position information of the object, so the edge detection [136] plays an important role in the application of image analysis. Based on this assumption, Rayleigh backscattered traces are composed of a two-dimensional image and location information of intruder can be measured by edge detection method [98]. Implementing this idea, it can be increased the SNR to 8.5 dB compared to these conventional methods [98].

Recently, a 2-D image restoration has been demonstrated to greatly improve SNR in distributed optical fiber sensors including Brillouin optical time domain analysis (BOTDA) and Raman-distributed sensor systems [137]. This method can enhance SNR dramatically by exploiting the redundancies and correlations contained in the multidimensional signal (frequency, time, position). Nevertheless, it might be not practically implementable for ϕOTDR system (which needs fast response for dynamic measurements) since it takes a lot of computational time and impractical for real-time monitoring [99]. In 2017, He proposed and demonstrated an adaptive 2-D image processing method of bilateral filtering algorithm [138–141] to enhance the SNR of vibration/intrusion location in ϕOTDR [99]. The proposed method achieves an extra SNR improvement over 13 dB compared to the edge detection method [98]. However, it takes a little more processing time.

Besides the conventional time-domain techniques mentioned above, transform domain methods are used as alternatives for SNR improvement. By Fourier transforming the Rayleigh backscattering traces, 9.5 dB of SNR was achieved with a spatial resolution of 3.7 m [100]. There is another method, called Wavelet Denoising, which tries to reduce the noise in the signal without reducing the bandwidth of detection [24,35,97]. In 2012, Qin described the principle of the method [35]. It consists on decomposing the signal into a series of base functions of dilated and translated versions of the mother wavelet function. The wavelet coefficients are obtained from the wavelet transform (which can be continuous [97] or discrete [35]). The corresponding coefficients to noise are removed and the reconstructed signal presents higher SNR. However, this method requires to be adapted to every different particular ϕOTDR configuration.

3.6 Other Distributed Sensing Techniques

In this section, some DOFSs based on Raman, Brillouin and Rayleigh scattering in terms of their linearity, speed, accuracy, range and spatial resolution measurement are analyzed.

Raman-based sensors present spatial resolutions around 1 m over a few of km. They present good linearity in temperature measurement with an accuracy of 1 K [4, 5]. However Raman-based sensors spend few minutes in each temperature measurement and they are immune to strain.

Another important group of DOFSs are the ones based on Brillouin scattering, which measures linearly strain and temperature changes in the fiber. Brillouin Optical Time Domain Analysis (BOTDA) is the most extended DOFS technique based on this inelastic scattering. In BOTDA a pump pulse wave, launched into one end of the sensing fiber, non-linearly interacts with a counter-propagating CW probe wave launched from the fiber opposite side. By scanning the relative optical frequency between the pump and probe waves, the Brillouin Gain Spectrum (BGS) and the Brillouin Frequency Shift (BFS) are recovered. BFS corresponds to the center of BGS and it is the frequency of maximum interaction between the pump and probe waves. It depends linearly on strain/temperature ($C_{\nu_B\varepsilon} \approx 50$ MHz/$\mu\varepsilon$ and $C_{\nu_B T} \approx 0.95$ MHz/K at 1550 nm for typical SMFs). Thus, from the BFS measurement the values of the local strain/temperature are extracted. BOTDA systems has been shown to allow presents spatial resolutions of 1 m over sensing ranges of 100 km [6]. The strain/temperature accuracy is around $20\mu\varepsilon$/1K. However, due to the requirement of a large of number averages and a frequency sweep, the measurement times are typically of several minutes making impossible the development of dynamic measurements. Brillouin Optical Time Domain Reflectometry (BOTDR) implementations allow to do dynamic strain/temperature measurements over a few kilometers with an accuracy of $20\mu\varepsilon$/1K and spatial resolution of 1 m [10]. However, sampling ratios higher than few Hz have not been achieved. Brillouin Optical Correlation Domain Analysis (BOCDA) achieves sampling rates of tens of Hz and strain/temperature accuracy similar to BOTDR [7]. However the sensing range is typically limited to some hundred of meters.

Real dynamic sensing in Brillouin DOFSs was achieved with the implementation of a Fast BOTDA by Peled et. al [8]. This technique implements sampling rates of tens of kHz with strain/temperature accuracy of $1\mu\varepsilon$/50mK, although the technique was best suited for short fibers (100 meters) and low number of averages. This technique still required frequency sweep, which implies maintaining some experimental complexity and cost. The same group later demonstrated a practical utilization of the Slope-Assisted BOTDA (SA-BOTDA) to allow for strain measurements without requiring a frequency sweep [9]. It is probably the most extended DOFS for dynamic sensing based on Brillouin scattering. In this case, the dynamic response is achieved by a tuning of the slope of the Brillouin gain response of the fiber (see Figure 3.24). The working point is fixed to the center of the linear region of one of the BGS slopes. Then, when the fiber suffers a strain/temperature change, the BGS shifts and the temporal gain increases or decreases, with respect to the gain at the working point, depending on the direction of the temporal BGS shift.

SA-BOTDA allows dynamic sensing with sampling rates of 10 kHz over hundreds of meters and strain/temperature accuracy of $1\mu\varepsilon$/50mK. However, the technique presents several limitations, particularly concerning the strain dynamic range. The useful dynamic range for strain/temperature measurements depends on the frequency extent of the slope, which is of the order of the FWHM of the BGS. In practice, pump pulse widths longer than $\sim$50 ns provide only a dynamic range of $\sim$600 $\mu\varepsilon$. Furthermore, if the BFS is not uniform along the whole fiber (due to non-uniformity temperature/strain distribution or the use of different fiber spools), the

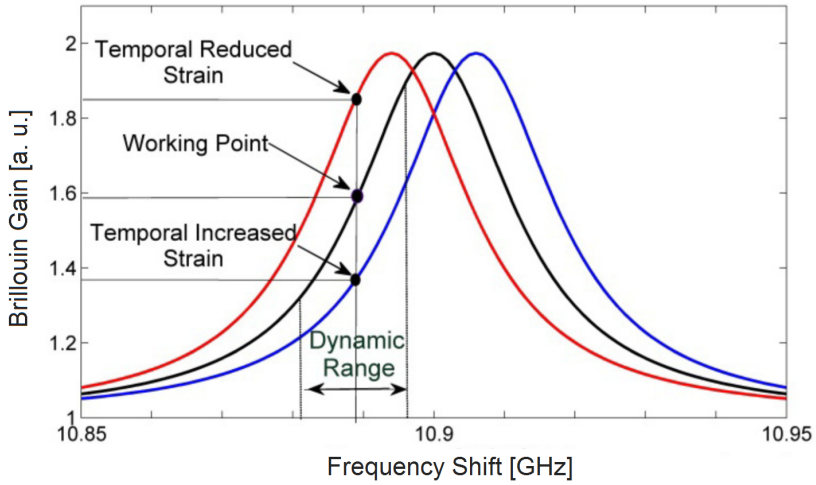

Figure 3.24: SA-BOTDA operation principle. Brillouin gain spectra of a fiber segment under time average (black), high (blue) and low (red) strain values. A frequency working point is chosen near the center of the left slope; see the black point on the black Lorentzian. Positive (negative) strains induced to the fiber, shift the BGS to higher (lower) frequencies, thereby modulating the Brillouin gain experienced by the propagating probe wave [9].

measurement along the entire fiber is not achievable.

Regarding DOFSs based on Rayleigh scattering, these sensors require lower averaging than Raman or Brillouin, therefore they are better suited for dynamic measurements as vibration sensing. In the frequency domain, Optical Frequency Domain Reflectometry (OFDR) can provide high spatial resolutions in the order of sub-decimeter (even sub-millimiter resolution), but is typically limited to short fiber sections (few hundred of meters maximum) due to the sweeping laser requirements [11–18]. The strain/temperature measurement accuracy is around $1\mu\varepsilon/0.1$K when phase detection is implemented [17]. However, OFDR do not allow sampling rates much higher than some tens of Hz. OFDR is based on swept-wavelength homodyne interferometry [11], in which the frequency of the pump signal is varied slowly by a time-linear sweep. Then, the backscattered wave is mixed with a coherent reference wave (pump signal) at the detector, thus implementing coherent detection. A general OFDR setup is shown in Figure 3.25 [3].

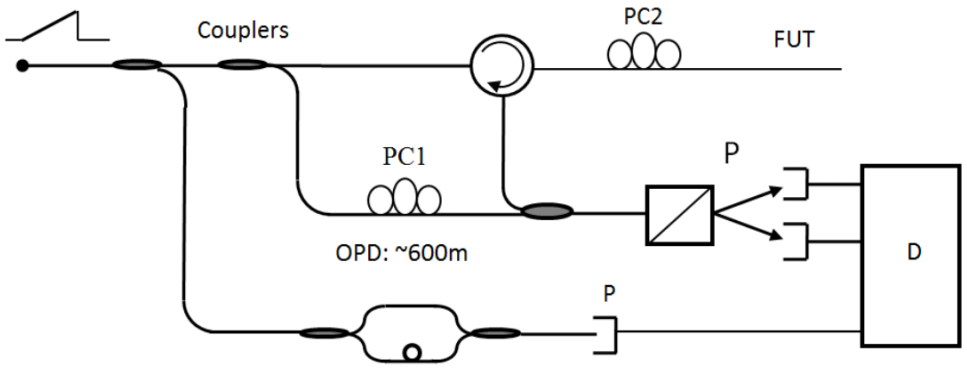

Figure 3.25: Typical OFDR system. PC, Polarization Controler; OPD, Optical Path Difference; P, Photodetector; D, Digitizer [3].

Temperature and strain changes induce phase differences via index variation. These phase

differences are measured by using optical coherent detection (see Figure 3.25). [12]. Hence, Coherent OFDR (C-OFDR) can be used for temperature [16], and strain [14] sensing by measuring the path length difference of the Rayleigh scattered light and a reference arm for their physical length change and index change [3].

The backscattered signal detected in a OFDR is in the frequency domain. Then the signal is transformed to the temporal domain using FFT. Next, the temporal trace is divided in segments and each segement is analyzed individually in the frequency domain (by using Inverse Fast Fourier Transform, IFFT). When a section suffers a refractive index change (induced by temperature or strain change) the spectrum of that section suffers a frequency shift (see Equation 3.21). Thus, by means of cross-correlations, it is possible to detect and measure refractive index changes in a OFDR from the frequency shift. The spatial resolution of the measurement, W, is directly related to the resolution in the time domain and is determined by the optical frequency sweep range ΔF as follows [3]:

$$W = \frac{c}{2n_g \Delta F} \tag{3.25}$$

An unbalanced auxiliary Mach-Zehnder interferometer is used to correct the non-linearity of the tunable laser, which is also employed as a trigger signal for sampling the Rayleigh scattering signal. Being τ_g the differential delay in the auxiliary interferometer used to calibrate the tunable laser induced non-linear wavelength sweep, the maximum measurement length $L_{\max}$ is [3]:

$$L_{\max} = \frac{c\tau_g}{4n_g} \tag{3.26}$$

However, OFDR systems present some limitations which are summarized below [3]:

1. Spatial resolution is limited by tuning range and chromatic dispersion. Higher spatial resolution is obtained increasing the tuning range Δf. However, due to chromatic dispersion, different frequencies present different group velocities. This results in larger spatial resolution since ordinary FFT processing treats all the frequency components with same speed.

2. Trigger interferometer induced limitation. If the sensing range is increased, the delay length of the trigger interferometer must be increased too. Temperature or strain changes due to environmental conditions destabilize the trigger. Due to accumulation of these environmental effects on the delay length of the trigger interferometer, the spatial location will be distorted at the far end of the fiber, since the data processing cannot correct this mistake

3. Maximum sensing length is limited by phase-noise of the laser, since the phase-noise increases with the separation between the local oscillator and the backscattered light. Thus, for long sensing lengths, the phase-noise could be higher than the Rayleigh scattered signal. For this reason, phase-noise limits the maximum sensing length.

In contrast, as for measurements in the time domain, Phase-Sensitive Optical Time Domain Reflectometry (ϕOTDR) can perform measurements over 100 km with spatial resolutions of a few meters [21, 23, 24, 26, 27]. As it was explained in Subsection 3.2.1, the maximum sampling

frequency is delimited by the fiber length. Thus, for a few kilometers the bandwidth can arrive to tens of kHz [34, 35]. Using direct detection however, measurements are based on intensity variations of the ϕOTDR signal which does not show a linear variation with the applied perturbation. Thus, true strain/temperature readings can not be performed unless coherent detection or frequency sweeps are deployed.

With the first technique, known as Coherent OTDR (C-OTDR), the dynamic measurement of strain/temperature has been demonstrated [31–33] with a very high strain/temperature accuracy of approximately 10nε/1mK, three orders of magnitude below the typical resolutions of 20$\mu\varepsilon$/1K provided by BOTDA sensors. The typical sensing ranges are around tens of kilometers with tens of meters spatial resolution [31,33]. In this case however, the system is more complex and laser coherence of at least the fiber length are required in order to avoid noise when beating the signal with the local oscillator. The long term-stability of such systems (i.e. after several minutes or hours) and therefore feasibility for static temperature measurements over several hours has also not been clearly addressed either.

On the other hand, by precisely sweeping the frequency of the pulses step by step, ϕOTDR has been shown to allow also for very sensitive static measurements of refractive index variations, which can be used for very high resolution temperature [36], strain [37] and birefringence [38,39] measurements. For instance, the demonstrated strain/temperature resolutions are similar to the obtained with C-OTDR [37]. However, due to the requirements of a frequency scan, in this case the measurement time and complexity of the system is increased. Generally this technique is not well-suitable for dynamic sensing.

Technique	Linearity	Dynamic Measurement	Strain/Temperature Accuracy	Range/Resolution
Raman [5]	✓	✗	- / 1 K	1 km / 1 m
BOTDA [6]	✓	✗	20 $\mu\varepsilon$ / 1 K	100 km / 1 m
BOTDR [10]	✓	1 Hz	20 $\mu\varepsilon$ / 1 K	1 km / 1 m
BOCDA [7]	✓	10's Hz	20 $\mu\varepsilon$ / 1 K	100's m / 1 m
Fast BOTDA [8]	✓	10 kHz	1 $\mu\varepsilon$ / 50 mK	100's m / 1 m
SA-BOTDA [9]	✓	10 kHz	1 $\mu\varepsilon$ / 50 mK	100's m / 1 m
C-OFDR [17]	✓	10's Hz	1 $\mu\varepsilon$ / 100 mK	10's m / 10's cm
ϕOTDR [34]	✗	10's kHz	-	10's km / 10's m
C-OTDR [31,33]	✓	10's kHz	10 $n\varepsilon$ / 1 mK	10's km / 10's m
Frequency-Swept ϕOTDR [37]	✓	1 kHz	10 $n\varepsilon$ / 1mK	10's km / 1 m

Table 3.1: Performance data of DOFSs used for linear and dynamic sensing.

Table 3.1 summarizes all the information presented in this section. A selection of the most representative works of each technique have been done. It is possible to conclude that, in general, the Rayleigh based sensors are more suitable for dynamic sensing than the based on Raman or Brillouin scattering, particularly the three that work in the time domain. These three techniques are the ϕOTDR and its two variants the C-OTDR and Frequency-Swept ϕOTDR. The first one presents the simplest implementation method, while the others show considerable higher

complexity. However, as it was commented, ϕOTDR technique does not allow for truly strain and temperature sensing. The main objective of this dissertation will be the development of a DOFS based on ϕOTDR technology which allows the real measurement of strain and temperature while maintaining the best features of a ϕOTDR sensor: simplicity, cost-effective, real-time measurement and competitive range and resolution. This sensor will be proposed in Chapter 5 and it will be based on the use of chirped-pulse optical pulses allowing strain/temperature measurement accuracy lower than $4n\varepsilon/0.5mK$. Moreover, some applications require high resolution measurements, in some cases, millimetrical resolutions. This is the case of wall or pipeline crack development monitoring. To achieve these high resolutions it is required to employ extremely short pulses, reducing considerably the SNR of the system which makes the measurement impossible in some cases. To solve this, in Chapter 4 it will be proposed a ϕOTDR upgrade based on Chirped Pulse Amplification (CPA) to detect deformations with 3 mm spatial resolution.

3.7 Summary

Along this chapter the essentials of the ϕOTDR technique as well as its main limitations have been reported: non-linear sensing and signal to noise ratio.

ϕOTDRs work analyzing in the time domain the backscattered signal generated by a highly coherent optical pulse traveling along a fiber cable. This generated power trace remains constant over the time if the optical fiber remains stable. However, when a point of the fiber is perturbed, the pattern presents changes in that point. This turns ϕOTDR a powerful technique that allows the fully distributed monitoring of vibrations along an optical fiber cable. As consequence of it, this technique becomes in an optical solution to long perimeters surveillance and long infrastructures monitoring [111].

One of the main limitations of this technology is its non-linear response to refractive index changes. It becomes an important issue when real acoustic sensing or temperature/strain measurement is required. In these cases, other techniques such as coherent detection [31] or frequency sweep [36, 38, 39] must be implemented. The fundamentals of these methods and their limitations have been described along this chapter. Different DOFSs based on the three scattering processes (Rayleigh, Brillouin and Raman) allow linear measurements of temperature/strain, however they present other limitations such as complexity, low maximum sensing range, poor strain/temperature accuracy or only capability for quasi-static measurements. This analysis is presented at the end of this chapter and summarized in Table 3.1. To solve this problem, a new method based on ϕOTDR using chirped pulses will be presented in Chapter 5. The technique allows to solve the the non-linear limitation of traditional ϕOTDR without the requirement of a frequency scan or coherent detection. Distributed sensing of strain and temperature, with resolutions of $0.5mK/4n\varepsilon$ and real acoustic sensing has been achieved with the proposed technique.

Regarding the SNR limitations, the critical trade-off that there is between the spatial resolution and range in ϕOTDR based sensors has been discussed. To be able to increase the range maintaining the resolution of a ϕOTDR, the trivial solution is to enhance the pulse peak power. However, the peak power cannot be increased indefinitely due to the onset of non-linear effects [106, 107]. The most important techniques to overcome this trade-off and their immediate limitations have been proposed: distributed amplification [19–27], coding techniques [4, 5, 85–93], Optical Pulse Compression Reflectometry (OPCR) [94–96] and signal post-processing [24, 30, 35, 97–100].

Chapter 4

Addressing the Limits of ϕOTDR

4.1 Introduction

In ϕOTDR-based sensing schemes, a highly coherent optical pulse is injected into the sensing fiber. The received power trace is produced by coherent interference of the light reflected via Rayleigh scattering in the inhomogeneities of the fiber. This yields in traces that show a static, noise-like interference pattern. Ideally, the probe pulse should be as narrow as possible to achieve high spatial resolution measurements, and it should have as much energy as possible to achieve the best possible Signal to Noise Ratio (SNR) in detection. This combination leads to high peak power pulses, which are subject to non-linear impairments in their propagation along the sensing fiber that degrade the received backscattered trace as well as the effective sensing detection [106, 107]. Preventing these effects imposes a maximum peak power of optical pulses, which in turn limits the SNR (and hence the measurement range) of the received backscattered trace. To improve these parameters, it is necessary to broaden the probe pulse width, which, at the same time, deteriorates the spatial resolution of the system. Hence, there is a trade-off between the spatial resolution (pulse width), length range (pulse peak power), and SNR of the received power trace.

In this chapter, two different approaches to address the limits of these systems are shown. First, the impact of the probe pulse shape in the backscattered trace of ϕOTDR-based systems is analyzed. Gaussian and triangular-shaped pulses show a higher robustness against Modulation Instability (MI). Thus, the use of these pulse shapes (instead the conventional rectangular shape) shows a better behavior in terms of evolution of the visibility along the distance, which should reflect into a better sensing performance [124]. Secondly, a method inspired by the concept of Chirped Pulse Amplification (CPA) is proposed [48, 49]. Spatial resolutions in the millimeter range, while increasing the SNR by several orders of magnitude with respect to conventional ϕOTDR techniques, are achieved with this method [142].

As it was discussed in Chapter 3, the intensity variation that a point of the trace suffers when the fiber is perturbed by any disturbance in that point is not lineal (see Equation 3.15). The use of coherent detection to solve this limitation was explained in Subsection 3.4.2. However, the fact that the backscattered signal is beaten with a Local Oscillator (LO) implies an increase of complexity, polarization and phase-noise limitations.

For this reason, finding a self-refereed technique that allows the complete electric field recovery (amplitude and phase) of the backscattered trace would be a disruptive solution with potential to address fundamental limitations of ϕOTDR. Phase Reconstruction using Optical Ultrafast Differentiation (PROUD) is a powerful candidate for this purpose. In this chapter, the possibility of using PROUD in a ϕOTDR sensor is explored [143].

4.2 SNR Enhancement in ϕOTDR Using Probe Pulse Shaping

In standard ϕOTDR schemes, the most common type of pulses used are the rectangular-shaped ones. The typical width is around tens of hundreds of nanosecond and peak powers under 1 W. With this pulse performance is possible to achieve intensity traces of tens of kilometers with acceptable SNR. In the literature, the effect of the probe pulse shape in the sensor performance has been investigated in the case of Brillouin-based distributed sensors [144]. This study has determined that the use of rectangular pulses is more convenient than other narrower-bandwidth shapes (e.g., Gaussian-like) for Brillouin sensors, since rectangular-shaped pulses suffer less spectral broadening due to Self-Phase Modulation (SPM), leading to a better determination of the Brillouin gain spectrum along the fiber. However, a similar analysis has not been done for

ϕOTDR technology to date, where the most important consideration is the visibility of the trace along the fiber. While the trace visibility (associated to the coherence of the probe pulse) is ultimately dependent on the pulse spectral form, the principle of operation (and mechanism leading to signal degradation) of ϕOTDR is substantially different from that of Brillouin-based sensors. Therefore, it is interesting to investigate the optimal pulse shape specifically for this ϕOTDR. Rectangular-shaped pulses show a continuous level of light power along a relatively long temporal width, which induces a reversible power exchange between the probe and the sidebands amplified by the MI gain at well-defined peak frequencies. This effect is known as the Fermi–Pasta–Ulam (FPU) recurrence, and it is ultimately responsible for a significant reduction of the trace visibility at specific positions in the trace [106, 122].

In this section, an analysis of the impact of the probe pulse shape in the backscattered trace of ϕOTDR-based sensing systems is presented. In particular, we compared the traces received after launching probe pulses into the fiber with the same energy and nominal spatial resolution (defined considering the Full Width at Half-Maximum (FWHM) of the probe pulses) and four different shapes: Gaussian-like, triangular, super-Gaussian (order 2), and rectangular. We performed numerical simulations that are subsequently validated by an experimental demonstration. Our analysis shows that the use of rectangular-like pulses is the most detrimental for sustaining an adequate visibility (and consequently, sensing sensitivity) all along the received power trace. Gaussian and triangular-shaped pulses show a better behavior in terms of evolution of the visibility along the distance, which should reflect into a better sensing performance.

4.2.1 Probe Pulse Shaping Technique

Prior to the realization of experimental tests, we have carried out a series of numerical simulations that have helped us to identify notable differences in the obtained power trace depending on the shape of the probe pulse envelope. The algorithm employed in the numerical simulations has been developed as follows: first, the propagation of the probe pulse is simulated by solving the Non-linear Schrödinger Equation (NLSE) using a split-step Fourier method with adaptive step size [121].

Figure 4.1 shows the input pulse shapes employed in the numerical simulations (dashed line), and compares them with the modulated probe pulses subsequently employed in the experimental demonstrations (solid line). All the pulses are centered at 1550 nm, and all of them have a FWHM of 100 ns (i.e., all of them achieve the same nominal spatial resolution). Two different values of pulse energy have been employed, namely, 91 nJ and 165 nJ (equivalent to values of peak power of 910 mW and 1650 mW, respectively, in the case of rectangular pulses). The peak power of the different pulses has been adapted to achieve the aforementioned pulse energy with the aim of generating traces that maintain the same SNR, considering that the energy of the pulse depends on its power shape and duration ($E = \int P(t)\mathrm{d}t$). For the simulations, the sensing fiber is considered to be a 25 km long Single-Mode Fiber (SMF-28). The specifications of the fiber: non-linear coefficient $\gamma = 1.1$ W^{-1}km^{-1}, second-order dispersion parameter $\beta = -21.7$ ps^2/km, and attenuation $\alpha = 0.2$ dB/km.

Once the evolution of the optical pulse is known, the Rayleigh scattering process is simulated using the algorithm described in [145]. In particular, the backscattering process is modeled by a set of discrete scatterers (reflectors) whose amplitude and phase are characterized as statistically independent random Gaussian variables, while their coordinates are deterministic (the random phase of the scatterers contributes to the final backscattered trace as if they had randomly distributed positions). The complex envelope of the optical probe pulse is updated while it propagates along the fiber, employing the results obtained from the NLSE resolution. Finally,

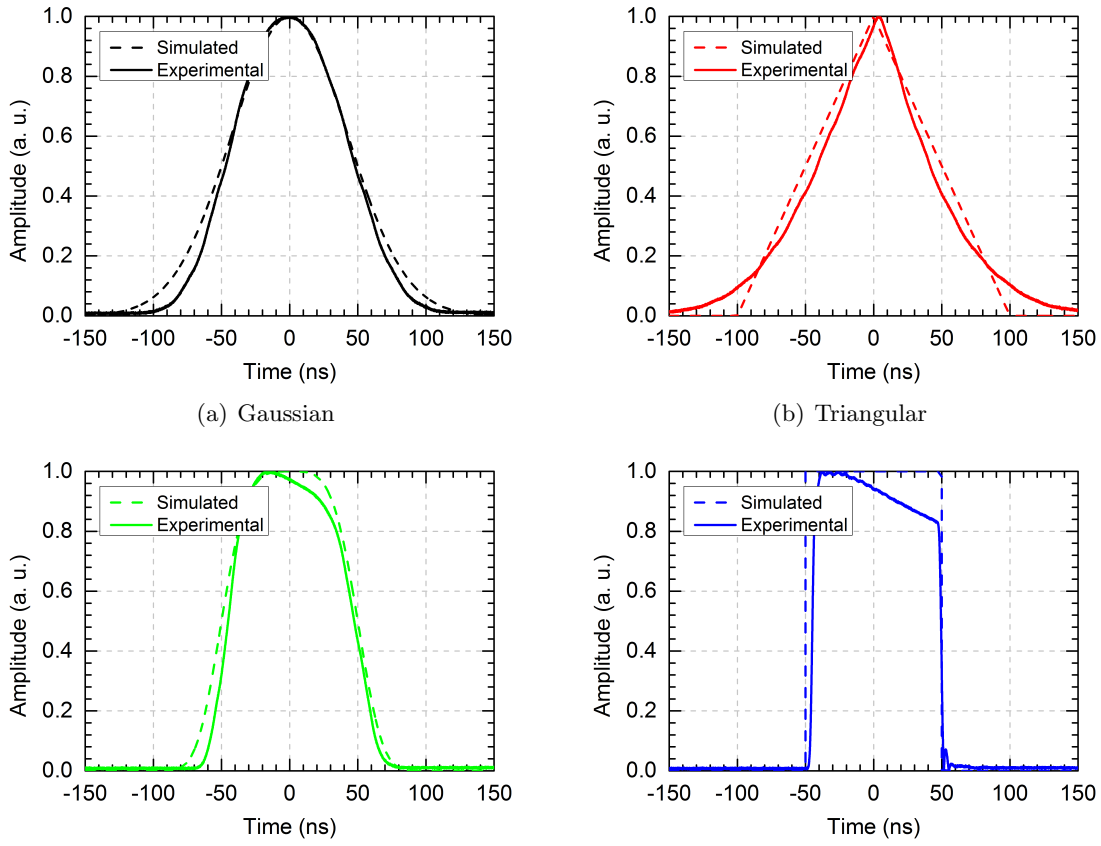

(a) Gaussian

(b) Triangular

(c) Supergaussian

(d) Rectangular

Figure 4.1: Input pulses launched into the ϕOTDR system. Dashed lines represent the pulses employed in numerical simulations, while solid lines show the pulses employed in the experimental demonstration [124].

the power trace is calculated from the resulting backscattered electromagnetic field by modeling the effect of a photodetector: the backreflected optical intensity is computed as a function of the time of flight of the pulse in the fiber, and the resulting signal is low-pass filtered according to the detection bandwidth of the photodetector. In this case, the bandwidth of the considered photodetector is 125 MHz. The visibility of the resulting traces is plotted in Figure 4.2, which is computed as [106]:

$$V = (T_{\max} - T_{\min})/(T_{\max} + T_{\min}) \tag{4.1}$$

where T max and T min are the maximum and minimum values of the trace over a certain distance record. In order to obtain a good estimation of the trace visibility, the size of the employed window should contain a statistically relevant number of trace maxima and minima. Generally, a window of several times the spatial resolution of the trace ($\sim$10 m in this case) is considered. In this case, a window of 60 m has been employed.

Note that in the case of a propagation of pulses with 165 nJ of energy, only a 15 km long trace is presented, since no additional information can be extracted from the last 10 km of trace. From the obtained numerical results, we observe that if rectangular pulses are used as a probe, the power trace suffers from fading at specific positions along the trace. At those positions, the sensing sensitivity is nearly lost. The positions where fading occurs are closer to the input

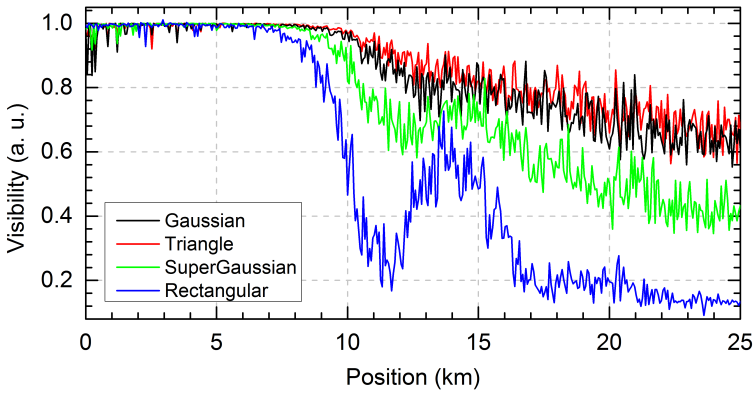

(a) When the energy of the input pulses is 91 nJ.

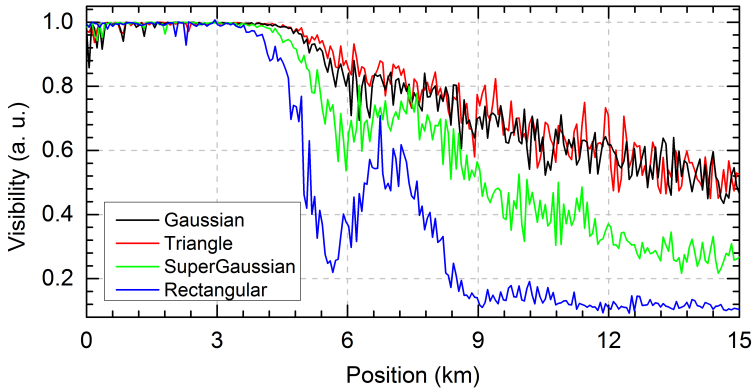

(b) When the energy of the input pulses is 165 nJ.

Figure 4.2: Visibility of the numerically obtained power trace [124].

end of the fiber for higher values of peak power, leading to a shorter usable length range of the sensors. However, when using probe pulses whose power is not constant along its width, e.g., with Gaussian-like or triangular shapes, the MI-induced trace fading is significantly reduced. The reason is to be found in the different behavior of the FPU recurrence associated to MI with these probe pulse shapes.

MI manifests as a breakup of Continuous Wave (CW) or quasi-CW radiation into a train of optical pulses [40]. The propagation of (quasi-) CW light is inherently unstable under anomalous dispersion. As a result, the signal of interest acts as a pump in an amplification process of any small perturbation (e.g., noise) present in the gain spectrum of MI, leading to a depletion of the signal power. In Figure 4.2, we observe that the visibility of all the traces decreases starting from a certain fiber length, ∼10 km for pulses with an energy of 91 nJ and ∼5 km for pulses of 165 nJ, due to MI. However, in the case of rectangular or super-Gaussian pulses, the trace visibility presents a strong fading immediately after those locations, and subsequently it is partially recovered, forming several lobes. Those lobes that appear in the visibility trace are caused by the FPU recurrence phenomenon [106]: the quasi-CW radiation (rectangular pulses) fosters an oscillating energy transfer between the initial pulsed light and the high-order amplified beams. The FPU recurrence requires a precise balance of energy transfer between a significant number of spectral modes. This situation is not accomplished when the pulse shape does not maintain the power level over a certain temporal width (i.e., when the pulse is not rectangular). In those cases, the different intensity levels are associated with different MI gains and frequencies, destroying the FPU process [122]. As we may observe, the trace obtained from a triangular or Gaussian input pulse barely suffers from FPU recurrence and the trace visibility

decreases in a smoother fashion than that obtained from rectangular pulses. The behavioral pattern ob- served from the simulation results states that the further the pulse envelope shape is from the rectangular, the smoother the reduction of visibility due to the FPU recurrence of the modulation unstable probe pulses for the same energy and same FWHM. We have verified through simulations that the effect of the SPM of the pulses, contrary to the case of Brillouin-based sensors [144], barely affects the final power trace as long as the spectral broadening of the pulse lies within the photodetector bandwidth. Otherwise, the smooth visibility decay of the traces will have an additional, reduced component due to the power filtered out by the photodetector.

4.2.1.1 Experimental Setup

The presented numerical results have been validated through an experimental demonstration. The setup employed is depicted in Figure 4.3. There, an external cavity laser generates the CW light at a wavelength of 1550 nm. Then, the target power envelope, which is electrically generated using a signal generator, is carved in the CW light using a Semiconductor Optical Amplifier (SOA). The pulse is amplified using an Erbium-Doped Fiber Amplifier (EDFA) to have the same peak power of the pulses employed in the numerical analysis.

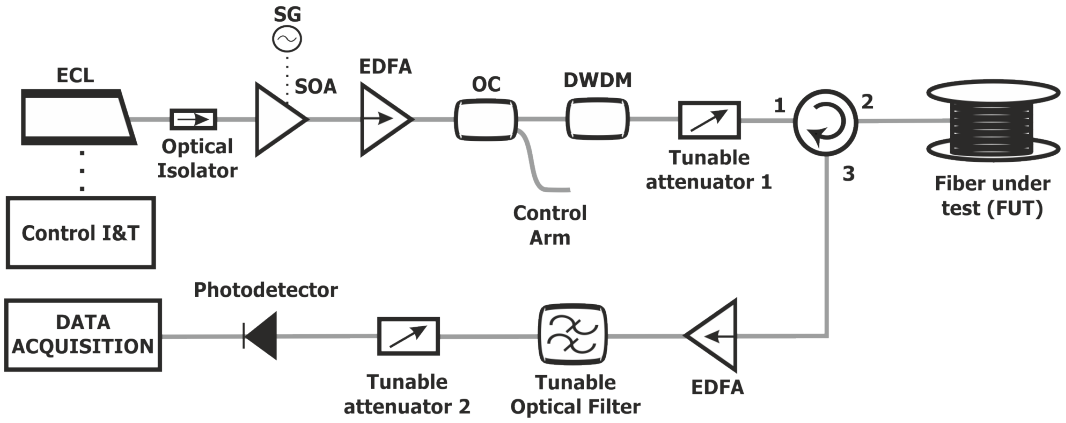

Figure 4.3: Experimental setup. ECL, External Cavity Laser; SG, Signal Generator; SOA, Semiconductor Optical Amplifier; EDFA, Erbium-Doped Fiber Amplifier; OC, Optical Coupler; DWDM, Dense Wavelength Division Multiplexer; I&T, Intensity & Temperature [124].

The synthesized shape and power of the pulses are verified using a control arm located after the EDFA (the measurements at this point are shown in Figure 4.1, solid line). The slope in the peak power of the generated pulses, clearly observed in the super-Gaussian and rectangular-like shapes, is due to the non-constant amplification gain of the SOA. A dense wavelength division multiplexer is employed to filter out the amplified spontaneous emission noise from the EDFA, and the resulting pulses propagate through a single mode fiber of 25 km.

4.2.1.2 Results

The received amplified traces are detected using a 125 MHz bandwidth photodetector, and are plotted in Figure 4.4.

Figure 4.4(a) compares the measured power traces for different input pulse shapes and a pulse energy of 91 nJ. For this value of peak power and rectangular pulses, the first fading induced by the FPU recurrence occurs at around 11 km. Figure 4.4(b) shows a similar comparison, but

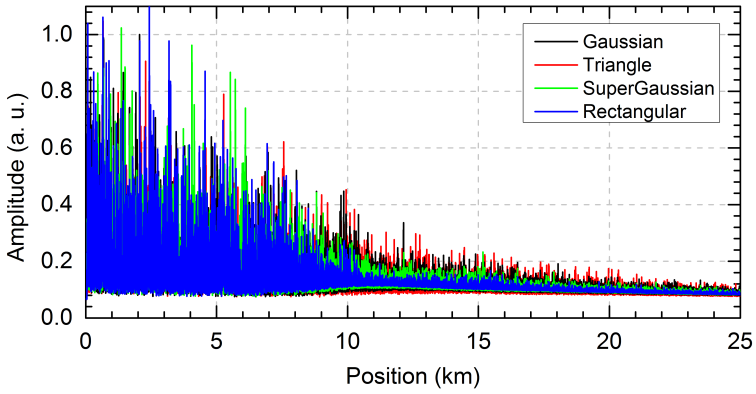

(a) When the energy of the input pulses is 91 nJ.

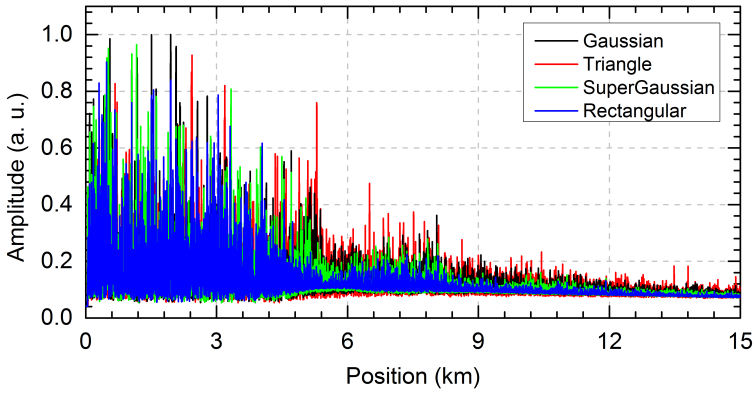

(b) When the energy of the input pulses is 165 nJ.

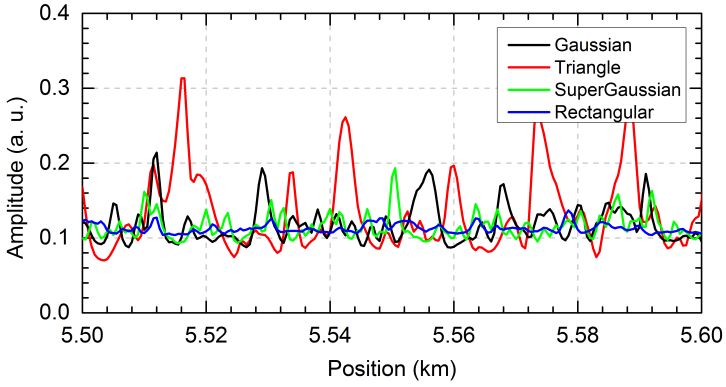

(c) A detail of 100 m around kilometer 5.55 of Figure (b).

Figure 4.4: Experimental backscattered power trace from the different realizations of the experiment [124].

in this case the input pulse energy is 165 nJ. For this value of energy, the fading induced by the FPU recurrence is more pronounced, and with rectangular pulses, the first fading point occurs at about 5.5 km.

These experimental results are in line with the previously presented simulations results. Note that at fading points, the trace practically disappears when rectangular pulses are employed (see the detail of trace in 4.4(c)). However, the fading is highly reduced for different pulse shapes. For example, when a probe pulse with Gaussian or triangular-like power envelope (blue and yellow line, respectively) is employed, there is a certain visibility loss at the specified lengths (i.e., 11 km for a pulse energy of 91 nJ and 5.5 km for an energy of 165 nJ), but the trace is still visible at those points. As such, by varying the power shape of the probe pulse, it is possible to increase the length range of ϕOTDR-based sensor systems while keeping the sensor resolution. The visibility of the measured traces is calculated using Equation 4.1. A window of 60 m has been employed for obtaining the maximum and minimum values of the power trace, similar to the numerical analysis. The obtained visibility curves are plotted in Figure 4.5.

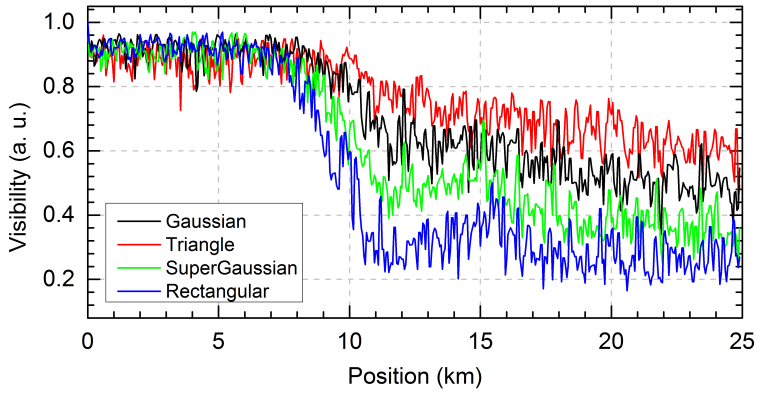

(a) When the energy of the input pulses is 91 nJ.

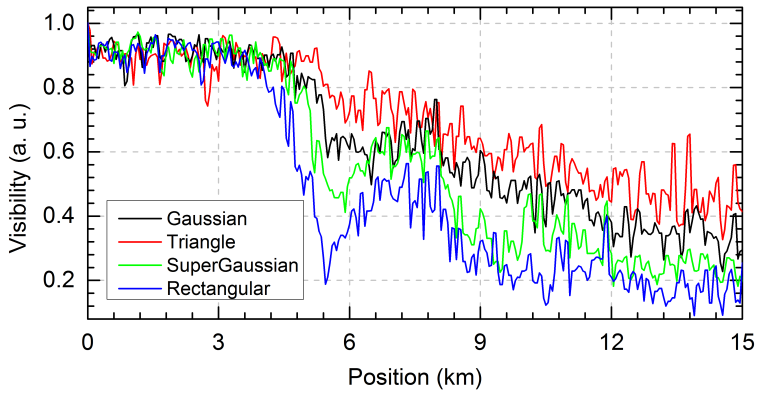

(b) When the energy of the input pulses is 165 nJ.

Figure 4.5: Visibility of the experimentally measured power trace [124].

We observe that the evolution of the trace visibility is very similar in our numerical and experimental results. In both situations, the graphs show the same pattern in terms of visibility versus probe pulse shape. The differences between these results are associated to an imperfect matching between the experimentally achieved peak powers as compared with the numerical ones. Moreover, it is worth noting that in the simulations, the effect of polarization has been neglected, and as such, a unidimensional problem is considered. In practice, the sum of the two orthogonal polarizations reduces the visibility of the final trace [92]. Moreover, the experimentally obtained traces have been averaged to reduce the noise.

The averaged traces have a sufficiently high SNR, so that the effect of noise on the calculated visibility can be neglected. Indeed, the phase-noise, together with temperature drifts that occurred during the averaging process may also contribute to the fact that the visibility obtained from the experimental results is lower than the numerically obtained visibility. It should be noted that changing the pulse width has no effect on the conclusions of this study, if the pulse spectral content is not significantly altered (e. g. going down to picosecond pulses).

4.3 SNR Enhancement in ϕOTDR Using CPA

To overcome the trade-off between the pulse width and the spatial resolution [106, 107], techniques based on sequences of multi-wavelength pulses have been proposed in conventional OTDR, in a method named Chirp-OTDR [146]. Regarding sensors using coherent probe pulses, a technique called Optical Pulse Compression Reflectometry (OPCR) was recently proposed for ϕOTDR [**?**, 94, 95]. This technique involves applying a Linear Frequency Modulation (LFM) to the probe pulse, followed by numerical compression of the received backscattered trace using a simulated matched filter. The spatial resolution (demonstrated value of 34 cm) was determined by the pulse frequency bandwidth induced by the LFM process, rather than the pulse duration (which could be raised up to 2 μs). This increase in pulse width, in principle, allows an increased dynamic range and SNR. However, the technique requires phase detection (thus increasing the complexity of the system) and shows some problems for a perfect compression, among them the effect of laser phase-noise and the effect of random polarization evolution along the trace. We demonstrated a new ϕOTDR configuration inspired by the concept of Chirped Pulse Amplification (CPA), which was explained in Chapter 2 (Section 2.5) [48, 49]. The method proposed here achieves spatial resolutions in the millimeter range, while increasing the SNR by several orders of magnitude with respect to conventional ϕOTDR techniques.

4.3.1 Chirped Pulse Amplification in ϕOTDR

The technique involves the temporal pulse stretching and amplification of an ultra-short (e.g., picosecond) probe optical pulse in a dispersive medium, followed by the propagation of such a pulse through the Fiber Under Test (FUT) and the subsequent compression of the resulting backscattered trace using the conjugated dispersive medium (i.e., a medium with the same dispersion magnitude as the first one, but with the opposite sign). This method is conceptually similar to that of OPCR, with the critical advantage that the process of pulse compression is directly realized in the optical domain, avoiding the need for phase detection of the backscattered trace and subsequent digital processing. This process not only greatly simplifies the scheme, but also largely reduces the polarization sensitivity. The proposed technique has been experimentally validated, proving a system with a spatial resolution of 1.8 cm and an SNR increase of 20 dB with respect to the traditional ϕOTDR scheme.

To model our scheme, we start by considering a highly coherent optical pulse with a complex envelope $P(t)$ that is injected into the FUT. Typically, a Full Width at Half-Maximum (FWHM) pulse width of nanoseconds is required for a sufficiently high SNR. The detected backscattered signal $E(t)$ is given by the convolution of $P(t)$ and the backscattering impulse response of the FUT $r(t)$ [21, 34, 106]:

$$E(t) = P(t) \otimes r(t) \tag{4.2}$$

The backscattered signal is expressed in the spectral domain as:

$$E(\omega) = P(\omega) \cdot r(\omega) \tag{4.3}$$

where $E(\omega)$, $P(\omega)$ and $r(\omega)$ are the Fourier transforms of $E(t)$, $P(t)$ and $r(t)$, respectively.

In our approach, the input pulse $P(t)$ has initially a width that is several orders of magnitude smaller than those used in conventional ϕOTDR (e.g., down to the picosecond regime). To reach a measurable energy in the measured trace, the probe pulse is first temporally stretched using a second-order dispersive device, providing predominantly a linear group delay with respect to frequency [49]. This leads to the spreading of the pulse energy over a longer temporal interval, thus reducing its peak power. The stretched pulse is then amplified to the limit of appearance of non-linear effects in the FUT (mainly MI), which are essentially dependent on the pulse peak power [106]. Assuming that only second-order dispersion is introduced, the spectrum of the stretched and amplified pulse P_{st} injected into the FUT is then:

$$P_{st}(\omega) = G \cdot P(\omega) \cdot e^{i\left(\ddot{\Phi}/2\right)\omega^2} \tag{4.4}$$

where G is the gain introduced by the amplification stage and $\ddot{\Phi}$ is the second-order dispersion coefficient of the dispersive device. The received backscattered trace in the temporal domain is:

$$E_{st}(t) = P_{st}(t) \otimes r(t) \tag{4.5}$$

which expressed in the spectral domain is:

$$E_{st}(\omega) = P_{st}(\omega) \cdot r(\omega) \tag{4.6}$$

Using Equations 4.3, 4.4 and 4.6, we can write the backscattered signal in the frequency domain as:

$$E_{st}(\omega) = G \cdot E(\omega) \cdot e^{i\left(\ddot{\Phi}/2\right)\omega^2} \tag{4.7}$$

Upon arrival of the backscattered contributions, a second dispersive device with an equal dispersion magnitude and an opposite sign is used to compensate for the dispersion induced in $P(t)$:

$$E_{comp}(\omega) = E_{st}(\omega) \cdot e^{-i\left(\ddot{\Phi}/2\right)\omega^2} \tag{4.8}$$

Substituting Equation 4.7 into Equation 4.8, the latter can be simplified as:

$$E_{comp}(\omega) = G \cdot E(\omega) \tag{4.9}$$

and therefore, the final compensated backscattered signal is expressed in the temporal domain as:

$$E_{comp}(t) = G \cdot E(t) \tag{4.10}$$

It can be concluded from Equation 4.10 that the presented system behaves essentially as a conventional ϕOTDR, with a spatial resolution given by the input pulse width before time stretching. The SNR of the measurement, however, is dictated by the energy of the transmitted pulse after time stretching and amplification, which can be substantially increased before reaching the non-linearity threshold.

4.3.1.1 Experimental Setup

The experimental setup used to demonstrate this concept (Figure 4.6) is similar to a traditional ϕOTDR, such as the ones reported in Chapter 3 (see Figure 3.8) or previously in Subsection 4.3 (see Figure 4.3), but including two opposite dispersive media in a configuration that emulates a CPA scheme. In this example, we use two Linearly-Chirped Fiber Bragg Gratings (LC-FBGs) as dispersive media [49].

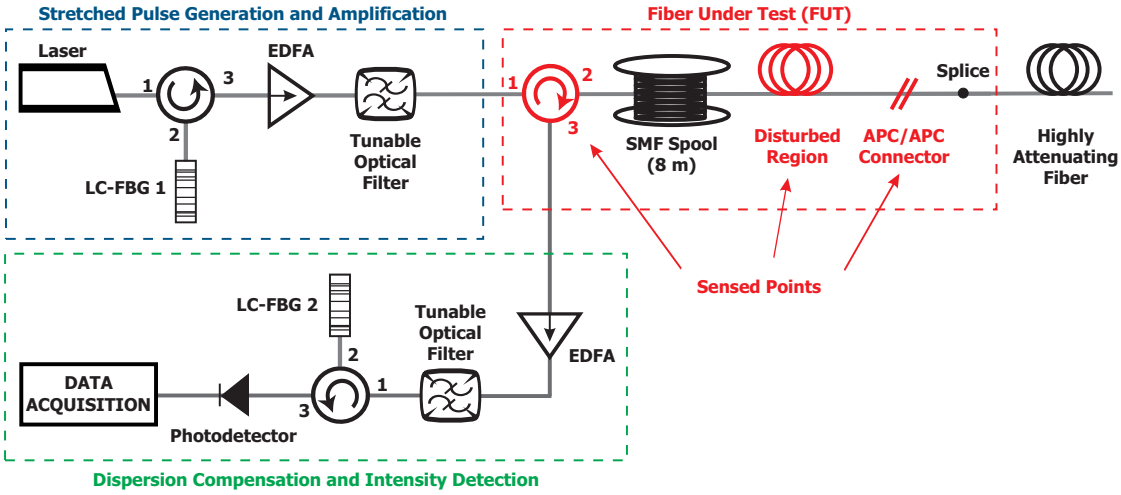

Figure 4.6: Experimental setup of a ϕOTDR using CPA concepts [142, 147]. EDFA, Erbium Doped Fiber Amplifier; LC-FBG, Linearly-Chirped Fiber Bragg Grating.

A passively mode-locked laser (working at a central wavelength of 1555.4 nm) generates transform-limited optical pulses with a FWHM of 7 ps (corresponding to a 3 dB bandwidth of 55 GHz), at a repetition rate of 10 MHz. The high repetition rate of the source limits the sensing range to a maximum length of 10 m. For this reason, the FUT used in this proof-of-concept is a spool of Single-Mode Fiber (SMF) with a length of approximately 8 m. The sensing range could be extended by simply choosing a lower-rate pulse source. However, it is worth noting that the range could not be extended arbitrarily: dispersion-induced pulse broadening will generally limit the maximum range attainable by the system in sub-centimetric resolution setups. In our case, the maximum measurable length should be around 120 m to maintain the resolution value.

The input pulse is first dispersed by an LC-FBG, with a second-order dispersion of ~2600 ps^2 (equivalent to ~120 km of a standard SMF). The dispersed pulse is then amplified by an Erbium-Doped Fiber Amplifier (EDFA) up to the peak power limit imposed by the non-linear

effects [106]. The Amplified Spontaneous Emission (ASE) added by the EDFA is subsequently minimized using a tunable optical filter. An optical circulator serves to launch the signal into the FUT and collect the backscattered response. This backscattered signal is also amplified and filtered to reduce the ASE.

Next, the dispersion is compensated on the backscattered signal using a second LC-FBG with opposite dispersion to the first one. Finally, the resulting traces are detected by a 35 GHz photodetector and recorded by an 80 GSps sampling oscilloscope (Tektronix CSA8200).

To test the proposed configuration, several regions of the employed FUT are used as sensed points, namely the interfaces at the port 2 of the circulator, an APC/APC connector, and a 1.5 cm long fiber section in which a controlled strain is applied; see Figure 4.6. The reflection produced by the last APC/APC connector is attenuated via a 15 dB/cm highly attenuating fiber spliced at the end of the FUT, in order to avoid saturation of the photodetector. Additionally, strain variations through a ∼1.5 cm fiber section glued to a micrometric translation stage are also well detected.

4.3.1.2 Results

Now, we present the experimental results obtained from the proposed scheme and compare them with the results obtained from a traditional ϕOTDR system (without the LC-FBGs). Figure 4.7 shows the temporal intensity profile of the pulse emitted by the laser (a) and the broadened pulse (b).

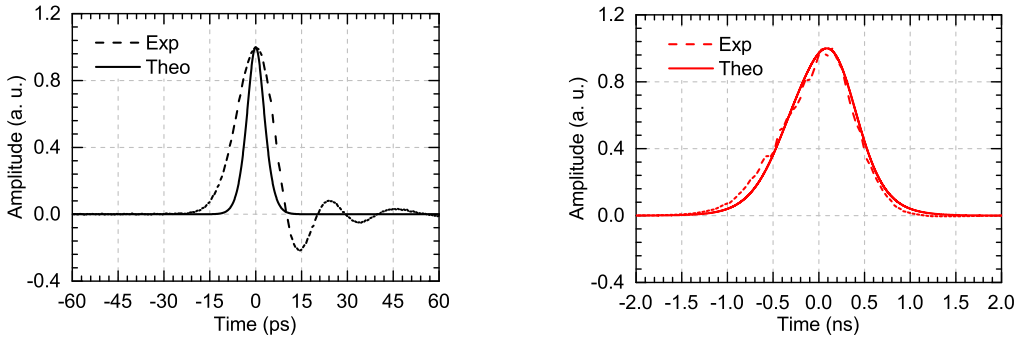

(a) (b)

Figure 4.7: Instantaneous power measurements of (a) a pulse emitted by the laser and (b) a pulse stretched by the LC-FBG. Notice the difference in the time scales in (a) and (b) [142].

The theoretical curve (in continuous line) for the pulse emitted by the laser is obtained from the measured signal spectrum (which will be shown below in Figure 4.9(a), black curve), assuming a transform-limited input. Note that the bandwidth of the employed photodetector is only 35 GHz, well below the nominal pulse bandwidth of 55 GHz. For this reason, the laser pulse measured by the detector (see Figure 4.7(a)) presents a temporal width wider than the nominal value and several ripples in the trailing edge. The maximum estimated resolution of the sensor will then be limited by the detector response which, in this case, is ∼30 ps, corresponding to a resolution of ∼3 mm [3]. The measured FWHM of the stretched pulse is ∼1 ns, which is roughly 100 times larger than the input pulse. The theoretical dispersed pulse in Figure 4.7(b) is obtained by simulating the propagation of the laser pulse through a dispersive medium with the characteristics of the LC-FBG used in the experiment. The experimental measurements present good agreement with the theoretical model.

SNR Increase

The SNR increase obtained with this method is demonstrated here. For this purpose, we show the detected backscattered traces, resulting from the 8 m SMF used as a FUT, when launching a 7 ps FWHM pulse non-dispersed (Figure 4.8(a)) and dispersed by the LC-FBG (Figure 4.8(b)). The optical peak power in both cases was boosted up to the limit of MI, i.e., around 40 W for this fiber length. In the second case, the trace is compressed by the second LC-FBG. Figure 4.8 shows the two detected traces after averaging 4000 times. Figure 4.8(b) shows the trace using the non-dispersed pulse (conventional ϕOTDR), while Figure 4.8(b) shows the trace obtained by employing the stretched and amplified pulse (FWHM of ∼1 ns) and compensating for the previously induced dispersion. It was essential to average the traces 4000 times to reach a minimum level of SNR in the trace obtained without CPA (4.8). Actually, the SNR of the trace obtained using CPA is ∼4 dB when no averaging is applied. The temporal length of the stretched pulse is almost 100 times higher than that of the non-stretched pulse, and both have the same peak power. Hence, the energy of the former is almost 100 times higher. This leads to an expected increase of the SNR of the sensor by ∼20 dB, which can be verified from the measured traces presented in Figure 4.8. It will be shown below that the spatial resolution is the same in both cases.

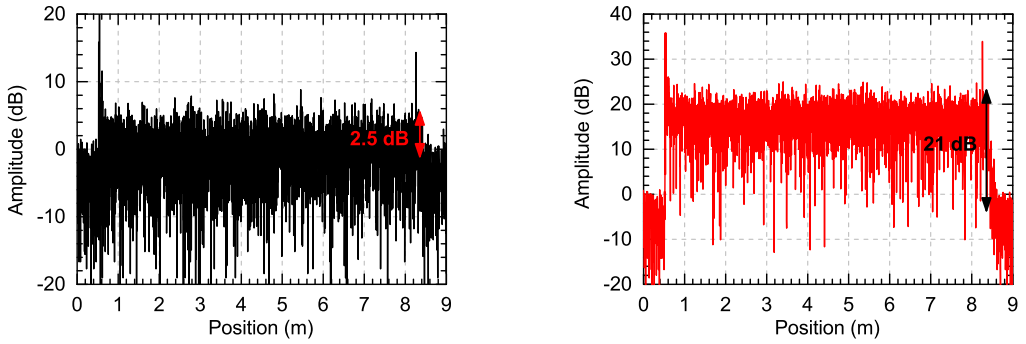

(a) (b)

Figure 4.8: Detected backscattering traces with (a) a pulse without chirp (FWHM of 7 ps) with an input peak power of 40 W and (b) a time- stretched pulse (FWHM of 1 ns) with an input peak power of 40 W and then temporally re-compressed. Both traces are normalized to the noise floor level. The SNR is calculated with respect to the average trace level [142].

Mitigation of Non-Linear Effects

An additional advantage of the proposed configuration is the fact that the system is more robust than the traditional scheme against other non-linearities. To validate this claim, the optical spectrum of the dispersed and non-dispersed pulses after propagation through the FUT are recorded and analyzed (maintaining the peak power at 40 W). These spectra are plotted in Figure 4.9(a). It can be observed that, after 8 m of fiber propagation, the spectrum of the non-dispersed pulse starts to broaden due to Self-Phase Modulation (SPM), increasing the bandwidth from 55 to 65 GHz. On the other hand, the dispersed pulse maintains the original bandwidth, as shown in Figure 4.9(b). This is owed to the fact that the SPM-induced broadening is larger for shorter Gaussian pulses. Time-stretched pulses are therefore more robust against this effect. The experimental results have also been confirmed theoretically. For this purpose, a Gaussian-like function was fitted to the spectrum of both input signals. Then, the non-linear

effects induced in the signals were simulated by solving the Non-Linear Schrödinger Equation (NLSE) 2.30 using a split-step Fourier method with an adaptive step size [146]. Figure 4.9 shows the numerically obtained pulse spectra in a continuous line, which are in good agreement with the experimental results (in dashed line).

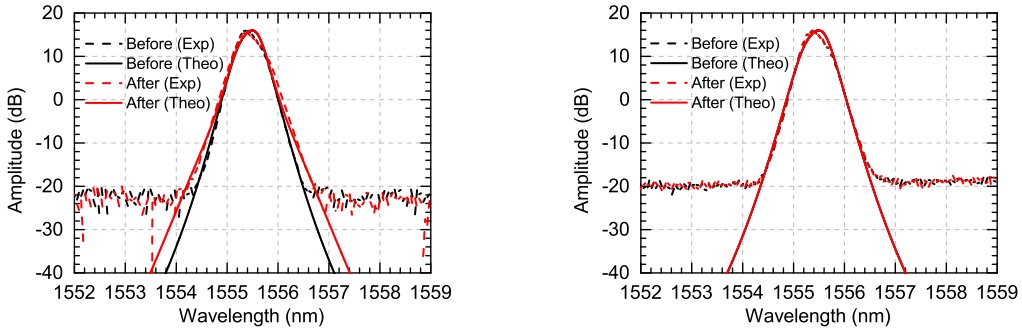

Figure 4.9: Signal spectra before and after propagation through 8 m of SMF (input peak power of 40 W). (a) Pulse without chirp (FWHM of 7 ps) and (b) a pulse stretched and amplified (FWHM of 1 ns) [142].

Millimeter Resolution Demonstration

The operation of the system is proved by detecting the reflection peaks generated from the sensed points in the FUT. In particular, two initial reflections separated by ∼2 cm are generated by the interfaces inside the circulator placed at the fiber input (port 2 of the circulator) and a final one produced by a fiber connector (APC/APC) before the highly attenuating fiber. Figure 4.10 represents the detailed measurements of these reflections.

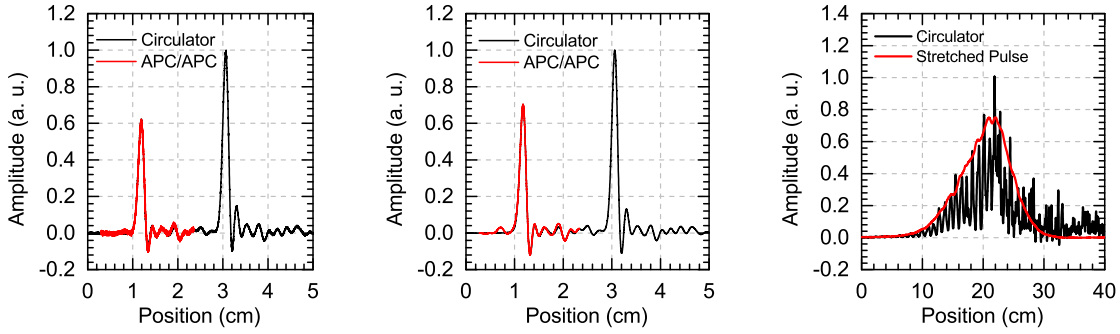

Figure 4.10: Connectors observed in the trace from (a) a non-dispersed pulse (FWHM of 7 ps); (b) a pulse stretched, amplified (FWHM of 1 ns), and then re-compressed; and (c) a pulse stretched and amplified (FWHM of 1 ns), not re-compressed. In all cases, the input peak power is 40 W [142].

Figure 4.10(a) shows the reflections detected when using the pulse without chirp (FWHM of 7 ps) and peak power of 40 W. The two reflections produced by the circulator are represented in black; the reflection produced by the APC/APC connector is represented in red and superimposed to the first reflection. (The intensity levels have been adjusted for comparison purposes.)

As it can be observed, the connector reflection fits perfectly with the first reflection of the circulator, i.e., there is no measurable temporal broadening. As such, the resolution is maintained along the fiber. The temporal width of the peaks, in both cases, is 30 ps, which corresponds to the initial pulse width (nominal resolution of 3 mm); thus, the two interfaces of the circulator can be resolved. The same results are obtained when the CPA scheme is used, as observed from Figure 4.10(b). The two input interfaces are clearly resolved, even though the duration of the stretched pulse covers both of them (recall that the FWHM of the stretched pulse is ∼1 ns, corresponding to a spatial resolution of ∼20 cm). If the dispersion was not compensated, the two reflections generated by the circulator would not be distinguishable; this situation is presented in Figure 4.10(c) (black). As expected, the resolution in this case corresponds to the temporal length of the stretched pulse (superimposed in red).

High resolution strain detection

Finally, strain perturbations are detected using the proposed configuration. These were applied in a ∼1.5 cm fiber section (disturbed region in Figure 4.6).

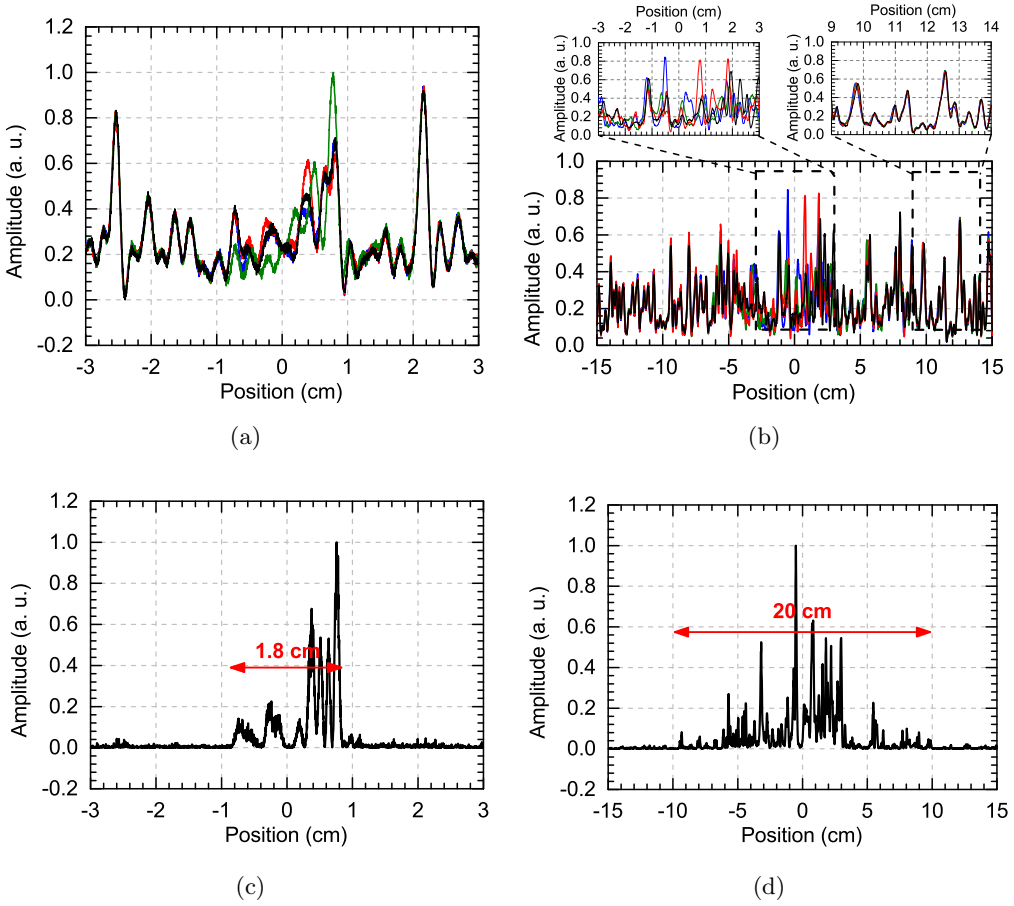

Figure 4.11: Strain event detection. (a) Detected traces after re-compression with different strains. (b) Detected traces not re-compressed with different strains. (c) and (d) show the accumulated square trace differences of (a) and (b), respectively. Notice the difference in the position scales in (a)-(c) and (b)–(d) [142].

For this purpose, the disturbed fiber section was glued to a micrometric translation stage, controlling the applied strain (in steps of 700 $\mu\varepsilon$). Perturbations below 1.5 cm could not be

applied due to the limitations on the available equipment. For this reason, in spite of the fact that the nominal resolution is 3 mm, sub-centimetric resolutions could not be demonstrated. The obtained results are plotted in Figure 4.11 (traces with different strain are plotted with different colors).

Figures 4.11(a) and 4.11(b) present the affected region in the re-compressed and non-recompressed traces, respectively. In the top of Figure 4.11(b), a detail of the affected and the non-affected region is presented for clarification purposes. As it was expected, the affected region in Figure 4.11(b) is much longer than in Figure 4.11(a), since the dispersion was not compensated for in the former case.

To further analyze these results, the accumulated square trace differences of Figures 4.11(a) and 4.11(b) are represented in Figures 4.11(c) and 4.11(d), respectively. This way, we can easily determine the length of the affected region in both cases, namely, 1.8 cm for the re-compressed traces and 20 cm for the non-recompressed traces. Hence, we have proved the ability of the proposed configuration to detect a perturbed fiber section much shorter than the stretched pulse width.

4.4 Linear Measurement in ϕOTDR Using PROUD

Linear measurements of strain, temperature and vibrations with ϕOTDR technology can be achieved using coherent detection [28–33]. Quantitative information of an induced refractive index change in a fiber section can be obtained recovering the phase information in the backscattered electric field, as it was explained in Chapter 3 (Section 3.4.2).

However, this technique presents some inconveniences and added complexity since it requires mixing a LO with the optical signal before photodetection. As in any interferometric technique, the amplitude of the interference between the LO and the backscattered field strongly depends on their relative state of polarization, which can even reach zero for the case of orthogonal polarizations. The required high coherence length represents another important limitation of this technique. For 100 km fiber the required laser linewidth is $\Delta f \approx 320$ Hz, which represents and important cost in the system.

By finding a self-refereed technique that allows the phase reconstruction of the backscattered signal, these limitations would vanish. In this context, Phase Reconstruction using Optical Ultrafast Differentiation (PROUD) has been demonstrated to be a viable technique for self-refereed phase detection [117–119, 148]. However, previous works, mostly aimed at the context of telecommunication signals, operated in very different regimes (in terms of pulse durations, signal bandwidths and correspondingly used optical filters), being several orders of magnitude off than those found in ϕOTDR. The type of signals are also radically different (usually digital step-like signals, rather than random patterns as in ϕOTDR). PROUD is therefore a good candidate for use in ϕOTDR, although its applicability is far from being trivial.

In this section, after describing the technique, the applicability of PROUD operating in the regimes of ϕOTDR is firstly demonstrated. This is done by using PROUD to characterize the propagation-induced distortions of optical pulses compatible to those used in ϕOTDR. Then, the use of the technique for recovering the amplitude and phase of the scattered signal in a ϕOTDR is proposed and its implications (both theoretical and practical advantages/drawbacks) are discussed.

4.4.1 Phase Reconstruction Using Optical Ultrafast Differentiation (PROUD)

PROUD techniques can be used for full characterization of optical signals, including continuous-time data streams, over a very wide range of pulse time durations. They can provide measurements in a single-shot and in a real-time with power sensitivities down to the microwatt level [148–150]. Real-time operation is in part enabled by the fact that the PROUD methods rely on a simple, non-iterative phase recovery numerical algorithm (simple analytic equation). The PROUD methods can be implemented using off-the-shelf fiber-optics and RF components and the resulting setups are thus very simple and fully compatible with fiber systems [119].

4.4.1.1 Single Time-Domain PROUD

In its most basic implementation, time-domain PROUD [118, 148], the temporal phase profile of an optical signal can be recovered from two time-domain intensity measurements, namely the time-domain intensity profiles of the signal under test and of the signal after propagation through a frequency-shifted temporal photonic differentiator.

Figure 4.12 illustrates the principle of operation of time-domain PROUD. The signal under test is supposed to be spectrally centered at the optical radial frequency ω_0, having a time-domain complex envelope defined by $x(t) = |x(t)| \cdot \exp[-i\phi(t)]$, where $|x(t)|^2$ and $\phi(t)$ are the signal's time-domain intensity and phase profiles, respectively. The field frequency spectrum of the signal envelope can be calculated as the Fourier Transform (FT) of $x(t)$; in particular $X(\omega) = \mathrm{FT}\{x(t)\} = |X(\omega)| \cdot \exp[i\Phi(\omega)]$, where $|X(\omega)|^2$ and $\Phi(\omega)$ are the spectral energy density and spectral phase profile of the signal, respectively. In this notation, ω is the base-band radial frequency, i.e. $\omega = \omega_{\mathrm{opt}} - \omega_0$ with ω_{opt} being the optical radial frequency variable.

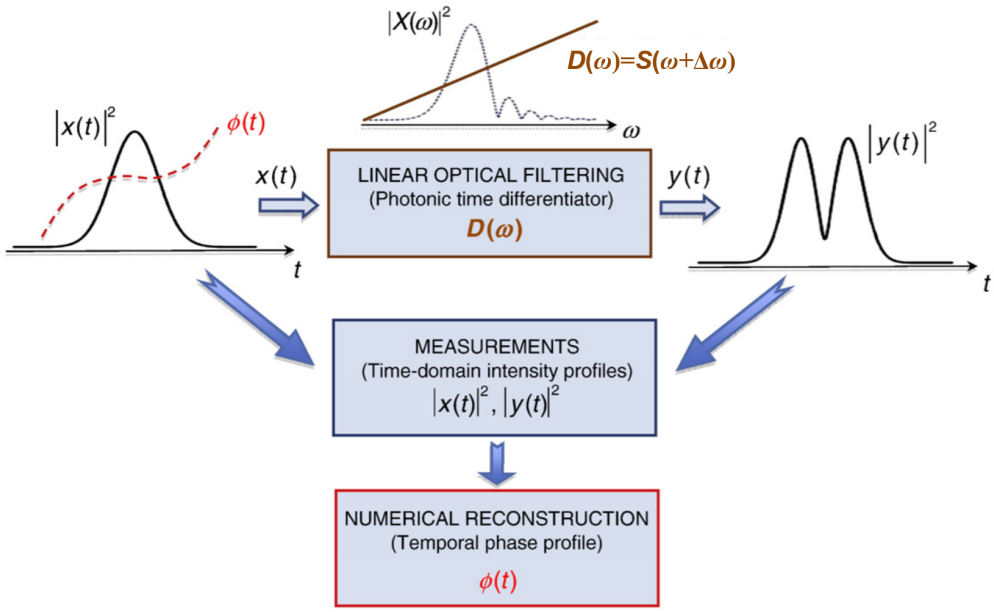

Figure 4.12: Schematic of the concept for time-domain phase reconstruction based on optical ultrafast differentiation (PROUD) [119].

The previously mentioned photonic temporal differentiator is a linear time-invariant optical filter characterized by a spectral transfer function having a linear-amplitude variation [151, 152], $D(\omega) = S(\omega + \Delta\omega)$, where S is the (positive or negative) slope of the linear spectral amplitude

variation and $\Delta\omega$ is the (positive) frequency shift between the signal's central frequency and the resonance frequency of the differentiator (frequency at which its spectral transfer function reaches zero) [119]. It is important to note that the filtering transfer function defined above, with $\Delta\omega$ being a positive number, corresponds to the case when the signal's carrier frequency is higher than the filter's resonance frequency.

The instantaneous-frequency profile of the input signal can be recovered from the measured temporal intensity profiles of the input signal, $|x(t)|^2$, and of the signal at the differentiator output, $|y(t)|^2$, using the following direct equation [118]:

$$\omega_{\text{inst}}(t) = -\frac{\partial\phi(t)}{\partial t} = +s(t) - \Delta\omega \tag{4.11}$$

where $s(t)$ is obtained from the following equation:

$$s(t) = \sqrt{\left(\frac{1}{|x(t)|^2}\right) \cdot \left(\left[\frac{|y(t)|}{S}\right]^2 - \left[\frac{\partial|x(t)|}{\partial t}\right]^2\right)} \tag{4.12}$$

It is worth to note that $\Delta\omega$ must be sufficiently large so that $\Delta\omega > |\omega_{\text{inst}}(t)|$ along the entire time duration of the signal under test, allowing to unambiguously recover the instantaneous-frequency profile of the input signal. The above given condition simply implies that the lowest optical frequency of the input signal spectral support must be higher than the differentiator's resonance frequency.

The pulse temporal phase profile can be obtained by cumulative numerical integration of the recovered instantaneous frequency, except for an undetermined phase constant ϕ_0, i.e. $\phi(t) = -\int_{-\infty}^{t} \omega_{\text{inst}}(\tau)\mathrm{d}\tau + \phi_0$. Thus, using time-domain PROUD, the capabilities of any available temporal intensity measurement setup, e.g. a conventional photo-detector attached to a sampling or real-time scope, can be easily upgraded to characterize the signal temporal phase profile.

4.4.1.2 Balanced Time-Domain PROUD

The numerical phase recovery algorithm in time-domain PROUD involves the calculation of the time derivative of the time-resolved input intensity, see Equation 4.12. This numerical procedure is very sensitive to the presence of noise in the measured waveform, thus requiring a large averaging in the intensity detection process. An advanced extension of PROUD, referred to as Balanced PROUD [148], has been proposed and demonstrated to overcome this main difficulty of the original technique. In this scheme, there is no need for calculation of the numerical derivative of the measured signal's time-resolved intensity waveform to obtain the target instantaneous frequency profile. This fact combined with the noise suppression characteristics intrinsic to a balanced measurement method allows us to avoid the previously required time-averaged acquisition of the intensity waveforms. By incorporating a balanced/differential photonic differentiation and photo-detection scheme, single-shot and real-time characterization of the instantaneous frequency and phase profiles of low-power (microwatt) continuous-time optical data streams with frequency bandwidths >10 GHz has been successfully demonstrated [148]. Whereas several self-referenced techniques have been specifically developed for instantaneous frequency characterization of telecommunication GHz-bandwidth optical signals, including methods based upon the use of photonic frequency-discriminator filters [153–157], they rarely offer single-shot and real-time capabilities, as desired for practical monitoring applications.

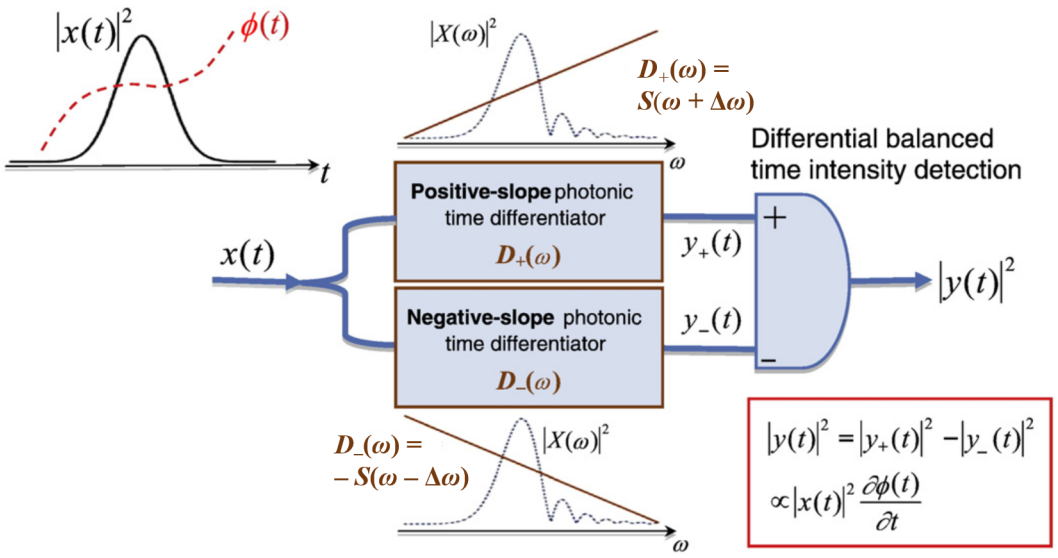

Figure 4.13: Schematic illustration of the concept of Balanced PROUD for single-shot and real-time optical signal characterization (time-domain implementation shown in the figure) [119].

A schematic of the balanced time-domain PROUD concept is shown in Figure 4.13. The signal under analysis, with temporal complex envelope $x(t)$, is launched at the input of a balanced frequency-shifted photonic temporal differentiator. This balanced differentiator consists of two frequency discriminators with their respective linear-amplitude spectral transfer functions having (i) an identical slope magnitude and (ii) an identical frequency shift but with opposite sign (with respect to the signal's carrier frequency). Mathematically, the base-band spectral transfer functions of the two filters in the balanced differentiator can be expressed as $D_+(\omega) = S(\omega+\Delta\omega)$ and $D_-(\omega) = -S(\omega - \Delta\omega)$, respectively, where we recall that $\Delta\omega$ is a positive number. In the notation used here, the spectral amplitude slopes of the two filters have been written down with an opposite sign. The filter with $D_+(\omega)$ will be referred to as a "positive-slope" differentiator whereas the filter with $D_-(\omega)$ will be referred to as a "negative-slope" differentiator. $y_+(t)$ and $y_-(t)$ are the two output signals of both filters $D_+(\omega)$ and $D_-(\omega)$, respectively.

Differential (balanced) time-resolved intensity detection is used after the balanced optical differentiator. This allows us to eliminate the common terms of the two intensity waveforms $|y_+(t)|^2$ and $|y_-(t)|^2$. The measured intensity signal at the output of the differential intensity detection stage is thus given by [148]:

$$|y(t)|^2 = |y_+(t)|^2 - |y_-(t)|^2 = 4S^2\Delta\omega|x(t)|^2\omega_{\text{inst}}(t) \tag{4.13}$$

The input signal intensity, $|x(t)|^2$, can be directly measured using a standard time-resolved intensity measurement. In this way, the target instantaneous frequency profile, $\omega_{\text{inst}}(t)$, can be directly obtained from the measured temporal intensity at the differential detector output; the corresponding phase response $\phi(t)$ can be recovered from the measured instantaneous frequency using numerical integration. Single-shot, real-time detection of the instantaneous frequency and temporal phase profiles can be obtained using a high-speed digitizer (or real-time scope). Balanced photonic differentiation can be practically realized in a very simple fashion by use of a standard two-arm (2×2) interferometer, e.g. a fiber-optics or integrated-waveguide MZI [148]. In our experiment, a DWDM is used for this purpose. DWDM shows two complementary linear

spectral responses at the wavelength of interest in the pass and reflect channel, as it will be shown in Subsection 4.4.2.

4.4.2 Applicability of PROUD operating in the regimes of ϕOTDR

In this Subsection, we develop and validate a simple and practical time-domain Balanced PROUD setup. PROUD is well adapted to the single-shot detection of low power signals, as is the case of ϕOTDR [118,119,148]. The effectiveness of this in-line method is demonstrated by evaluating the impact of SPM and GVD in a 4–20 Gbps NRZ optical link. Characterizing the propagation-Induced Distortions in NRZ Data Signals is also interesting for ϕOTDR sensors since they are similar to the ones employed when coding techniques are implemented (see Subsection 3.5.2.2 in Chapter 3) [92]. Using different NRZ data signal scenarios is equivalent to the use of coding with different bit size/code length. Furthermore, characterizing GHz signals would be very useful since in the next chapter the use of chirped optical pulses is proposed. The temporal duration and spectral content of these optical pulses are around 100 ns and a few GHz, respectively.

The compensation of Group Velocity Dispersion (GVD) and Self-Phase Modulation (SPM) can be realized by physically propagating optical pulses through optical media with opposite GVD/non-linear parameters [158], by electronically designing the pulses to meet a certain desired shape [159, 160], thus achieving distortion-free pulses at the output of the link, or even digital post-detection compensation [161]. In any case, an accurate characterization of the complex field of the optical pulses after the propagation is required to have an accurate model of the response of the link and compensate distortions accordingly. Conventional square-law fast photodetectors can be used to accurately characterize the instantaneous power distribution of a given optical signal, but provide no information regarding its phase profile. A number of techniques that can be used to characterize arbitrary phase variations can be found in the literature [162], but these typically require a coherent detection system(i.e., a local oscillator and a synchronization mechanism), which represents a complex technological solution that may not always be available. Well-known techniques [163] overcome this limitation by using a self-referenced setup (i.e., one that does not require a local oscillator), but these typically rely on using non-linearities, which can be a drawback when characterizing low-power signals, as in the case of ϕOTDR signals. In this context, phase reconstruction using optical ultrafast differentiation (PROUD) is a set of direct self-referenced techniques well adapted for the characterization of low-power telecommunications signals [118, 119, 148]. Nonetheless, to the best of our knowledge, no results have been reported in the literature to validate the use of PROUD for signal characterization in fiber-optic propagation experiments.

Experiments were modeled using conventional propagation equations, showing good agreement with the measured data. The chromatic dispersion and non-linear coefficients of the fiber were easily and precisely quantified. For typical C-band telecommunications signals (around the 1.55 μm wavelength) with "well-behaved" pulse shapes and bit modulation rates well below 200 GHz (i.e., pulse widths >5ps), the pulse propagation can be described accurately by solving the Non-Linear Schrödinger's Equation (NLSE) for the scalar electric field envelope $A(z,t)$ (previously introduced in Chapter 2) [40]:

$$\frac{\partial A}{\partial z} + \frac{i\beta_2}{2}\frac{\partial^2 A}{\partial t^2} - \frac{i\beta_3}{6}\frac{\partial^3 A}{\partial t^3} + \frac{\alpha}{2}A = i\gamma|A|^2 A \tag{4.14}$$

where γ is the nonlinear fiber coefficient, β_2 is the GVD coefficient, β_3 is the third-order dispersion coefficient, and α is the attenuation coefficient. In this model, high-order dispersion and

non-linear effects, as well as scattering processes, are neglected [40]. For standard SMF, the zero of dispersion wavelength is ∼1.3 μm, and the effects of β_3 are usually negligible at 1.55 μm. In this case, GVD and SPM are the most important phenomena to be accounted for [40]. For a transform-limited Gaussian pulse, second-order dispersion introduces a linear frequency chirp (i.e., a parabolic phase shift) on the pulse, with an associated pulse broadening, which can limit the data rate. Due to GVD, in the anomalous dispersion regime ($\beta_2 < 0$), the blue-shifted (red-shifted) frequency components are moved toward the leading (trailing) edge of the pulse. SPM is a result of the Kerr non-linearity of the fiber [40]. For long pulses, neglecting the effect of GVD, pure SPM leads to a non-linear phase shift $\phi_{\mathrm{NL}}(t)$ proportional to the instantaneous power of the pulse $|A(t)|^2$ after propagation over a fiber of length L:

$$\phi_{\mathrm{NL}}(z = L, t) = \gamma L_{\mathrm{eff}} |A(t)|^2 \tag{4.15}$$

where $L_{\mathrm{eff}} = (1 - e^{-\alpha L})/\alpha$ is the effective fiber length which was introduced in Chapter 2. The variations of $\phi_{\mathrm{NL}}(t)$ are translated into variations of the instantaneous frequency ω_{inst}, which leads to spectral broadening, with red (blue) frequency shifts occurring in the leading (trailing) edge of the pulse, for a Gaussian-like pulse. The combined effect of GVD and SPM will introduce undesired distortion in both the spectrum and the temporal shape of the pulse. Thus, SPM limits the peak power of the pulses. The impact of GVD is higher for shorter pulses (broad spectral content) while the impact of SPM is higher for sharper pulse power variations. In any case, an accurate measurement of the instantaneous phase and frequency along the pulse profile would be important to allow for an accurate characterization and compensation of the propagation-induced distortions. For this purpose, this Subsection demonstrates a simple in-line technique based on Balanced PROUD [148] (see Subsection 4.4.1.2).

4.4.2.1 Experimental Setup

The experimental setup is shown in Figure 4.14. A Laser Diode (LD) operating at 1547.66 nm followed by a 20 GHz external optical modulator and an amplification and filtering scheme (using an Erbium-Doped Fiber Amplifier (EDFA) followed by a narrowband tunable 10 GHz optical filter) are used to generate optical pulses with different duration and variable peak power P_0. After propagation over a standard SMF spool, the complex field of the pulses $x(t)$ is characterized using a time-domain Balanced PROUD detection scheme. A Polarization Scrambler (PS) is used to avoid polarization dependence issues in the PROUD filter. In the detection stage, the output of the fiber is split using a calibrated 50/50 coupler: one output is used as the PROUD reference signal $|x(t)|^2$, while the other output is injected into a commercial 100 GHz DWDM centered at 1547.32 nm (manufactured by Opneti). This DWDM filter shows two complementary linear spectral responses at the wavelength of interest in the pass and reflect channel (see Figure 4.15). In particular, the pass (reflect) channel is used as positive D_+ (negative D_-) slope linear optical frequency filter with $D_{\pm}(\omega) = S(\omega \pm \Delta\omega)$, where $\Delta\omega \approx 2\pi \cdot 6$ GHz (corresponding to a wavelength range of ∼0.05 nm); and $S = 0.5/\Delta\omega$. The two outputs of the DWDM are then used as the PROUD photonic differentiated signals $|y_{\pm}(t)|^2$.

Other solutions have been tested to be used as D_+/D_- filters in PROUD. Using an unbalanced Mach–Zender interferometer allows flexibility in the filter parameters, but requires a non-standard component, usually with temperature stabilization [148], which increases the complexity of the system. In our case, the use of a commercial DWDM provides a stable and off-the-shelf, low-cost filter solution. For a given DWDM, the filter parameters are fixed, but with a proper choice of DWDM, some flexibility in the choice of ω_0 can be achieved. In our case, the

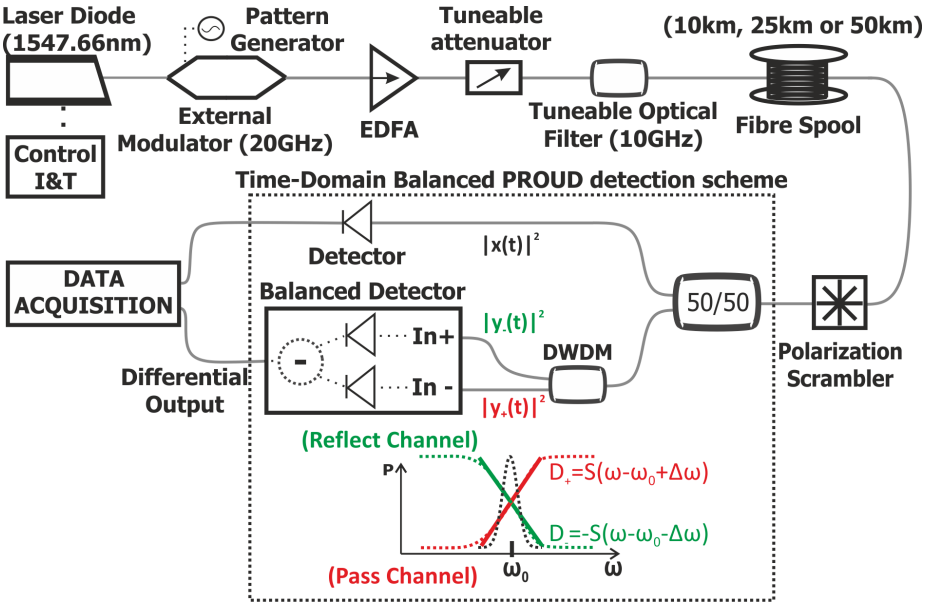

Figure 4.14: Experimental setup: data signal characterization by time-domain Balanced PROUD detection scheme [117]. EDFA, Erbium Doped Fiber Amplifier; DWDM, Dense Wavelength Division Multiplexer; I&T, Intensity & Temperature.

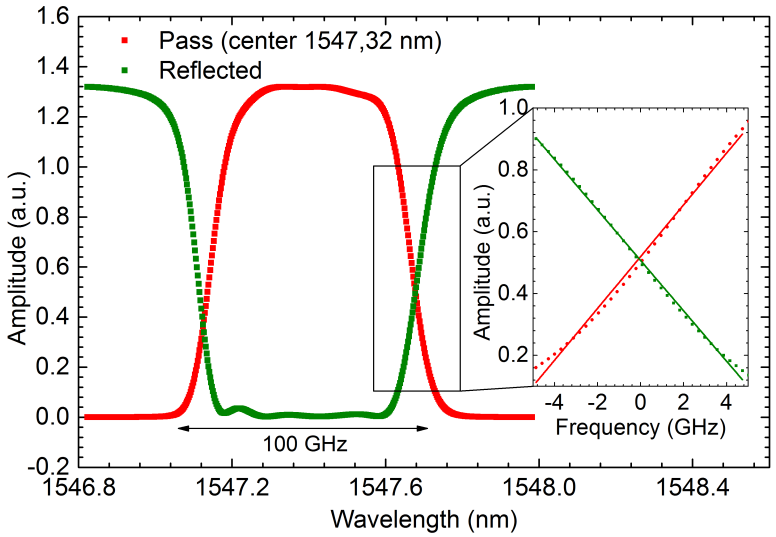

Figure 4.15: Spectral response of the DWDM used as D_+/D_- filter for the PROUD [117].

operation wavelength is near the ITU 100 GHz grid channel 37 (193.70 THz ≈ 1547.72 nm). The D_+ (D_-) signal is detected in the negative (positive) terminal of a 20 GHz p-i-n balanced photodetector. As a result, the output of the balanced photodetector ($|y(t)|^2 = |y_+(t)|^2 - |y_-(t)|^2$) is proportional to ω_{inst} (Equation 4.13). The reference signal $|x(t)|^2$ is also measured using a calibrated 20 GHz p-i-n photodetector, and a synchronization is ensured between the $|x(t)|^2$ and $|y(t)|^2$ signals. Lastly, the value of ω_{inst} is recovered by performing the normalization of the balanced signal with the reference signal (Equation 4.13).

To provide a high number of sampling points and facilitate the comparison between experiments and simulations, the signals are recorded with an 86116C sampling scope from Keysight with 80 GHz of electrical bandwidth and an equivalent sampling of ∼200 GS/s. In any case, real-time acquisition could also be achieved with a real-time oscilloscope, provided that the bandwidth/sampling was adjusted to the intended pulse features to be measured.

4.4.2.2 Results

Using the experimental setup presented in Figure 4.14, the optical power $P(t)$, instantaneous frequency profile $\nu(t) = \omega_{\text{inst}}/2\pi$, and instantaneous phase shift temporal profile $\phi(t)$ of the data signal are directly characterized. $\phi(t)$ is recovered using $\phi(t) = -2\pi \int \nu(t)\mathrm{d}t$. Different distortion profiles are expected for different width/shape optical pulses. To show the flexibility of the technique, a variety of signals corresponding to several data sequences were characterized. In our case, only the instantaneous phase shift normalized to the input temporal phase profile (i.e., $\phi(t) = \phi_{z=L}(t) - \phi_{z=0}(t)$), is presented. Therefore, the presence of the frequency chirp in the input pulse is neglected, which, in any case, was observed to be small in comparison with the chirp acquired after the propagation.

The experimental results were compared with the theoretical expectations, obtained by numerically solving Equation 4.14 using a split-step Fourier method with an adaptive step size. The used input scalar electric field envelopes $A(z = 0, t)$ are transform-limited, super-Gaussian pulses:

$$A(z = 0, t) = \sqrt{P_0} \cdot \exp[-0.5(t/T_0)^{2m}] \tag{4.16}$$

where m is the order of the super-Gaussian, P_0 is the peak power, and T_0 determines the width of the pulse. The fiber parameters are those of a standard SMF-28 at a reference wavelength of 1550 nm: $\gamma = 1.4$ W^{-1}km^{-1}, $\beta_2 = 15$ ps^{2}km^{-1}, $\beta_3 = 0.1$ ps^{3}km^{-1}, and $\alpha = 0.2$ dB·km^{-1}.

First, the $\phi(t)$ of a 90 ps optical pulse after propagation over 10 km of fiber was characterized for varying input P_0 (6–14 dBm). A complete set of results is shown in Figure 4.16. Because of the non-linear response of the modulator, the optical pulse resembled a Gaussian shape. The normalized input pulse's instantaneous power profile is shown in Figure 4.17(c). For a Gaussian pulse under anomalous dispersion, GVD and SPM will introduce almost linear frequency chirps with opposite signs around the pulse center. Therefore, the results can be interpreted as follows: for $P_0 = 10$ dBm, the effects of GVD and SPM are comparable and almost cancel each other. Hence, an almost flat $\phi(t)$ is obtained. As P_0 is decreased (increased) from 10 dBm, the effects of GVD (SPM) have a higher impact, thus, resulting in positive (negative) and close to parabolic (Gaussian) $\phi(t)$, as expected [40].

Figures 4.17(a)–4.17(c) and 4.17(d)–4.17(f) show the $\phi(t)$, $\nu(t)$, and $P(t)$ of a 90 ps optical pulse (the same input pulse of Figure 4.16) and a 470 optical pulse, respectively, for different peak power values P_0 (6–14 dBm), after propagation over 50 km of SMF-28. Note that the

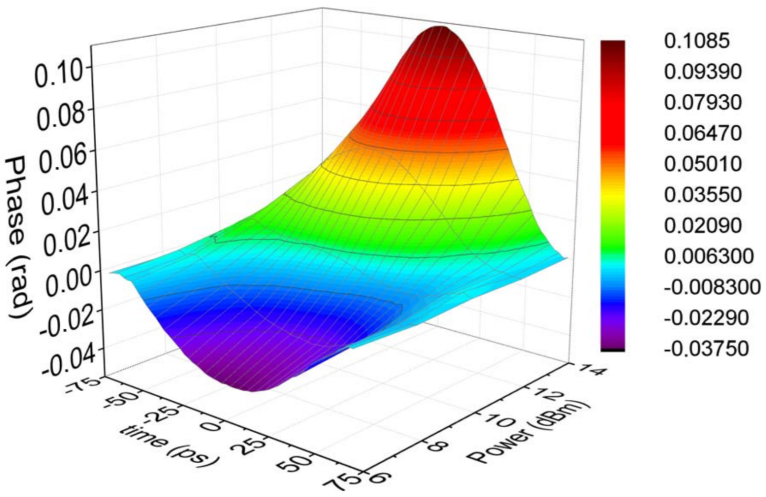

Figure 4.16: Experimental characterization of $\phi(t)$ of a Gaussian-like pulse with ∼90 ps FWHM after propagation over 10 km of fiber, for varying input P_0 (6-14 dBm) [117].

leading (trailing) edge of the pulses corresponds to the negative (positive) times of Figures 4.16-4.18. With higher P_0, the impact of SPM is increased: a $\phi(t)$ approximately proportional to $P(t)$ is obtained (Figures 4.17(a) and 4.17(d)), with red (blue) frequency shifts occurring in the leading (trailing) edge of the pulse (Figures 4.17(b) and 4.17(e)). In the low power regime, an increase of the effect of GVD is observed clearly, with blue (red) frequency shifts occurring in the leading (trailing) edge of the pulse, where the spectral content of the pulse is broader and a gradual shift of $\phi(t)$ toward negative phases in the center of the pulse (Figures 4.17(a) and 4.17(d)). The impact of GVD (SPM) is observed to be higher for the shorter (longer) pulse, as expected, because of its broader (narrower) spectral content.

The measured instantaneous power profile, normalized to P_0, is given in Figures 4.17(c) and 4.17(f). The fiber losses are numerically compensated to facilitate pulse shape comparisons. The pulse keeps its original shape, although noticeable distortions are observed, especially near the edges of the pulse in Figure 4.17(f). The distortions are higher for higher P_0, as expected [40]. The evolution of the pulses shown in Figure 4.17 were simulated using super-Gaussian pulses as input (see Equation 4.16) with $m = 1$ (a), (b) and $T_0 = 35$ ps (FWHM ≈ 80 ps); $m = 3$ (d), (e) and $T_0 = 165$ ps (FWHM ≈ 440 ps), showing good agreement with the experimental results.

Figures 4.18(a)–4.18(c) show the evolution of the $\phi(t)$, $\nu(t)$, and $P(t)$ of an almost flat-top input pulse with ∼220 ps (FWHM) after propagation over 10, 25, and 50 km of fiber ($L_{\text{eff}} \approx 8$, 14.8 and 19.5 km), with a relatively high $P_0 = 14$ dBm. Here, the mechanisms of the propagation distortions can be understood clearly.

For the shorter fiber distances (10 and 25 km), the optical power of the pulse is high and the impact of SPM is dominant. In this case, the shape of $\phi(t)$ (Figure 4.18(a)) should resemble $P(t)$, with an amplitude that increases proportionally to L_{eff} (see Equation 4.15). The corresponding $\nu(t)$ is also as expected (Figure 4.18(b)): red (blue) $\nu(t)$ shifts occurring in the leading (trailing) edge of the pulse and a maximum $\nu(t)$ shift that increases with L_{eff}. In Figure 4.18(c), the input $P(t)$, normalized to P_0, is given. The fiber losses are numerically compensated in the plots to facilitate pulse shape comparisons. Note that the $P(t)$ of the pulse (Figure 4.18(c)) experienced a small, but noticeable, deformation with the length increase, thus indicating that the effect of GVD is not negligible. Between the distances of 25 and 50 km, the optical power decreases because of the fiber losses, and the impact of SPM is reduced: a much smaller increase of the

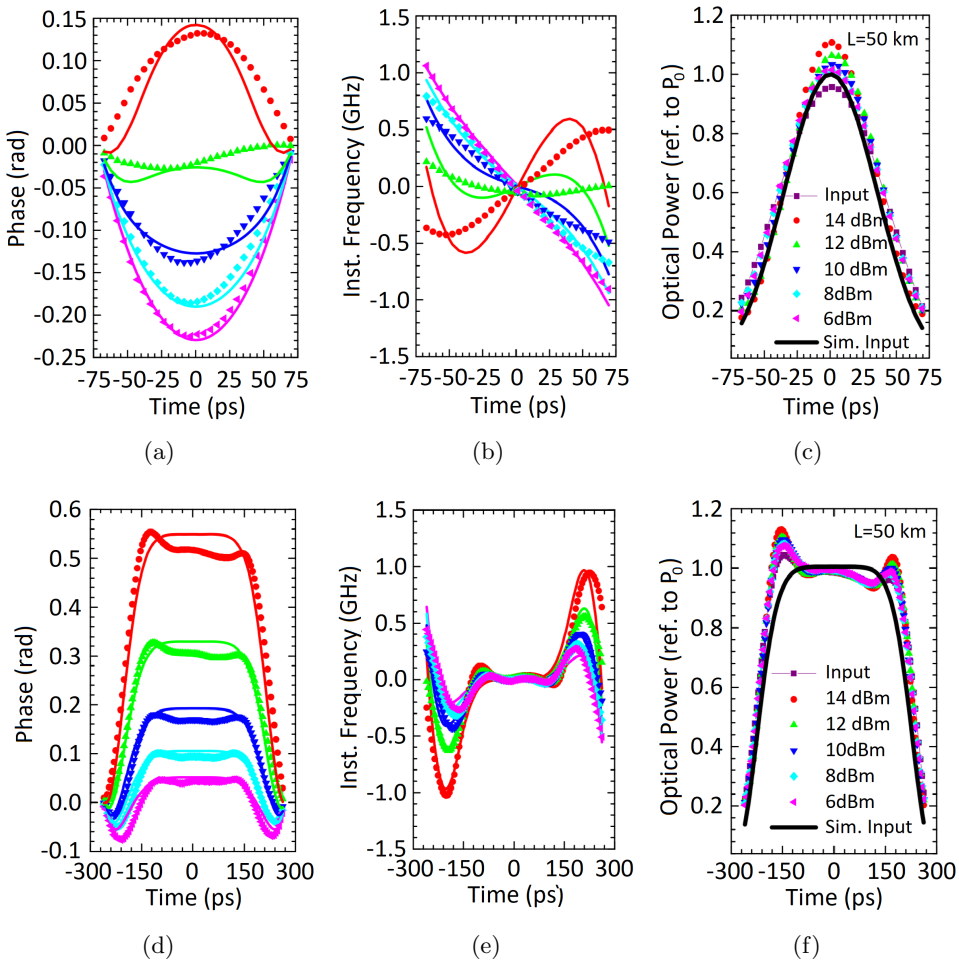

Figure 4.17: Measured (dotted lines) $\phi(t)$, $f_{\text{inst}}(t)$, and $P(t)$ for a ~90 ps FWHM pulse (a)–(c), and a ~470 ps FWHM pulse (d)–(f) after 50 km of fiber, for various values of the input P_0. Theoretical simulations (solid lines) are plotted for comparison [117].

maximum $\nu(t)$ shift of the pulse is observed between 25 and 50 km than between 0 and 25 km (Figure 4.18(b)). On the other hand, the frequencies previously generated by SPM were moved closer to the pulse center, as it would be expected in the case where GVD is dominant. As for the form of $\phi(t)$, after 50 km, the acquired phase shift is smoothed to the point of resembling that of a Gaussian pulse (Figure 4.17(a)). Lastly, Figures 4.18(d)–4.18(f) present the $\phi(t)$, $\nu(t)$, and $P(t)$ of this pulse after propagation over $L = 50$ km of fiber for various values of the input P_0, presenting consistent results with those found in Figure 4.17.

For comparison purposes, the presented experimental conditions are simulated using a super-Gaussian pulse (see Equation 4.16) with $m = 2$ and $T_0 = 82$ ps (FWHM $\approx$ 210 ps) as input pulse, as depicted in Figure 4.18(c). A smoothing of the measured $\nu(t)$ (Figure 4.18(b)) seems to occur, which could be because of the limited bandwidth of the photodetector. It should be noted that, for the 10, 25, and 50 km measurements, different fiber spools were used, and, therefore, small variations in the fiber parameters are possible. In any case, a good agreement between the theoretical simulations and experimental results is observed for all the measurements.

Note that employed optical pulses in ϕOTDR or telecommunications applications typically present low peak powers to avoid the impact of non-linearities. Therefore, the pulse power range used here (6-14 dBm) was significantly higher than that typically used in those cases, as it was

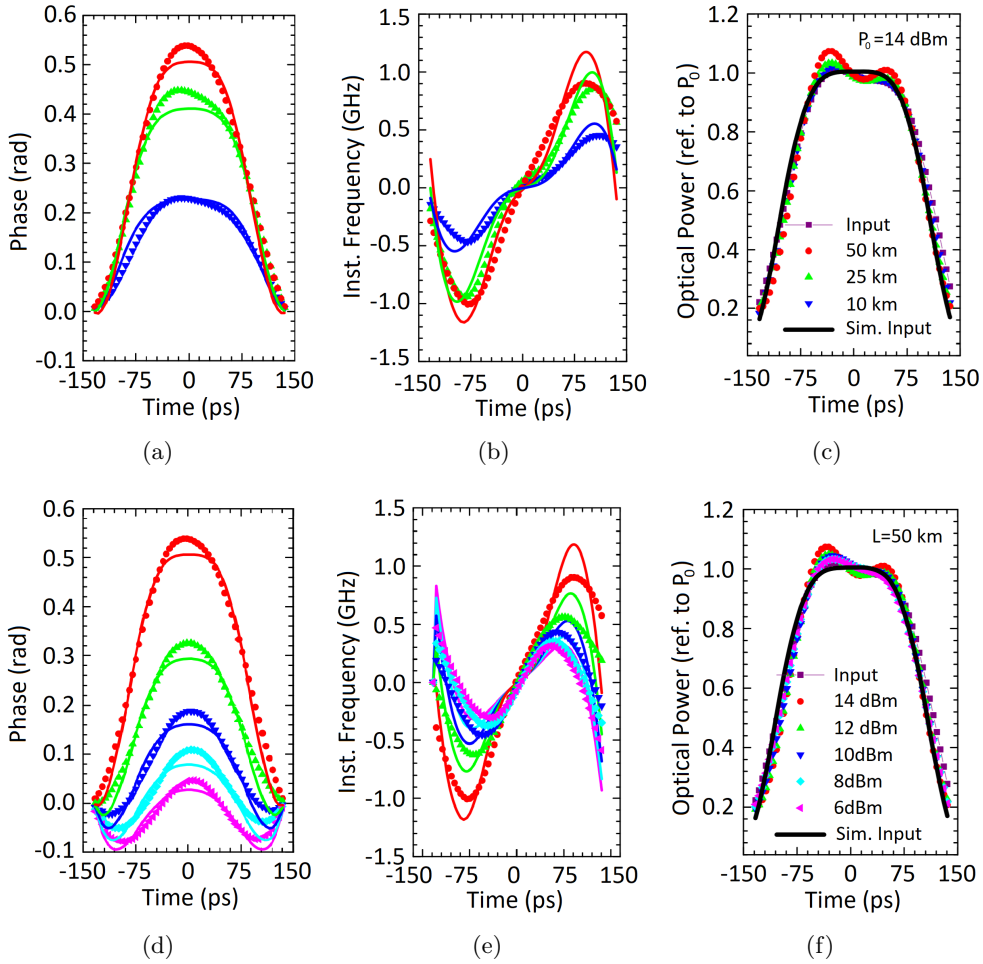

Figure 4.18: Measured (dotted lines) $\phi(t)$, $f_{\text{inst}}(t)$, and $P(t)$ for a ~220 ps FWHM pulse with $P_0 = 14$ dBm after propagation over 10, 25, and 50 km (a)–(c), and after propagation over 50 km with $P_0 = (6 - 14)$ dBm (d)–(f). Theoretical simulations (solid lines) are plotted for comparison [117].

chosen to study the limiting situation where the impact of SPM and GVD were both relevant and demonstrate the PROUD flexibility in characterizing the propagation-induced distortions in such a scenario.

4.4.3 Possibility of implementing PROUD in ϕOTDR sensors (Discussion)

As it was studied in Chapter 3 (Subsection 3.4.2), the phase information in the ϕOTDR signal will give quantitative information of an induced refractive index change, allowing for the linear measurement of strain, temperature and vibrations. Coherent detection is an extensively used technique for this purpose. However, it presents some limitations that implies an increase in the price and the complexity of the system.

In the previous subsection, the capability of PROUD for the measurement of phase profiles of optical pulses has been demonstrated. The lowest bandwidth of the characterized pulses was 4 GHz, similar to the employed in ϕOTDR when coding techniques are implemented [92]. Thus, the performed experiments helped us to understand better the advantages and disadvantages of the PROUD technique, which allows to develop a correct analysis of its applicability in ϕOTDR

technology [143].

Coherent detection requires to beat the LO with the signal to be measured (the ϕOTDR backscattered trace), in which this case the phase-noise of the local oscillator will be added as noise to the measurement [115]. Thus, the phase-noise is accumulated and increases with the fiber length. For this reason, the required laser in the system must present low phase-noise (low linewidth). In other words, the required laser coherence length for coherent detection schemes is considerably high (twice the fiber size). As an example, the required linewidth for sensing 100 km of SMF is $\Delta f \approx 320$ Hz (see Equations 2.52 and 2.53). This linewidth requirement increase considerably the final cost of the system. This limitation is eliminated when PROUD is implemented, since this technique is self-referenced, i.e., a LO is not required. Whereas the phase-noise is increased with the fiber length in conventional coherent detection setups, the noise when PROUD is implemented remains uniform along the fiber.

The amplitude of the interference between the LO and the backscattered signal strongly depends on their relative state of polarization and can even reach zero for the case of orthogonal polarizations. Since the light polarization in continuously rotating due to the intrinsic birefringence of the fiber [40], coherent detection is therefore generally dependent on changes of the State Of Polarization (SOP) along the optical paths of both signals (LO and backscattered) [58]. This limitation can be solved using Polarization-Maintaining Fibers (PMFs) or using dual-polarization coherent receivers [115], which also increases the complexity/cost and can decrease the system performance. Using PROUD techniques this problem would be eliminated.

The conventional signals employed in a traditional ϕOTDR present bandwidths around 100's of MHz and the laboratory does not have a filter that fits with these signal characteristics. Due to this practical limitation, it was not possible to experimentally demonstrate the full potential of PROUD in ϕOTDR. However, this practical limitation does not invalidate the applicability of the technique, as these type of filters do exist and are readily commercially available on the market. PROUD has been demonstrated using a integrated-waveguide Mach–Zehnder interferometer for characterizing GHz-rate signals [164]. The ideal solution could come from integrated photonics. The fabrication of an optical filter with this characteristics is not more difficult than fabricate the optical hybrid required in homodyne detection. On a more readily available solution, DWDM centered shifted by 1/2 channel from the laser could provide a very stable filter. Recently a programmable photonic processor, inspired by electronic Field Programmable Gate Arrays (FPGA), can implement functionalities with a simple seven hexagonal cell structure [165]. Theoretically, a filter as the required in PROUD could be implemented using this technology.

The algorithm for obtaining the instantaneous frequency implies to divide the differential signal $|y(t)|^2$ by the signal intensity $|x(t)|^2$ (see Equation 4.13), which typically presents zeros. In those points the obtained instantaneous frequency is indeterminate. This is the most important limitation of PROUD technique. However, this also happens in homodyne detection, which requires divide the extracted signals from the hybrid (I and Q) and implement an arc tangent function.

4.5 Conclusions

In this chapter, three techniques for addressing the limits of range, resolution and linearity of ϕOTDR-based sensors are proposed.

Firstly, the impact of the use of probe pulses with different beam shapes on the backscattered power trace of ϕOTDR systems have been analyzed. The obtained results indicate that the typically used rectangular-like pulses are the most detrimental for the length range and sensitivity

of ϕOTDR-based sensors, while the use of Gaussian or triangular-like pulses contributes to a smoother reduction of the trace's visibility along the sensing fiber length. A Gaussian or triangular envelope pulse limits the effect of MI and mitigates the advent of the FPU recurrence, which enables an increase of the length range and sensitivity of the sensing system for the same peak power and nominal spatial resolution. The experimental validation of our analysis suggests that under comparable conditions (same peak power and same nominal spatial resolution), the length range of the sensor can be duplicated by using a Gaussian-envelope pulse instead of a rectangular one.

Secondly, we have proposed a novel technique to increase the SNR of high-resolution ϕOTDR systems using concepts borrowed from CPA. The input pulses are temporally stretched by a suitable dispersive device, and the backscattered traces are re-compressed in the optical domain prior to detection. This allows us to substantially increase the probe pulse energy, while avoiding non-linear interaction within the fiber under test, resulting in an increased SNR without compromising the spatial resolution of the sensor. This configuration allows for high resolution measurements without the need for coherent detection or signal post-processing (as required for instance in OPCR). By compressing in the optical domain with a polarization-insensitive element, we avoid the need for phase detection (which is typically polarization dependent). Thus, our method should exhibit very low polarization dependence. The reported experiment demonstrated an SNR increase of 20 dB over the traditional ϕOTDR architecture in a system with 3 mm spatial resolution. Using this new approach that achieves millimetrical resolutions, wall or pipeline crack development monitoring will be possible. A new ϕOTDR technique based also on the use of chirped pulses will be presented in the following chapter. The technique allows to solve the the non-linear limitation of traditional ϕOTDR without the requirement of a frequency scan or coherent detection. Distributed sensing of strain and temperature, with resolutions of $0.5\text{mK}/4\text{n}\varepsilon$ and real acoustic sensing has been achieved with the proposed technique.

Finally, a methodology to obtain a linear response of a ϕOTDR is proposed. Traditional coherent detection schemes requires mixing a LO with the optical signal before photodetection. It implies a relative state of polarization dependence between the LO and the backscattered field. The second main limitation is related with the phase-noise of the optical source, since the required laser linewidth is very narrow. Solving these limitations will increase considerably the cost and complexity of the system. Here we have proposed to use the self-refereed technique named PROUD. Since no LO is required, all the mentioned limitations of traditional coherent detection do not exist. The applicability of this technique to ϕOTDR is demonstrated by characterizing propagation-induced distortions in pulses in bandwidth regimes similar to those typically used in ϕOTDR. The bandwidth of the employed optical pulses was around 4 GHz, which fits with the employed commonly when coding is implemented in ϕOTDR. The advantages and disadvantages of the technique are also analyzed.

Chapter 5

Chirped-Pulse Phase-Sensitive Optical Time Domain Reflectometry

5.1 Introduction

As it was explained in Chapter 3, traditional Phase-Sensitive Optical Time Domain Reflectometry (ϕOTDR) without phase recovery, allows for distributed vibration measurements with a high bandwidth. However, these measurements are based on intensity variations of the ϕOTDR signal which does not show a linear variation with the applied perturbation. Solutions addressing this limitation have been proposed in the state of the art. On the one hand, by precisely sweeping the frequency of the pulses step by step, ϕOTDR has been shown to allow for very sensitive static measurements of refractive index variations, which can be used for very high resolution temperature [36], strain [37] and birefringence [38, 39] measurements. For instance, the demonstrated temperature resolutions of 0.01 ^{o}C [36] are two orders of magnitude below the typical resolutions of $\sim$1 ^{o}C provided by Brillouin sensors. However, due to the requirements of a frequency scan, in this case the measurement time and complexity of the system is increased. On the other hand, by recovering the phase of the ϕOTDR signal, the dynamic measurement of strain has been demonstrated [31–33]. In this case however, the system is more complex and laser coherences of at least the fiber length are required in order to avoid noise when beating the signal with the local oscillator. The long term-stability of such systems (i.e. after several minutes or hours) and therefore feasibility for static temperature measurements over several hours has also not been clearly addressed either.

In this chapter, we provide a method based on ϕOTDR using linearly chirped pulses to allow for the measurement of distributed strain and temperature changes, in a single shot without the requirement of a frequency scan. The technique was named Chirped-Pulse Phase-Sensitive Optical Time Domain Reflectomery (Chirped-Pulse ϕOTDR) [166]. The complexity of the system is not significantly increased when compared to traditional ϕOTDR systems using intensity-based detection. With the proposed method, it is possible to combine the best features of ϕOTDR which had been previously demonstrated by separate: on the one hand, fast measurements with a bandwidth only limited by the fiber length, potentially over several tens of kilometers with metric spatial resolutions; on the other hand, the linear measurement of temperature/strain variations with resolutions which can be several orders of magnitude below those provided by Brillouin. Since the measurement is relative, the range of temperature/strain measurements is in principle not limited, being in practice determined by how the cumulative errors of the measurement are handled. The technique allows for measurements at kHz rates, while maintaining reliability over several hours of measurement. The sensitivity can also be tuned by acting on the chirp of the pulses. Temperature/strain resolutions of 0.5mK/4nε are demonstrated.

5.2 Chirped-Pulse ϕOTDR Principle

As it was presented in Chapter 3, a ϕOTDR is a distributed sensing technique which makes use of the Rayleigh scattering effect and allows for the measurement of perturbations along an optical fiber. In this method, highly coherent optical pulses are injected into an optical fiber. The Rayleigh backscattered light is monitored in the time domain, which is then associated with fiber position using the time of flight of the light pulses in the fiber. As coherent pulses are used, the ϕOTDR signal will be the result of the coherent interference between the fields which are Rayleigh backscattered from the multiple fiber scattering centers [145]. Ideally, the phase-noise existent in the pulses should be kept to a minimum, as it will increase the noise of the ϕOTDR signal. With this in mind, the phase of the optical pulses used in ϕOTDR systems has never been really engineered, as it has always been a priority to keep this phase as flat and constant as possible. The idea in this chapter is that a deterministic (but non-flat) phase profile in the

pulses may be used to render the ϕOTDR implementation more linear and sensitive.

The ϕOTDR signal depends on the multiple (random) contributions given by the scattering centers (see Subsection 3.3.1), but also on the intensity and phase profiles of the pulses. Typically, the resulting detected intensity will present a random noise-like shaped pattern. This pattern will remain constant and reproducible if the fiber and measuring conditions do not change over time. Perturbations in the fiber can be detected by monitoring local changes in the ϕOTDR signal with a bandwidth of detection which is only limited by the fiber length [34]. However, it is often hard to precisely quantify the amplitude of the perturbations, as the intensity variations of the ϕOTDR signal do not show a linear correlation with the amplitude of the applied perturbations (see Section 3.4). Conventional ϕOTDR systems using a single pulse frequency are therefore best suited to detect the frequency of a dynamic perturbation rather than its amplitude, and are most commonly used for vibration/intrusion detection [21, 23, 24, 26, 27, 34].

While the intensity variations of the ϕOTDR signal cannot be predicted for a given perturbation, the changes in optical path difference between the scattering centers induced by a uniform refractive index change Δn can be compensated by a shift of the pulse frequency $\Delta\nu$, which allows the recovery of the original ϕOTDR pattern (see Subsection 3.4.3). Assuming small refractive index changes ($\Delta n \ll n$), the $\Delta\nu$ necessary to compensate a given Δn was shown in Equation 3.21. Based on this principle, ϕOTDR systems have been demonstrated to allow for quantitative measurements of temperature/strain [36] and birefringence [38, 39] with high measurand resolutions. However, as it was explained before, a frequency sweep of the pulse is required, which greatly increases the measurement time, typically up to a few seconds or a few minutes. The system turns out then to present similar trade-offs to traditional Brillouin temperature sensors, having a temperature resolution and range which is dependent on the used frequency scan step and range. High measurand resolutions over long ranges can therefore be highly time consuming. The maximum achievable resolution is also limited by the pulse spectral content [38], in a somewhat similar manner to the temperature resolution limitation imposed by the spectral width of the Brillouin gain curve in Brillouin sensors.

5.2.1 Theoretical Model

The method proposed for temperature/strain variation measurements originates from the principle described in Equation 3.21 that a refractive index change Δn in the fiber can be compensated (in terms of the shape of the trace) by a frequency shift $\Delta\nu$ of the pulse sent into the fiber. This is the same principle as used in [36, 38, 39], and is typically implemented by performing a laser frequency sweep. In our case, instead of requiring a time-consuming frequency sweep to determine $\Delta\nu$ and calculate Δn, a single pulse which has linear chirp is used. Since different positions of the pulse have different frequencies, when a Δn is applied, the same trace pattern at a given position can be generated by a temporally-shifted region of the pulse, leading essentially to a longitudinal shift Δz of the local ϕOTDR trace. It is then possible to calculate $\Delta\nu$ (and consecuently Δn and the temperature/strain shift) from Δz, which is obtained directly from the time-domain trace measurements. Thus, in our method, a single trace measurement should be sufficient to determine temperature/strain changes. The theoretical description of the proposed method is presented in detail in this section.

Although it is a general concern in conventional ϕOTDR systems to have flat-phase profiles, it should be clear that the optical pulses used in a ϕOTDR can in principle have any arbitrary phase profile, and therefore any arbitrary spectral content. What is important to avoid additional noise in the trace is that the phase profile does not change from pulse to pulse (i.e. that the master laser has a low phase-noise). Therefore, except for the fact that the detection band-

width should be higher in the case of chirped pulses, no extra noise source should be expected in our implementation over the traditional one, and therefore similar spatial resolutions and sensing ranges should be achievable in both methods. An evaluation of the propagation-induced distortions may be required when operating with pulses with large spectral contents and long fiber distances, mainly due to dispersion. However, using a few tens of kilometers and pulses with spectral contents of up to ∼1 GHz, this effect is negligible for ϕOTDR operation, as it is demonstrated in Chapter 7.

To describe the proposed ϕOTDR sensor, we start by describing a pulse $P(t,z)$, with a rectangular intensity profile of amplitude E_0, width τ_p and an instantaneous frequency profile $\nu(t) = \nu_0 + \delta\nu/2 - \delta\nu \cdot (t/\tau_p)$. $P(t,z)$ is therefore a linearly chirped pulse with a spectral content $\delta\nu$, around a central frequency ν_0, and frequency slope $\delta\nu/\tau_p$. The propagation of $P(t,z)$ along an optical fiber is described by:

$$P(t,z) = E_0 \cdot rect\left[\frac{(t - \int_0^z n(z)\mathrm{dz}/c)}{\tau_p}\right] \cdot e^{-2\pi i\left(\nu_0+\delta\nu/2-\delta\nu/(2\tau_p)\cdot\left[t-\int_0^z n(z)\mathrm{dz}/c\right]\right)\left(t-\int_0^z n(z)\mathrm{dz}/c\right)} \quad (5.1)$$

Note that the phase of the pulse is calculated using $\phi = -\int 2\pi\nu \mathrm{dt}$. In Equation 5.1, t is the time and z the position along the fiber, $z = 0$ being the fiber entrance where the pulses are lauched and $t = 0$ the moment when the front part of the pulse enters the fiber in $z = 0$. $rect(x) = 1$ when $0 \leq x \leq 1$ and zero elsewhere, c is the speed of light in the vacuum and $n(z)$ is the local refractive index of the fiber at the pulse central frequency ν_0. The spectral content $\delta\nu$ is assumed to be small in comparison to the center frequency and ν_0 to be away from resonant frequencies of the fiber, so that the dependency of n in the optical frequency (i.e., dispersion) is negligible. In any case, this dependency can be introduced if a more precise theoretical model is required.

As the pulse $P(t,z)$ propagates along the fiber, at each instant t each infinitesimal part of P will generate a counter-propagating wave via Rayleigh backscattering. The backscattered signal is therefore continuously generated, and different parts of backscattered signals generated at different instants will overlap to produce the ϕOTDR signal $E(t)$, received at $z = 0$, at a given time t.

The reflection of $P(t,z)$ in each location of the fiber z is described by the fiber's Rayleigh backscattering profile function $r(z)$. $E(t)$ will be given by the convolution of $P(t,z)$ and $r(z)$, for the fiber section $z[(t-\tau_p)\cdot c/(2n), t\cdot c/(2n)]$:

$$E(t) = \int_{z=tc/(2n)-\tau_p c/(2n)}^{tc/(2n)} r(z) \cdot E_0 e^{-2\pi i\left(\nu_0+\delta\nu/2-\delta\nu/(2\tau_p)\cdot\left[t-2\int_0^z n(z)\mathrm{dz}/c\right]\right)\left(t-2\int_0^z n(z)\mathrm{dz}/c\right)} dz \quad (5.2)$$

Note that while the signal $E(t)$ is generated from the interference of reflections occurring in a fiber section with 1/2 of the pulse width, it accounts for the passage of the entire pulse $P(t,z)$. This characteristic is the basis for the well known fact that the spatial resolution for OTDR systems is determined by 1/2 of the pulse width.

Figure 5.1 depicts the reflections of the pulse $P(t,z)$ as it propagates along the fiber which will generate $E(t)$. The contribution to $E(t)$ will be given by a convolution of P with the fiber sections $z\epsilon[z_1,z_2],[z_2,z_3]$, which reflect the instantaneous frequencies $\nu\epsilon[\nu_4,\nu_3]$,$[\nu_3,\nu_1]$, respectively, as shown in Figure 5.1(a). The contribution to $E(t+\Delta t)$ will be given by a convolution of P with the fiber sections $z\epsilon[z_2,z_3]$,$[z_3,z_4]$ which reflect the instantaneous frequencies $\nu\epsilon[\nu_4,\nu_2]$,$[\nu_2,\nu_1]$,

respectively, as shown in Figure 5.1(b). For a small enough Δt, so that $[z_1, z_2]$,$[z_3, z_4] \ll [z_2, z_3]$, then the contributions to $E(t)$ and $E(t + \Delta t)$ generated from reflections in $[z_1, z_2]$,$[z_3, z_4]$ are essentially negligible. In this case, $E(t)$ and $E(t + \Delta t)$ can be thought of as generated from reflections of the same fiber section $[z_2, z_3]$, by pulses with frequencies $\nu\epsilon[\nu_3, \nu_1]$ and $\nu\epsilon[\nu_4, \nu_2] = [\nu_3, \nu_1] + \Delta\nu$, respectively, i.e., two pulses with a frequency shift $\Delta\nu$ between them.

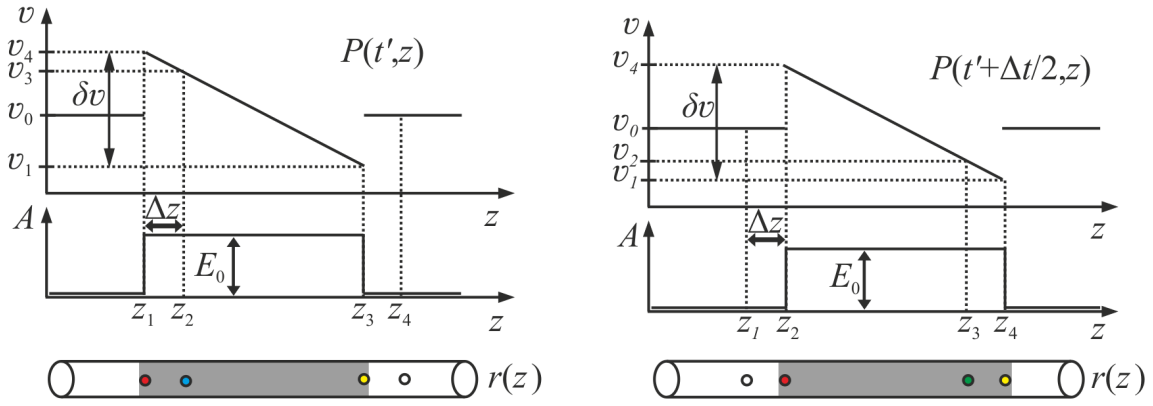

(a) $E(t)$ (b) $E(t + \Delta t)$

Figure 5.1: Reflection of the chirped pulse $P(t, z)$ as it propagates along the fiber.

In this case, if n remains constant along $[z_2, z_3]$, then $E(t) \neq E(t + \Delta t)$. However, if a homogeneous Δn occurs, so that the equality of Equation (3.21) is verified, then the Δn is compensated by the frequency shift $\Delta\nu$ and therefore $E(t) = E(t+\Delta t)$. This can be mathematically directly derived from Equation (5.2), assuming that the contributions to the integral from $[z_1, z_2]$ (to $E(t)$) and $[z_3, z_4]$ (to $E(t+\Delta t)$) are negligible. In practice, this relation holds if Δn is small enough, as discussed at the end of this section. The relation between these quantities can be derived by analyzing the phase difference $\phi_{i,j}$ between the backscattered waves reflected from the fiber locations z_i and z_j, similarly to what is derived in [36]:

$$\phi_{i,j} = -2\pi \cdot \frac{2n(z_i - z_j)}{c} \cdot \left(\nu_0 + \frac{\delta\nu}{2} - \frac{\delta\nu}{\tau_p} \cdot \left[2t - \frac{2n(z_i + z_j)}{c} \right] \right) \tag{5.3}$$

From Equation 5.3 it follows that a small variation Δn can be compensated by a longitudinal shift of the trace Δt (after neglecting terms of small amplitude). The relationship between Δn and Δt is given by:

$$\left(\frac{\Delta n}{n} \right) = - \left(\frac{1}{\nu_0} \right) \cdot \left(\frac{\delta\nu}{\tau_p} \right) \cdot \Delta t \tag{5.4}$$

A similar derivation can be done for strain changes, which in addition lead to a change in the relative positions of z_i,z_j. The measuring principle of the proposed Chirped-Pulse ϕOTDR sensor derives from this result. If a Δn occurs at a certain location of the fiber z, then the local ϕOTDR pattern $E(t)$ will be longitudinally shifted by a Δt at that location, corresponding to the $\Delta\nu$ which compensates for the Δn. Note that local Δt changes among two different traces can be determined along the fiber by calculating a local correlation of the trace segments obtained for the two consecutive measurements. As the reader can observe, the technique presents some

similarities to OFDR sensing [11, 13, 15, 16, 18]. In OFDR the probe signal is a CW whose wavelength is linearly swept and the backscattered signal is detected in the frequency domain. While in Chirped-Pulse ϕOTDR the trace pattern suffer a temporal shift when a section suffers a refractive index change, in OFDR it is the spectrum that suffers the shift. Thus, also by means of cross-correlations, it is possible to detect and measure refractive index changes in a OFDR from the frequency shift.

The measurement of Δn along the fiber then allows for distributed temperature measurements ΔT. A similar derivation can be performed for applied strains $\Delta\varepsilon$, (which are translated into shifts of the scattering positions of the fiber Δz). If a $\Delta\varepsilon$ occurs then $E(t)$ will be longitudinally shifted by a Δt, which will be added to existing Δt caused by ΔT (if existant). The relation between Δt and the quantities ΔT and $\Delta\varepsilon$ is given by [2, 36]:

$$-\left(\frac{1}{\nu_0}\right)\cdot\left(\frac{\delta\nu}{\tau_p}\right)\cdot\Delta t \approx \frac{\Delta\nu}{\nu_0} \approx -0.78\cdot\Delta\varepsilon \tag{5.5}$$

$$-\left(\frac{1}{\nu_0}\right)\cdot\left(\frac{\delta\nu}{\tau_p}\right)\cdot\Delta t \approx \frac{\Delta\nu}{\nu_0} \approx -\left(6.92\cdot 10^{-6}\right)\cdot\Delta T \tag{5.6}$$

In this case, the measurement is essentially continuous, and the minimum detectable Δn is determined by the chirp ($\delta\nu/\tau_p$) and the sampling (and bandwidth) with which $E(t)$ is detected. For large Δn, the contributions of $[z_1, z_2], [z_3, z_4]$ may become relevant and introduce significant deformations to the ϕOTDR trace, thus limiting the validity of the approach. Experimental results indicate that to ensure correct measurements, the maximum measurable Δn should correspond to a frequency change $\Delta\nu$ (Equation 5.4) so that $\Delta\nu/\delta\nu \approx 2-3\%$. This imposes a maximum measurable Δt which should correspond to $2-3\%$ of the pulse length (τ_p). However, under low noise conditions and depending on the local trace conditioning, measurable frequency changes of as much as 50% have been observed. Since the measurements can be made quite fast (there is no requirement for a frequency sweep and single-shot acquisitions are perfectly feasible) the expectable changes from trace to trace should be quite small. Measurements of large Δn variations (which typically should take long times to develop) can be also be done, in this case accumulating the measured delay values (Δt) between consecutive traces. In this way, values of Δn which are corresponding to a $\Delta\nu$ arbitrarily larger than $\delta\nu$ can be detected, as long as the errors accumulated between the consecutive measurements are kept small. This allows for fast measurements of temperature or strain, with high resolution and over long ranges, as will be demonstrated in this chapter.

5.2.2 Measuring Technique: Temporal Correlations

While traditional ϕOTDR measure intensity variations of all the points of the trace over time, the proposed Chirped-Pulse ϕOTDR sensor analyses the longitudinal ϕOTDR trace shifts that occur along the fiber. We denote this profile of local trace shift variations as $\Lambda(t)$, which is related to the temperature or strain gradients suffered by the fiber, as discussed in the previous section. The fiber is measured at two different (consecutive) times t_1 and t_2, by sending two (equal) pulses P_1 and P_2 into the fiber, from which result two traces $E_1(t)$ and $E_2(t)$. Note that the ϕOTDR pattern $E(t)$ is associated with a fiber position z, by $t = 2nz/c$. The $\Lambda(t)$ occurred between the $E_1(t)$ and $E_2(t)$ is calculated using a moving window of cross-correlation along $E_1(t)$ and $E_2(t)$, defined by a certain correlation time τ_{corr}:

$$\Lambda(t) = \max\Big(\text{correlation}\Big[E_1\left(t-\tau_{corr}, t+\tau_{corr}\right), E_2\left(t-\tau_{corr}, t+\tau_{corr}\right)\Big]\Big) \tag{5.7}$$

Here τ_{corr} should be of the order of τ_p, and will set the spatial resolution. The temperature/strain variations which occurred in the fiber between t_1 and t_2, can then be calculated using Equations 5.4-5.7. A continuous measurement of temperature/strain along time is possible by simply integrating the successive measurements obtained for $[E_1(t), E_2(t)]$, $[E_2(t), E_3(t)]$, ... , $[E_{n-1}(t), E_n(t)]$.

However, a simple analysis will show that this is not the best way to minimize the cumulative errors of a measurement. For very small values of index change, close to the resolution of the sensor (set by the chirp and the sampling of $E(t)$), the error will increase due to quantization error. For large values of index change, the error will increase because the contributions for $E(t)$ generated from $[z_1, z_2], [z_3, z_4]$ (see Figure 5.1) are no longer negligible. Therefore, for a certain measurement setup, there will be a certain range of index change values for which the measurement error is minimum. An efficient way of minimizing the error in case of small variations is then to use the measurement of consecutive traces as a first estimate and then compare pairs of $[E_i(t), E_j(t)]$ that are more spaced in time, and for which the calculated temperature/strain variations are close to the shifts where the error is known to be minimum. Other algorithms taking into account multiple comparisons of traces to reduce the measurement error can be thought of.

5.3 Distributed Sensing of Temperature, Strain and Vibrations

5.3.1 Experimental Setup

The experimental setup used to measure temperature/strain changes with the new proposed technique is depicted in Figure 5.2. It is based on a traditional ϕOTDR scheme [34] but introducing a linear chirp in the pulse through the current control of the laser.

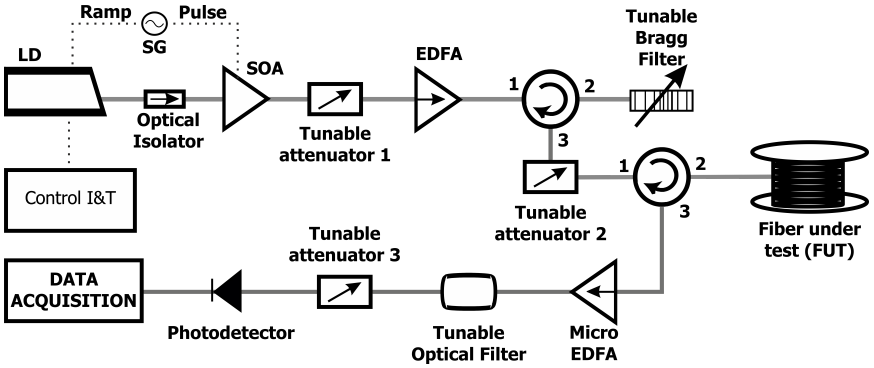

Figure 5.2: Experimental setup of Chirped-Pulse ϕOTDR [134, 167–172]. LD, Laser Diode; SG, Signal Generator; EDFA, Erbium Doped Fiber Amplifier; I&T, Intensity and Temperature.

The light source is a Laser Diode (LD) with a linewidth of 1.6 MHz emitting at 1546.66 nm and working in continuous emission. The LD is driven by a standard current and temperature controller to select the laser central wavelength. A secondary current control applies a repetitive electric ramp signal in the laser driver, which introduced a linear chirp at certain times in the outputted laser light. This light is then gated in the time domain by a Semiconductor Optical

Amplifier (SOA), whose driver is synchronized with the secondary laser current control, thus generating linearly chirped pulses. The SOA has rise/fall times in the order of 2.5 ns, and is driven by a waveform Signal Generator (SG), to create 100 ns square pulses, which implies a spatial resolution of 10 m in this case. An optical isolator is used between the LD and the SOA to avoid laser instabilities due to reflections in the following devices. Three different chirp slopes are on the optical pulses, resulting in total pulse spectral contents ranging from 0.8 GHz to 2.3 GHz. To avoid errors, they are characterized experimentally by means of Phase Reconstruction using Optical Ultrafast Differentiation (PROUD), a self-referenced technique which allows recovering the instantaneous frequency and phase of arbitrary optical signals (previously presented in Subsection 4.4.2). Particularly, Balanced PROUD has been used in this experiment, which allows obtaining in real-time the instantaneous frequency profile of a pulse [117–119]. The setup for this characterization is exactly the same presented in Figure 4.14 in Chapter 4 (Subsection 4.4.2.1) [117]. The three chirp slopes induced in the optical pulses are presented in Figure 5.3, having the following spectral contents: $\text{Chirp}_1 = 0.81 \pm 0.02$ GHz (black), $\text{Chirp}_2 = 1.62 \pm 0.04$ GHz (red) and $\text{Chirp}_3 = 2.32 \pm 0.05$ GHz (green). The main source of uncertainty in these values is the slope of the optical filter used to derivate the signal [117] which could be at least 1%. The chirp profile of the pulses showed a good linearity, and should therefore introduce small errors in the temperature/strain measurements.

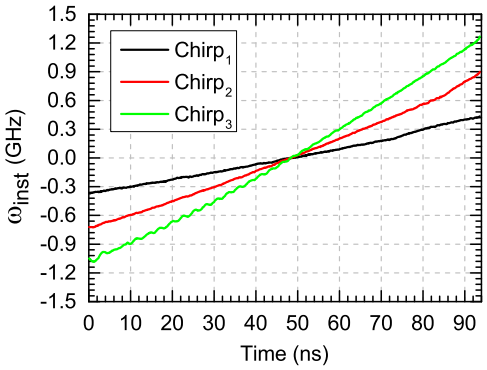

Figure 5.3: Instantaneous frequency profile of the three different chirps induced in 100 ns optical pulses [167].

An Erbium-Doped Fiber Amplifier (EDFA) is used to amplify the pulse peak power to achieve longer sensing distances. Between the SOA and the EDFA, a variable optical attenuator is introduced to control the EDFA input power and to avoid possible non-linearities generated in it. Note that if no non-linearities occur in the EDFA, this attenuator (attenuator 1) is not required in the setup, since the power of the optical pulse injected into the fiber can be tuned using only attenuator 2. In order to filter the Amplified Spontaneous Emission (ASE) added by the EDFA, a tunable Fiber Bragg Grating (FBG) working in reflection is inserted. The FBG spectral width is 0.8 nm.

Before injecting the optical pulse in the Fiber Under Test (FUT), another tunable attenuator controls the input power to avoid non-linearities in the fiber, mainly due to Modulation Instability (MI) [106]. The backscattered signal is amplified with another EDFA and filtered with a 0.5 nm spectral width optical filter. Finally, the light is detected in a p-i-n photo-detector with a bandwidth of 13 GHz and a high-speed digitizer with 40 GHz sampling rate. Furthermore, to avoid damaging the p-i-n photodetector, another tunable attenuator controls its input power. Note that, in comparison with traditional ϕOTDR systems, here the detection bandwidth and digitizing speed need to be much higher, as they should cover the total bandwidth of the chirp

signal used.

The FUT used in the experiment has a length of 1 km. All the FUT is immersed in a water bath, to maintain the fiber temperature stable. For the temperature measurements, the last 20 m of the FUT were placed inside an oven which allowed to control the temperature. The temperature inside the oven is registered with a thermometer with a resolution of 0.1 °C, for a later comparison with the fiber measurements. Later, for the strain measurements, the last 20 m of the FUT were strapped around a Piezoelectric Transducer (PZT) which allowed the controlled application of deformations.

5.3.2 Temperature Sensing

To illustrate the principle of the measurement, Figure 5.4 presents the evolution of the trace at given positions when the FUT experiments a local temperature change. The figure was obtained with the Chirp_3 frequency profile, showing a total spectral content of 2.32 GHz. For this demonstration, heat is applied in the last 20 m of the 1 km FUT, while the remaining FUT is keep at the same temperature. Traces are acquired with a frequency of 1 Hz, without averaging. As expected, the trace remains the same outside the heated point, but starts to shift longitudinally in the the last 20 m. In Figure 5.4(a) (non-heated region) it can be observed that the three consecutive traces remain constant over the time. In contrast, in Figure 5.4(b) (heated region) it is possible to observe a longitudinal shift of the trace. The traces are separated by around 17 samples each with 40 GHz sampling rate, i.e., 425 ps. This corresponds to an approximate variation of $\sim 8 \cdot 10^{-3}$ °C in temperature from trace to trace (in agreement with the expectation), which gives us an idea of the potential of this system for high resolution measurements.

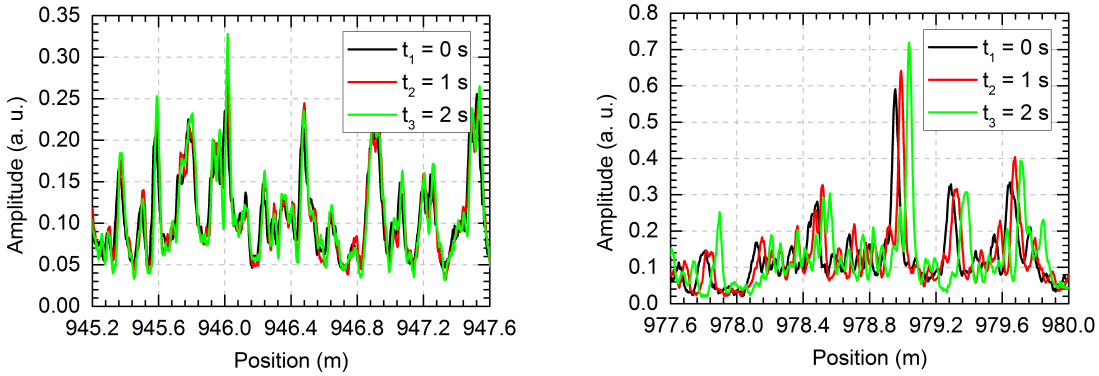

(a) Non-heated region

(b) Heated region

Figure 5.4: Longitudinal shift of the ϕOTDR trace when temperature changes are applied to the FUT [167].

As it was demonstrated in Equation 5.4, the longitudinal shift for a given refractive index change ($\Delta n/\Delta t$) depends on the chirp slope ($\delta\nu/\tau_p$) used. To experimentally demonstrate this principle, a controlled temperature variation of 5 °C is applied on the same point employing the three different chirp slopes. The results are shown in Figure 5.5. For the same temperature changes, the observed longitudinal shifts are inversely proportional to the chirp slope, as expected. This principle allows for the sensitivity of the sensor to be tuned by acting on the chirp of the interrogating pulses. Using Equations 5.4 and 5.6, the total temperature change is calculated for each chirp: $\Delta T_{\text{Chirp}_1} = 4.957$ °C, $\Delta T_{\text{Chirp}_2} = 5.005$ °C, $\Delta T_{\text{Chirp}_3} = 5.116$ °C.

These are therefore in agreement with the temperature change of 5 ± 0.1 °C recorded by a manual thermometer with 0.1 °C resolution. Note that the temperature variations correspond to a frequency shift of ~ 6.7 GHz (Equation 5.6), which exceeds the pulse spectral content in all three cases.

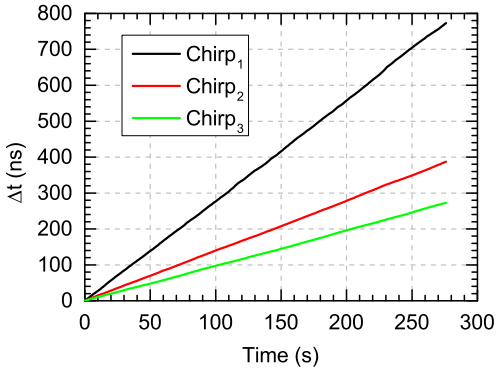

Figure 5.5: Longitudinal trace shifts corresponding to a linear temperature variation of 5 °C applied over 280 s for the three different pulse chirp slopes shown in Figure 5.3 of meter 979.

To evaluate the long term stability of the sensor, the last 20 m of the FUT are heated from 23 °C to 27.5 °C and cooled to the starting temperature, over approximately 270 minutes, while the entire FUT is monitored. Figure 5.6(a) shows the temperature evolution of the meter 979 of the FUT (the center of the heated section). The black line represents the fiber temperature measured with the ϕOTDR, while the green dots are the thermometer measurements (green lines represent the measurement error of the thermometer). As it is observed, the fiber follows perfectly the temperature variations with a negligible accumulated error. Finally, Figure 5.6(b) shows the temperature profile along 70 m of fiber around the heated section at different times. The heated section is perfectly detected by the system which has enough spatial resolution (10 m) to observe a heated section of 20 m. As expected, in the regions outside the heated section (which are kept at constant temperature), the ϕOTDR sensor recorded a constant temperature with no variations over time.

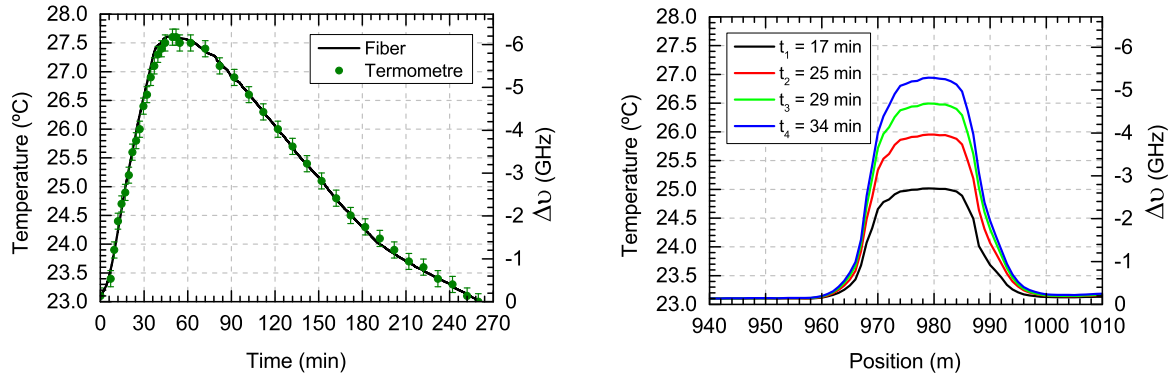

(a) (b)

Figure 5.6: Measured temperature variations when temperature is rised from 23 °C to 27.5 °C and back to 23 °C in 20 m of fiber around meter 979 of the FUT, over 270 minutes. (a) Temperature evolution of meter 979 along time; (b) Temperature profile along 70 m of fiber at different times [167].

5.3.3 Strain Sensing

After the temperature measurements, the feasibility of the proposed sensor for dynamic and static strain measurements is analyzed. As in the previous section, 100 ns optical pulses with a spectral content of $\text{Chirp}_3 = 2.32$ GHz are used to realize the measurements.

Firstly, the stability of the sensor over several minutes for large applied strains is analyzed. For this, deformations are applied by manually acting on a linear translation stage to which a fiber section near the end of the FUT is glued. The ϕOTDR traces are acquired with a frequency of 2 kHz and the total measured strain is calculated by integrating the strain variations measured from trace to trace. Figure 5.7 presents the strain variations measured by the ϕOTDR when deformations corresponding to strains varying from 0 $\mu\varepsilon$ to $\pm$300 $\mu\varepsilon$ and back to 0 $\mu\varepsilon$ are applied. Note that the total frequency shift corresponding to 300 $\mu\varepsilon$ is $\sim$ 45.4 GHz (Equation 5.5), and that the total integrated strain variation applied is 1200 $\mu\varepsilon$ ($\sim$ 181.4 GHz), which largely exceeds the pulse spectral content (2.32 GHz). However, the calculated strain is observed to return to zero when the applied strain is returned to zero after 160 s. This again clearly demonstrates the long term stability of the sensor and that large measurement ranges (which largely exceed the equivalent to the pulse spectral content) are achievable.

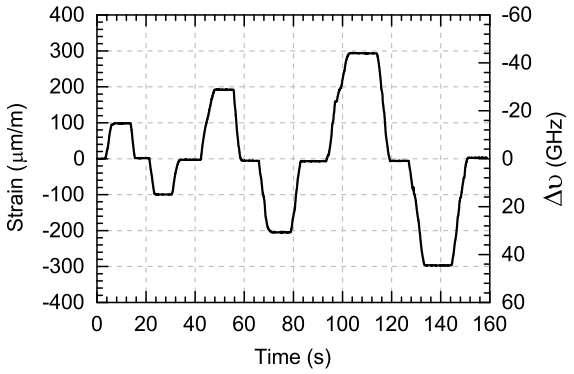

Figure 5.7: Measured strain variations when strain applied to the fiber is manually varied (using a linear translation stage) from 0 $\mu\varepsilon$ to $\pm$300 $\mu\varepsilon$ and back to 0 $\mu\varepsilon$, near the end of the FUT, over 160 seconds [167].

5.3.4 Vibration (Dynamic Strain) Sensing

In order to characterize the dynamic strain sensing capability of the sensor, the last 20 m of the FUT are strapped around a PZT, which applied deformations controlled by an electrical input. The ϕOTDR traces are now acquired with a frequency of 4 kHz.

The dynamic strain measurements are presented in Figure 5.8. Figure 5.8(a) presents the measured strain when a 1 Hz sinusoidal strain is applied to the fiber by the PZT, with a maximum amplitude of 100 nε. As it is clearly observed, a good agreement between the experimental measure and the applied strain is observed. Furthermore, the quantization error (set by the system minimum temporal resolution in determing Δt of 25 ps, i.e., 1 sample at 40 GHz) is clearly observed, thus demonstrating the resolution limit of the system of 4 nε (Equations 5.4, 5.5). It should be mentioned that in this case, the total measured strain is calculated by simply using the strain variations calculated with reference to the first trace of the measurement (at t = 0). This is possible as in the frequency shift (17 MHz) corresponding to the maximum applied

strain ($\pm$100 nε) was significantly lower (<1%) than the pulse total spectral content (2.32 GHz) in this case.

Figure 5.8(b) presents a spectrogram of the frequencies measured by the ϕOTDR when the PZT apply a frequency sweep between the frequencies 450 Hz to 850 Hz with a period of 1 s. The instantaneous frequency of the spectrogram is calculated using a moving window of 40 ms width over the recovered correlation shift profile. The high linearity of the transfer function of the sensor is clearly demonstrated as no harmonics are observed in frequencies of up to 2 kHz. The Signal to Noise Ratio (SNR) of the measured frequencies is >25 dB, which clearly indicates the potential of this technique for achieving simultaneously true strain measurements, high linearity and good signal to noise ratio.

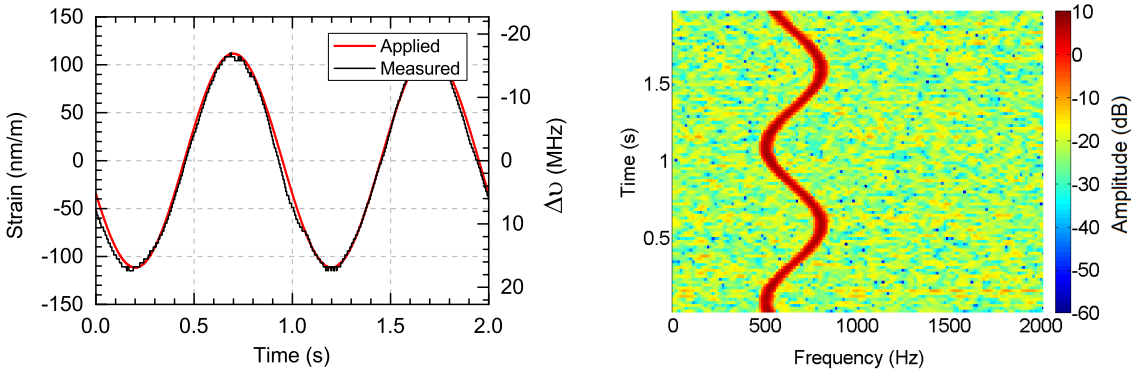

(a) (b)

Figure 5.8: Measured dynamic strain variations when strain is applied by a PZT in 20 m of fiber around meter 979 of the FUT. (a) Measured strain for a 1 Hz sinusoidal strain with 100 nε maximum amplitude; (b) Spectrogram (logarithmic scale - dB) for an applied strain of a frequency sweep between 450 Hz to 850 Hz with a period of 1 s (instantaneous frequency calculated using a moving window of 40 ms width of the measured dynamic strain) [167].

5.3.5 Acoustic Sensing: experimental demonstration

These results demonstrate the capability of this sensor for performing truly linear and dynamic strain measurements using the presented technique. For this purpose, different sounds are applied to the PZT in order to create controllable dynamic strain variations on the fiber, which is controlled by an electrical input. The ϕOTDR traces are acquired with a frequency of 4 kHz.

Firstly, we apply three pure tones with known amplitudes onto the fiber and recovered the applied strain. The results are presented in Figure 5.9. The applied signal has a duration of 3.5 seconds and contains three frequencies of 523 Hz, 659 Hz and 784 Hz. Figure 5.9(a) shows the full measurements, with a maximum amplitude of 80 nε. As it is clearly observed, a good agreement between the experimental measure and the applied strain is observed. The small amplitude disagreement at 784 Hz is caused by the amplitude response of the PZT element and not the optical sensor. In Figure 5.9(b) it is shown a zoom of the first tone in Figure 5.9(a) where a good correspondence between the measured and applied strain variation is visible. To demonstrate the linear behavior of the sensor, Figure 5.9(c) presents the spectrogram of the recorded signal. The spectrogram is calculated using a moving window of 90 ms width over the recovered signal. The high linearity of the transfer function of the sensor is clearly demonstrated as no harmonics are observed in frequencies up to 2 kHz. The SNR of the measured frequencies

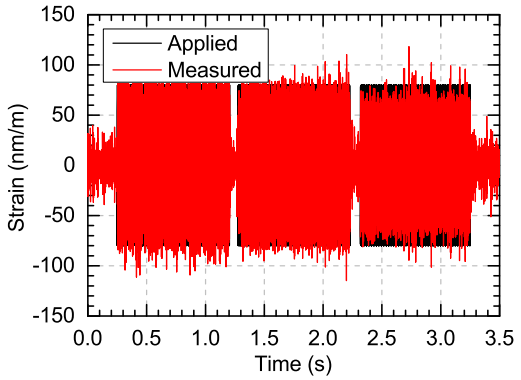

(a) Full vibration

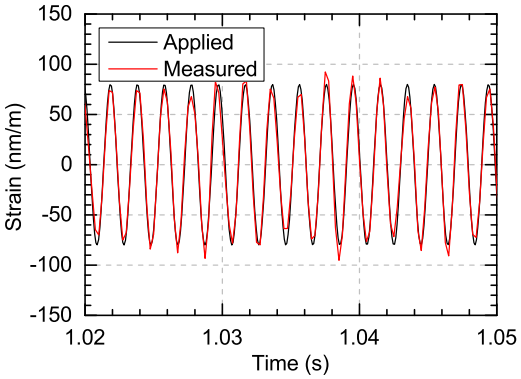

(b) A detail of 0.03 s of Figure (a)

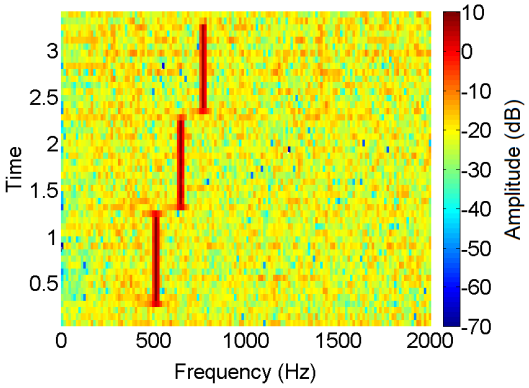

(c) Spectrogram for the full vibration (instantaneous frequency calculated using a moving window of 90 ms)

Figure 5.9: Measured strain variations when strain applied by a PZT in 20 m of fiber around meter 979 of the FUT. Three pure tones of 523 Hz, 659 Hz and 784 Hz have been applied [168].

is >25 dB, which clearly indicates the potential of this technique for achieving simultaneously true strain measurements, high linearity and good SNR.

Finally, the first 5 seconds of the 5th symphony of Beethoven are applied to the fiber. The recorded signal is presented in Figure 5.10. Again, there is a good agreement between the experimental measure and the applied strain, the small disagreements coming more from the non-flat spectral PZT response and fiber mechanical coupling than from the ϕOTDR response. The signal recorded by the ϕOTDR is also perfectly understandable by human hearing when played by a speaker.

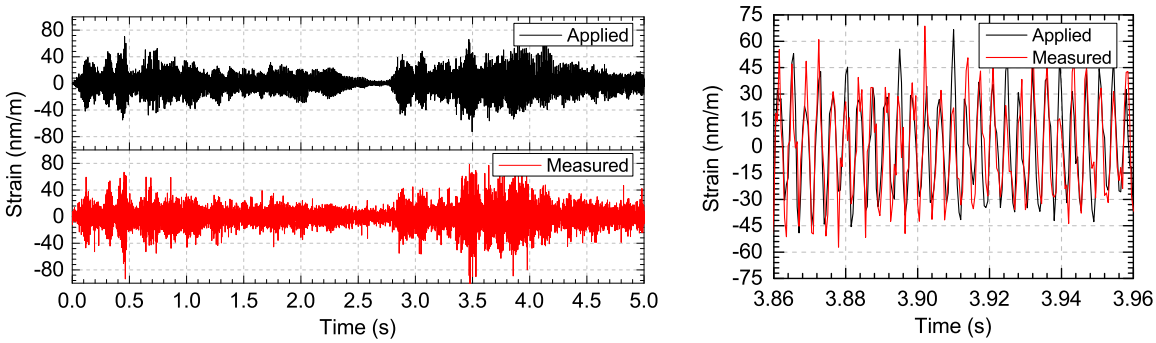

(a) Full vibration

(b) A detail of 0.1 s of Figure (a)

Figure 5.10: Measured strain variations when strain applied by a PZT in 20 m of fiber around meter 979 of the FUT. First 5 seconds of 5th symphony of Beethoven has been recorded [168].

5.4 Limitations

The presented technology, compared to the rest of Distributed Optical Fiber Sensors (DOFSs), presents huge advantages such as high-resolution, dynamic measurement and quantitative temperature or strain variation measurements, all this in a simple, robust and time-effective manner. However it presents two main limitations. Firstly, as the photodetection bandwidth is wider comparing to a traditional ϕOTDR, the resulting electrical noise caused by the photodetection process is higher. However, information is taken from a trace section, rather than a trace point (as in traditional ϕOTDR). Therefore the maximum measurable ranges of both technique are expected to be similar. Secondly, the laser phase-noise has an important impact in Chirped-Pulse ϕOTDR signals. In particular, it will be shown that the noise in the readings of strain/temperature changes along the fiber scales directly with the frequency noise power spectral density of the laser note that this issue is shared with traditional ϕOTDR). A deep analysis of these limitations and proper solutions to mitigate their effects in Chirped-Pulse ϕOTDR will be presented in Chapter 6 and Chapter 7. Lastly, the technique requires a higher computational consumption than traditional ϕOTDR. This however is not a fundamental limiting issue since real-time operation has been demonstrated using GPUs commercially available at prices well below the cost of the optical setup.

5.5 Conclusions

In this chapter, a simple and innovative distributed fiber sensor for dynamic measurement of temperature and strain variations was presented. It is based on ϕOTDR using linearly chirped

pulses. The system avoids the need of performing laser frequency sweeps, replacing them by the computation of simple correlations from trace to trace. It also avoids the use of complex and unstable phase recovery techniques relying on a local oscillator. The resolution of the sensor can be tuned by acting on the pulse chirp slope. With simple setups, temperature/strain resolutions of 0.5mK/4nε could be readily demonstrated. It was also shown that the sensing method can cumulatively track large total temperature/strain variations (much larger than those equivalent to the total spectral content of the pulse), as long as the variations from trace to trace are small enough and care in the processing is taken so as to keep the cumulative errors bounded.

The system allows for the precise quantification of temperature/strain change variations in a single shot, reaching measurement speeds at kHz rates, while maintaining reliability over several hours. Thus, this new sensor open the use of distributed optical sensing to a large number of new applications such as chemical, wind or light sensing, which require high sensitive temperature measurements. Also ionizing radiation could be detected with this system since it has been demonstrated the dependence of the fiber refractive index with it [173, 174]. The high vibration sensitivity of the sensor could be also applied to detect and quantify micro-earthquakes.

A conceptual demonstration with a spatial resolution of 10 m over 1 km is provided, but the system should in principle allow for similar settings to traditional ϕOTDR, with metric spatial resolutions over tens of kilometers. The presented sensor has potential to greatly extend the operating ranges of ϕOTDR, as it will be demonstrated in Chapter 7. The only cost increase of the sensor appears in the detection scheme and in the digitizer, both of which scale with the amount of chirp applied. While the work here presented was aimed at maximizing the performance of the technique for an initial conceptual demonstration, note that the setup can be scaled to operate with a few hundred MHz of chirp/detection bandwidth/sampling rates, thus bringing the system closer to the operation of traditional ϕOTDR. The system proves to be far more simple and robust than other dynamic and distributed strain/temperature measurement methods reported in the literature. Temperature, strain, vibrations and acoustic sensing has been demonstrated along the whole chapter.

Chapter 6

Laser Phase-Noise Cancellation in Chirped-Pulse ϕOTDR

6.1 Introduction

In Chapter 5, we have proposed a novel methodology to achieve high-resolution, quantitative dynamic temperature or strain variation measurements using Phase-Sensitive Optical Time Domain Reflectometry (ϕOTDR) and linearly chirped-pulses [167]. It was demonstrated that using a linearly chirped probe pulse, a perturbation in the refractive index of the Fiber Under Test (FUT) is translated into a localized, controlled temporal shift of the backscattered trace. This temporal shift is proportional to the applied perturbation, allowing a systematic quantification of the refractive index variation with no need for phase detection systems or time-consuming frequency sweeping strategies [175]. Hence, by calculating local correlations of trace segments between two consecutive power measurements, the absolute value of the applied perturbation can be readily obtained. However, the accuracy in the correlation measurements broadly depends on two factors, the correlation noise, which is in turn related to the linear chirp applied to the probe signal, the correlation window, and the Signal to Noise Ratio (SNR) of the trace; and also on the phase-noise of the light source.

In this chapter the impact of the laser phase-noise in Chirped-Pulse ϕOTDR systems is analyzed theoretically and experimentally [176–178]. To validate the developed model, an experimental study has been performed using three lasers with different static linewidths (5 MHz, 50 kHz and 25 kHz), i.e., with different phase-noise. Besides, it is presented a simple technique to mitigate the effect of the laser phase-noise in Chirped-Pulse ϕOTDR measurements. As it will be demonstrated along this chapter, the proposed procedure enables to detect perturbations with high SNR even when using relatively broad linewidth lasers (high phase-noise). In particular, a SNR increase of 17 dB has been experimentally achieved by applying the proposed noise cancellation technique.

6.2 Impact of Laser Phase-Noise in Chirped-Pulse ϕOTDR

In order to provide a deep analysis of the impact of laser phase-noise in Chirped-Pulse ϕOTDR, we develop here a theoretical model that describes it. Let us assume that probe pulse $P(t,z)$ has a rectangular intensity profile of amplitude E_0 and temporal length τ_p, and whose instantaneous frequency profile is given by $\nu(t) = \nu_0 + \delta\nu/2 - \delta\nu \cdot (t/\tau_p)$. The expression of $P(t,z)$ can be written as:

$$P(t,z) = E_0 \cdot \mathrm{rect}\left[\frac{t-t_z}{\tau_p}\right] \cdot e^{-2\pi i\left(\nu_0+\delta\nu/2-\delta\nu/(2\tau_p)[t-t_z]\right)\left(t-t_z\right)} \cdot e^{i\varphi_r(t)} \tag{6.1}$$

where t_z is considered the time taken by the pulse to reach the position z in the fiber and $\varphi_r(t)$ is the random phase-noise induced by the laser. The random instantaneous frequency due to $\varphi_r(t)$ is defined as:

$$\nu_r(t) = -\frac{1}{2\pi}\frac{d\varphi_r(t)}{dt} \tag{6.2}$$

Following a similar derivation as in Chapter 5, it can be easily demonstrated that, to first order, the frequency noise of the laser $\nu_r(t)$ induces a local temporal shift in the trace

$$\Delta t_r(t) = \frac{\tau_p}{\delta\nu} \cdot \nu_r(t) \tag{6.3}$$

Hence, the temporal shift induced in the trace will be then associated to a variation in the refractive index of the FUT, inducing an error in the strain measurement. Thereby, this induced error is related with $\nu_r(t)$ as:

$$S_\varepsilon = \frac{S_{\nu_r}}{\left(0.78 \cdot \nu_0\right)^2} \propto \Delta f \tag{6.4}$$

where S_ε and S_{ν_r} are the strain and the random instantaneous frequency noise power spectral densities (PSD), respectively, and Δf is the laser static linewidth, which is directly proportional to S_{ν_r} [179]. From Equation 6.4, it can be concluded that the strain uncertainty of the sensor is also proportional to the laser static linewidth. Hence, choosing a laser with low phase-noise is, in principle, essential to realize low uncertainty measurements [176].

Equation 6.3 shows the inverse relationship between the chirped pulse bandwidth and the Δt_r error induced by the laser phase-noise. Thus, when the laser phase-noise is the limiting factor, the higher the probe pulse chirp, the lower the uncertainty in the determination of the delay. However, the nominal delay induced by the refractive index variation to be measured is also inversely proportional to the pulse chirp (see Equation 5.4 in Chapter 5). Eventually, the chosen pulse chirp will have no effect on the accuracy of the measurand in Chirped-Pulse ϕOTDR schemes (i.e. both signal amplitude and laser phase-noise effects scale inversely with the chirp). Still, it is important to consider that, due to the relationship between delay and probe pulse width inherent to the system ($\Delta t < 0.03\tau_p$), a higher pulse chirp will enable the proper measurement of higher vibration amplitude between two consecutive traces, see Equation 5.4 in Chapter 5. As such, the most convenient choice in terms of chirp values appears to be the higher chirp value allowed by the available system detection bandwidth.

6.2.1 Experimental Setup

The conclusions reached in the previous section are experimentally validated in what follows. The setup employed to carry out the analysis of the phase-noise is shown in Figure 6.1 (similar to Figure 5.2 presented in Chapter 5), which can be divided in three main blocks.

The first block accounts for the generation of the chirped probe pulse. Here, a Laser Diode (LD) working in continuous emission is driven by a Current and Temperature (I&T) controller to select the central wavelength. The I&T controller is a Laser Diode Controller (Newport LDC-3724C) with a laser output Noise/Ripple of 4 μA which ensures a very low noise transfer to the LD. A secondary current control applies a repetitive electric ramp signal to the laser driver, inducing a linear chirp at certain times in the outputted light. Then, a Semiconductor Optical Amplifier (SOA) gates the chirped signal creating square optical pulses of 100 ns width with an extinction ratio >50 dB and a repetition rate of 40 kHz. The chirp spectral content of the pulses is controlled by the peak voltage of the ramp, which is varied to induce spectral contents of 350 MHz, 590 MHz and 860 MHz. An Erbium-Doped Fiber Amplifier (EDFA) boosts the power of the optical pulses before injecting them into the fiber. A Dense Wavelength Division Multiplexer (DWDM) follows the EDFA to filter out part of the generated Amplified Spontaneous Emission (ASE). The bandwidth of this DWDM is 0.8 nm. Finally, a tunable attenuator is used to control the peak power of the pulses so that non-linear effects along the FUT are avoided. The second block corresponds to the FUT. It consists of a fiber spool of 1 km whose last 20 m are coiled around a Piezoelectric Transducer (PZT). The PZT is connected to an electrical signal generator and allows us to apply controlled vibrations on the fiber. The third block handles the detection of the backscattered trace. For this purpose, the signal is first amplified and filtered in. Then,

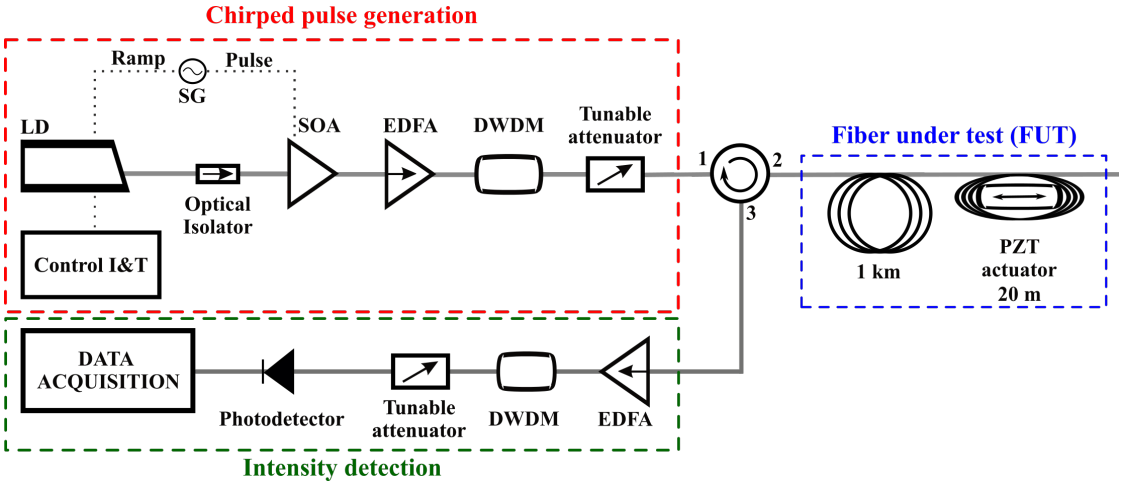

Figure 6.1: Experimental setup of Chirped-Pulse ϕOTDR for laser phase-noise cancellation [176, 177]. LD, Laser Diode; SG, Signal Generator; SOA, Semiconductor Optical Amplifier; EDFA, Erbium Doped Fiber Amplifier; DWDM, Dense Wavelength Dense Multiplexer; TA, Tunable Attenuator; I&T, Current and Temperature.

the resulting signal is directly detected using a p-i-n photo-detector with a bandwidth of 1 GHz and a high-speed digitizer with 40 GSps sampling rate.

To study the relationship between the measurement uncertainties and the laser phase-noise, three LDs with different linewidths, namely 5 MHz, 50 kHz and 25 kHz, have been employed. These values were obtained using a delayed self-heterodyne method [180]. In this method, one portion of the laser beam is sent through a long optical fiber (larger than the coherence length of the laser) which provides some time delay. Another portion is sent through an intensity modulator, which is driven with a constant frequency and shifts all the optical frequency components by that frequency. Both beams are finally superimposed using an optical coupler, and the resulting beat note is recorded with a photodetector. Since the fiber delay is large, the superimposed beams are essentially uncorrelated, and the output spectrum becomes a simple self-convolution of the laser output spectrum, from which the laser linewidth is easily retrieved. The employed lasers are commercially available lasers, namely a Fitel FRL15DCWD, Thorlabs SFL1550P, and Rio Planex (Grade 1), respectively. The PZT induces a sinusoidal perturbation of 2 kHz and amplitude of 40 nε, which is first detected using the three lasers and the chirped pulses of 860 MHz. In this case, the resolution of the measurement is 1 nε.

6.2.2 Results

The three strain measurements are presented in Figure 6.2, which shows the last 100 m of FUT. In the remainder of this chapter, we refer all the mentioned fiber positions to those last 100 m. In the figure, the noise level difference between measurements is clearly noticeable. In particular, Figure 6.2(a) shows the measurement obtained when using the laser with the highest linewidth, i.e., 5 MHz. The region affected by the vibration, between 70 m and 90 m in the figure, can be discerned but it is slightly diffuse due to the high level of noise covering the measurement. In contrast, the lasers with lower linewidths (lower phase-noise) present better results, as observed in Figure 6.2(b) and 6.2(c). Here, the region affected by the vibration is clearly defined and the non-affected region is almost totally flat. As expected, the laser with lowest linewidth (25 kHz) presents the best results.

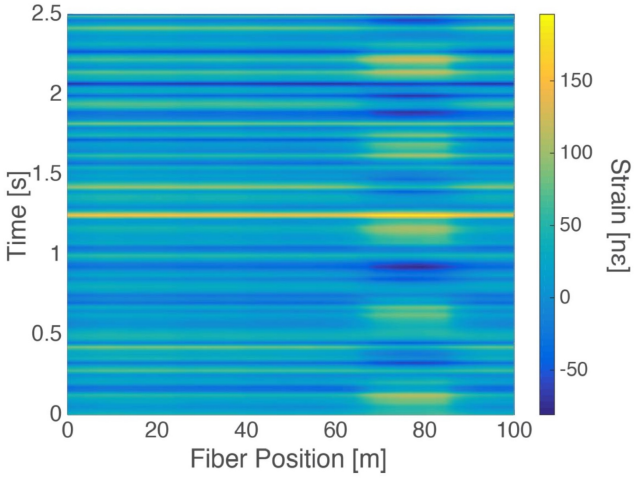

(a) $\Delta f = 5$ MHz

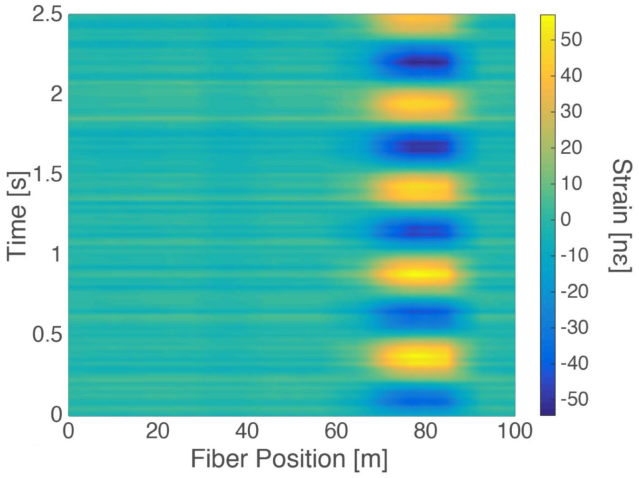

(b) $\Delta f = 50$ kHz

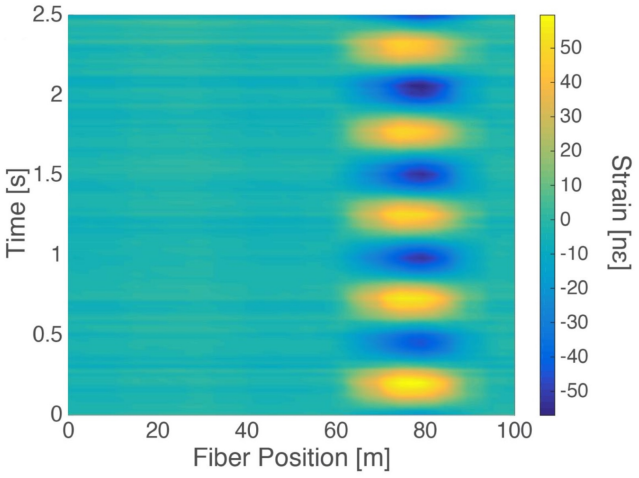

(c) $\Delta f = 25$ kHz

Figure 6.2: Strain measurements from the last 100 m of the FUT, employing three lasers with different linewidths [176].

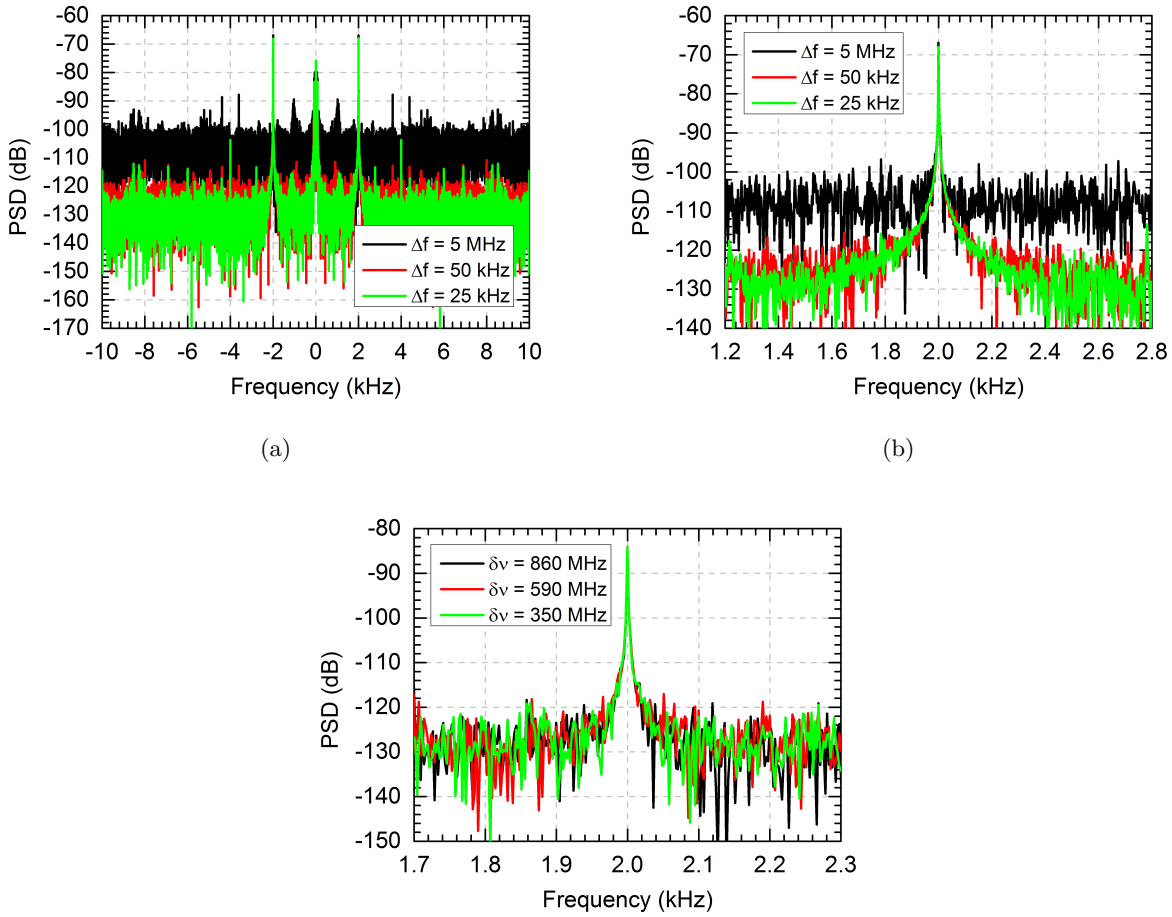

Figure 6.3: Power Spectral Density (PSD) of 2 kHz vibrations detected along 0.4 s recording time. (a) Results obtained when using a probe pulse with chirp spectral content of 860 MHz, generated from the laser with linewidth of 5MHz (black line), 50 kHz (red line) and 25 kHz (green line); (b) Detail of the 2 kHz frequency peak; (c) Results obtained when using the laser with 25 kHz linewidth and different values of chirp, namely 860 MHz (black line), 590 MHz (red line), and 350 MHz (green line) [176].

In order to quantify the SNR improvement in the measurements obtained from the different lasers, we compare the Power Spectral Density (PSD) of the recorded vibrations, namely at 78 m (point of maximum amplitude), over a recording time of 0.4 s. The obtained PSDs are plotted in Figures 6.3(a) and 6.3(b), from which we can verify that the 2 kHz vibration has been correctly detected. A low frequency, noise of about <100 Hz is also present in the measurements, which is mainly attributed to mechanical and thermal fluctuations along the measurements. The frequency peak has almost the same amplitude (-68 dB) (as expected, since the signal applied is constant) in the three curves while the background noise is substantially different in each case, leading to an SNR of 34.4 dB when using the laser with 5 MHz linewidth (black line); while the SNR increases to 54.7 dB and 56.7 dB for the lasers of 50 kHz (red line) and 25 kHz (green line), respectively. Thus, an SNR increase of 20.3 dB (laser with linewidth of 50 kHz) and 22.3 dB (laser with linewidth of 25 kHz) is obtained as compared with the results obtained from the 5 MHz-linewidth laser. The experimental results show a good agreement with the theoretical model: according to Equation 6.3, the expected SNR increase between the 5 MHz-linewidth

laser and the 50 kHz and 25 kHz-linewidth lasers should be of 20 dB (20.3 dB experimental) and 23 dB (22.3 dB experimental), respectively.

Besides, we also experimentally verify that the chosen pulse chirp does not affect the measurement SNR. For this purpose, the recovered strain variation is obtained for three different chirp values, corresponding to pulse spectral contents of 350 MHz, 590 MHz and 860 MHz, respectively, using the laser with lowest phase-noise (i.e., 25 kHz static linewidth). To carry out these measurements, we have reduced the amplitude of the applied sinusoidal perturbation to match with a value of properly measurable strain when using the lowest pulse chirp [167]. The PSD of the obtained results is plotted in Figure 6.3(c). As it can be observed from the figure, the strain amplitudes and noise levels are independent on the employed chirp. Note that, although lower values of chirp lead to higher measures of delay 5.4, the strain amplitude is adequately attained in all cases. Similarly, the level of noise has scaled proportionally, in good agreement with the expected outcome.

6.3 Laser Phase-Noise Cancellation

6.3.1 Proposed Method

As explained in Section 6.2, in Chirped-Pulse ϕOTDR-based sensors the phase-noise directly induces an error in the strain measurement, which is proportional to the laser frequency fluctuations (see Equations 6.2 and 6.3). In this section, it is presented a simple methodology to significantly reduce the error induced by the laser phase-noise in this sensing technology. The finite linewidth of commercially available lasers produces a deviation in the emitting frequency over the nominal central frequency ν_0. This variation must be slower than the pulse width, as this is a general restriction of ϕOTDR setups (i.e., the laser source must have a coherence time longer than the pulse width). However, the central frequency of each pulse may differ from pulse to pulse, $\nu_0 + \nu_{r,k}$, where the subscript k stands for each different pulse within the input pulse train. Under these considerations, it is inferred that each detected backscattered trace may suffer a particular deviation (i.e. a local delay) that is maintained along the whole trace, but different from the other traces. This phenomenon is clearly observed in Figure 6.2(a), in which horizontal lines, corresponding to a noise pattern which is constant along the fiber position but varying in time, appear superimposed to the signal. This means that the frequency fluctuations of the input laser can be, to some extent, measured with the Chirped-Pulse ϕOTDR scheme. This is the basis that allows compensation of this noise. Hence, to mitigate the effect of that laser phase-noise in ϕOTDR measurements, we propose the following simple strategy. A portion of FUT must be kept unperturbed. The trace resulting from this fiber section will only contain low frequency environmental fluctuations (which can be minimized e.g., by introducing this section of fiber under a water bath or in a soundproof box) and the frequency fluctuations caused by the laser linewidth. By averaging the temporal shift induced in the trace along this unperturbed fiber section, it is possible to obtain the temporal pattern of laser frequency fluctuations ($\nu_{r,k}$) and compensate them along the complete fiber length. The length of the unperturbed section has to be chosen long enough so that fast phase-noise fluctuations plus additional terms of thermal and optical noise are completely averaged.

6.3.2 Results

To prove the validity of the proposed technique, we have calculated the laser frequency-noise fluctuations from the first 20 m of FUT shown in Figure 6.2 (recall that the figure shows the last

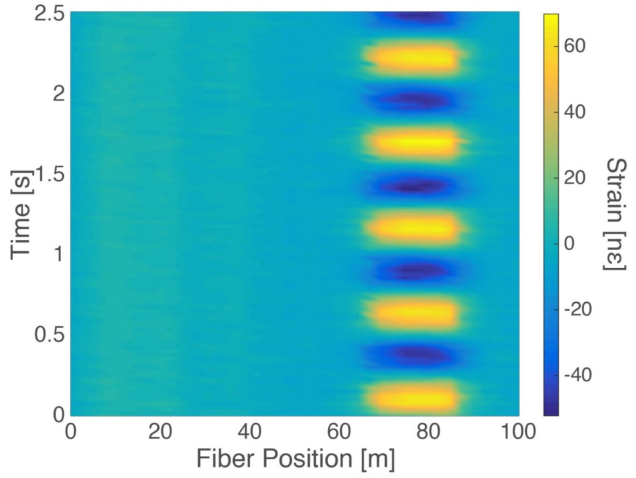

(a) $\Delta f = 5$ MHz

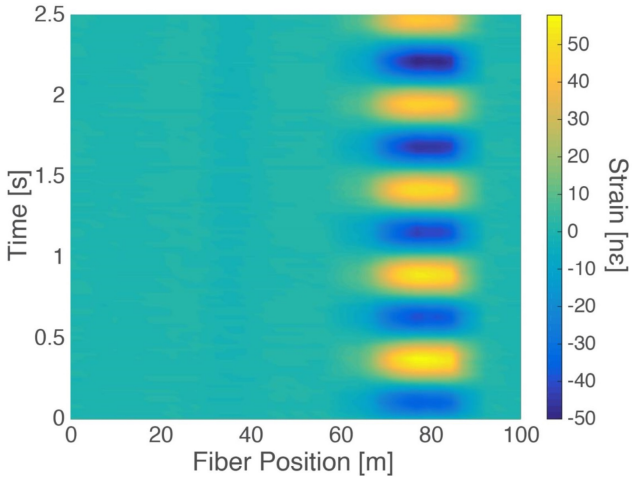

(b) $\Delta f = 50$ kHz

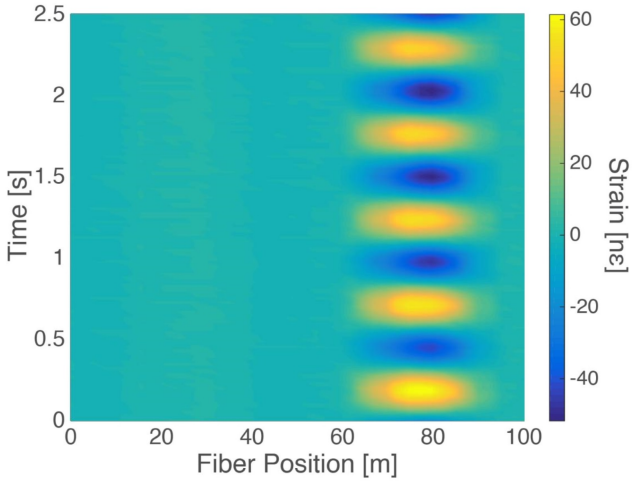

(c) $\Delta f = 25$ kHz

Figure 6.4: Strain measurements from the last 100 m of the FUT, employing three lasers with different linewidths [176].

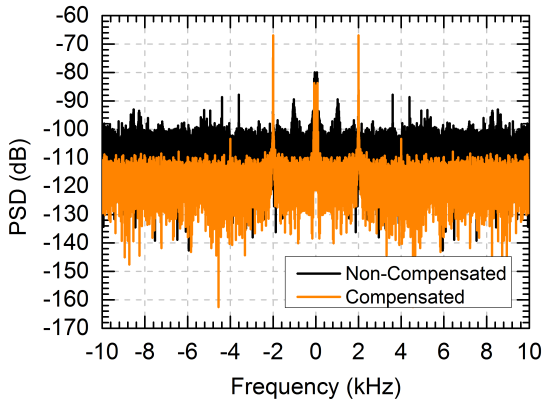

(a) $\Delta f = 5$ MHz

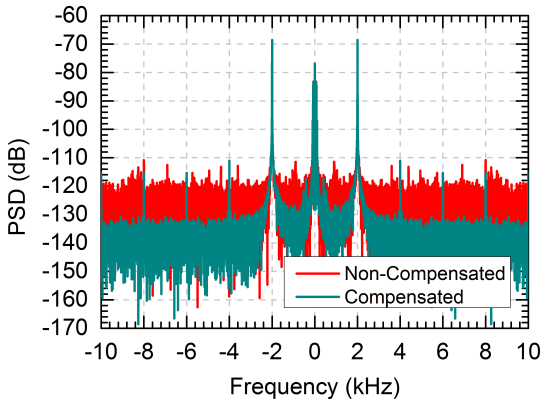

(b) $\Delta f = 50$ kHz

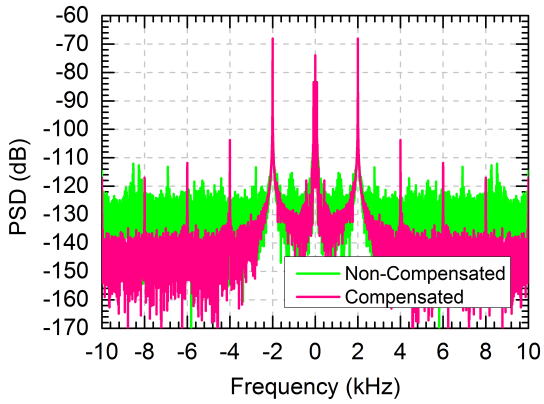

(c) $\Delta f = 25$ kHz

Figure 6.5: Power spectral density (PSD) of 2 kHz vibrations when using a probe pulse with chirp spectral content of 860 MHz, generated from the laser with linewidth of (a) 5MHz (black line), (b) 50 kHz (red line) and (c) 25 kHz (green line), before and after laser phase-noise compensation [177].

100 m of fiber). We have subtracted the fluctuation average obtained from these 20 m to the whole detected traces. The obtained results are plotted in Figure 6.4, from which we can observe a substantial improvement in the detection of the sinusoidal vibrations. This improvement is particularly evident in the case in which the 5 MHz-linewidth laser is employed (Figure 6.4(a)). In this case, the background noise has been almost completely eliminated, in such a way that the sinusoidal perturbation is now clearly distinguishable.

To quantify the attained improvement, we have measured the SNR from the PSD of the resulting curves. Figure 6.5 presents the PSD of the compensated measurements at 78 m, over 0.4 s. The SNR improvement achieved from the proposed frequency-noise compensation method is 14.1 dB for the 5 MHz-linewidth laser (Figure 6.5(a)); 17.1 dB for the 50 kHz-linewidth laser (Figure 6.5(b)); and 16.4 dB for the 25 kHz-linewidth laser (Figure 6.5(c)). The fact that the noisiest laser presents the lowest frequency-noise compensation can be due to the fact that the proposed technique only compensates for the instantaneous frequency fluctuation (i.e., the first derivative of the laser phase-noise, see Equation 6.2).

In general, a noisier laser will have higher values of higher-order phase-noise components,

which cannot be compensated by the proposed methodology. In addition, in Figure 6.5, we can also observe that the low frequency fluctuations (< 100 Hz) are maintained after the laser frequency-noise compensation, which corroborates the fact that we have only affected the frequency noise fluctuations of the laser, but not the small thermal and mechanical drifts of the reference fiber section. Also, in the PSD obtained from the lasers with 50 kHz and 25 kHz bandwidth it is possible to observe harmonics of the fundamental vibration frequency that could be barely observed prior to the frequency noise compensation. It is worth mentioning that those harmonics have an amplitude about 25 dB below the fundamental peak, attesting for the high linearity of the Chirped-Pulse ϕOTDR sensing technology. The obtained results expose the strong potential of Chirped-Pulse ϕOTDR for high SNR strain measurements even when using relatively low coherence lasers (although always much longer than the probe pulse width).

6.4 Conclusions

The negative impact of the laser phase-noise in Chirped-Pulse ϕOTDR-based sensors has been studied both theoretically and experimentally. In particular, we have proven that the laser phase-noise induces an uncertainty in the temperature/strain measurement which is directly proportional to the laser frequency fluctuations. This is owed to the fact that the random frequency drifts of the laser generate different temporal shifts in the traces, which are readily associated with variations in the refractive index of the FUT. Hence, we have shown that narrower laser linewidths allow a significant increase in the SNR of the strain recording. The experimental analysis has been performed using three different lasers with linewidths of 5 MHz, 50 kHz and 25 kHz, respectively. An SNR enhancement of ∼22 dB has been obtained when decreasing the linewidth from 5 MHz to 25 kHz, in good agreement with the expected theoretical trend.

Additionally, considering the way the laser phase-noise impacts on the detected traces, we have presented a simple technique to mitigate the induced temperature/strain uncertainty. The basis of the technique lies on the fact that small frequency deviations in the input laser can be quantified in a section of fiber that is mechanically and thermally isolated. This unperturbed fiber section allows us to measure the pulse-to-pulse frequency deviation, and therefore compensate for this deviation in each trace by simple subtraction of the corresponding delay. By using this method, up to 17 dB SNR enhancement has been achieved (14 dB when using the noisiest laser, i.e., that one with 5 MHz linewidth). The presented results reveal the robustness of Chirped-Pulse ϕOTDR, since it allows single shot, quantitative, high SNR strain measurements with relatively low coherent laser sources (still always with much longer coherence times than the pulse width, but not required to be of the size of the fiber length) and direct detection schemes.

Chapter 7

Long Range Chirped-Pulse ϕOTDR

7.1 Introduction

Chirped-Pulse Phase-Sensitive Optical Time-Domain Reflectometry (Chirped-Pulse ϕOTDR), presented in Chapter 5, has allowed to perform high-resolution, quantitative dynamic temperature or strain variation measurements in a simple, robust and time-effective manner [134, 167–170, 176]. The presented technology, compared to the rest of Distributed Optical Fiber Sensors (DOFSs), presents huge advantages such as high-resolution, dynamic measurement and quantitative temperature or strain variation measurements, all this in a simple, robust and time-effective manner.

As with traditional ϕOTDR, range and resolution are tightly related parameters of the system. In order to increase the measurable range, higher energy probe pulses are required. This could be achieved by increasing the pulse width, which translates however into a reduction of the sensing spatial resolution. On the other hand, the peak power of the pulse could be alternatively risen, but this solution is limited by the advent of non-linear effects [40, 106, 107]. As it was presented in Chapter 3 (Section 3.5), usually Modulation Instability (MI) is the first non-linear effect that appears in a ϕOTDR-based sensor, which generates two sidebands at each side of the probe carrier frequency. Furthermore, the use of traditional rectangular probe pulses generally induces a power exchange between the pump and the sidebands known as Fermi-Pasta-Ulam (FPU) recurrence [122, 123]. This effect is revealed in the trace as a visibility fading at certain specific positions and, consequently, a loss in the sensing sensitivity at those positions. In Chapter 4 (Section 4.2), the impact of the use of probe pulses with different beam shapes on the backscattered power trace of ϕOTDR systems have been analyzed. It was concluded that a Gaussian or triangular envelope pulse limits the effect of MI and mitigates the advent of the FPU recurrence, which enables an increase of the length range and sensitivity. However, for a substantial increase of the ϕOTDR range, distributed amplification [19–27] is also a more suitable solution.

As it was presented in Chapter 3 (Subsection 3.5.2), distributed non-linear amplification techniques (Raman, Brillouin or parametric) have been extensively implemented in Distributed Optical Fiber Sensors (DOFSs) [19–24, 70, 125, 126]. As the attenuation losses are compensated along the measuring fiber, the sensing range can be enlarged without compromising the resolution. Regarding sensors based on Rayleigh scattering, spatial resolutions of 10 m over sensing lengths exceeding 100 km have been demonstrated [19–27]. Nevertheless, when distributed amplification is to be applied to Chirped-Pulse ϕOTDR, it is important to consider that the non-linear, chromatic dispersion and pump depletion effects that the pulse may suffer along the fiber will affect not only the pulse shape but also its instantaneous frequency profile. In this case, distortions in the linear frequency profile of the pulse can be detrimental for the proper operation of a Chirped-Pulse ϕOTDR system. For this reason, increasing the sensing range using non-linear distributed amplification is not trivial, and deserves a careful study. To date, the maximum sensing range reported in this technique is 11 km [134] without distributed amplification.

The use of distributed Raman amplification for increasing the sensing range of distributed optical fiber sensors has been previously introduced in Chapter 3 (see Subsection 3.5.2.1). In this chapter, the possibility of using this technique for increasing the sensing range of Chirped-Pulse ϕOTDR is studied. Additionally, we thoroughly analyze the possible distortions induced in the phase and intensity profiles of the optical probe pulse in its propagation along the sensing fiber. A sensing range of 75 km with 10 m spatial resolution and 1 nε resolution in the measurement of strain perturbations is successfully demonstrated [181].

7.2 First-Order Raman-Assisted Chirped-Pulse ϕOTDR

7.2.1 Fundamentals and Theoretical Model

Raman amplification is a well-known solution to increase the sensing range of distributed fiber sensors [19–27]. A commonly used configuration works by injecting two CW Raman pumps (centered around 1455 nm) through both ends of the fiber. The provided Raman gain (g_{R}) will appear at the wavelength of the ϕOTDR pulse, which is around 1550 nm.

Assuming that the optical pulse propagates in the forward direction (towards increasing values of z), it is defined that the pulse is injected at the position $z = 0$ and the position of the other fiber end is $z = L$. Typically, pump depletion is neglected since the power of the Raman pumps is about two orders of magnitude above the pulse peak power [70].

The power evolution of the system can be analyzed considering an incoherent light source, simplifying the equations since no interference process is considered. The forward (+) and backward (−) propagation of the Raman pump powers along the fiber ($P_{\mathrm{R}}^{\pm}(z)$) can be obtained solving the following equations [70]:

$$\frac{dP_{\mathrm{R}}^{\pm}(z)}{dz} = \mp\alpha_{\mathrm{R}} P_{\mathrm{R}}^{\pm}(z) \tag{7.1}$$

where α_{R} is the loss at the wavelength of the Raman pump. Considering the Raman gain g_{R} and the fiber attenuation α_{p}, the power evolution of the probe pulse $P_{\mathrm{p}}(z)$ can be obtained solving the equation:

$$\frac{dP_{\mathrm{p}}(z)}{dz} = -\alpha_{\mathrm{p}} P_{\mathrm{p}}(z) + g_{\mathrm{R}} P_{\mathrm{p}}\Big(P_{\mathrm{R}}^{+}(z) + P_{\mathrm{R}}^{-}(z)\Big) \tag{7.2}$$

Equations 7.1 and 7.2 can be solved considering the following boundary conditions: the input Raman pump powers in the forward (+) and backward (−) directions are $P_{\mathrm{R}}^{+}(0)$ and $P_{\mathrm{R}}^{-}(L)$, respectively, and the input pulse peak power is $P_{\mathrm{p}}(0)$. Thus, it is obtained the next power evolution equations:

$$P_{\mathrm{R}}^{+}(z) = P_{\mathrm{R}}^{+}(0) \cdot e^{-\alpha_{\mathrm{R}} z} \tag{7.3}$$

$$P_{\mathrm{R}}^{-}(z) = P_{\mathrm{R}}^{-}(L) \cdot e^{\alpha_{\mathrm{R}}(z-L)} \tag{7.4}$$

$$P_{\mathrm{p}}\,(z) = P_{\mathrm{p}}(0) \cdot e^{-\alpha_{\mathrm{p}} z} \left(\frac{\exp\left(\frac{g_{\mathrm{R}}}{\alpha_{\mathrm{R}}} P_{\mathrm{R}}^{-}(L) \left(e^{\alpha_{\mathrm{R}}(z-L)} - e^{-\alpha_{\mathrm{R}} L} \right) \right)}{\exp\left(\frac{g_{\mathrm{R}}}{\alpha_{\mathrm{R}}} P_{\mathrm{R}}^{+}(0) \left(e^{-\alpha_{\mathrm{R}} z} - 1 \right) \right)} \right) \tag{7.5}$$

Considering an incoherent process for simplicity, the power of the backscattered signal from a position z_0 will be:

$$P_b^{z_0}(z_0) = \alpha_{\mathrm{Rb}} W P_{\mathrm{p}}(z_0) \tag{7.6}$$

The backscattered signal will travel along the fiber in the backward direction suffering fiber losses and Raman gain. Thus, the power evolution of $P_b^{z_0}$ will be obtained solving the following equation:

$$\frac{dP_{\mathrm{b}}^{z_0}(z)}{dz} = +\alpha_{\mathrm{p}} P_{\mathrm{b}}^{z_0}(z) - g_{\mathrm{R}} P_{\mathrm{b}}^{z_0}(z)\Big(P_{\mathrm{R}}^{+}(z) + P_{\mathrm{R}}^{-}(z)\Big) \tag{7.7}$$

Solving the Equation 7.7, the evolution of the backscattered power is:

$$P_{\mathrm{b}}^{z_0}(z \leq z_0) = P_{\mathrm{b}}^{z_0}(z_0) \cdot e^{\alpha_{\mathrm{p}}(z-z_0)} \left(\frac{\exp\left(\frac{g_{\mathrm{R}}}{\alpha_{\mathrm{R}}} P_{\mathrm{R}}^{-}(L)\Big(e^{\alpha_{\mathrm{R}}(z_0-L)} - e^{\alpha_{\mathrm{R}}(z-L)}\Big)\right)}{\exp\left(\frac{g_{\mathrm{R}}}{\alpha_{\mathrm{R}}} P_{\mathrm{R}}^{+}(0)\Big(e^{-\alpha_{\mathrm{R}} z_0} - e^{-\alpha_{\mathrm{R}} z}\Big)\right)} \right) \tag{7.8}$$

Finally, the power that reaches the detector ($z = 0$) backscattered from the position z_0 will be:

$$P_{\mathrm{b}}^{z_0}(0) = \frac{P_{\mathrm{p}}(z_0)}{P_{\mathrm{p}}(0)} P_{\mathrm{b}}^{z_0}(z_0) = \frac{P_{\mathrm{p}}(z_0)^2}{P_{\mathrm{p}}(0)} \alpha_{\mathrm{Rb}} W \tag{7.9}$$

7.2.2 Experimental Setup

Distributed amplification has proven to be a powerful tool to enhance the range of conventional ϕOTDR sensors, as the probe power along the fiber can be kept at a relatively high level all along the sensing fiber without reaching non-linearities [21,26,27]. Nevertheless, the use of distributed amplification in these schemes requires a careful optimization of both the probe peak power and the Raman pump powers launched in both directions of the sensing fiber [21]. The optimization not evident, and is generally done with two basic guidelines: (1) the power of the input pulse has to be kept low enough to avoid MI in the probe pulse and (2) the Raman gain is only interesting up to the point of overcoming the thermal noise limitations of the detector. Beyond that point, the expectable SNR increase is marginal, and moreover the RIN transfer from the Raman pump to the detected signal starts to dominate, as it grows exponentially with the pump power.

The setup used to measure vibrations over long fiber distances is presented in Figure 7.1. It is based on a Chirped-Pulse ϕOTDR scheme [134, 167–170, 176] but including a Continuous Wave (CW) Raman pump. The Raman pump is applied at the two ends of the sensing fiber aimed at compensating the energy loss of both the probe pulse and the reflected trace along the fiber, and consequently achieving larger measurement ranges.

The probe light source is a Laser Diode (LD) with a linewidth of 10 kHz emitting at 1549.35 nm and working in continuous emission. A standard current and temperature (I&T) controller is used to select the emitted central wavelength of the LD. A secondary current control generates a repetitive ramp signal to induce a linear chirp in the LD output. A Semiconductor Optical Amplifier (SOA), fed by an electrical square signal, gates the output LD light creating linearly chirped optical pulses. The 2.5 ns rise/fall times and Extinction Ratio (ER) of >50 dB of the SOA allow us to generate 100 ns-width quasi-square-shaped pulses with high ER. This leads to a spatial resolution of 10 m in the phase-sensitive reflectometer scheme [3]. The ramp signal is controlled so that the resulting linearly chirped pulse has a total spectral content of 630 MHz.

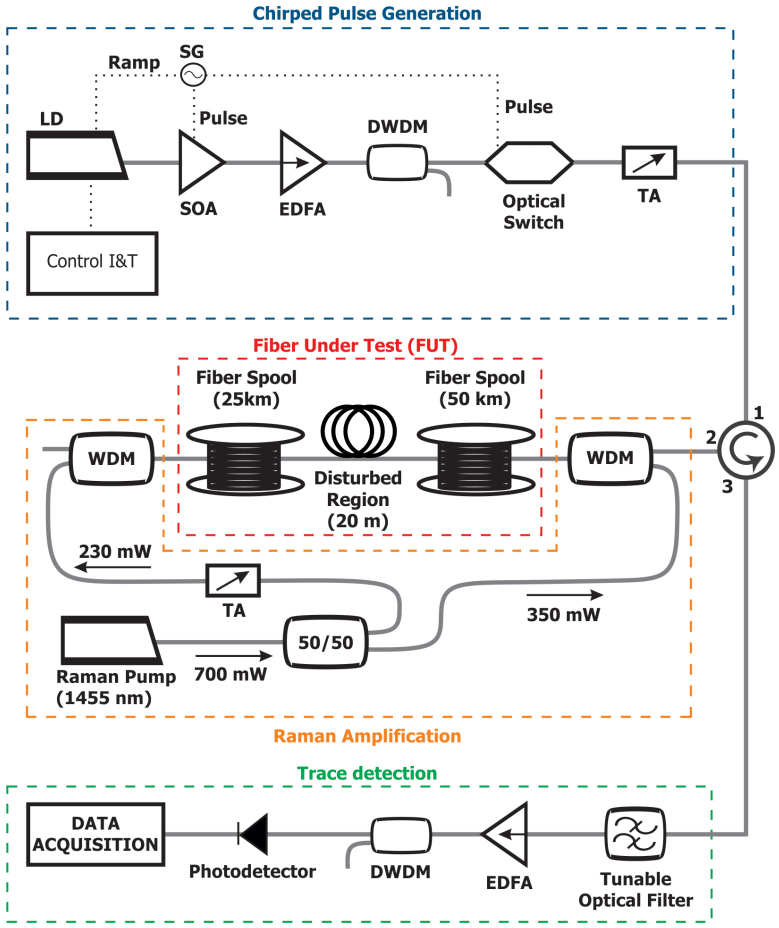

Figure 7.1: Experimental setup of Chirped-Pulse ϕOTDR with first-order Raman amplification [181]. LD, Laser Diode; SG, Signal Generator; SOA, Semiconductor Optical Amplifier; EDFA, Erbium Doped Fiber Amplifier; DWDM, Dense Wavelength Dense Multiplexer; TA, Tunable Attenuator; I&T, Current and Temperature.

The pulse power is boosted using an Erbium Doped Fiber Amplifier (EDFA). In order to eliminate the Amplified Spontaneous Emission (ASE) added by the EDFA, a Dense Wavelength Division Multiplexer (DWDM) with a spectral width of 100 GHz is used. The remained ASE centered at the pulse frequency (distributed temporally outside the pulse), induces intra-band noise, which generally is an important limitation in phase-sensitive reflectometers [34]. To avoid this, in addition to the optical filter, the pulse is temporally gated using an optical switch with rise/fall times of 100 ns and a typical ER of 25 dB. The three used electrical signals (i.e., the ramp applied at the secondary current control, and the square signals for the SOA and switch) are generated by the same Signal Generator (SG), which ensures a perfect synchronization between them.

The generated linearly chirped optical pulse is then launched into the Fiber Under Test (FUT). Previously, a Tunable Attenuator (TA) controls the power injected into the FUT to avoid non-linearities in the fiber such as MI [106, 107]. The FUT is composed of two fiber spools of 50 and 25 km respectively, constituting a total sensing fiber of 75 km. Vibrations were applied along 20 meters strapped around a Piezoelectric Transducer (PZT) and situated after the first fiber spool at the kilometer 50, which is the point with less Signal to Noise Ratio (SNR) when the bidirectional distributed Raman amplification is applied. The Raman pump is a CW Raman Fiber Laser (RFL) emitting at 1455 nm with a Relative Intensity Noise (RIN)

< -110 dBc/Hz, which can achieve emission powers of up to 2 W. In our scheme, the RFL was emitting a total power of ∼700 mW. The RFL beam is divided by a 50/50 optical coupler resulting in two beams of 350 mW. A TA is employed to reduce one of the beams to 230 mW. Two Wavelength Division Multiplexers (WDM) are used to inject the Raman pump into the FUT. The chirped probe pulse and the Raman pumps are conducted through the 1550 and 1450 ports of the WDMs, respectively (see Figure 7.1). The 350 mW and 230 mW beams are co-propagated and contra-propagated with the pulse, respectively. This unbalanced bidirectional pumping scheme has been chosen as it provides a good trade-off between noise and non-linear impairments.

The light backscattered from the fiber is first filtered in using a tunable optical filter with a spectral width of 15 GHz to minimize the ASE generated by the Raman pump before detection. Then, the filtered backscattered signal is amplified by another set of EDFA and DWDM. Finally, the resulting backscattered signal is detected by a p-i-n photodetector with a bandwidth of 1 GHz and recorded by a high-speed digitizer with 40 GHz sampling rate.

7.2.3 Results

7.2.3.1 Analysis of the System Limitations: SNR and Non-Linear Effects

In this subsection, the SNR of the Raman-assisted Chirped-Pulse ϕOTDR and the induced distortions in the propagating probe pulses are analyzed.

The theoretical models of signal and noise evolution used in this study have been already described in the literature [21, 182], and the different component parameters have been adapted to our particular devices. Compared to a conventional Raman-assisted ϕOTDR, it is interesting to note here that the problem of optimization in the Raman-assisted Chirped-Pulse ϕOTDR case is quite different, as the bandwidth of the signal of interest is typically one order of magnitude larger than in conventional ϕOTDR. This implies that the photodetector bandwidth is much larger, and that the weight of thermal noise in the equations is substantially larger than in the conventional scheme.

To illustrate which is the maximum range measurable in a non-amplified and in an amplified Chirped-Pulse ϕOTDR respectively, we provide a clarifying example in what follows. Figure 7.2 - top shows a trace obtained in our system by injecting 100 ns-width square pulses with 150 mW peak power in a 75 km fiber. This value of peak power has been proven experimentally to be the limit for the onset on non-linear effects in this case. As it can be observed, the maximum measurable range with a reasonable SNR in the detected trace is around 20 km. Here, the most important sources of noise are the thermal noise of the photodetector and the ASE noise introduced by the EDFA. Next, we examine the achievable range when using distributed amplification. For this purpose, we employ the configuration described in the previous section; namely, using first-order Raman amplification. Figure 7.2 – bottom shows the detected trace when the input pulse peak power is 25 mW (limit for the onset on non-linear effects in this case, as proved below) and first-order Raman amplification is implemented. In this case, although the noise level is higher due to the Raman ASE, the entire trace shows good SNR, which will allow for the monitoring of vibrations along the whole fiber (75 km).

A deeper SNR analysis of the optimized Raman-assisted and the conventional configuration is subsequently developed and presented in Figure 7.3. The average value of the experimentally obtained traces (in Figure 7.2) is shown in black in Figure 7.3, which is obtained by calculating a moving average of the traces after 100 times averaging. The resulting curves are normalized to the noise level of a single trace. As mentioned, a theoretical analysis of the evolution of

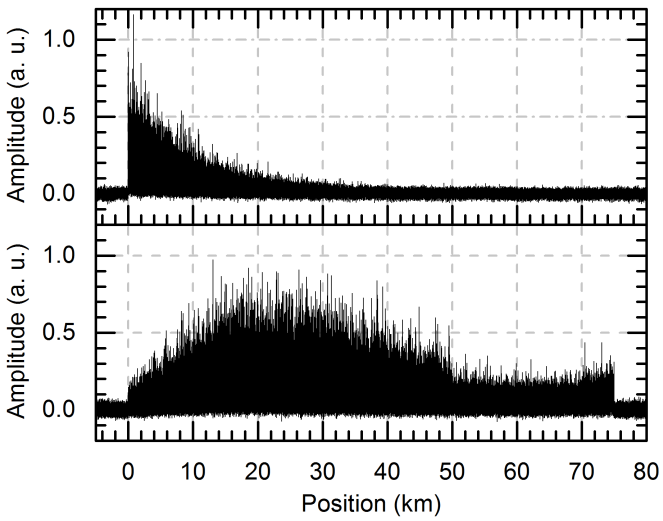

Figure 7.2: Detected traces in the experiment. Top - without distributed amplification and input peak power of 150 mW; Bottom - with distributed amplification and input peak power of 25 mW [181].

the traces are carried out using available models [21, 182], and the results are presented in red showing an excellent agreement with the experimental results.

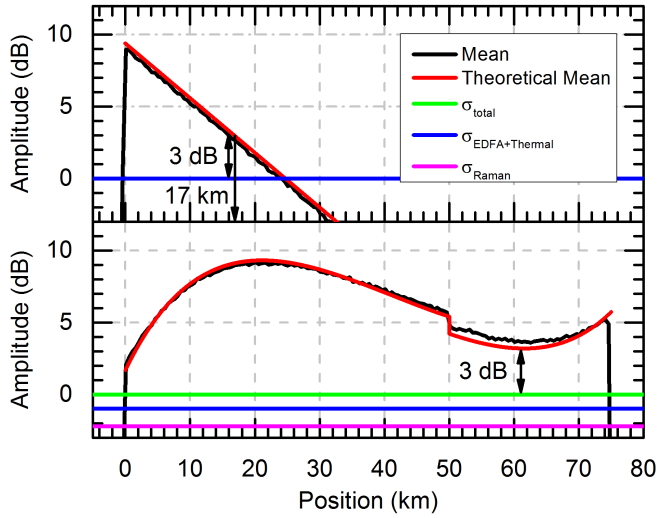

Figure 7.3: Detected traces and noise levels in logarithmic scale. The traces are normalized to their noise floor level. Top - without distributed amplification and input peak power of 150 mW; Bottom - with distributed amplification and input peak power of 25 mW [181].

In the case without distributed amplification (Figure 7.3 – top), an exponentially decaying trace is clearly visible, with an attenuation coefficient of $\alpha_T \sim 0.4$ dB/km. This corresponds to the double of the attenuation coefficient of the used fiber (∼0.2 dB/km), as expected from the fact that the pulse is attenuated in the forward direction while the backscattered light is attenuated in the backward direction (i.e. the net attenuation suffered by the optical trace is twice that of a single pass). On the other hand, the standard deviation of the different noise sources that affect the trace are also included in the figure. In particular, the thermal noise induced by the photodetector and the ASE noise introduced by the used EDFA have been

accounted for, resulting in a standard deviation of $\sigma_{\text{EDFA+Thermal}} = 1.86$ μW. It can be easily observed that the trace is completely buried under the noise after 25 km, and shows an SNR of 3 dB (minimum target SNR) at around only 17 km.

However, regarding the case with distributed amplification (Figure 7.3 – bottom), the trace SNR is always higher than 3 dB along the entire fiber (75 km). It is worth mentioning that this value of SNR is enough to measure vibrations, as it will be shown in the following Subsection 7.2.3.2. In this case, the theoretical signal and noise evolutions are obtained by considering the experimental input pulse peak power (25 mW) and Raman pump powers (350 mW and 230 mW co-propagating and counter-propagating to the pulse, respectively) [21, 182]. Losses of around 1 dB are estimated in the connection between the two fiber spools. Moreover, the noise produced by the Raman ASE is to the total noise, together with the ASE-ASE beat of the Raman pump [182]. An excellent match between experimental and theoretical values is obtained, including the noise levels. In particular, the estimated noise generated by these two contributions from the Raman source is $\sigma_{\text{Raman}} \sim 1.40$ μW (an optical bandwidth of 15 GHz and detection bandwidth of 1 GHz were considered). Thus, the total noise is given by $\sigma_{\text{T}} = \sqrt{\sigma^2_{\text{EDFA+Thermal}} + \sigma^2_{\text{Raman}}} = 2.28$ μW. The estimation of σ_{Raman} is in good agreement with the value obtained experimentally for σ_{T}, which is ~ 1.32 μW.

Next, the effects of MI on the proposed system are analyzed. For this purpose, probe pulses with different values of peak power are injected into the fiber, propagated along the 75 km fiber and subsequently analyzed with an Optical Spectrum Analyzer (OSA). The results are presented in Figure 7.4. The obtained results reveal that the pulses are spectrally distorted when their peak power is higher than 50 mW. In contrast, the effect of MI is negligible when the pulse peak power is 25 mW or below. Thus, a peak power of 25 mW seems in this case ideal to obtain the best SNR in the detected trace while avoiding non-linear effects.

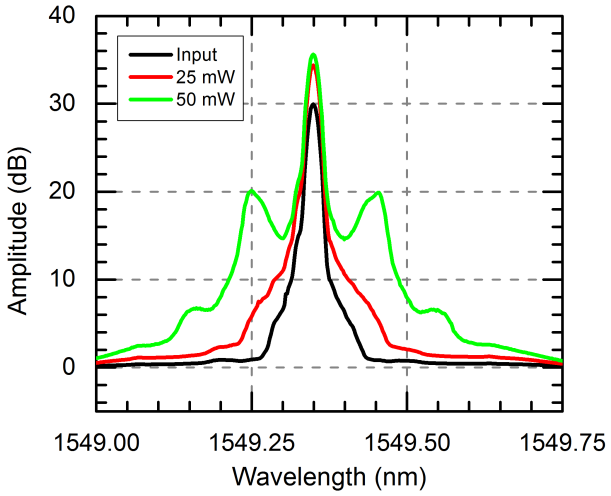

Figure 7.4: Measured spectrum after the propagation along the FUT (75 km) of pulses with 25 mW and 50 mW. The reference pulse spectrum is represented in black [181].

In addition, as it was previously explained, it is essential to maintain the linearity in the pulse instantaneous frequency profile for the proper behavior of the sensor. Therefore, we finally study whether the instantaneous frequency profile is distorted during the pulse propagation along the fiber. Hence, the intensity and instantaneous frequency profiles of the probe pulse at the beginning and at the end of the FUT are measured by means of coherent detection [115]. Recall that the pulse peak power is 25 mW and the fiber length is 75 km. The measurements are represented in Figure 7.5. In particular, Figure 7.5 – top shows the intensity profile of the pulse

at the beginning of the fiber (in black) and after propagation (red). It can be concluded that the intensity profile remains almost unchanged after the propagation. Figure 7.5 – bottom shows the instantaneous frequency profile of the pulse before (black) and after propagation (red). It is also possible to observe that the instantaneous frequency profile is not distorted and remains basically linear after the 75 km propagation. These results confirm that the employed optical pulse does not suffer from non-linear effects along the FUT when its peak power is kept below 25 mW. Under this precondition, vibrations can be properly measured using the presented scheme, as we will demonstrate in the next section.

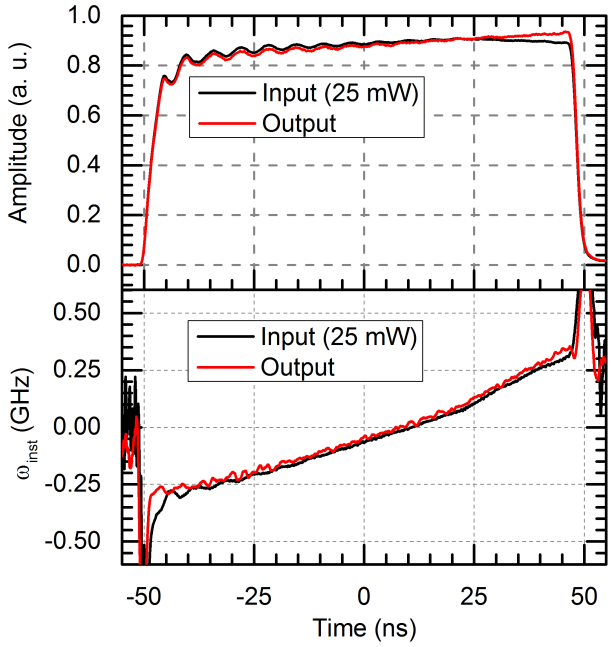

Figure 7.5: Measured optical pulses for characterization of distortions induced in the propagation along the FUT (75 km). The input pulse and the transmitted pulse are represented in black and red, respectively. The intensity profile is represented in the top of the figure and the instantaneous frequency profile in the bottom [181].

Other important concerns of the use of Raman-assisted configurations are usually the RIN transfer from the pump to the signal and the pump depletion. Interestingly, in our system the effect of the RIN transfer is equivalent to the effect in a standard ϕOTDR, since the affected bandwidth remains essentially similar in both cases (for these distances, the RIN transfer problem is spectrally bounded below 100 MHz for standard fibers, so it fully enters into the bandwidth of standard ϕOTDR detection) [21]. This means that there is basically no extra RIN noise in this case over the standard ϕOTDR case. Besides, simulations indicate that the temporal pulse degradation due to the pump depletion typically arises at peak powers much higher than the MI threshold, so we are always working within the safe operation range of the amplifier.

7.2.3.2 Vibration Sensing Over Long Distances

The feasibility of the presented sensor for dynamic measurement of strain with nano-strain resolution over 75 km of standard single-mode fiber is demonstrated in this section. A 20 m fiber section is strapped around a PZT in the 50 km of the FUT (which is the point with less SNR in the detected trace, namely 3 dB). The PZT is fed with a sinusoidal signal whose

frequency is modulated from 70 Hz to 150 Hz with a period of 10 s, thus applying a controlled vibration in the perturbed fiber section. The optical pulses are injected into the fiber with a repetition rate of 1 kHz, allowing us to measure up to 500 Hz vibrations, which is very close to the limit imposed by the pulse time of flight (700 Hz) [34]. The optical pulse length is 100 ns, its spectral content is 630 MHz and the traces are digitized with 40 GSps sampling rate. With these parameters, the system has a spatial resolution of 10 m and strain resolution of 1 nε [167].

The dynamic strain measurements are shown in Figure 7.6. The applied vibration is measured along 20 s (two frequency modulation periods between 70 Hz and 150 Hz). Figure 7.6(a) shows a detail of the measured strain between the instants 4.6 s and 4.8 s. The observed vibration amplitude is $\sim$50 nε. In this case, the measured strain is calculated by correlating all the measured traces always with the first one. Due to the fact that the maximum applied strain is $\sim$50 nε, the maximum frequency shift is $\sim$8 MHz, which is much lower than the spectral content of the pulse (630 MHz). For this reason, the measurement process is developed properly.

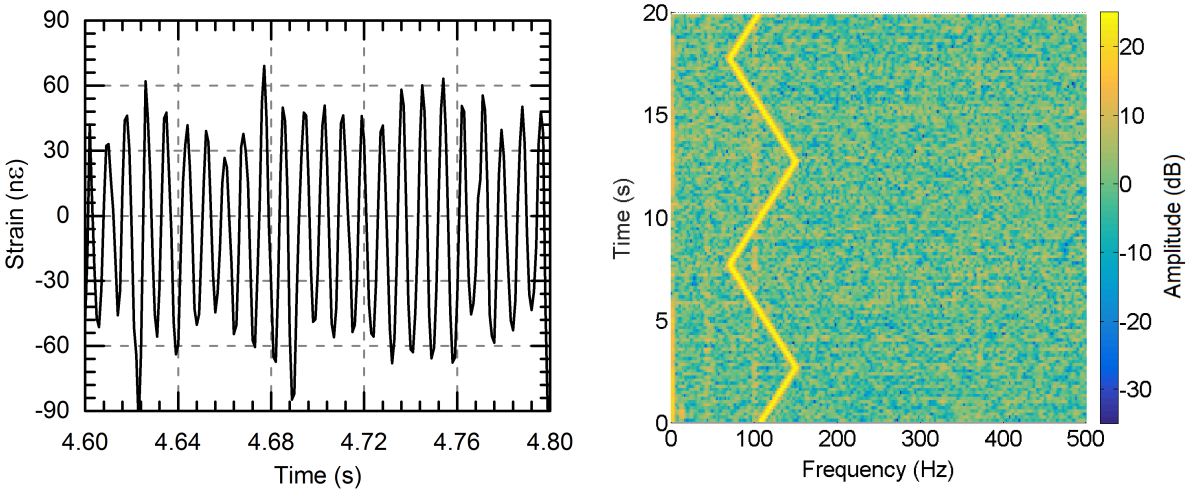

(a) (b)

Figure 7.6: Measured strain variations when a vibration (with linearly modulated frequency from 70 Hz to 150 Hz with a period of 5 s) is applied by a PZT in 20 m of fiber around kilometer 50 of the FUT during 20 s. a) Detail between 4.6 s and 4.8 s; b) Spectrogram (logarithmic scale – dB) along 20 s (instantaneous frequency calculated using a moving window of 300 ms width of the measured dynamic strain) [181].

Figure 7.6(b) presents the spectrogram of the measured vibration along 20 s. The instantaneous frequency of the spectrogram is calculated using a moving window of 300 ms width. It is observed that the vibration is measured with an SNR >20 dB, which allows us to successfully detect and quantify the applied sinusoidally-varying vibration signal. Here it is worth noting that in Chirped-Pulse ϕOTDR, the vibration measurement SNR relies on measurements of time shifts in sections of the trace, rather than on intensity/phase variations in single point of the trace. That is why it is possible to obtain a measurement SNR higher than the trace SNR. Also, as it has been previously demonstrated in Chapter 5, Chirped-pulse ϕOTDRs, unlike traditional ϕOTDRs, can provide absolute values of refractive index variations from the direct detection of the trace. This is well demonstrated herein, where the amplitude of the applied vibrations is well recorded and moreover, no harmonic component appears in Figure 7.6(b). It is worth highlighting that the presented results are obtained with no averaging (single shot), using direct detection (no phase recovery) and in the fiber point with lower SNR, which clearly demonstrates the potential of this system.

7.3 Conclusions

In this chapter, it has been proposed first-order Raman amplification as a suitable technique to extend the range of Chirped-Pulse ϕOTDR. To prove the viability of using this distributed amplification technique and experimental set up with 75 km of optical fiber has been implemented. The spatial resolution is in the order of typical values for this technology (10 m) and no averages were applied. The experimental measurements have been compared with numerical results and it has been shown their agreement. In terms of measurement range, this implies a six-fold improvement over the previous best published result using this technique [134]. Dynamic linear strain has been measured with a resolution of 1 nε, allowing precise detection and characterization of vibrations up to 500 Hz. The system was tested with a vibration whose frequency was modulated from 70 Hz to 150 Hz with a period of 10 s. The system can measure those vibrations with 20 dB SNR in the position of worse SNR of the trace, which is obtained in km 50 of the FUT. To date, it is the first system capable to realize linear and dynamic strain measurements along such long distance without the need for coherent detection, to the best of our knowledge. Additionally, the power limits for the onset of non-linear effects in the probe pulse during its propagation along the fiber have been studied. It is confirmed that the probe pulse does not suffer any distortion in its propagation along the FUT (neither in the intensity shape nor in the linear instantaneous frequency profile) whenever a proper value of input peak power is selected (below 25 mW in our particular setup).

Chapter 8

Conclusions and Open Lines

8.1 Conclusions and Original Contributions

Throughout this thesis dissertation, all the proposed objectives presented in Chapter 1 have been accomplished. The main original contributions of this dissertation and the final conclusions are the following ones:

- The most important linear and non-linear effects involved in a phase-sensitive Optical Time Domain Reflectometry (ϕOTDR) sensor have been studied. Particularly, the study has been focused on the phenomena of: Scattering Rayleigh, non-linear refraction, Self-Phase Modulation (SPM) and Modulation Instability (MI). The first is the basis of the sensor, and the others are the origin of its limitations. Other concepts such as Raman and Brillouing scattering processes, optical coherence and Chirped Pulse Amplification (CPA) are explained for the complete understanding of the text.

- A proper state of the art on ϕOTDR sensors has been presented. Two of the main limitations of this technique were studied and analyzed in detail. First, ϕOTDR presents a non-linear response to refractive index changes. Thus, in principle, ϕOTDR cannot quantify strain or temperature changes. Phase recovery or frequency sweep is required for that purpose. Second, as every distributed fiber sensor, there is a critical trade-off between the spatial resolution and range in ϕOTDR based sensors. Signal to Noise Ratio (SNR) depends on the amount of energy of the employed optical pulses. Increasing the input pulse peak power or the pulse duration (loosing spatial resolution) the SNR can be increased. However, the peak power cannot be increased indefinitely due to the onset of non-linear effects. This is a huge problem when high resolution measurements must be implemented as in wall or pipeline crack development monitoring, in which there is not enough SNR to develop any measurement.

- The impact of the use of probe pulses with different beam shapes on the backscattered power trace of ϕOTDR systems has been studied. The results show that rectangular-like pulses are the most detrimental for the range and sensitivity of ϕOTDR-based sensors, which are the most commonly used in these sensors. Nevertheless, Gaussian and triangular-shaped pulses show a better behavior in terms of evolution of the visibility along the distance, since a Gaussian or triangular envelope pulse limits the effect of modulation instability and mitigates the advent of the FPU recurrence. This enables an increase of the length range and sensitivity of the sensing system for the same peak power and nominal spatial resolution.

- In collaboration with the Institut National de la Recherche Scientifique (INRS) in Montreal (Canada), millimeter spatial resolution measurements were performed using a ϕOTDR sensor combined with CPA concepts. In the proposed technique, input pulses are temporally stretched by a suitable dispersive device, and the backscattered traces are re-compressed in the optical domain prior to detection. Implementing this idea, the probe pulse energy is substantially increased and the resulting SNR is higher without compromising the spatial resolution of the sensor. In our particular case, the chosen dispersive device is a Linearly Chirped Fiber Bragg Grating (LC-FBG). An SNR increase of 20 dB over the traditional ϕOTDR architecture in a system with 3 mm spatial resolution is demonstrated. The technique does not need coherent detection or signal post-processing. To the best of our knowledge, this is the first ϕOTDR capable of developing millimeter spatial resolution measuring.

- A methodology to obtain a linear response of a ϕOTDR based on the phase reconstruction of the backscattered signals using a self-refereed technique has been proposed. To

do this, we have study the applicability of Phase Reconstruction using Optical Ultrafast Differentiation (PROUD) in the regimes of ϕOTDR. The applicability of this technique to ϕOTDR is demonstrated by characterizing propagation-induced distortions in pulses in bandwidth regimes similar to those typically used in ϕOTDR. The bandwidth of the employed optical pulses was around 4 GHz, which fits with the commonly employed when coding is implemented in ϕOTDR.

- It has been provided a method based on ϕOTDR using chirped pulses to allow for the measurement of distributed strain and temperature changes, in a single shot and without the requirement of a frequency scan. In this system, a perturbation in the refractive index of the fiber is translated into a localized, controlled temporal shift of the backscattered trace. This temporal shift is proportional to the applied perturbation. The temporal shifts are calculated by means of temporal cross-correlations trace to trace. The complexity of the system is therefore not significantly increased when compared to traditional ϕOTDR systems using intensity-based detection. With the proposed method, it is possible to combine the best features of ϕOTDR which had been previously demonstrated by separate: on the one hand, fast measurements with a bandwidth only limited by the fiber length, potentially over several tens of kilometers with metric spatial resolutions; on the other hand, the linear measurement of temperature/strain variations with resolutions which can be several orders of magnitude below those provided by Brillouin. Since the measurement is relative, the range of temperature/strain measurements is in principle not limited, being in practice determined by how the cumulative errors of the measurement are handled. The technique allows for measurements at kHz rates, while maintaining reliability over several hours of measurement. The sensitivity can also be tuned by acting on the chirp of the pulses. Temperature/strain resolutions of 0.5mK/4nε were demonstrated.

- It was noticed that the laser phase-noise has an important detrimental impact in Chirped-Pulse ϕOTDR-based sensors. The random frequency drifts of the laser generate different temporal shifts in the traces. Thus, laser phase-noise induces an uncertainty in the temperature/strain measurement which is directly proportional to the laser frequency fluctuations (also proportional to the linewidth). Hence, narrower laser linewidths allow a significant increase in the SNR of the strain recording. Particularly, when the laser linewidth was decreased from 5 MHz to 25 kHz, an SNR enhancement of $\sim$22 dB was obtained. Additionally, a simple technique was presented to mitigate the induced temperature/strain uncertainty. When a fiber section is mechanically and thermally isolated, it is possible to quantify the laser frequency deviations and then compensate them. By using this method, up to 17 dB SNR enhancement has been achieved. This method reveals the robustness of Chirped-Pulse ϕOTDR. Without phase recovery or frequency sweep, single shot and quantitative strain/temperature measurements with high SNR are implemented using relatively low coherent laser sources.

- First-order Raman amplification was implemented to increment the sensing range of Chirped-Pulse ϕOTDR. The system was tested detecting vibrations in a 75 km fiber. The system can measure those vibrations with 20 dB SNR in the position of worse SNR of the trace, which is obtained in km 50 of the FUT. To date, it is the first system capable to realize linear and dynamic strain measurements along such long distance without the need for coherent detection, to the best of our knowledge. Additionally, the power limits for the onset of non-linear effects in the probe pulse during its propagation along the fiber was studied, showing no distortion when the peak power selected was below 25 mW.

8.2 Open Lines

The work presented in this thesis represents a remarkable improvement in the performance of ϕOTDR-based sensors. Chirped-Pulse Phase-Sensitive Time Domain Reflectometry has enabled a new generation of distributed acoustic sensors with improved performances, including notably a total absence of fading points in the signal sensitivity, a linear response and high sensitivity for measuring in real time temperature and strain. This technique would be a very interesting option for seismic, security and energy/environmental applications. In last months, it has attracted the interest of a large number of institutions (e.g Caltech, CEA) and companies (ADIF, INDRA, FLUVES, INPHOTECH...). Some of the possible applications of this new sensor that would be interesting to explore are the following ones:

- Chemical gas, ionizing radiation and magnetic fields sensing.
- Micro-leaks and micro-earthquakes detection.
- Distributed anemometer and bolometer.
- Monitoring the rolling process of optical fiber in a coil.

Noting that the "raw signal" for ϕOTDR is based on trace local displacements (differing from the traditional ϕOTDR), it would also be interesting to research for specific algorithms for this task, analyzing a suitable trade-off between computational cost and performance improvement. While the use of 2D algorithms (space & time) for the determination of trace local displacements can surely achieve better results than using the information of a single trace, such algorithms may be computationally too heavy and not suitable for real-time operation, as is intended for these sensors. On the other hand, simpler algorithms and/or trace pre-processing/denoising could provide better results than a simple use of cross-correlation.

While in this thesis high sensitivities have been achieved with Chirped-Pulse ϕOTDR, an in-depth discussion on the performance limits of the technique is yet to be developed. It would be interesting to analyse pratical/theoretical limits both on the optical domain (chirp slope, optical setup, etc.) and digital domain (signal processing/denoising, etc), as well as the performance trade-offs (spatial resolution vs SNR vs performance vs computational costs), aiming to understand what are the ultimate performance limits of this technique.

Further investigations on new signal processing approaches for further signal de-noising, enhanced sensitivity, improved spatial resolution and extended distance range are to be done. Furthermore, the development of pioneering artificial intelligence methods for pattern recognition, interpretation and alarm-raising in various possible end user scenarios (dike monitoring, offshore windfarms, energy transport, seismic array monitoring, perimeter security, etc) should also be developed.

While the absence of fading points in Chirped-Pulse ϕOTDR technique provides a remarkable improvement compared to the traditional ϕOTDR, where phase cannot be measured in trace points with low optical power, this improvement has not been quantified. A statistical study comparing the SNR variability of traditional ϕOTDR VS Chirped-Pulse ϕOTDR, providing a mathematical description of the system performance from the best to the worst point of trace SNR, would help quantifying one of the main improvements of this technique.

Another open line is related to the use of PROUD in ϕOTDR and measure real strain and temperature variations in an optical fiber using this phase recovery technique. In Chapter 4 the possibility of using PROUD in ϕOTDR is discussed. The applicability was demonstrated by

characterizing propagation-induced distortions in pulses in bandwidth regimes similar to those typically used in ϕOTDR. However, the phase of the backscattered signal has not been recovered. There is still a lot of work to be done on this subject.

Studying the applicability of the developed millimetrical ϕOTDR based on CPA concepts in new applications would be also interesting. We think the technique is particularly suitable for wall or pipeline crack development monitoring. These kind of breaks are characterized by being very small. For this reason, a conventional ϕOTDR sensor is not well adapted to this applications. In contrast, our proposal based on CPA concepts could give a reliable solution.

Finally, we found interesting to develop a ϕOTDR employing both CPA concepts and the advantages of using chirped-pulses. As the reader can imagine, a hybrid sensor based on the use of chirped-pulses for linear sensing and CPA concepts to increase the resolution would be disruptive.

Bibliography

[1] B. Culshaw and A. Kersey, "Fiber-Optic Sensing: A Historical Perspective," *Journal of Lightwave Technology*, vol. 26, no. 9, pp. 1064–1078, may 2008.

[2] A. Kersey, M. Davis, H. Patrick, M. LeBlanc, K. Koo, C. Askins, M. Putnam, and E. Friebele, "Fiber grating sensors," *Journal of Lightwave Technology*, vol. 15, no. 8, pp. 1442–1463, 1997.

[3] X. Bao and L. Chen, "Recent progress in distributed fiber optic sensors," *Sensors (Basel)*, vol. 12, no. 7, pp. 8601–8639, 2012.

[4] G. Bolognini, J. Park, M. A. Soto, N. Park, and F. Di Pasquale, "Analysis of distributed temperature sensing based on Raman scattering using OTDR coding and discrete Raman amplification," *Measurement Science and Technology*, vol. 18, no. 10, pp. 3211–3218, oct 2007.

[5] M. A. Soto, T. Nannipieri, A. Signorini, A. Lazzeri, F. Baronti, R. Roncella, G. Bolognini, and F. Di Pasquale, "Raman-based distributed temperature sensor with 1 m spatial resolution over 26 km SMF using low-repetition-rate cyclic pulse coding," *Optics Letters*, vol. 36, no. 13, pp. 2557–2559, jul 2011.

[6] X. Angulo-vinuesa, S. Martin-lopez, J. Nuño, P. Corredera, J. D. Ania-castañon, L. Thévenaz, and M. González-herráez, "Raman-Assisted Brillouin Distributed Temperature Sensor Over 100km Featuring 2m Resolution and 1.2C Uncertainty," *IEEE Journal of Lightwave Technology*, vol. 30, no. 8, pp. 1060–1065, 2012.

[7] K. Y. Song, M. Kishi, Z. He, and K. Hotate, "High-repetition-rate distributed Brillouin sensor based on optical correlation-domain analysis with differential frequency modulation," *Optics Letters*, vol. 36, no. 11, p. 2062, jun 2011.

[8] Y. Peled, A. Motil, and M. Tur, "Fast Brillouin optical time domain analysis for dynamic sensing," *Optics Express*, vol. 20, no. 8, p. 8584, apr 2012.

[9] Y. Peled, A. Motil, I. Kressel, and M. Tur, "Monitoring the propagation of mechanical waves using an optical fiber distributed and dynamic strain sensor based on BOTDA," *Optics Express*, vol. 21, no. 9, p. 10697, may 2013.

[10] A. Masoudi, M. Belal, and T. P. Newson, "Distributed dynamic large strain optical fiber sensor based on the detection of spontaneous Brillouin scattering." *Optics letters*, vol. 38, no. 17, pp. 3312–5, sep 2013.

[11] W. Eickhoff and R. Ulrich, "Optical frequency domain reflectometry in single-mode fiber," *Applied Physics Letters*, vol. 39, no. 9, pp. 693–695, nov 1981.

[12] S. Kingsley and D. Davies, "OFDR diagnostics for fibre and integrated-optic systems," *Electronics Letters*, vol. 21, no. 10, pp. 434–435, may 1985.

[13] J. von der Weid, R. Passy, G. Mussi, and N. Gisin, "On the characterization of optical fiber network components with optical frequency domain reflectometry," *Journal of Lightwave Technology*, vol. 15, no. 7, pp. 1131–1141, jul 1997.

[14] M. Froggatt and J. Moore, "High-spatial-resolution distributed strain measurement in optical fiber with Rayleigh scatter," *Applied Optics*, vol. 37, no. 10, p. 1735, apr 1998.

[15] P. Oberson, B. Huttner, O. Guinnard, L. Guinnard, G. Ribordy, and N. Gisin, "Optical frequency domain reflectometry with a narrow linewidth fiber laser," *IEEE Photonics Technology Letters*, vol. 12, no. 7, pp. 867–869, jul 2000.

[16] B. J. Soller, D. K. Gifford, M. S. Wolfe, and M. E. Froggatt, "High resolution optical frequency domain reflectometry for characterization of components and assemblies," *Optics Express*, vol. 13, no. 2, p. 666, 2005.

[17] D.-P. Zhou, Z. Qin, W. Li, L. Chen, and X. Bao, "Distributed vibration sensing with time-resolved optical frequency-domain reflectometry," *Optics Express*, vol. 20, no. 12, p. 13138, 2012.

[18] D. Yang, L. Tiegen, D. Zhenyang, H. Qun, L. Kun, J. Junfeng, C. Qinnan, and F. Bowen, "Cryogenic temperature measurement using Rayleigh backscattering spectra shift by OFDR," *Photonics Technology Letters*, vol. 26, no. 11, pp. 1150–1153, 2014.

[19] Y.-J. Rao, J. Luo, Z.-L. Ran, J.-F. Yue, X.-D. Luo, and Z. Zhou, "Long-distance fiber-optic Φ-OTDR intrusion sensing system," J. D. C. Jones, Ed., vol. 7503. International Society for Optics and Photonics, oct 2009, p. 75031O.

[20] J. Wang, X.-H. Jia, Y.-J. Rao, and H.-J. Wu, "Phase-sensitive optical time-domain reflectometer based on bi-directional Raman amplification," *Acta Physica Sinica*, vol. 62, no. 4, 2013.

[21] H. F. Martins, S. Martin-Lopez, P. Corredera, M. L. Filograno, O. Frazao, and M. Gonzalez-Herraez, "Phase-sensitive optical time domain reflectometer assisted by first-order raman amplification for distributed vibration sensing over >100 km," *Journal of Lightwave Technology*, vol. 32, no. 8, pp. 1510–1518, 2014.

[22] H. F. Martins, S. Martin-Lopez, M. L. Filograno, P. Corredera, O. Frazão, and M. Gonzalez-Herraez, "Comparison of the use of first and second-order Raman amplification to assist a phase-sensitive optical time domain reflectometer in distributed vibration sensing over 125 km," in *23rd International Conference on Optical Fibre Sensors*, vol. 9157, 2014, p. 91576K.

[23] H. F. Martins, S. Martin-Lopez, P. Corredera, J. D. Ania-Castanon, O. Frazao, and M. Gonzalez-Herraez, "Distributed Vibration Sensing Over 125 km With Enhanced SNR Using Phi-OTDR Over a URFL Cavity," *Journal of Lightwave Technology*, vol. 33, no. 12, pp. 2628–2632, 2015.

[24] F. Peng, H. Wu, X.-H. Jia, Y.-J. Rao, Z.-N. Wang, and Z.-P. Peng, "Ultra-long high-sensitivity Φ-OTDR for high spatial resolution intrusion detection of pipelines," *Optics Express*, vol. 22, no. 11, p. 13804, jun 2014.

[25] J. Li, Z. Wang, L. Zhang, F. Peng, S. Xiao, H. Wu, and Y. Rao, "124km phase-sensitive OTDR with Brillouin amplification," in *23rd International Conference on Optical Fibre Sensors, 2014*, vol. 9157, 2014, p. 91575Z.

[26] Z. N. Wang, J. Li, M. Q. Fan, L. Zhang, F. Peng, H. Wu, J. J. Zeng, Y. Zhou, and Y. J. Rao, "Phase-sensitive optical time-domain reflectometry with Brillouin amplification," *Optics Letters*, vol. 39, no. 15, p. 4313, 2014.

[27] Z. N. Wang, J. J. Zeng, J. Li, M. Q. Fan, H. Wu, F. Peng, L. Zhang, Y. Zhou, and Y. J. Rao, "Ultra-long phase-sensitive OTDR with hybrid distributed amplification," *Optics Letters*, vol. 39, no. 20, pp. 5866–5869, 2014.

[28] P. Healey and D. J. Malyon, "Otdr in single-mode fiber at 1.5-mu-m using heterodine-detection," *Electronics Letters*, vol. 18, no. 20, pp. 862–863, 1982.

[29] R. Posey Jr., G. A. Johnson, and S. T. Vohra, "Strain sensing based on coherent Rayleigh scattering in an optical fibre," *Electronics Letters*, vol. 36, no. 20, pp. 1688–1689, 2000.

[30] Y. Lu, T. Zhu, L. Chen, and X. Bao, "Distributed vibration sensor based on coherent detection of phase-OTDR," *Journal of Lightwave Technology*, vol. 28, no. 22, pp. 3243–3249, 2010.

[31] A. Masoudi, M. Belal, and T. P. Newson, "A distributed optical fibre dynamic strain sensor based on phase-OTDR," *Measurement Science and Technology*, vol. 24, no. 8, p. 085204, aug 2013.

[32] Z. Wang, L. Zhang, S. Wang, N. Xue, F. Peng, M. Fan, W. Sun, X. Qian, J. Rao, and Y. Rao, "Coherent Φ-OTDR based on I/Q demodulation and homodyne detection," *Optics Express*, vol. 24, no. 2, p. 853, jan 2016.

[33] G. Tu, X. Zhang, Y. Zhang, F. Zhu, L. Xia, and B. Nakarmi, "The development of an Φ-OTDR system for quantitative vibration measurement," *IEEE Photonics Technology Letters*, vol. 27, no. 12, pp. 1349–1352, jun 2015.

[34] H. F. Martins, S. Martín-López, P. Corredera, M. L. Filograno, O. Frazão, and M. González-Herráez, "Coherent noise reduction in high visibility phase sensitive optical time domain reflectometer for distributed sensing of ultrasonic waves," *Journal of Lightwave Technology*, vol. 31, no. 23, pp. 3631–3637, 2013.

[35] Z. Qin, L. Chen, and X. Bao, "Wavelet denoising method for improving detection performance of distributed vibration sensor," *IEEE Photonics Technology Letters*, vol. 24, no. 7, pp. 542–544, 2012.

[36] Y. Koyamada, M. Imahama, K. Kubota, and K. Hogari, "Fiber-optic distributed strain and temperature sensing with very high measurand resolution over long range using coherent OTDR," *Journal of Lightwave Technology*, vol. 27, no. 9, pp. 1142–1146, 2009.

[37] L. Zhou, F. Wang, X. Wang, Y. Pan, Z. Sun, J. Hua, and X. Zhang, "Distributed Strain and Vibration Sensing System Based on Phase-Sensitive OTDR," *IEEE Photonics Technology Letters*, vol. 27, no. 17, pp. 1884–1887, sep 2015.

[38] M. A. Soto, X. Lu, H. F. Martins, M. Gonzalez-Herraez, and L. Thevenaz, "Distributed phase birefringence measurements based on polarization correlation in phase-sensitive optical time-domain reflectometers," *Optics express*, vol. 23, no. 19, pp. 24 923–24 936, 2015.

[39] X. Lu, M. A. Soto, and L. Thévenaz, "Temperature-strain discrimination in distributed optical fiber sensing using phase- sensitive optical time-domain reflectometry," vol. 25, no. 14, pp. 1523–1525, 2017.

[40] G. P. Agrawal, *Nonlinear fiber optics*. Academic Press, 2013.

[41] R. W. Boyd, *Nonlinear Optics*, third edit ed., 2008.

[42] E. G. Neumann, *Single-Mode Fibers*. Springer-Verlag, 1988.

[43] A. Ghatak and K. Thyagarajan, *Introduction to Fiber Optics*. Cambridge University Press, 1999.

[44] D. Keck, R. Maurer, and P. Schultz, "On the ultimate lower limit of attenuation in glass optical waveguides," *Applied Physics Letters*, vol. 22, no. 7, pp. 307–309, apr 1973.

[45] X. Angulo-Vinuesa, "Ultra-Long Range Brillouin Optical Time Domain Analysis," Ph.D. dissertation, Universidad de Acalá, 2014.

[46] S. Martin-Lopez, "Generación de supercontinuo en fibras ópticas monomodo con fuentes de bombeo continuo," Ph.D. dissertation, Universidad Complutense de Madrid, 2006.

[47] B. J. Ainslie and C. R. Day, "A Review of Single-Mode Fibers with Modified Dispersion Characteristics," *Journal of Lightwave Technology*, vol. 4, no. 8, pp. 967–979, 1986.

[48] D. Strickland and G. Mourou, "Compression of amplified chirped optical pulses," *Optics Communications*, vol. 56, no. 3, pp. 219–221, dec 1985.

[49] C. Caucheteur, D. Bigourd, E. Hugonnot, P. Szriftgiser, A. Kudlinski, M. Gonzalez-Herraez, and A. Mussot, "Experimental demonstration of optical parametric chirped pulse amplification in optical fiber," *Optics Letters*, vol. 35, no. 11, p. 1786, jun 2010.

[50] K. Tai, A. Hasegawa, and A. Tomita, "Observation of modulational instability in optical fibers," *Physical Review Letters*, vol. 56, no. 2, pp. 135–138, jan 1986.

[51] M. Alem, "Impact of modulation instability on distributed optical fiber sensors," Ph.D. dissertation, École Polytechnique Fédérale de Lausanne, 2016.

[52] M. Born and E. Wolf, *Principles of optics: electromagnetic theory of propagation, interference and diffraction of light*. Cambridge University Press, 1999.

[53] B. E. A. Saleh and M. C. Teich, *Fundamentals of photonics*. Wiley, 2007.

[54] L. Abrardi, "Experimental study of new mechanisms for the development of spectrally-controlled supercontinuum sources in optical fibres under continuous-wave pumping," Ph.D. dissertation, Universidad de Alcalá, 2008.

[55] I. Fabelinskii, *Molecular Scattering of Light*. New York: Plenum Press, 1968.

[56] R. P. Feynman, R. B. Leighton, and M. Sands, *The Feynman Lectures on Physics, Vol. I*. MA: Addison-Wesley, 1963.

[57] X. Lu, "Coherent Rayleigh time domain reflectometry: novel applications for optical fiber sensing," Ph.D. dissertation, École Polytechnique Fédérale de Lausanne, 2016.

[58] H. F. Martins, "Distributed and remote fiber sensing assited by raman effect," Ph.D. dissertation, Universidade do Porto, 2014.

[59] W. Zou, X. Long, and J. Chen, "Brillouin Scattering in Optical Fibers and Its Application to Distributed Sensors," in *Adv. Opt. Fiber Technol. Fundam. Opt. Phenom. Appl.*, 2015, pp. 3–54.

[60] J. W. S. Lord Rayleigh, "On the light from the sky, its polarization and colour," *Philosophical Magazine*, vol. 41, no. 273, pp. 274–279, 1871.

[61] R. B. Miles, W. R. Lempert, and J. N. Forkey, "Laser Rayleigh scattering," *Meas. Sci. Technol*, vol. 12, pp. 33–51, 2001.

[62] J. D. Jackson, *Classical Electrodynamics*. New York: Wiley, 1982.

[63] A. T. Young, "Rayleigh scattering," *Physics Today*, vol. 35, no. 1, pp. 42–48, jan 1982.

[64] R. Hui and M. O'Sullivan, *Fiber Optic Measurement Techniques*. Academic Press, 2009.

[65] M. J. Damzen, V. I. Vlad, V. Babin, and A. Mocofanescu, *Stimulated Brillouin Scattering: Fundamentals and Applications*. Institute of Physics Publishing„ 2003.

[66] C. V. Raman, "A new radiation," *Indian J. Phys.*, vol. 37, no. 2, pp. 387–398, 1928.

[67] E. J. Woodbury and W. K. Ng, "Ruby laser operation in the near IR," *Proc. IRE*, vol. 50, no. 11, p. 2367, 1962.

[68] G. Eckhardt, R. W. Hellwarth, F. J. McClung, S. E. Schwarz, D. Weiner, and E. J. Woodbury, "Stimulated Raman Scattering From Organic Liquids," *Phys. Rev. Lett.*, vol. 9, no. 11, pp. 455–457, 1962.

[69] J. D. Ania-Castañón, T. J. Ellingham, R. Ibbotson, X. Chen, L. Zhang, and S. K. Turitsyn, "Ultralong Raman Fiber Lasers as Virtually Lossless Optical Media," *Physical Review Letters*, vol. 96, no. 2, 2006.

[70] F. Rodriguez-Barrios, S. Martin-Lopez, A. Carrasco-Sanz, P. Corredera, J. D. Ania-Castanon, L. Thevenaz, and M. Gonzalez-Herraez, "Distributed Brillouin Fiber Sensor Assisted by First-Order Raman Amplification," *Journal of Lightwave Technology*, vol. 28, no. 15, pp. 2162–2172, aug 2010.

[71] R. G. Smith, "Optical power handling capacity of low loss optical fibers as determined by stimulated Raman and Brillouin scattering," *App. Optics*, vol. 11, no. 11, pp. 2489–2494, 1972.

[72] H. F. Taylor and C. E. Lee, "Apparatus and method for fiber optic intrusion sensing," 1993.

[73] M. K. Barnoski and S. M. Jensen, "Fiber waveguides: a novel technique for investigating attenuation characteristics," *Applied Optics*, vol. 15, no. 9, pp. 2112–2115, 1976.

[74] M. K. Barnoski, M. D. Rourke, S. M. Jensen, and R. T. Melville, "Optical time domain reflectometer," *Applied Optics*, vol. 16, no. 9, pp. 2375–2379, sep 1977.

[75] D. Philen, I. White, J. Kuhl, and S. Mettler, "Single-mode fiber OTDR: experiment and theory," *IEEE Journal of Quantum Electronics*, vol. QE-18, no. 10, pp. 1499–1508, 1982.

[76] A. J. Rogers, "Polarization optica-time domain reflectometry," *Electronics Letters*, vol. 16, no. 13, pp. 489–490, 1980.

[77] M. Wuilpart, P. Megret, M. Blondel, A. Rogers, and Y. Defosse, "Measurement of the spatial distribution of birefringence in optical fibers," *IEEE Photonics Technology Letters*, vol. 13, no. 8, pp. 836–838, aug 2001.

[78] F. Corsi, A. Galtarossa, and L. Palmieri, "Polarization mode dispersion characterization of single-mode optical fiber using backscattering technique," *Journal of Lightwave Technology*, vol. 16, no. 10, pp. 1832–1843, 1998.

[79] J. Elhison and A. Siddiqui, "A fully polarimetric optical time-domain reflectometer," *IEEE Photonics Technology Letters*, vol. 10, no. 2, pp. 246–248, feb 1998.

[80] B. Huttner, B. Gisin, and N. Gisin, "Distributed PMD measurement with a polarization-OTDR in optical fibers," *Journal of Lightwave Technology*, vol. 17, no. 10, pp. 1843–1848, 1999.

[81] A. Galtarossa and L. Palmieri, "Spatially Resolved PMD Measurements," *Journal of Lightwave Technology*, vol. 22, no. 4, pp. 1103–1115, apr 2004.

[82] F. Peng, Z. Wang, Y.-J. Rao, and X.-H. Jia, "106km fully-distributed fiber-optic fence based on P-OTDR with 2nd-order Raman amplification," in *Optical Fiber Communication Conference/National Fiber Optic Engineers Conference 2013*. Washington, D.C.: OSA, mar 2013, p. JW2A.22.

[83] N. Linze, P. Megret, and M. Wuilpart, "Development of an Intrusion Sensor Based on a Polarization-OTDR System," *IEEE Sensors Journal*, vol. 12, no. 10, pp. 3005–3009, oct 2012.

[84] Z. Zhang and X. Bao, "Distributed optical fiber vibration sensor based on spectrum analysis of Polarization-OTDR system," *Optics Express*, vol. 16, no. 14, p. 10240, jul 2008.

[85] S. Le Floch, F. Sauser, M. A. Soto, and L. Thévenaz, "Time/frequency coding for Brillouin distributed sensors," in *Optical Fiber Sensors*, 2012.

[86] M. A. Soto, G. Bolognini, and F. Di Pasquale, "Analysis of pulse modulation format in coded BOTDA sensors," *Optics Express*, vol. 18, no. 14, pp. 14 878–14 892, jul 2010.

[87] M. A. Soto, G. Bolognini, F. Di Pasquale, and L. Thévenaz, "Simplex-coded BOTDA fiber sensor with 1 m spatial resolution over a 50 km range," *Optics Letters*, vol. 35, no. 2, pp. 259–261, jan 2010.

[88] M. Jones, "Using simplex codes to improve OTDR sensitivity," *IEEE Photonics Technology Letters*, vol. 5, no. 7, pp. 822–824, jul 1993.

[89] Duckey Lee, Hosung Yoon, Pilhan Kim, Jonghan Park, and Namkyoo Park, "Optimization of SNR improvement in the noncoherent OTDR based on simplex codes," *Journal of Lightwave Technology*, vol. 24, no. 1, pp. 322–328, jan 2006.

[90] Y. Muanenda, C. J. Oton, S. Faralli, T. Nannipieri, A. Signorini, and F. Di Pasquale, "Hybrid distributed acoustic and temperature sensor using a commercial off-the-shelf DFB laser and direct detection," *Optics Letters*, vol. 41, no. 3, pp. 587–590, 2016.

[91] Y. Muanenda, C. J. Oton, S. Faralli, and F. D. Pasquale, "A Cost-Effective Distributed Acoustic Sensor Using a Commercial Off-the-Shelf DFB Laser and Direct Detection A Cost-Effective Distributed Acoustic Sensor Using a Commercial Off-the-Shelf DFB Laser and Direct Detection Phase-OTDR," vol. 8, no. 1, 2016.

[92] H. F. Martins, K. Shi, B. C. Thomsen, S. Martin-Lopez, M. Gonzalez-Herraez, and S. J. Savory, "Real time dynamic strain monitoring of optical links using the backreflection of live PSK data," *Optics Express*, vol. 24, no. 19, p. 22303, 2016.

[93] H. F. Martins, K. Shi, B. C. Thomsen, S. Martin-Lopez, M. Gonzalez-Herraez, and S. J. Savory, "Code length limit in phase-sensitive OTDR using ultralong (>1M bits) pulse sequences due to fading induced by fiber optical path drifts," in *25th International Conference on Optical Fibre Sensors*, apr 2017, p. 103235W.

[94] W. Zou, S. Yang, X. Long, and J. Chen, "Optical pulse compression reflectometry: proposal and proof-of-concept experiment," *Optics Express*, vol. 23, no. 1, p. 512, jan 2015.

[95] B. Lu, Z. Pan, Z. Wang, H. Zheng, Q. Ye, R. Qu, and H. Cai, "High spatial resolution phase-sensitive optical time domain reflectometer with a frequency-swept pulse," *Optics Letters*, vol. 42, no. 3, p. 391, feb 2017.

[96] J. J. Mompó, S. Martín-López, M. González-Herráez, and A. Loayssa, "Sidelobe apodization in optical pulse compression reflectometry for fiber optic distributed acoustic sensing," *Optics Letters*, vol. 43, no. 7, 2018.

[97] Z. Qin, L. Chen, and X. Bao, "Continuous wavelet transform for non-stationary vibration detection with phase-OTDR," *Optics Express*, vol. 20, no. 18, p. 20459, aug 2012.

[98] T. Zhu, X. Xiao, Q. He, and D. Diao, "Enhancement of SNR and Spatial Resolution in phi-OTDR System by Using Two-Dimensional Edge Detection Method," *Journal of Lightwave Technology*, vol. 31, no. 17, pp. 2851–2856, 2013.

[99] H. He, L. Shao, H. Li, W. Pan, B. Luo, X. Zou, and L. Yan, "SNR Enhancement in Phase-Sensitive OTDR with Adaptive 2-D Bilateral Filtering Algorithm SNR Enhancement in Phase-Sensitive OTDR with Adaptive 2-D Bilateral," vol. 9, no. 3, 2017.

[100] H. Yue, B. Zhang, Y. Wu, B. Zhao, J. Li, Z. Ou, and Y. Liu, "Simultaneous and signal-to-noise ratio enhancement extraction of vibration location and frequency information in phase-sensitive optical time domain reflectometry distributed sensing system," *Optical Engineering*, vol. 54, no. 4, p. 047101, 2015.

[101] Corning, "Product information: Corning SMF-28 Ultra Optical Fiber." [Online]. Available: https://www.corning.com/media/worldwide/coc/documents/Fiber/SMF-28Ultra.pdf

[102] S. Haykin and M. Moher, *Communication Systems*, 5th ed. John Wiley & Sons Ltd, 2009.

[103] A. V. Oppenheim and A. S. Willsky, *Signals And Systems*, 2nd ed. Pearson, 2017.

[104] A. K. Wojcik, "Signal Statistics of Phase Dependent Optical Time Domain Reflectometry," Ph.D. dissertation, Texas A&M University, 2006.

[105] K. Shimizu, T. Horiguchi, and Y. Koyamada, "Characteristics and Reduction of Coherent Fading Noise in Rayleigh Backscattering Measurement for Optical Fibers and Components," *Journal of Lightwave Technology*, vol. 10, no. 7, pp. 982–988, 1992.

[106] H. F. Martins, S. Martin-Lopez, P. Corredera, P. Salgado, O. Frazão, and M. González-Herráez, "Modulation instability-induced fading in phase-sensitive optical time-domain reflectometry," *Optics Letters*, vol. 38, no. 6, p. 872, 2013.

[107] H. Izumita, Y. Koyamada, and S.-i. Furukawa, "The performance limit of coherent OTDR enhanced with optical fiber amplifiers due to optical nonline - Lightwave Technology, Journal of," *Lightwave*, vol. 12, no. 7, pp. 1230–1238, 1994.

[108] J. Park and H. F. Taylor, "Fiber optic intrusion sensor," *Fiber Optic Sensors V*, vol. 2895, pp. 214–221, 1996.

[109] J. H. Park, W. K. Lee, and H. F. Taylor, "A fiber optic intrusion sensor with the configuration of an optical time domain reflectometer using coherent interference of Rayleigh backscattering," *Optical and Fiber Optic Sensor Systems*, vol. 3555, pp. 49–56, 1998.

[110] K. N. Choi and H. F. Taylor, "Spectrally stable Er-fiber laser for application in phase-sensitive optical time-domain reflectometry," *Photonics Technology Letters*, vol. 15, no. 3, pp. 386–388, 2003.

[111] J. C. Juarez, E. W. Maier, K. N. Choi, and H. F. Taylor, "Distributed fiber-optic intrusion sensor system," *Journal of Lightwave Technology*, vol. 23, no. 6, pp. 2081–2087, 2005.

[112] J. C. Juarez and H. F. Taylor, "Field test of a distributed fiber-optic intrusion sensor system for long perimeters," *Applied Optics*, vol. 46, no. 11, pp. 1968–1971, 2007.

[113] Z. Pan, Z. Wang, Q. Ye, H. Cai, R. Qu, and Z. Fang, "High sampling rate multi-pulse phase-sensitive OTDR employing frequency division multiplexing," in *23rd International Conference on Optical Fibre Sensors*, 2014, p. 9157.

[114] S. V. Shatalin, V. N. Treschikov, and A. J. Rogers, "Interferometric optical time-domain reflectometry for distributed optical-fiber sensing." *Applied optics*, vol. 37, no. 24, pp. 5600–5604, 1998.

[115] E. Ip, A. Pak, T. Lau, D. J. F. Barros, and J. M. Kahn, "Coherent detection in optical fiber systems," *Optics Express*, vol. 16, no. 2, pp. 753–791, 2008.

[116] H. Izumita, Y. Koyamada, S. I. Furukawa, and I. Sankawa, "Stochastic amplitude fluctuation in coherent OTDR and a new technique for its reduction by stimulating synchronous optical frequency hopping," *Journal of Lightwave Technology*, vol. 15, no. 2, pp. 267–277, 1997.

[117] H. F. Martins, J. Pastor-Graells, L. R. Cortés, D. Piote, S. Martin-Lopez, J. Azaña, and M. Gonzalez-Herraez, "PROUD-based method for simple real-time in-line characterization of propagation-induced distortions in NRZ data signals," *Optics Letters*, vol. 40, no. 18, p. 4356, 2015.

[118] F. Li, Y. Park, and J. Azaña, "Complete temporal pulse characterization based on phase reconstruction using optical ultrafast differentiation (PROUD)," *Optics Letters*, vol. 32, no. 22, p. 3364, nov 2007.

[119] J. Azaña, Y. Park, and F. Li, "Linear self-referenced complex-field characterization of fast optical signals using photonic differentiation," *Optics Communications*, vol. 284, no. 15, pp. 3772–3784, 2011.

[120] G. Agrawal, *Fiber Optic Communication Systems*. New York: Wiley, 2002.

[121] O. V. Sinkin, R. Holzlöhner, J. Zweck, and C. R. Menyuk, "Optimization of the Split-Step Fourier Method in Modeling Optical-Fiber Communications Systems," *Journal of Lightwave Technology*, vol. 21, no. 1, p. 61, jan 2003.

[122] G. Van Simaeys, P. Emplit, and M. Haelterman, "Experimental Demonstration of the Fermi-Pasta-Ulam Recurrence in a Modulationally Unstable Optical Wave," *Physical Review Letters*, vol. 87, no. 3, p. 033902, jun 2001.

[123] ——, "Experimental study of the reversible behavior of modulational instability in optical fibers," *Journal of the Optical Society of America B*, vol. 19, no. 3, p. 477, mar 2002.

[124] M. R. Fernández-Ruiz, H. F. Martins, J. Pastor-Graells, S. Martin-lopez, and M. González-herráez, "Phase-sensitive OTDR probe pulse shapes robust against modulation-instability fading," *Optics letters*, vol. 41, no. 24, pp. 5756–5759, 2016.

[125] M. N. Alahbabi, Y. T. Cho, and T. P. Newson, "150-km-range distributed temperature sensor based on coherent detection of spontaneous Brillouin backscatter and in-line Raman amplification," *Journal of the Optical Society of America B*, vol. 22, no. 6, p. 1321, jun 2005.

[126] S. Martin-Lopez, M. Alcon-Camas, F. Rodriguez, P. Corredera, J. D. Ania-Castañon, L. Thévenaz, and M. Gonzalez-Herraez, "Brillouin optical time-domain analysis assisted by second-order Raman amplification," *Optics Express*, vol. 18, no. 18, p. 18769, aug 2010.

[127] H. Martins, M. B. Marques, and O. Frazão, "300 km-ultralong Raman fiber lasers using a distributed mirror for sensing applications," *Optics Express*, vol. 19, no. 19, pp. 18 149–18 154, 2011.

[128] J. Hegarty, N. Olsson, and L. Goldner, "CW pumped Raman preamplifier in a 45 km-long fibre transmission system operating at 1.5 μm and 1 Gbit/s," *Electronics Letters*, vol. 21, no. 7, pp. 290–292, 1985.

[129] Y. Aoki, "Properties of fiber Raman amplifiers and their applicability to digital optical communication systems," *Journal of Lightwave Technology*, vol. 6, no. 7, pp. 1225–1239, 1988.

[130] P. Hansen, L. Eskildsen, S. Grubb, A. Stentz, T. Strasser, J. Judkins, J. DeMarco, R. Pedrazzani, and D. DiGiovanni, "Capacity upgrades of transmission systems by Raman amplification," *IEEE Photonics Technology Letters*, vol. 9, no. 2, pp. 262–264, 1997.

[131] B. Bristiel, S. Jiang, P. Gallion, and E. Pincemin, "New Model of Noise Figure and RIN Transfer in Fiber Raman Amplifiers," *IEEE Photonics Technology Letters*, vol. 18, no. 8, pp. 980–982, 2006.

[132] J. Nuño, M. Alcon-Camas, and J. Ania-Castañón, "RIN transfer in random distributed feedback fiber lasers," *Optics Express*, vol. 20, no. 24, pp. 27 376–27 381, nov 2012.

[133] M. Alcón-Camas and J. D. Ania-Castañón, "RIN transfer in 2nd-order distributed amplification with ultralong fiber lasers," *Optics Express*, vol. 18, no. 23, pp. 23 569–23 575, 2010.

[134] A. Garcia-Ruiz, H. F. Martins, J. Pastor-Graells, S. Martin-Lopez, and M. Gonzalez-Herraez, "Single-Shot True Distributed Strain Variation Measurements Over >10 km Using Phase-Sensitive OTDR with Chirped Pulses," in *Asia Pacific Optical Sensors Conference*. OSA, 2016, p. Th3A.2.

[135] M. A. Richards, *Fundamentals of Radar Signal Processing*. McGraw-Hill Education, 2005.

[136] D. Marr and E. Hildreth, "Theory of edge detection," in *Proc. R. Soc. Lond., vol. B207*, 1980, pp. 187–217.

[137] M. A. Soto, J. A. Ramírez, and L. Thévenaz, "Intensifying the response of distributed optical fibre sensors using 2D and 3D image restoration," *Nature Communications*, vol. 7, no. 10870, 2016.

[138] M. Elad, "On the origin of the bilateral filter and ways to improve it," *IEEE Trans. Image Process.*, vol. 11, no. 10, pp. 1141–1151, 2002.

[139] M. Zhang and B. K. Gunturk, "Multiresolution bilateral filtering for image denoising," *IEEE Trans. Image Process.*, vol. 17, no. 12, pp. 2324–2333, 2008.

[140] S. Paris and F. Durand, "A fast approximation of the bilateral filter using a signal processing approach," *Int. J. Comput. Vis.*, vol. 81, no. 1, pp. 24–52, 2009.

[141] F. Durand and J. Dorsey, "Fast bilateral filtering for the display of high-dynamic-range images," *ACM Trans. Graph.*, vol. 21, no. 3, pp. 257–266, 2002.

[142] J. Pastor-Graells, L. R. Cortés, M. R. Fernández-Ruiz, H. F. Martins, J. Azaña, S. Martin-Lopez, and M. Gonzalez-Herraez, "SNR enhancement in high-resolution phase-sensitive OTDR systems using chirped pulse amplification concepts," *Optics Letters*, vol. 42, no. 9, p. 1728, may 2017.

[143] J. Pastor Graells, S. Martin-Lopez, M. Gonzalez-Herraez, A. Villafranca-Velasco, P. Corredera-Guillen, and H. F. Martins, "System and method of distributed scattering profile characterization of an optical fibre," 2015.

[144] S. M. Foaleng, F. Rodríguez-Barrios, S. Martin-Lopez, M. González-Herráez, and L. Thévenaz, "Detrimental effect of self-phase modulation on the performance of Brillouin distributed fiber sensors." *Optics letters*, vol. 36, no. 2, pp. 97–9, jan 2011.

[145] L. Liokumovich, N. Ushakov, O. Kotov, M. Bisyarin, and A. Hartog, "Fundamentals of optical fiber sensing schemes based on coherent optical time domain reflectometry: Signal model under static fiber conditions," *Journal of Lightwave Technology*, vol. 33, no. 17, pp. 1–1, 2015.

[146] T. Sato, Y. Azuma, K. Yoshiba, and Y. Hibino, "A chirp-OTDR using an AWG compressor," in *ECOC'96*. Telenor R & D, 1996, pp. WeP.04, vol. 3, pp. 225–228.

[147] J. Pastor-Graells, L. Romero Cortés, H. F. Martins, M. R. Fernández-Ruiz, J. Azaña, S. Martin-Lopez, and M. Gonzalez-Herraez, "20 dB SNR enhancement in phase-sensitive OTDR using pulse stretching and recompression," in *International Society for Optics and Photonics*, apr 2017, p. 103230R.

[148] F. Li, Y. Park, and J. Azaña, "Single-shot real-time frequency chirp characterization of telecommunication optical signals based on balanced temporal optical differentiation," *Optics Letters*, vol. 34, no. 18, p. 2742, sep 2009.

[149] Y. Park, M. Scaffardi, A. Malacarne, L. Potì, and J. Azaña, "Linear, self-referenced technique for single-shot and real-time full characterization of (sub-)picosecond optical pulses," *Optics Letters*, vol. 35, no. 15, p. 2502, aug 2010.

[150] Y. Park, M. Scaffardi, L. Potì, and J. Azaña, "Simultaneous single-shot real-time measurement of the instantaneous frequency and phase profiles of wavelength-division-multiplexed signals," *Optics Express*, vol. 18, no. 6, p. 6220, mar 2010.

[151] J. Azana, "Ultrafast Analog All-Optical Signal Processors Based on Fiber-Grating Devices," *IEEE Photonics Journal*, vol. 2, no. 3, pp. 359–386, jun 2010.

[152] N. Ngo, S. Yu, S. Tjin, and C. Kam, "A new theoretical basis of higher-derivative optical differentiators," *Optics Communications*, vol. 230, no. 1-3, pp. 115–129, jan 2004.

[153] N. Bergano, "Wavelength discriminator method for measuring dynamic chirp in DFB lasers," *Electronics Letters*, vol. 24, no. 20, p. 1296, 1988.

[154] R. A. Saunders, J. King, and I. Hardcastle, "Electronics letters," *Electronics Letters*, vol. 30, no. 16, pp. 1336–1338, 1994.

[155] C. Laverdiere, A. Fekecs, and M. Tetu, "A new method for measuring time-resolved frequency chirp of high bit rate sources," *IEEE Photonics Technology Letters*, vol. 15, no. 3, pp. 446–448, mar 2003.

[156] K. Sato, S. Kuwahara, and Y. Miyamoto, "Chirp Characteristics of 40-Gb/s Directly Modulated Distributed-Feedback Laser Diodes," *Journal of Lightwave Technology, Vol. 23, Issue 11, pp. 3790-*, vol. 23, no. 11, p. 3790, nov 2005.

[157] M. Matsuura, N. Iwatsu, K. Kitamura, and N. Kishi, "Time-Resolved Chirp Properties of SOAs Measured With an Optical Bandpass Filter," *IEEE Photonics Technology Letters*, vol. 20, no. 23, pp. 2001–2003, dec 2008.

[158] C. Paré, N. J. Doran, A. Villeneuve, and P.-A. Bélanger, "Compensating for dispersion and the nonlinear Kerr effect without phase conjugation," *Optics Letters*, vol. 21, no. 7, p. 459, apr 1996.

[159] R. Killey, P. Watts, V. Mikhailov, M. Glick, and P. Bayvel, "Electronic dispersion compensation by signal predistortion using digital Processing and a dual-drive Mach-Zehnder Modulator," *IEEE Photonics Technology Letters*, vol. 17, no. 3, pp. 714–716, mar 2005.

[160] K. Roberts, Chuandong Li, L. Strawczynski, M. O'Sullivan, and I. Hardcastle, "Electronic precompensation of optical nonlinearity," *IEEE Photonics Technology Letters*, vol. 18, no. 2, pp. 403–405, jan 2006.

[161] Y. Mori, C. Zhang, K. Igarashi, K. Katoh, and K. Kikuchi, "Unrepeated 200-km transmission of 40-Gbit/s 16-QAM signals using digital coherent receiver," *Optics Express*, vol. 17, no. 3, p. 1435, feb 2009.

[162] N. K. Fontaine, R. P. Scott, L. Zhou, F. M. Soares, J. P. Heritage, and S. J. B. Yoo, "Real-time full-field arbitrary optical waveform measurement," *Nature Photonics*, vol. 4, no. 4, pp. 248–254, apr 2010.

[163] C. Iaconis and I. A. Walmsley, "Spectral phase interferometry for direct electric-field reconstruction of ultrashort optical pulses," *Optics Letters*, vol. 23, no. 10, p. 792, may 1998.

[164] H. P. Bazargani, J.-B. Quelene, P. Dumais, A. Malacarne, M. Clerici, R. Morandotti, C. L. Callender, and J. Azana, "On-Chip, Single-Shot Characterization of GHz-Rate Complex Optical Signals," *IEEE Photonics Technology Letters*, vol. 26, no. 23, pp. 2345–2348, dec 2014.

[165] D. Pérez, I. Gasulla, L. Crudgington, D. J. Thomson, A. Z. Khokhar, K. Li, W. Cao, G. Z. Mashanovich, and J. Capmany, "Multipurpose silicon photonics signal processor core," *Nature Communications*, vol. 8, no. 1, p. 636, dec 2017.

[166] A. Garcia-Ruiz, J. Pastor-Graells, S. Martin-Lopez, M. Gonzalez-Herraez, A. Villafranca-Velasco, and H. F. Martins, "Sistema y metodo de caracterizacion distribuida de variaciones de indice de refraccion de una fibra optica," 2015.

[167] J. Pastor-Graells, H. F. Martins, A. Garcia-Ruiz, S. Martin-Lopez, and M. Gonzalez-Herraez, "Single-shot distributed temperature and strain tracking using direct detection phase-sensitive OTDR with chirped pulses," *Optics Express*, vol. 24, no. 12, p. 13121, jun 2016.

[168] J. Pastor-Graells, H. F. Martins, A. Garcia-Ruiz, S. Martin-Lopez, and M. Gonzalez-Herraez, "Truly Linear and Dynamic Distributed Strain Sensor using intensity-only measurements," in *Advanced Photonics 2016*. Vancouver, Canada: OSA, 2016, p. SeM3D.5.

[169] M. Gonzalez Herraez, A. Garcia-Ruiz, P. Corredera, J. Pastor-Graells, M. R. Fernández-Ruiz, H. F. Martins, and S. Martin-Lopez, "Chirped-pulse Phase-sensitive Optical Time Domain Reflectometry," in *Asia Communications and Photonics Conference 2016*. Washington, D.C.: OSA, 2016, p. AF1A.1.

[170] M. Gonzalez-Herraez, J. Pastor-Graells, A. García-Ruiz, M. R. Fernández-Ruiz, H. F. Martins, and S. Martin-Lopez, "Chirped-pulse phase-sensitive reflectometry: hearing behind the walls with high fidelity," in *25th International Conference in Optical Fiber Sensors*, Y. Chung, W. Jin, B. Lee, J. Canning, K. Nakamura, and L. Yuan, Eds. 25th International Conference in Optical Fiber Sensors, apr 2017, p. 1032302.

[171] M. R. Fernandez-Ruiz, A. Garcia-Ruiz, H. F. Martins, J. Pastor-Graells, S. Martin-Lopez, and M. Gonzalez-Herraez, "Monitoring and Early Threat Detection of Fiber-optic Links using Phase-Sensitive Optical Time-domain Reflectometry," in *19th Photonics North Conference*, Ottawa, 2017.

[172] H. F. Martins, J. Pastor-Graells, A. Garcia-Ruiz, S. Martin-Lopez, and M. Gonzalez-Herraez, "PhiOTDR with chirped pulses: a new technique for quantitative high sensitivity distributed fiber measurements," in *III International Conference on Applic- ations of Optics and Photonics (AOP)*, Faro, 2017.

[173] S. Rizzolo, E. Marin, M. Cannas, A. Boukenter, Y. Ouerdane, J. Périsse, J.-R. Macé, S. Bauer, C. Marcandella, P. Paillet, and S. Girard, "Radiation effects on optical frequency domain reflectometry fiber-based sensor," *Optics Letters*, vol. 40, no. 20, p. 4571, 2015.

[174] S. Rizzolo, C. Sabatier, A. Boukenter, E. Marin, Y. Ouerdane, M. Cannas, J. Perisse, J. R. Macé, S. Bauer, and S. Girard, "Radiation Characterization of Optical Frequency Domain Reflectometry Fiber-Based Distributed Sensors," *IEEE Transactions on Nuclear Science*, vol. 63, no. 3, pp. 1688–1693, 2016.

[175] H. Iida, Y. Koshikiya, F. Ito, and K. Tanaka, "High-Sensitivity Coherent Optical Time Domain Reflectometry Employing Frequency-Division Multiplexing," *Journal of Lightwave Technology*, vol. 30, no. 8, pp. 1121–1126, apr 2012.

[176] J. Pastor-Graells, M. R. Fernández-Ruiz, H. F. Martins, A. Garcia-Ruiz, S. Martin-Lopez, and M. Gonzalez-Herraez, "Impact of the laser phase noise on chirped-pulse phase-sensitive OTDR," in *25th International Conference on Optical Fiber Sensors*, apr 2017, p. 103238T.

[177] M. R. Fernandez-Ruiz, J. Pastor-Graells, H. F. Martins, A. Garcia-Ruiz, S. Martin-Lopez, and M. Gonzalez-Herraez, "Laser Phase-Noise Cancellation in Chirped-Pulse Distributed Acoustic Sensors," *Journal of Lightwave Technology*, vol. 36, no. 4, pp. 979–985, feb 2018.

[178] M. R. Fernández-ruiz, J. Pastor-graells, H. F. Martins, A. Garcia-ruiz, S. Martin, and M. Gonzalez-herraez, "> 10 dB SNR Enhancement in Distributed Acoustic Sensors through First Order Phase Noise Cancellation," in *Optical Fiber Communication Conference*. Washington, D.C.: OSA, mar 2018, pp. 2–4.

[179] S. Camatel and V. Ferrero, "Narrow Linewidth CW Laser Phase Noise Characterization Methods for Coherent Transmission System Applications," *Journal of Lightwave Technology, Vol. 26, Issue 17, pp. 3048-3055*, vol. 26, no. 17, pp. 3048–3055, 2008.

[180] T. Okoshi, K. Kikuchi, and A. Nakayama, "Novel method for high resolution measurement of laser output spectrum," *Electronics Letters*, vol. 16, no. 16, p. 630, 1980.

[181] J. Pastor-Graells, J. Nuno, M. R. Fernandez-Ruiz, A. Garcia-Ruiz, H. F. Martins, S. Martin-Lopez, and M. Gonzalez-Herraez, "Chirped-Pulse Phase-Sensitive Reflectometer Assisted by First-Order Raman Amplification," *Journal of Lightwave Technology*, vol. 35, no. 21, pp. 4677–4683, nov 2017.

[182] J. Ania-Castañón and S. Turitsyn, "Noise and gain optimisation in bi-directionally pumped dispersion compensating amplifier modules," 2003.

List of Publications

Publications Related to This Thesis

Refereed Journal Publications

- Maria R. Fernández-Ruiz, **Juan Pastor-Graells**, Hugo F. Martins, Andres Garcia-Ruiz, S. Martin-Lopez, and Miguel Gonzalez-Herraez, "Laser Phase-noise Cancelation in Chirped-pulse Distributed Acoustic Sensors," *Journal Lightwave Technology*, vol. 36, no. 4, pp. 979-985, 2018.
- **Juan Pastor-Graells**, Javier Nuño, Maria R. Fernández-Ruiz, Andres Garcia-Ruiz, Hugo F. Martins, S. Martin-Lopez, and Miguel Gonzalez-Herraez, "Chirped-pulse Phase-sensitive Reflectometer Assisted by First Order Raman Amplification," *Journal Lightwave Technology*, vol. 35, no. 21, pp. 4677-4683, 2017.
- **Juan Pastor-Graells**, Luis Romero Cortés, Maria R. Fernández-Ruiz, Hugo F. Martins, José Azaña, S. Martin-Lopez, and Miguel Gonzalez-Herraez, "SNR enhancement in high-resolution phase-sensitive OTDR systems using chirped pulse amplification concepts," *Optics Letters*, vol. 42, no. 9, pp. 1728-1731, 2017.
- Maria R. Fernández-Ruiz, Hugo F. Martins, **Juan Pastor-Graells**, S. Martin-Lopez, and Miguel Gonzalez-Herraez, "Phase-sensitive OTDR probe pulse shapes robust against modulation-instability fading," *Optics Letters*, vol. 41, no. 24, pp. 5756–5759, 2016.
- **Juan Pastor-Graells**, Hugo F. Martins, Andres Garcia-Ruiz, Sonia Martin-Lopez, and Miguel Gonzalez-Herraez, "Single-shot distributed temperature and strain tracking using direct detection phase-sensitive OTDR with chirped pulses," *Optics Express*, vol. 24, no. 12, pp. 13121-13133, 2016.
- Hugo F. Martins, **Juan Pastor-Graells**, Luis Romero Cortés, Daniel Piote, Sonia Martin-Lopez, José Azaña, and Miguel Gonzalez-Herraez, "PROUD-based method for simple real-time in-line characterization of propagation-induced distorsions in NRZ data signals," *Optics Letters*, vol. 40, no. 18, pp. 4356-4359, 2015.

Conference with Proceeding

- María R. Fernández-Ruiz, **Juan Pastor-Graells**, Hugo F. Martins, Andres Garcia-Ruiz, Sonia Martin-Lopez, Miguel Gonzalez-Herraez, ">10 dB SNR Enhancement in Distributed

Acoustic Sensors through First Order Phase Noise Cancellation," *Proc. of OSA Technical Digest (online) (Optical Society of America, 2016)*, W1K.2, 2018.

- María R. Fernández-Ruiz, Andres Garcia-Ruiz, Hugo F. Martins, **Juan Pastor-Graells**, Sonia Martin-Lopez, Miguel Gonzalez-Herraez, "Protecting fiber-optic links from third party intrusion using distributed acoustic sensors", *Proc. of IEEE, 19th International Conference on Transparent Optical Networks (ICTON)*, We.C3.3 (July 2-6, 2017). (Invited).

- María R. Fernández-Ruiz, Andres Garcia-Ruiz, Hugo F. Martins, **Juan Pastor-Graells**, Sonia Martin-Lopez, Miguel Gonzalez-Herraez, "Monitoring and Early Threat Detection of Fiber-optic Links using Phase-Sensitive Optical Time-domain Reflectometry", *Proc. of IEEE, Photonics North*, (June 6-8, 2017). (Invited).

- Hugo F. Martins, **Juan Pastor-Graells**, Andres Garcia-Ruiz, Sonia Martin-Lopez, Miguel Gonzalez-Herraez, "PhiOTDR with chirped pulses: a new technique for quantitative high sensitivity distributed fiber measurements", *Proc. III International Conference on Applications in Optics and Photonics (AOP 2017)*, (May 8-12, 2017). (Invited).

- Hugo F. Martins, María R. Fernández-Ruiz, **Juan Pastor-Graells**, Andres Garcia-Ruiz, Sonia Martin-Lopez, Miguel Gonzalez-Herraez, "Quantitative high sensitivity distributed fiber measurements using PhiOTDR with chirped pulses", *Proc. Commercial and Scientific Sensing and Imaging*, (April 9-13, 2017).

- **Juan Pastor-Graells**, Luis Romero Cortés, Hugo F. Martins, María R. Fernández-Ruiz, José Azaña, Sonia Martin-Lopez, Miguel Gonzalez-Herraez, "20 dB SNR enhancement in phase-sensitive OTDR using pulse stretching and recompression", *Proc. of SPIE 10323, 25th International Conference on Optical Fiber Sensors*, 103230R (April 23, 2017).

- Miguel Gonzalez-Herraez, **Juan Pastor-Graells**, Andres Garcia-Ruiz, María R. Fernández-Ruiz, Hugo F. Martins, Sonia Martin-Lopez, "Chirped-pulse phase-sensitive reflectometry: hearing behind the walls with high fidelity," *Proc. of SPIE 10323, 25th International Conference on Optical Fiber Sensors*, 1032302 (April 23, 2017). (Invited).

- **Juan Pastor-Graells**, María R. Fernández-Ruiz, Hugo F. Martins, Andres Garcia-Ruiz, Sonia Martin-Lopez, Miguel Gonzalez-Herraez, "Impact of the laser phase noise on chirped-pulse phase-sensitive OTDR," *Proc. of SPIE 10323, 25th International Conference on Optical Fiber Sensors*, 103238T (April 23, 2017).

- María R. Fernández-Ruiz, Hugo F. Martins, **Juan Pastor-Graells**, Sonia Martin-Lopez, Miguel Gonzalez-Herraez, "Impact of the probe pulse shape on the performance of phase-sensitive optical time-domain reflectometry sensors," *Proc. of SPIE 10323, 25th International Conference on Optical Fiber Sensors*, 103236P (April 23, 2017).

- Miguel Gonzalez-Herraez, Andres Garcia-Ruiz, Pedro Corredera, **Juan Pastor-Graells**, María R. Fernández-Ruiz, Hugo F. Martins, and S. Martin-Lopez, "Chirped-pulse phase-sensitive optical time-domain reflectometry," *Proc. of OSA Technical Digest (online) (Optical Society of America, 2016)*, AF1A.1, 2016. (Invited).

- **Juan Pastor Graells**, Hugo F. Martins, Andres Garcia-Ruiz, Sonia Martin-Lopez, and Miguel Gonzalez-Herraez, "Truly Linear and Dynamic Distributed Strain Sensor using intensity-only measurements," *Proc. of OSA Technical Digest (online) (Optical Society of America, 2016)*, SeM3D.5, 2016.

- **Juan Pastor-Graells**, Hugo F. Martins, Andres Garcia-Ruiz, S. Martin-Lopez, and Miguel Gonzalez-Herraez, "Dynamic distributed measurement of temperature changes using phase-sensitive OTDR with chirped pulses," *Proc. of SPIE 9916, Sixth European Workshop on Optical Fibre Sensors*, 99162Q (May 30, 2016).

Patents

- A. Garcia-Ruiz, **Juan Pastor-Graells**, S. Martin-Lopez, Miguel Gonzalez-Herraez, A. Villafranca-Velasco and H. F. Martins, "Sistema y método de caracterización distribuida de variaciones de índice de refracción de una fibra óptica," University of Alcala, P201531736.
- **J. Pastor Graells**, S. Martin-Lopez, M. Gonzalez-Herraez, A. Villafranca-Velasco, P. Corredera-Guillen and H. Fidalgo-Martins,"System and method of distributed scattering profile characterization of an optical fibre," University of Alcala, P201530793.

Other Publications

Refereed Journal Publications

- Andres Garcia-Ruiz, Alejandro Dominguez-Lopez, **Juan Pastor-Graells**, Hugo F. Martins, Sonia Martin-Lopez, and Miguel Gonzalez-Herraez, "Long-range distributed optical fiber hot-wire anemometer based on chirped-pulse ϕOTDR," *Optics Express*, vol. 26, no. 1, pp. 463-476, 2018.
- Javier Tejedor, Javier Macias-Guarasa, Hugo F. Martins, **Juan Pastor-Graells**, Sonia Martin-Lopez, Pedro Corredera, Guy De Pauw, Filip De Smet, Willy Postvoll, Carl Ahlen, and Miguel Gonzalez-Herraez, "Real Field Deployment of a Smart Fiber Optic Surveillance System for Pipeline Integrity Threat Detection: Architectural Issues and Blind Field Test Results," *Journal Lightwave Technology*, vol. 36, no. 4, pp. 1052-1062, 2018.
- Javier Tejedor, Javier Macias-Guarasa, Hugo F. Martins, **Juan Pastor-Graells**, Pedro Corredera, and Sonia Martin-Lopez, "Machine Learning Methods for Pipeline Surveillance Systems based on Distributed Acoustic Sensing: A Review," *Applied Sciences*, vol. 7, no. 8, pp. 841, 2017.
- Javier Tejedor, Javier Macias-Guarasa, Hugo F. Martins, **Juan Pastor-Graells**, Pedro Corredera, and Sonia Martin-Lopez, "Machine Learning Methods for Pipeline Surveillance Systems based on Distributed Acoustic Sensing: A Review," *Applied Sciences*, vol. 7, no. 8, pp. 841, 2017.
- Javier Tejedor, Javier Macias-Guarasa, Hugo F. Martins, Daniel Piote, **Juan Pastor-Graells**, Sonia Martin-Lopez, Pedro Corredera, and Miguel Gonzalez-Herraez, "A Novel Fiber Optic Based Surveillance System for Prevention of Pipeline Integrity Threats," *Sensors*, vol. 17, no. 2, pp. 355-373, 2017.

- Andres Garcia-Ruiz, **Juan Pastor-Graells**, Hugo F. Martins, Kenny Hey Tow, Luc Thévenaz, S. Martin-Lopez, and Miguel Gonzalez-Herraez,"Distributed photothermal spectroscopy in microstructured optical fibers: towards high-resolution mapping of gas presence over long distances," *Optics Express*, vol. 25, no. 3, pp. 1789-1805, 2017.

- Andres Garcia-Ruiz, **Juan Pastor-Graells**, Hugo F. Martins, Sonia Martin-Lopez, and Miguel Gonzalez-Herraez, "Speckle analysis method for distributed detection of temperature gradients with ϕOTDR," *Photonic Technology Letters*, vol. 28, no. 18, pp. 2000-2003, 2016.

- Javier Tejedor, Hugo F. Martins, Daniel Piote, Javier Macias-Guarasa, **Juan Pastor-Graells**, Sonia Martin-Lopez, Pedro Corredera, Filip De Smet, Willy Postvoll, and Miguel Gonzalez-Herraez, "Towards Prevention of Pipeline Integrity Threats using a Smart Fiber Optic Surveillance System," *Journal of Lightwave Technology*, vol. 34, no. 19, pp. 4445-4453, 2016.

Conference with Proceeding

- Andres Garcia-Ruiz, Alejandro Dominguez-Lopez, **Juan Pastor-Graells**, Hugo F. Martins, Sonia Martin-Lopez, and Miguel Gonzalez-Herraez, "Long-range, Power-efficient Distributed Flow Measurements Using Chirped-pulse Phase-sensitive Reflectometry," *Proc. of OSA Technical Digest (online) (Optical Society of America, 2016)*, W1K.3, 2018.

- Andres Garcia-Ruiz, **Juan Pastor-Graells**, Hugo F. Martins, Kenny Hey Tow, Luc Thévenaz, Sonia Martin-Lopez, Miguel Gonzalez-Herraez, "Distributed photothermal measurements of gas presence along holey optical fibers," *Proc. of SPIE 10323, 25th International Conference on Optical Fiber Sensors*, 1032361 (April 23, 2017).

- J. Tejedor, J. Macias-Guarasa, H. F. Martins, D. Piote, **Juan Pastor-Graells**, S. Martin-Lopez, P. Corredera, G. De Pauw, F. De Smet, W. Postvoll, C. H. Ahlen, M. Gonzalez-Herraez, "Towards detection of pipeline integrity threats using a smart fiber optic surveillance system: PIT-STOP project blind field test results," *Proc. of SPIE 10323, 25th International Conference on Optical Fiber Sensors*, 103231K (April 23, 2017).

- Andres Garcia-Ruiz, H. F. Martins, **Juan Pastor-Graells**, S. Martin-Lopez, and Miguel Gonzalez-Herraez,"Single-Shot True Distributed Strain Variation Measurements Over >10 km Using Phase-Sensitive OTDR with Chirped Pulses," *Proc. of OSA Technical Digest (online) (Optical Society of America, 2016)*, Th3A.2, 2016.

- Andres Garcia-Ruiz, **Juan Pastor-Graells**, Hugo F. Martins, S. Martin-Lopez, and Miguel Gonzalez-Herraez, "Distributed detection of temperature gradients with single-wavelength phase-sensitive OTDR and speckle analysis methods," *Proc. of SPIE 9916, Sixth European Workshop on Optical Fibre Sensors*, 99162R (May 30, 2016).

- H. F. Martins, D. Piote, J. Tejedor, J. Macias-Guarasa, **J. Pastor-Graells**, S. Martin-Lopez, P. Corredera, F. De Smet, W. Postvoll, C. H. Ahlen, and Miguel Gonzalez-Herraez, "Early Detection of Pipeline Integrity Threats using a SmarT Fiber-OPtic Surveillance System: The PIT-STOP Project," *Proc. of SPIE 9634, 24th International Conference on Optical Fiber Sensors*, 96347X (September 28, 2015).

- **Juan Pastor Graells**, Hugo F. Martins, Sonia Martin-Lopez, and Miguel Gonzalez-Herraez, "Distributed measurement of vibrations in a ramified fiber structure using phase sensitive optical time domain reflectometry and wavelength routing concepts," *Proc. of OSA Technical Digest (online) (Optical Society of America, 2014)*, SeW1C.5, 2014.

Patents

- **Juan Pastor-Graells**, S. Martin-Lopez, Miguel Gonzalez-Herraez, A. Villafranca-Velasco, "Sistema y método de caracterización distribuida continúa de un medio de fibra óptica," University of Alcala, P201400607.

Appendix A

List of Symbols

Symbol	Physical Meaning	Units
α (α_{dB})	*Fiber Attenuation*	km^{-1} (dB/km)
α_R	*Fiber Attenuation due to Rayleigh Scattering*	dB/km o km^{-1}
α_{Rb}	*Rayleigh Backscattering Coefficient*	dB/m o m^{-1}
β	*Fiber Propagation Constant*	m^{-1}
β_1	*Group Velocity Inverse*	ps/km
β_2	*Group Velocity Dispersion*	ps^2/km
$\ddot{\Phi}$	*Second-Order Dispersion*	ps^2
γ	*Non-Linear Parameter*	1/W·km
ε (ε_0)	*Electric Permittivity in the Medium (in Vacuum)*	F/m
ε_r ($\varepsilon_{r,NL}$)	*Relative Permittivity (Non-Linear)*	-
λ	*Wavelength*	nm
λ_D	*Zero Dispersion Wavelength*	nm
μ_0	*Magnetic Permeability in Vacuum*	N/A^2
ω	*Angular Frequency*	rad/s
$\chi^{(i)}$	*Linear/Non-Linear Susceptibility*	$(m/V)^{i-1}$
τ_c	*Coherence Time*	s
A_{eff}	*Effective Core Area*	μm^2
c	*Speed of Light in Vacuum*	m/s
D	*Chromatic Dispersion Coefficient*	$ps \cdot nm^{-1} \cdot km^{-1}$
h	*Plank Constant*	J·s
k_B	*Boltzmann Constant*	$J \cdot K^{-1}$
l_c	*Coherence Length*	m
n	*Refractive Index*	-
n_0	*Lineal Refractive Index*	-
n_2	*Non-Lineal Refractive Index*	-
P	*Optical Power*	dBm or mW
v_p	*Phase Velocity*	m/s
v_g	*Group Velocity*	m/s

Appendix B

List of Acronyms

Acronym	Meaning
ASE	*Amplified Spontaneous Emission*
BFS	*Brillouin Frequency Shift*
BGS	*Brillouin Gain Spectrum*
BOCDA	*Brillouin Optical Correlation Domain Analysis*
BOTDA	*Brillouin Optical Time Domain Analysis*
BOTDR	*Brillouin Optical Time Domain Reflectometry*
OFDR	*Coherent Optical Frequency Domain Reflectometry*
COTDR	*Coherent Optical Time Domain Reflectometry*
CPA	*Chirped Pulse Amplification*
CW	*Continuous Wave*
DC	*Direct Current*
DCF	*Dispersion-Compensating Fiber*
DFB	*Distributed Feedback*
DOFS	*Distributed Optical Fiber Sensor*
DWDM	*Dense Wavelength Division Multiplexer*
ECL	*External Cavity Laser*
EDFA	*Erbium Doped Fiber Amplifier*
EOM	*Electro-Optic Modulator*
ER	*Extinction Ratio*
FBG	*Fiber Bragg Grating*
FIR	*Far-Infrared*
FFT	*Fast Fourier Transform*
FPGA	*Field Programmable Gate Arrays*

Acronym	Meaning
FPU	*Fermi-Pasta-Ulam*
FUT	*Fiber Under Test*
FWHM	*Full-Width at Half Maximum*
GVD	*Group Velocity Dispersion*
IFFT	*Inverse Fast Fourier Transform*
INRS	*Institut National de la Recherche Scientifique*
I&T	*Current and Temperature*
LC-FBG	*Linearly Chirped Fiber Bragg Gratings*
LFM	*Linear Frequency Modulation*
LD	*Laser Diode*
LO	*Local Oscillator*
MI	*Modulation Instability*
NLSE	*Non-Linear Schrödinger's Equation*
NRZ	*Non-Return-to-Zero*
OFDR	*Optical Frequency Domain Reflectometry*
OPCR	*Optical Pulse Compression Reflectometry*
OSA	*Optical Spectrum Analyzer*
OTDR	*Optical Time Domain Reflectometry*
PS	*Polarization Scrambler*
PMF	*Polarization-Maintainer Fiber*
POTDR	*Polarization Optical Time Domain Reflectometry*
PRBS	*Pseudorandom Binary Sequence*
PROUD	*Phase Reconstruction using Optical Ultrafast Differentiation*
PSD	*Power Spectral Density*
PSK	*Phase-Shift Keying*
PZT	*Piezoelectric Transducer*
ϕOTDR	*Phase Sensitive Optical Time Domain Reflectometry*
RFL	*Raman Fiber Laser*
RFS	*Raman Frequency Shift*
RIN	*Relative Intensity Noise*
RZ	*Return-to-Zero*
SA-BOTDA	*Slope-Assited Brillouin Optical Time Domain Analysis*
SBS	*Stimulated Brillouin Scattering*
SG	*Signal Generator*

Acronym	Meaning
SMF	*Single Mode Fiber*
SNR	*Signal to Noise Ratio*
SOA	*Semiconductor Optical Amplifier*
SOP	*State Of Polarization*
SPM	*Self-Phase Modulation*
SRS	*Stimulated Raman Scattering*
THG	*Third−Harmonic Generation*
UV	*Ultraviolet*
WDM	*Wavelength Division Multiplexer*